TECHNISCHE UNIVERSITÄT MÜNCHEN

Lehrstuhl E23 für Technische Physik

Walther-Meißner-Institut für Tieftemperaturforschung
der Bayerischen Akademie der Wissenschaften

Spin Caloritronics in Ferromagnet/Normal Metal Hybrid Structures

Sibylle Ursula Meyer

Vollständiger Abdruck der von der Fakultät für Physik der Technischen
Universität München zur Erlangung des akademischen Grades eines

Doktors der Naturwissenschaften

genehmigten Dissertation.

Vorsitzender:	Univ.–Prof. Dr. J. L. van Hemmen (i. R.)
Prüfer der Dissertation:	1. Univ.–Prof. Dr. R. Gross
	2. apl. Prof. Dr. M. S. Brandt

Die Dissertation wurde am 19.11.2015 bei der Technischen Universität München
eingereicht und durch die Fakultät für Physik am 17.12.2015 angenommen.

To Carolin and her grandfather.

Abstract

The field of spin caloritronics encloses interactions between temperature, charge and spin currents. The rapidly emerging information technology up to now is based on electronic transport effects. However, it's ongoing miniaturization is limited by the generation of Joule heating. Motivated by this thermodynamic limitation, pure spin currents are a cutting-edge approach paving the way for further developments.

In the first part of this thesis, we discuss the interplay of charge and spin currents in ferromagnet/normal metal hybrid structures. This results in a characteristic modulation of the resistivity in a normal metal with respect to the magnetization orientation of the ferromagnetic insulator. In a series of experiments on yttrium iron garnet(YIG)/platinum (Pt) bilayer samples, we characterize this so-called spin Hall magnetoresistance (SMR) as a function of the platinum thickness. thereby, we establish a novel method to extract spin transport properties from all-electrical measurements. We investigate the temperature dependence of the magnetoresistive signal and link the decrease of the resistance modulation with the spin Hall angle θ_{SH} in platinum, i.e. a charge to spin conversion efficiency.

We furthermore report on an anomalous Hall-like effect in platinum that is directly connected to the presence of YIG. Our observation can be linked to the SMR theory. This interpretation enables the study of the interface spin transport properties in terms of the complex spin mixing conductance $G_{\uparrow\downarrow}$. Our experiments indicate that transverse magnetoresistive effects in YIG/Pt are dominated by the imaginary part G_i of $G_{\uparrow\downarrow}$ and we extract a strong temperature dependence for G_i.

Finally, we demonstrate the generation of a spin current in platinum transverse to an applied temperature gradient, known as the spin Nernst effect. We proof the existence of the spin Nernst spin current by externally controlling the boundary conditions for a spin current flow across the interface to an adjacent layer of YIG. This results in a characteristic modulation of the thermopower voltage in platinum. We develop a theoretical framework based on the spin diffusion theory and the interaction of the spin Nernst and inverse spin Hall effect. We find an excellent qualitative agreement with our experimental data. This enables a first experimental estimation of the heat to spin conversion efficiency, the spin Nernst angle θ_{SN}. We find that θ_{SN} is about a factor of two larger than θ_{SH} in platinum, but is of opposite sign. This observation is also corroborated by recent first-principle calculations. The experimental proof of the spin Nernst effect motivates the combination of existing heat losses in electronic components with spin caloritronic effects.

Kurzfassung

Das Gebiet der Spinkaloritronik beschreibt das Wechselspiel von Temperatur, elektrischer Ladung und Spinströmen. Die sich rasch entwickelnde Informationstechnologie basiert bisher auf elektronischen Transporteffekten und ist in ihrer Miniaturisierung durch die Entstehung Joule'scher Wärme begrenzt. Dies macht Spinströme, die dieser thermodynamischen Limitierung nicht unterliegen, zu einem innovativen Ansatz für weiterführende Entwicklungen.

Im ersten Teil dieser Arbeit diskutieren wir das Wechselspiel aus elektrischen Strömen und Spinströmen in Hybridsystemen aus einem Normalmetall und einem ferromagnetischen Isolator. Dieses Wechselspiel führt zu einer charakteristischen Modulation des Metallwiderstandes als Funktion der Magnetisierungsorientierung des ferromagnetischen Isolators. Anhand einer Messereihe an Yttrium-Eisen-Granat (engl. yttrium iron garnet, YIG)/Platin Bilagen charakterisieren wir die Platin-Schichtdickenabhängigkeit des sogenannten Spin Hall Magnetwiderstands (engl. spin Hall magnetoresistance, SMR). Damit etablieren wir eine neuartige Bestimmungsmethode für Spin-Transport Parameter aus einer rein elektrischen Detektion. Wir untersuchen die Temperaturabhängigkeit des Magnetwiderstandes und können den Signalabfall mit dem Spin-Hall-Winkel θ_{SH} für Platin verknüpfen.

Des Weiteren diskutieren wir einen anomalen Hall-Effekt in Platin, der direkt an die Präsenz der YIG-Schicht gekoppelt ist. Diese Beobachtung kann mit der SMR Theorie verknüpft werden und ermöglicht so die Untersuchung der komplexen Grenzflächen-Spinleitfähigkeit $G_{\uparrow\downarrow}$. Unsere Experimente zeigen, dass transversale Magnetwiderstandseffekte in YIG/Platin von dem Imaginärteil G_i von $G_{\uparrow\downarrow}$ dominiert werden und lassen auf eine starke Temperaturabhängigkeit von G_i schließen.

Außerdem demonstrieren wir die Erzeugung von Spinströmen transversal zu einem Temperaturgradienten in Platin, genannt der Spin-Nernst-Effekt. Wir weisen die Existenz dieses Spinstroms experimentell nach, indem wir die Randbedingungen für einen Spintransport über die Grenzfläche zu einer benachbarten YIG-Schicht extern manipulieren. Dies führt zu einer charakteristischen Modulation der Thermokraft. Basierend auf der Spindiffusionstheorie und dem Wechselspiel aus Spin-Nernst und inversem Spin-Hall-Effekt entwickeln wir ein theoretisches Modell, das eine exzellente qualitative Übereinstimmung mit unseren experimentellen Daten zeigt. Dies ermöglicht eine erste Abschätzung der Umwandlungseffizienz von Wärme in Spinströme, parametrisiert durch den Spin-Nernst-Winkel θ_{SN}. Dieser nimmt etwa den doppelten Wert von θ_{SH} ein, zeigt aber ein umgekehrtes Vorzeichen, was durch theoretische Berechnungen bestätigt wird. Der experimentelle Nachweis des Spin-Nernst-Effekts motiviert die Kombination aus bestehenden Wärmeverlusten in elektrischen Bauteilen mit Effekten der Spinkaloritronik.

Contents

List of Figures

1 Introduction

> *Quoque magis tegitur, tectus magis aestuat ignis.*
> The more the fire was hidden, the more it blazed.

These words were written around 8 AD by the Roman poet Publius Ovidius Naso, better known as *Ovid*, in the saga of Pyramus and Thisbe, part of his famous *Metamorphoses* [1]. By only slightly modifying this sentence to "the more the fire was *discovered*, the more it blazed", one can quite accurately describe a rising field in solid state physics, the so-called *spin caloritronics*.

Around two centuries ago, the effect of a temperature gradient on the electronic system of a metal was discovered [2] and the Seebeck-, Peltier- and Thomson-effects formed the basis of thermoelectrics [3–5]. The following time was dedicated to charge current based phenomena, comprised by the generic term *electrics*. However, the introduction of the spin angular momentum or just spin as the electron's internal degree of freedom besides its elementary properties like charge and mass [6,7] opened up a new era called *spintronics*. While spintronics studies the coupling between spin and charge transport, Johnson and Silsbee [8] predicted that the transport of heat in a ferromagnetic system is also associated with the transport of spin. Thus, the combination of well-known phenomena from thermoelectrics with spintronics led to a new sub-area called *spin caloritronics*. The artificial word "Caloritronics" coined around 2010 [9–11] is a conjunction of *calor*, the Latin word for heat, and spintronics, meeting the key message of Johnson and Silsbee's proposal: a novel field dealing with non-equilibrium phenomena related to spin, charge, entropy and energy transport in (mostly) magnetic structures and devices [10].

However, dealing with heat is not what makes a topic "hot". The invention of the transistor in 1947 triggered the fast development of semiconductor based electronics to the point of today's ubiquitous modern information technology. Themed e.g. by Fujitsu's guiding principle "the possibilities are infinite", the ongoing miniaturization of devices combined with an enhancement of the processing power (Moore's law [12]) culminated in the formulation of Intel's *tick-tock* model in 2006 [13]: Every "tick" represents a shrinking of the process technology of the previous microarchitecture and every "tock" designates a new microarchitecture. According to Intel, the appearance of a tick or tock is expected every twelve to 18 months. Over a period of almost one decade, this led to a processor architecture size reduction down from over $100\,\mathrm{nm}$ to $22\,\mathrm{nm}$ in 2012. In September 2014, the

1

latest tick was announced by Intel under the codename *Broadwell* with a process length scale of 14 nm [13]. However, further possibilities for miniaturizations will be limited by the impending breakdown of Moore's Law by the "thermodynamic bottleneck" [10]: charge currents applied to the nanostructures inherent in modern electronics devices are insuperably accompanied by an Ohmic energy dissipation, which severely limits downscaling.

In contrast to charge-mediated electronics, spin current based concepts are promising candidates to solve this issue. Murakami *et al.* predicted that pure spin currents, i.e., a flow of spin angular momentum without an accompanying charge current, are dissipationless [14] such that spin-based electronics might be much less restricted by heat management issues. Additionally, harvesting the heat dissipated in electronic devices in (add-on) spin caloritronic structures is an elegant way for future developments. Therefore, spin caloritronics indeed is a "hot" topic for the 21st century's society.

This thesis aims to provide an experimental approach towards a fundamental understanding of spin caloritronics in ferromagnet/normal metal bilayers. Within this work, the advantage of the ferrimagnetic insulator[1] yttrium iron garnet (YIG) capped with a thin platinum layer represents a common ground for the different chapters. This material combination became quite popular during the past years: On the one hand, the electrically insulating properties of YIG allow for a clear separation of charge currents (restricted to the normal metal) and spin currents (allowed to propagate in both layers) in this bilayer system. On the other hand, the normal metal platinum (Pt) features a distinct spin orbit interaction, resulting in large spin current generation efficiencies. The interplay of both characteristics makes this material combination a promising candidate for industrial applications.

This work is organized as follows:
In Chapter 2, we start with the basic ingredients of electrical spin current generation and its consecutive detection in a normal metal. By attaching a ferromagnetic insulator (FMI) to a normal metal (N), a spin current excited in N can cross the FMI/N interface via spin transfer torque. Since this spin angular momentum transfer is governed by the orientation of the magnetization in the FMI layer, one obtains a powerful tool to control spin currents by manipulating the magnetization vector of the ferromagnet. This effect is called the spin Hall magnetoresistance (SMR). Taking advantage of a theoretical model suggested by Chen *et al.* [15], we utilize the SMR for a study of spin transport characteristics in the charge channel in YIG/Pt bilayers. We find an excellent qualitative and

---

[1]Within this thesis, we use the term "ferromagnetic" for both ferro- and ferri-magnetic materials for simplicity reasons. In this context, the term "ferromagnetic insulator" describes an electrically insulating material which exhibits a long-range ferro- or ferrimagnetic order.

quantitative agreement of our experimental data with this theory, and our experiments on a set of YIG/Pt bilayers with different Pt thicknesses enable the extraction of a full set of spin transport parameters as a function of temperature. Furthermore, we show that by studying the SMR as a function of the external magnetic field strength, the anisotropy of the insulating YIG can be probed electrically. This work motivates the advantage of the SMR as a new, easy-to-handle characterization technique e.g. to probe novel FMI/N material combinations for their applicability in spintronics.

While Chapter 2 focuses on the longitudinal magnetoresistance in YIG/Pt hybrids, we study the transverse magnetoresistive signal in Chapter 3. We perform a temperature dependent study of the transverse Pt resistance as a function of the magnetic field amplitude in a Hall-like geometry and find a distinct anomalous Hall-like signal in Pt deposited on YIG, which is unexpected for a non-magnetic normal metal at first sight. However, by linking our findings with the spin transfer torque at the YIG/Pt interface, we can explain this phenomenon with a transverse SMR-related effect, the so-called spin Hall anomalous Hall effect. The absence of this feature in plain Pt thin films directly deposited onto the substrate as well as an excellent agreement with the transverse SMR theory confirm our findings. Therefore, our analysis allows for an experimental extraction of the imaginary part of the spin mixing conductance, which according to theory describes the phase shift of the spin current in N with respect to the spin current injected to the ferromagnetic layer. Additionally, a study of the transverse magnetoresistance as a function of the magnetization orientation reveals higher order contributions to this anomalous Hall like features, again only visible in the presence of YIG. Even though - or just because - a fundamental explanation of this discovery is still under discussion, our experiments show that spin caloritronics can not be interpreted as "just" a spin-mediated resumption of thermoelectric effects, but as a precursor on the way to deeper insights to solid state physics.

In Chapter 4, we report on the first experimental observation of the spin Nernst effect (SNE) in platinum, i.e. the generation of a spin current perpendicular to a temperature gradient. This effect can be interpreted as a thermal relative of the spin Hall effect and represents one of the last experimentally elusive links between thermoelectrics and spin caloritronics. We take advantage of the spin transfer torque into an adjacent YIG layer to enable the detection of the spin Nernst spin current in the charge channel as a thermopower voltage. Via magnetization orientation dependent experiments, we are able to visualize the SNE as a modulation of the thermopower. Our data enables a first experimental estimation of the heat to spin conversion efficiency, the spin Nernst angle θ_{SN}. Interestingly, our analysis suggests an opposite sign for θ_{SN} compared to its charge

current driven counterpart, the spin Hall angle θ_{SH}. Our experimental findings coincide with recent first-principle calculations for the spin Nernst angle. The observation of the spin Nernst effect reported in this work not only reveals one of the last missing links between temperature and spin transport, but also opens a new opportunity to combine electric heat losses with spintronic information processing.

Finally, the obtained experimental results are summarized in Chapter 5. Thereby, we propose further investigations in the field of spin caloritronics based on the results presented in this thesis. Fanned by this contribution, too, the fire of spin caloritronics will blaze even brighter in the years to come.

2 Spin Hall magnetoresistance

Pure spin currents - a flow of spin angular momentum with no accompanying charge current - represent a new paradigm for spin electronics. In the past decade, two distinctly different methods to develop a pure spin current have been evolved: the spin pumping effect [16–27] and the spin Seebeck effect (SSE) [28–41]. In both effects, ferromagnet (F)/normal metal (N) hybrid structures are utilized to generate and detect spin currents. In the beginning, those bilayers were consisting of conductive F and conductive N layers. However, in the past five years ferromagnetic insulators (FMI) came into focus. FMIs are materials with a long-range magnetic order, that enable the propagation of magnetic excitations (spin currents), but at the same time are electrically insulating. Therefore, they allow for a clean separation of spin and charge currents, since the charge current is restricted to the conductive N layer, while spin currents can propagate in the FMI as well as in N. This in particular resulted in a renewed interest in the ferrimagnetic insulator yttrium iron garnet ($Y_3Fe_5O_{12}$, YIG) [34, 37, 41–48]. Recently, a characteristic magnetoresistive effect was reported in YIG/Pt heterostructures by different groups [41, 43–49]. This magnetoresistance in FMI/N hybrids can be understood as a spin current-based effect, the so-called spin Hall magnetoresistance (SMR) [15, 44, 46]. On the other hand, Huang *et al.* [43] and Lu *et al.* [47, 49] ascribed the observed magnetoresistance to a static magnetic proximity effect at the YIG/Pt interface.

In this chapter, we experimentally study this novel magnetoresistance in a set of YIG/Pt bilayer samples with different Pt thicknesses. We therefore start with a theoretical approach in Sec. 2.1, introducing the basic mechanism behind the spin Hall magnetoresistance from both a gedankenexperiment (cf. Sec. 2.1.5) and a theoretical calculation (cf. Sec. 2.1.6). We additionally take into account the competing interpretation in a magnetic proximity effect framework in Sec. 2.1.7. After a brief introduction to the experimental setup and measurement techniques in Sec. 2.2, we enter the experimental part of this chapter with a detailed discussion of the magnetoresistive signals in YIG/Pt at room temperature in Sec. 2.3. Afterwards, we experimentally study the temperature-dependent evolution of the magnetoresistance in a set of YIG/Pt bilayer samples with different Pt thicknesses. Using the SMR theory, we extract the spin transport characteristics of the YIG/Pt bilayer, namely the effective spin diffusion length $\lambda(T)$ in Pt, the real part of the

spin mixing conductance $G_r(T)$ of the YIG/Pt interface, as well as the spin Hall angle $\theta_{SH}(T)$ in Pt. We close this section with a study of the influences from the ferromagnetic layer by varying the FMI thickness in YIG/Pt bilayer samples with constant Pt thicknesses in Sec. 2.5. A condensed form of the key results presented in this chapter is published in Refs. [46] and [50].

2.1 Spin currents in normal metal/ferromagnetic insulator hybrids

This section introduces the concept and theoretical model of the spin Hall magnetoresistance. We start with a definition of spin currents in Sec. 2.1.1 and discuss their generation and detection via the (inverse) spin Hall effect (cf. Sec. 2.1.2). After a brief introduction into the characteristic length scales in Sec. 2.1.3, we discuss the scenario of a spin current flowing across a N/F interface in Sec. 2.1.4. Combining the concept of the spin Hall effect and its inverse for a N/FMI bilayer leads to the recently reported effect of the spin Hall magnetoresistance. Starting from a phenomenological description in Sec. 2.1.5, a quantitative model of the spin Hall magnetoresistance follows in Sec. 2.1.6. Finally, in Sec. 2.1.7 we will introduce the competing model of the magnetic proximity magnetoresistance.

2.1.1 Spin currents

More than 90 years ago, the Stern-Gerlach experiment [51,52] demonstrated the quantized nature of angular momentum and formed the basis for *quantum mechanics* [53]. On the basis of this experiment, Goudsmith and Uhlenbeck [6, 7] proposed the existence of an intrinsic angular momentum for electrons, the spin angular momentum or short *spin*. The discovery of this additional degree of freedom beside the charge $q = -e$ [1] of electrons enabled the emergent field of *spintronics*, covering the generation, propagation and detection of spin information. In the following, we consider electric charge currents carried by electrons. In a two spin channel model of "spin up" and "spin down" states, $n_\uparrow$ ($n_\downarrow$) represent the number of electrons with spin up (spin down) propagating with a velocity $\mathbf{v}_\uparrow$ ($\mathbf{v}_\downarrow$). The electric charge current density $\mathbf{j}_q$ can be written as the sum of spin up and spin down charge current densities $\mathbf{j}_{q,\uparrow} = qn_\uparrow\mathbf{v}_\uparrow$ and $\mathbf{j}_{q,\downarrow} = qn_\downarrow\mathbf{v}_\downarrow$ propagating along the same direction,

$$\mathbf{j}_q = (\mathbf{j}_{q,\uparrow} + \mathbf{j}_{q,\downarrow}), \tag{2.1}$$

---

[1] we use $e = |e|$, where e is the absolute value of the elementary charge, $e \approx 1.602 \times 10^{-19}$ C.
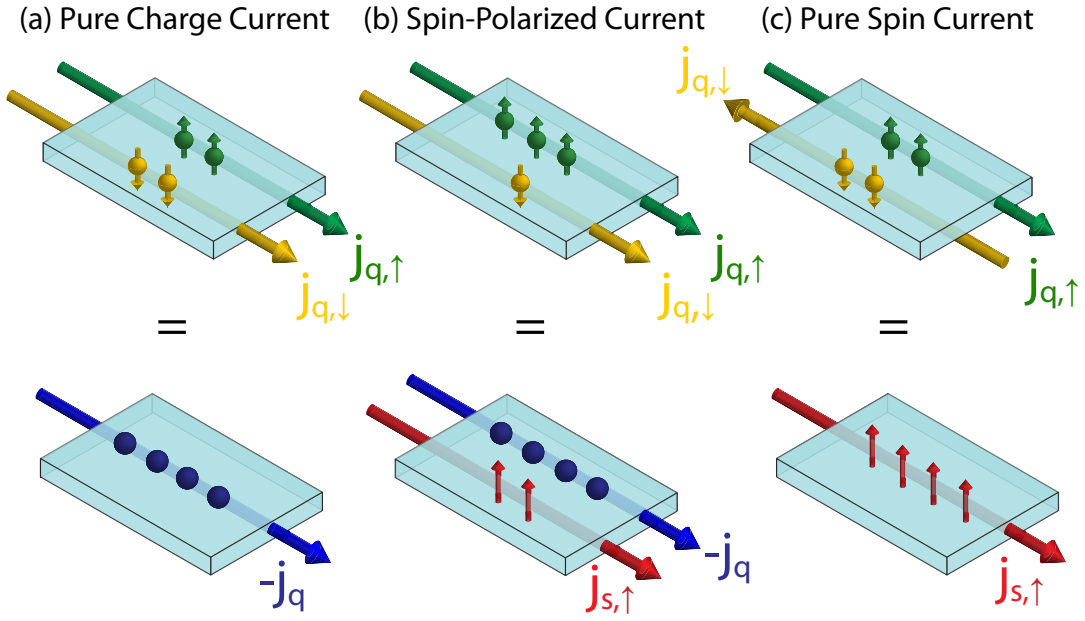
Figure 2.1: The three different types of currents. **(a)** In a pure charge current, an equal number of spin up ($|\uparrow\rangle$) and spin-down ($|\downarrow\rangle$) electrons propagate in the same direction, $\mathbf{j}_{q,\uparrow} \parallel \mathbf{j}_{q,\downarrow}$. This leads to a propagation of charge, but no net flow of angular momentum. **(b)** If $|\uparrow\rangle$ and $|\downarrow\rangle$ propagate in the same direction, but the number of $|\uparrow\rangle$ and $|\downarrow\rangle$ are different, this results in a transport of both, spin and charge. In this case, one speaks of a spin-polarized current. **(c)** Assuming $|\uparrow\rangle$ and $|\downarrow\rangle$ spins of equal number propagating in opposite directions, this leads to a net transport of spin, but no net charge current contribution. This scenario is called pure spin current. Figure in analogy to [54].

while a spin current density $\mathbf{j}_{s,\mathbf{s}}$ associated with the charge current[2] is given by the difference of spin up and spin down charge current densities,

$$\mathbf{j}_{s,\mathbf{s}} = \frac{\hbar}{2q} \left(\mathbf{j}_{q,\uparrow} - \mathbf{j}_{q,\downarrow} \right) . \tag{2.2}$$

As an electron carries both, it's charge $-e$ and it's spin angular momentum $\hbar/2$, in literature the prefactor $\hbar/2e$ is used for $\mathbf{j}_{s,\mathbf{s}}$ sometimes [54]. This reflects the fact that the charge current density $\mathbf{j}_q$ as well as $\mathbf{j}_{q,\uparrow}$ and $\mathbf{j}_{q,\downarrow}$ are considered as the flow of charge carriers in units of $[\mathrm{A/m^2}]$, whereas $\mathbf{j}_{s,\mathbf{s}}$ is considered as a flow of angular momentum and therefore is written in units of $[\mathrm{A/m^2} \cdot \hbar/e]$. In our notation, a positive spin current thus represents the propagation direction of $|\uparrow\rangle$ particles. With the definitions given in Eqs. (2.1) and (2.2), we additionally distinguish three different cases:

1. If the numbers of both spin states $|\uparrow\rangle$ and $|\downarrow\rangle$ are equal and $\mathbf{j}_{q,\uparrow}$ is parallel to $\mathbf{j}_{q,\downarrow}$ [yellow and green arrow in Fig. 2.1(a), respectively], this corresponds to a net charge current that is not accompanied by a transport of angular momentum. We define

---

[2]The index $\mathbf{s}$ in $\mathbf{j}_{s,\mathbf{s}}$ denotes the spin polarization axis. Therefore, $\mathbf{j}_{s,\mathbf{s}}$ is a tensor.

this as a *pure charge current*. This case is applicable e.g. for conventional param-
agnetic conductors without spin-orbit coupling.

2. If the numbers of both spin states are not equal, like depicted in Fig. 2.1(b), both
   charge and spin information are transported and we speak of a *spin-polarized cur-
   rent*. This scenario can be found in materials with an imbalance of spin-up and
   spin-down charge carriers at the Fermi level, which are called charge conductors.

3. Assuming that both spin current densities are equal in amplitude, but flowing in
   opposite directions [cf. yellow and green arrows in Fig. 2.1(c)], $\mathbf{j}_{q,\uparrow} = -\mathbf{j}_{q,\downarrow}$, leads
   to a transport of spin angular momentum that is not accompanied by a net charge
   current. This pure flow of spin is called a *pure spin current*.

2.1.2 Spin current generation and detection in normal metals: SHE and ISHE

It was already discussed above that spin polarized currents can be found in ferromagnetic
conductors, whereas paramagnetic conductors contain pure charge currents. Taking this
into account, the prediction of the generation of a pure spin current in a paramagnetic
metal from a charge current via the so-called *spin Hall effect* is even more surprising
[55, 56]. The spin-orbit interaction in a conductor leads to an asymmetric scattering of
spin up and spin down electrons. The scattering mechanisms are divided into extrinsic
mechanisms, named *skew scattering* [57] and *side-jump scattering* [58] and intrinsic effects,
which are related to the Berry curvature [59–62]. A detailed overview of the mechanisms
can e.g. be found in Ref. [63] and [64].

In ferromagnetic conductors, these effects lead to a spin polarized current perpendicular
to the charge current flow that is observable even in the absence of an external magnetic
field. This phenomenon is referred to as the *anomalous Hall effect* [65] and will be
addressed later (cf. Ch. 3). Additionally, the same mechanisms give rise to a pure spin
current perpendicular to an applied charge current, even in non-ferromagnetic materials.
In analogy to the conventional Hall effect [66] the existence of a spin current transverse
to a charge current is named *spin Hall effect* (SHE) and was observed experimentally in
2004 by Kato *et al.* for the first time [67].

To illustrate the SHE, we consider a plain non-ferromagnetic metal film. In the following,
we assume an electric charge current $\mathbf{j}_q \parallel \mathbf{j}$ (cf. Fig. 2.2). Without loss of generality, we
consider the spin polarization axis $\mathbf{s}$ along the $\mathbf{n}$ direction. The electrons moving along
$-\mathbf{j}$ carry both, spin up and spin down angular momentum in equal distribution $n_\uparrow = n_\downarrow$,
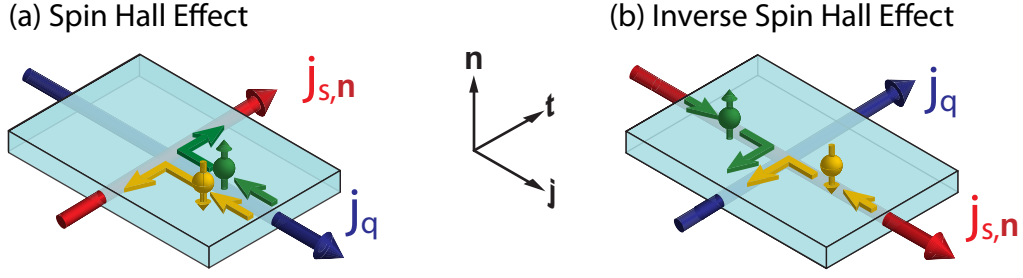
Figure 2.2: (a) Spin Hall effect. A pure charge current $\mathbf{j}_q$ consists of both, spin up and spin down electrons in equal parts. Due to spin orbit interaction, both spin species are deflected in opposite directions perpendicular to both, the charge current direction and the spin polarization axis. This results in a pure spin current $\mathbf{j}_{s,\mathbf{n}}$. In **(b)**, we consider the opposite scenario. A pure spin current $\mathbf{j}_{s,\mathbf{n}}$ gives rise to a charge current perpendicular to the spin current direction and spin polarization axis (inverse spin Hall effect). Figure in analogy to [54].

where $n_\uparrow$ and $n_\downarrow$ again indicate the number of $|\uparrow\rangle$ and $|\downarrow\rangle$ particles, respectively. The mechanisms based on spin orbit interaction introduced above give rise to a force on the electrons that is perpendicular to both, the propagation axis $\mathbf{j}$ and the spin polarization axis $\mathbf{n}$. Due to this interaction, spin up electrons are deflected along $+\mathbf{t}$, while spin down electrons are deflected along $-\mathbf{t}$. This separation of both spin species leads to a pure spin current $\mathbf{j}_{s,\mathbf{n}}$ along the $+\mathbf{t}$ direction with spin polarization $\mathbf{s} \parallel \mathbf{n}$.

Considering the scenario the other way round, a pure spin current $\mathbf{j}_{s,\mathbf{n}}$ consists e.g. of spin up electrons flowing along the $+\mathbf{j}$ direction and spin down electrons flowing along the $-\mathbf{j}$ direction [cf. Fig. 2.2(b)]. Both spin species will be deflected along the same direction, as they are opposite in both, spin orientation and flow direction. This leads to a charge current $\mathbf{j}_q \parallel \mathbf{t}$ perpendicular to the initial spin current. The conversion of a spin current into a transverse charge current is called the *inverse spin Hall effect* (ISHE) and was discovered in 2006 [17].

The efficiency of the charge to spin current interconversion depends on the spin-orbit interaction and therefore is specific for each material. In literature, this is parametrized by the spin Hall angle θ_{SH}. θ_{SH} is dimensionless and can vary from a few per mill for e.g. gold ($\theta_{\mathrm{SH}}^{\mathrm{Au}} = 0.0016$ [68]) to some ten per cent for e.g. tungsten ($\theta_{\mathrm{SH}}^{\mathrm{W}} = 0.33$ [69]). In the definition of spin and charge currents given above in Eqs. (2.1) and (2.2), we can formulate the SHE and its inverse as

$$\mathbf{j}_{s,\mathbf{s}} = \theta_{\mathrm{SH}} \left(\frac{\hbar}{2e} \right) (\mathbf{s} \times \mathbf{j}_q) \tag{2.3}$$

$$\mathbf{j}_q = \theta_{\mathrm{SH}} \left(\frac{2e}{\hbar} \right) (\mathbf{s} \times \mathbf{j}_{s,\mathbf{s}}) \tag{2.4}$$

where **s** denotes a unit vector pointing along the spin polarization axis. Taken together, in conductive materials with finite spin-orbit interaction, any charge current is accompanied by a perpendicular spin current and vice versa. Thus, these phenomena are powerful tools to generate (via SHE) and detect (via ISHE) a spin current electrically. The interplay of both, SHE and ISHE, will form the basis for the spin Hall magnetoresistance introduced in Sec. 2.1.5.

2.1.3 Spin diffusion in normal metals

In Sec. 2.1.1, we considered electrons to be particles carrying both, electric charge and spin angular momentum. In a perfect crystal, the electron movement can be described in analogy to its movement in vacuum via an effective mass [70]. However, in experiments one has to assume deviations from a perfect crystallinity of the samples. Collisions of the electron with either other electrons or interactions with the crystallographic lattice will influence the transport of charge and spin [71]. Here, we distinguish between the transport of momentum and the transport of spin. For the definition of the momentum relaxation mean free path λ_{p}, both spin conserving and spin flipping types of collision are considered. λ_{p} can be linked to the Fermi velocity v_{F} via $\lambda_{\mathrm{p}} = v_{\mathrm{F}}\tau_{\mathrm{p}}$ by defining τ_{p} as the momentum relaxation time. To give an example value for λ_{p}, we assume a metallic sample with $v_{\mathrm{F}} = 10^8\,\mathrm{cms}^{-1}$. For metals, τ_{p} is about $10^{-14}\,\mathrm{s}$. This results in a momentum relaxation mean free path $\lambda_{\mathrm{p}} \approx 10\,\mathrm{nm}$.

For the spin relaxation mean free path one can identify two length scales, the spin-flip length and spin diffusion length. In analogy to the momentum relaxation mean free path, the spin-flip length λ_{sf} in the ballistic limit is defined as the mean distance between two spin-flip collisions. By introducing the mean spin-flip time τ_{sf} between two scattering events, one again can link λ_{sf} with the Fermi velocity via $\lambda_{\mathrm{sf}} = v_{\mathrm{F}}\tau_{\mathrm{sf}}$. Since τ_{sf} is of the order of $1\,\mathrm{ps}$ [72], one expects $\lambda_{\mathrm{p}} < \lambda_{\mathrm{sf}}$.

In contrast, the spin diffusion length λ_{sd} describes the mean distance electrons propagate between two spin flip events. λ_{sd} is linked to the spin-flip time τ_{sf} via the (charge) diffusion constant $D = 1/3\lambda_{\mathrm{p}}v_{\mathrm{F}}$, $\lambda_{\mathrm{sd}} = \sqrt{D\tau_{\mathrm{sf}}} = \sqrt{1/3\lambda_{\mathrm{p}}\lambda_{\mathrm{sf}}}$. λ_{sd} thus (except for a factor) can be interpreted as a geometric mean of λ_{p} and λ_{sf}. As this length scale is fundamental for the propagation of spin currents in normal metals, we will use the shortened notation $\lambda_{\mathrm{sd}} = \lambda$ in the following. At room temperature, λ^{Au} is reported to be about $35\,\mathrm{nm}$ for Au [73–75], while $\lambda^{\mathrm{Pt}} \approx 1.2-3.7\,\mathrm{nm}$ for Pt [76,77] in the thin film regime. In the diffusive limit, λ can be specified via the spin diffusion equation [78]. This will be the starting point for the theory of the spin Hall magnetoresistance in Sec. 2.1.6.
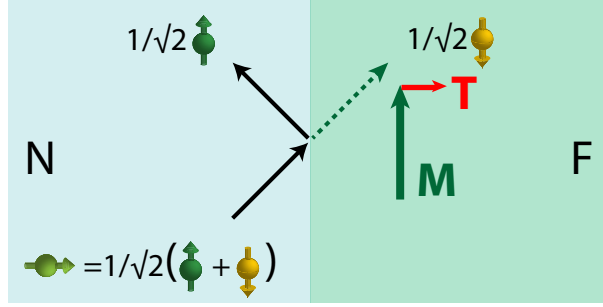
Figure 2.3: Concept of the spin transfer torque in analogy to Ref. [84] . For details, see text.

2.1.4 Spin transfer torque

If a spin current density $\mathbf{j}_{s,\mathbf{s}}$ propagating in a normal metal N reaches an interface to a ferromagnet F, the angular momentum from the spins in $\mathbf{j}_{s,\mathbf{s}}$ can be transferred to the magnetic moment of the ferromagnet by exerting a torque on the magnetization $\mathbf{M}$. This concept called the *spin transfer torque* (STT) or spin torque effect was first introduced by Slonczewski and Berger [79, 80] and confirmed experimentally in F/N/F pillars [81]. At the N/F interface, a transfer of angular momentum from the conduction electron spins to $\mathbf{M}$ can be achieved by either spin-dependent interfacial scattering (causing a spin rotation and filtering of the spin current) or spin-dephasing [82, 83]. To illustrate the STT, we consider a N/F bilayer (cf. Fig. 2.3). For simplicity, we assume F to be half-metallic, in a way that only electrons of spin orientation $|\downarrow\rangle$ can enter the ferromagnet. A $|\leftarrow\rangle$ electron propagating from N towards the interface is a linear combination of spin up and spin down electrons; the orientation of $\mathbf{M}$ sets the quantization axis. While the $|\downarrow\rangle$ state is allowed to cross the interface, the $|\uparrow\rangle$ will be reflected towards N. One therefore observes a loss of angular momentum in N. In F, the lost momentum is transferred to $\mathbf{M}$, therefore a torque $\mathbf{T}$ is exerted on $\mathbf{M}$. Now we imagine a second scattering process in which a spin-left hole hits the interface from the left. This causes an identical spin transfer towards $\mathbf{M}$, but both the charge and the longitudinal momentum carried by the $|\rightarrow\rangle$ electron cancel out. Combining both processes, this results in a reflection plus flip of the spin angular momentum with a spin-transfer of $\hbar$. This can be interpreted as a transverse polarized spin current that is absorbed completely at the interface. The concept of the STT can be interpreted in analogy to the Andreev reflection at a N/superconductor interface. However, while the superconductor is a condensate of charge, the ferromagnet in the STT concept is a condensate of angular momentum [84].

The efficiency of the transfer of spin angular momentum across an N/F interface depends on the material combination considered and is described theoretically by the *spin mixing interface conductance* $G_{\uparrow\downarrow}$. $G_{\uparrow\downarrow}$ was proposed as a measure for the number of spin transport channels per unit area across the N/F interface, in analogy to the Landauer-

Büttiker picture in ballistic charge transport [85,86]. Here, $G_{\uparrow\downarrow} = G_r + \imath G_i$ is introduced as a complex quantity [87–91]. The real part G_r is linked to the in-plane magnetic field torque [92,93] and accessible e.g. from spin pumping experiments [17,24,85,86,94]. The imaginary part G_i is related to the spin precession and interpreted as a phase shift between the spin current in N and the one in F. G_i thus can be either positive or negative [86]. As suggested recently, the spin Hall magnetoresistance [15,44,95] that will be introduced in the next section allows for quantifying both G_r and G_i experimentally in N/F hybrids.

2.1.5 Spin currents in N/FMI hybrid systems: the spin Hall magnetoresistance

In Sec. 2.1.2 we found that any charge current in a non-magnetic normal metal is accompanied by a transverse spin current. In general, this spin current is not visible in experiments on plain normal metal samples. To illustrate this, we assume a free standing metal film at first [cf. Fig. 2.4(a)]. In our gedankenexperiment, we apply a *dc* charge current $\mathbf{j}_q$ to the normal metal along $-\mathbf{j}$. As described above, spin-orbit interaction gives rise to a transverse spin current density. In our geometry, we assume the spin polarization axis $\mathbf{s}$ along the $-\mathbf{t}$ direction and the pure spin current density $\mathbf{j}_{s,\mathbf{s}}$ due to the spin Hall effect propagating along $-\mathbf{n}$. This spin current flow builds up a spin accumulation $\boldsymbol{\mu}_s$ in the $(\mathbf{j}, \mathbf{t})$ plane at the boundaries, and will be followed by a spin current back flow $\mathbf{j}_{s,\mathbf{s}}^{\text{back}}$ towards the N. Thus, in steady state there is no net spin current flow in N, $\mathbf{j}_{s,\mathbf{s}} = -\mathbf{j}_{s,\mathbf{s}}^{\text{back}}$. In our considerations, we also have to take into account the inverse spin Hall effect acting on both the spin current and the back flow. As both spin currents have the same spin orientation, but opposite propagation directions, the charge currents $\mathbf{j}_{q,\text{ISHE}}$ and $\mathbf{j}_{q,\text{ISHE}}^{\text{back}}$ will be along $-\mathbf{j}$ and $\mathbf{j}$, respectively, and thus again no net contribution from the spin current superimposes the initial charge current $\mathbf{j}_q$.

However, the interplay of the SHE and the ISHE becomes visible, if one manipulates the boundary conditions for the formation of a spin chemical potential at one surface of the normal metal. This can be achieved by putting a ferromagnetic insulator (FMI) in close vicinity to N and using the concept of spin transfer torque as introduced in Sec. 2.1.4. Thus, we expand our model and assume the normal metal to be attached to a FMI as shown in Fig. 2.4(b). In our gedankenexperiment, we again apply a *dc* charge current to the normal metal. Since the ferromagnet is assumed to be an insulator, the charge current flow is restricted to N. As N now is attached to a FMI at one boundary, a spin transfer torque (cf. Sec. 2.1.4) between N and FMI is possible if the magnetization $\mathbf{M}$ of the ferromagnet is not collinear with the spin polarization $\mathbf{s}$. Therefore, we have to distinguish between two scenarios where a transfer of angular momentum across the N/FMI

(a) SHE and ISHE interplay

(b) open boundary conditions   (c) closed boundary conditions
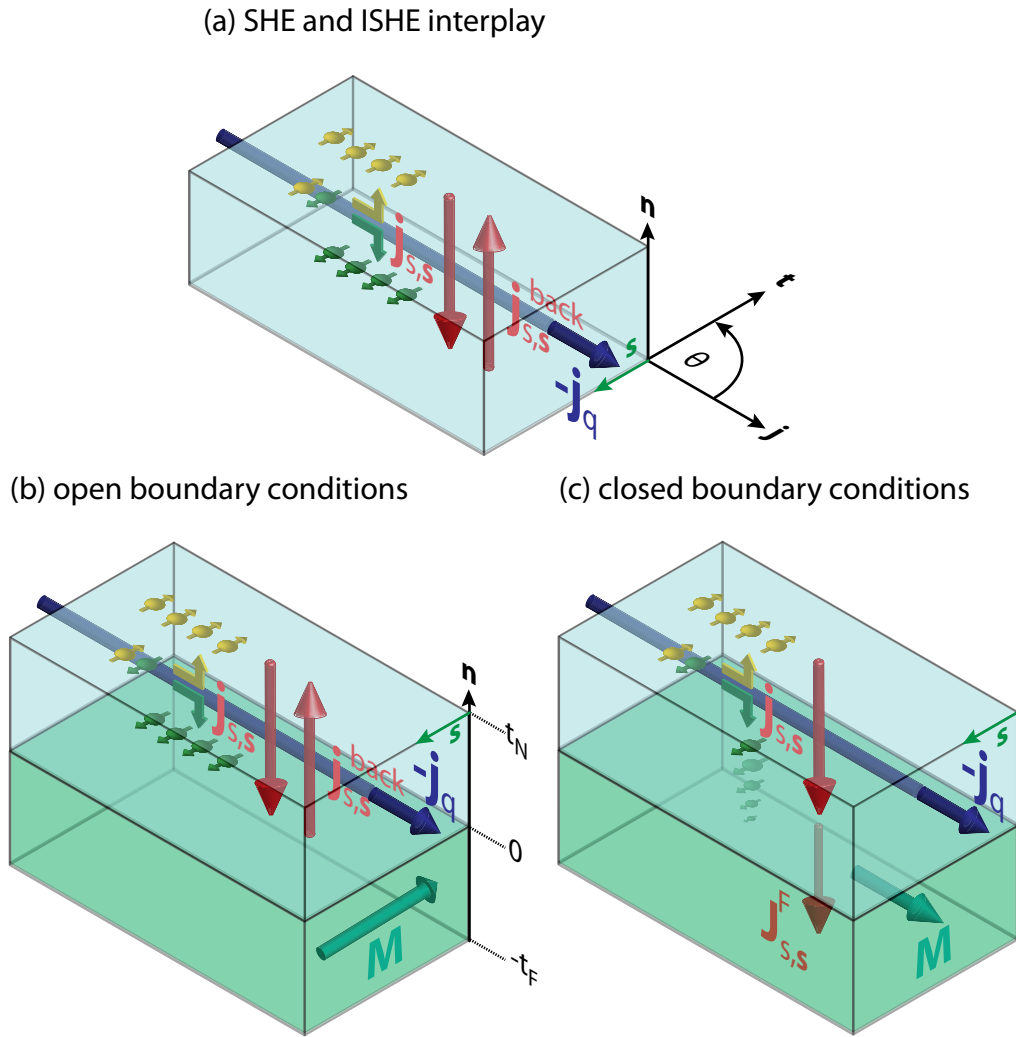
Figure 2.4: **(a)** In a normal metal with applied charge current along $\mathbf{j}$, the spin Hall effect leads to a transverse spin current density $\mathbf{j}_{s,\mathbf{s}} \parallel -\mathbf{n}$, generating the formation of a spin accumulation at the boundaries. This spin chemical potential results in a diffusive spin current $\mathbf{j}_{s,\mathbf{s}}^{\text{back}}$ compensating $\mathbf{j}_{s,\mathbf{s}}$. **(b)** In vicinity to a ferromagnetic insulator with magnetization $\mathbf{M} \parallel \mathbf{s}$, $\mathbf{j}_{s,\mathbf{s}}$ is not able to enter the FMI layer, which is referred to *open boundary conditions* in analogy to the conventional Hall effect. **(c)** *Closed boundary conditions*: If $\mathbf{M}$ is perpendicular to $\mathbf{s}$, a spin transfer torque is possible and therefore the spin accumulation is suppressed at the N/FMI interface, leading to a suppression of $\mathbf{j}_{s,\mathbf{s}}^{\text{back}}$.

interface is allowed and prohibited, respectively.

1. **open boundary conditions**: Considering $\mathbf{M} \parallel \mathbf{s}$, the spin transfer torque at the N/FMI interface is prohibited and therefore the spin current can not enter the FMI. In that configuration, the charge current contributions given from both spin current and back flow cancel out [cf. Fig. 2.4(b)].

2. **closed boundary conditions**: If we assume $\mathbf{M} \perp \mathbf{s}$, a spin transfer torque between

the N and the FMI is possible. In this configuration, the spin current density $\mathbf{j}_{s,\mathbf{s}}$ will flow across the interface and induce a magnetization precession in the FMI layer. Therefore, the formation of a spin accumulation at the N/FMI interface as well as the spin current back flow towards the N is suppressed [see Fig. 2.4(c)]. In this scenario, the initial charge current $\mathbf{j}_{\mathrm{q}}$ is superimposed by the charge current contribution $\mathbf{j}_{q,\mathrm{ISHE}}$ stemming from the SHE/ISHE interplay.

Therefore, the resistance of N is affected by the magnetization orientation of the FMI, giving rise to a novel magnetoresistance referred to as *spin Hall magnetoresistance* (SMR) [15, 44–46, 96]. The SMR effect was postulated in 2013 by Nakayama *et al.* and discussed in various material combinations in the last years [96–98]. However, to utilize the SMR as a powerful tool to access spin transport characteristics electrically, a theoretical description of the mechanisms is necessary.

2.1.6 Theoretical description of the spin Hall magnetoresistance

To quantitatively model the SMR, it is necessary to take into account the diffusive nature of transport as well as the spin dissipation in N. A theoretical approach based on spin diffusion theory and spin transfer torque was published by Chen *et al.* in 2013 [15]. A brief introduction to the main assumptions and results of the SMR theory will be presented in the following section. For mathematical details, we refer to Ref. [15].

Again, we consider a N/FMI bilayer in the geometry introduced in Fig. 2.4(b). In the non-relativistic limit, the spin current density $\mathbf{j}_{s,\mathbf{s}}$ can be written as a second-order (3×3) tensor,

$$\mathbf{j}_s = \left(\mathbf{j}_s^{\mathbf{j}}, \mathbf{j}_s^{\mathbf{t}}, \mathbf{j}_s^{\mathbf{n}} \right). \tag{2.5}$$

Please note that for simplicity reasons, the spin current density $\mathbf{j}_s$ is formulated in units of the charge current density $\mathbf{j}_{\mathrm{q}}$ in the following section. The column vectors $\mathbf{j}_s^i = en < \mathbf{v}_i \Sigma + \Sigma \mathbf{v}_i > /2$ denote spin current densities with polarization $\mathbf{s}$ flowing along the $\mathbf{i} = (\mathbf{j}, \mathbf{t}, \mathbf{n})$ direction, while the row vectors $\mathbf{j}_{sk} = en < \mathbf{v}\Sigma_k + \Sigma_k \mathbf{v} > /2$ denote spin current densities polarized along the $\mathbf{k}$ direction. $\mathbf{v}$ represents the velocity vector, Σ denotes the vector of Pauli spin matrices and $< \cdots >$ the expectation value. The relations between driving forces and currents in N can be summed up in a response matrix (linear response regime) for a particle with charge q [78]

$$\begin{pmatrix} \mathbf{j}_{\mathrm{q}} \\ \mathbf{j}_{s,\mathbf{j}} \\ \mathbf{j}_{s,\mathbf{t}} \\ \mathbf{j}_{s,\mathbf{n}} \end{pmatrix} = \sigma_{\mathrm{N}} \begin{pmatrix} 1 & \theta_{\mathrm{SH}}\mathbf{j}\times & \theta_{\mathrm{SH}}\mathbf{t}\times & \theta_{\mathrm{SH}}\mathbf{n}\times \\ \theta_{\mathrm{SH}}\mathbf{j}\times & 1 & 0 & 0 \\ \theta_{\mathrm{SH}}\mathbf{t}\times & 0 & 1 & 0 \\ \theta_{\mathrm{SH}}\mathbf{n}\times & 0 & 0 & 1 \end{pmatrix} \begin{pmatrix} -\nabla\mu_0/q \\ -\nabla\mu_{s,\mathbf{j}}/(2q) \\ -\nabla\mu_{s,\mathbf{t}}/(2q) \\ -\nabla\mu_{s,\mathbf{n}}/(2q) \end{pmatrix}, \tag{2.6}$$

where σ_N denotes the electrical conductivity of the N layer, θ_{SH} its spin Hall angle and $(\mathbf{j}, \mathbf{t}, \mathbf{n})$ represent unity vectors along the coordinate axes as introduced in Fig. 2.4. The spin Hall effect [lower non-diagonal and non-vanishing matrix elements in Eq. (2.6)] generates spin currents in the presence of an applied electric field, here chosen to be along the $\mathbf{j}$ direction, $\mathbf{E} = E_j\mathbf{j} = -\mathbf{j}\partial_j\Phi$ where Φ is the electro-chemical potential applied along $\mathbf{j}$. The inverse spin Hall effect [elements above the diagonal in Eq. (2.6)] links the gradients of the spin accumulation to the charge current density. $\boldsymbol{\mu}_s = (\mu_{s,\mathbf{j}}, \mu_{s,\mathbf{t}}, \mu_{s,\mathbf{n}})^T - \mu_0\hat{1}$ is the spin accumulation, which can be interpreted as the spin-dependent chemical potential relative to the charge chemical potential $\mu_0 = q\Phi$ (in units of Joule).

$\boldsymbol{\mu}_s$ can be obtained from the spin diffusion equation [78] in the normal metal

$$\nabla^2\boldsymbol{\mu}_{\mathrm{s}} = \frac{\boldsymbol{\mu}_{\mathrm{s}}}{\lambda^2}, \tag{2.7}$$

with its general solution

$$\boldsymbol{\mu_s} = \mathbf{A}\exp(-n/\lambda) + \mathbf{B}\exp(n/\lambda). \tag{2.8}$$

Here, λ denotes the spin diffusion length of the normal metal. The vector constants $\mathbf{A}$ and $\mathbf{B}$ are determined by the boundary conditions at the interfaces at $n = 0$ between N and the FMI and $n = t_N$ between N and the vacuum, where t_N denotes the thickness of the N layer in $\mathbf{n}$ direction [cf. Fig. 2.4 (b)].

From Eq. (2.6) we can write down the spin current density in N, reading

$$\mathbf{j}_s^{\mathbf{n}}(n) = -J_{s0}^{\mathrm{SH}}\mathbf{t} - \frac{\sigma_N}{2q}\partial_n\mu_{sn}. \tag{2.9}$$

As expected from Sec. 2.1.5, the spin current in the normal metal layer consists of two contributions, given by the initial spin current $-J_{s0}^{\mathrm{SH}}\mathbf{t}$ stemming from the spin Hall effect acting on the applied charge current $\mathbf{j}_q$ and a diffusive spin current $-\sigma_N\partial_n\mu_{sn}/2q$ due to the spin accumulation at the boundaries. Here, we used the abbreviation $J_{s0}^{\mathrm{SH}} = \theta_{SH}\sigma_N E_j$ for the bare spin Hall current. Since the geometry restricts the spin transfer torque to the N/FMI interface at $n = 0$, we neglect contributions to the spin current with spin polarizations along $\mathbf{n}$ traveling parallel to the $\mathbf{t}$ axis in the following. The spin current in N is required to be continuous at the interfaces. In particular, the spin current vanishes at the N/vacuum interface at $n = t_N$. At the magnetic interface $n = 0$, the spin current density $\mathbf{j}_s^F$ is governed by the spin accumulation $\boldsymbol{\mu}_s$ and the spin mixing interface

conductance per unit area[3] $G_{\uparrow\downarrow} = G_r + \imath G_i$ introduced in Sec. 2.1.4:

$$q\mathbf{j}_s^{\text{F}}(\mathbf{m}) = G_r\mathbf{m} \times (\mathbf{m} \times \boldsymbol{\mu}_s) + G_i (\mathbf{m} \times \boldsymbol{\mu}_s) \,. \tag{2.10}$$

Here, $\mathbf{m} = (m_j, m_t, m_n)^{\text{T}}$ is the normalized unit vector of the magnetization direction and a positive current in Eq. (2.10) corresponds to up spins flowing towards the N. Since we assume an insulating ferromagnet, the spin current density $\mathbf{j}_s^{\text{F}}$ is proportional to the spin transfer torque acting on the ferromagnet (cf. Sec. 2.1.4).

To solve the spin diffusion equation in Eq. (2.7), we determine the coefficients $\mathbf{A}$ and $\mathbf{B}$ by inserting the ansatz shown in Eq. (2.8) to Eq. (2.9). At the vacuum interface $n = t_{\text{N}}$, where $\mathbf{j}_s^{\mathbf{n}}(n)$ is required to vanish, Eq. (2.9) reads

$$\frac{-\sigma_{\text{N}}}{2q\lambda} \left(-\mathbf{A}e^{\frac{-t_{\text{N}}}{\lambda}} + \mathbf{B}e^{\frac{t_{\text{N}}}{\lambda}} \right) - J_{s0}^{\text{SH}}\mathbf{t} = \mathbf{j}_s^{\mathbf{n}}(t_{\text{N}}) = 0. \tag{2.11}$$

For the N/FMI interface at $n = 0$, the spin current reads $\mathbf{j}_s^{\mathbf{n}}(0) = \mathbf{j}_s^{\text{F}}(\mathbf{m})$ and we obtain

$$\frac{\sigma_{\text{N}}}{2q\lambda} (\mathbf{A} - \mathbf{B}) - J_{s0}^{\text{SH}}\mathbf{t} = \mathbf{j}_s^{\text{F}}(\mathbf{m}) \tag{2.12}$$

Determined by Eqs. (2.11) and (2.12) the solution for the spin chemical potential $\boldsymbol{\mu}_s$ reads

$$\boldsymbol{\mu}_s = \frac{2q\lambda}{\sigma_{\text{N}}} \left[- \left(\mathbf{j}_s^{\mathbf{n}}(t_{\text{N}}) + j_{s0}^{\text{SH}}\mathbf{t} \right) \frac{\cosh\frac{n}{\lambda}}{\sinh\frac{t_{\text{N}}}{\lambda}} + \left(\mathbf{j}_s^{\text{F}}(\mathbf{m}) + J_{s0}^{\text{SH}}\mathbf{t} \right) \frac{\cosh\frac{n-t_{\text{N}}}{\lambda}}{\sinh\frac{t_{\text{N}}}{\lambda}} \right] \tag{2.13}$$

For bilayers, we take into account $\mathbf{j}_s^{\mathbf{n}}(t_{\text{N}}) = 0$ and re-formulate Eq. (2.13) to

$$\boldsymbol{\mu}_s(n) = -\mathbf{t}\mu_s^0 \frac{\sinh\frac{2n-t_{\text{N}}}{2\lambda}}{\sinh\frac{t_{\text{N}}}{2\lambda}} + \mathbf{j}_s^{\text{F}}(\mathbf{m}) \frac{2q\lambda}{\sigma_{\text{N}}} \frac{\cosh\frac{n-t_{\text{N}}}{\lambda}}{\sinh\frac{t_{\text{N}}}{\lambda}} \tag{2.14}$$

using the spin accumulation μ_s^0 at the interface in the absence of STT, i.e. for $G_{\uparrow\downarrow} = 0$, $\mu_s^0 = \frac{2q\lambda}{\sigma_{\text{N}}} J_{s0}^{\text{SH}} \tanh\frac{t_{\text{N}}}{2\lambda}$. Utilizing the definition of $\mathbf{j}_s^{\text{F}}(\mathbf{m})$ given in Eq. (2.10) and the vector

---

[3]$G_{\uparrow\downarrow}$ is written in units of $[G_{\uparrow\downarrow}] = A/(Vm^2)$, not to be confused with the spin mixing conductance per unit of interface area and per conductance quantum e^2/h called $g_{\uparrow\downarrow}$ that is sometimes used in literature. The connection between both quantities is given by $g_{\uparrow\downarrow} = G_{\uparrow\downarrow} \cdot h/e^2$.

identity $\mathbf{a} \times (\mathbf{b} \times \mathbf{c}) = \mathbf{b} \, (\mathbf{a} \cdot \mathbf{c}) - \mathbf{c} \, (\mathbf{a} \cdot \mathbf{b})$, leads to

$$
\begin{aligned}
\boldsymbol{\mu}_s(0) = {} & \mathbf{t}\mu_s^0 \frac{\left(1 + \frac{2\lambda}{\sigma_\mathrm{N}} G_r \coth \frac{t_\mathrm{N}}{\lambda}\right)}{\left(1 + \frac{2\lambda}{\sigma_\mathrm{N}} G_r \coth \frac{t_\mathrm{N}}{\lambda}\right)^2 + \left(\frac{2\lambda}{\sigma_\mathrm{N}} G_i \coth \frac{t_\mathrm{N}}{\lambda}\right)^2} \\
& + \mathbf{m} m_t \mu_s^0 \frac{\frac{2\lambda}{\sigma_\mathrm{N}} G_r \coth \frac{t_\mathrm{N}}{\lambda} \left(1 + \frac{2\lambda}{\sigma_\mathrm{N}} G_r \coth \frac{t_\mathrm{N}}{\lambda}\right) + \left(\frac{2\lambda}{\sigma_\mathrm{N}} G_i\right)^2 \coth^2 \frac{t_\mathrm{N}}{\lambda}}{\left(1 + \frac{2\lambda}{\sigma_\mathrm{N}} G_r \coth \frac{t_\mathrm{N}}{\lambda}\right)^2 + \left(\frac{2\lambda}{\sigma_\mathrm{N}} G_i \coth \frac{t_\mathrm{N}}{\lambda}\right)^2} \\
& + \mathbf{m} \times \mathbf{t}\mu_s^0 \frac{\frac{2\lambda}{\sigma_\mathrm{N}} G_i \coth \frac{t_\mathrm{N}}{\lambda}}{\left(1 + \frac{2\lambda}{\sigma_\mathrm{N}} G_r \coth \frac{t_\mathrm{N}}{\lambda}\right)^2 + \left(\frac{2\lambda}{\sigma_\mathrm{N}} G_i \coth \frac{t_\mathrm{N}}{\lambda}\right)^2}.
\end{aligned}
\tag{2.15}
$$

We now insert Eq. (2.15) into the boundary condition at the interface and obtain the spin current at the interface:

$$
\begin{aligned}
e\mathbf{j}_s^\mathrm{F}(\mathbf{m}) = {} & \mu_s^0 \sigma_\mathrm{N} \mathrm{Re}\left[\frac{G_{\uparrow\downarrow}}{\left(\sigma_\mathrm{N} + 2\lambda \coth \frac{t_\mathrm{N}}{\lambda} G_{\uparrow\downarrow}\right)}\right] \mathbf{m} \times (\mathbf{m} \times \mathbf{t}) \\
& + \mu_s^0 \sigma_\mathrm{N} \mathrm{Im}\left[\frac{G_{\uparrow\downarrow}}{\left(\sigma_\mathrm{N} + 2\lambda \coth \frac{t_\mathrm{N}}{\lambda} G_{\uparrow\downarrow}\right)}\right] (\mathbf{m} \times \mathbf{t})
\end{aligned}
\tag{2.16}
$$

The spin accumulation $\boldsymbol{\mu}_s(n)$ can now be calculated by inserting Eq. (2.16) into Eq. (2.14):

$$
\begin{aligned}
\frac{\boldsymbol{\mu}_s(n)}{\mu_s^0} = {} & -\mathbf{t} \frac{\sinh \frac{2n-t_\mathrm{N}}{2\lambda}}{\sinh \frac{t_\mathrm{N}}{2\lambda}} + 2\lambda \left(\mathbf{m} \times (\mathbf{m} \times \mathbf{t}) \, \mathrm{Re} + (\mathbf{m} \times \mathbf{t}) \, \mathrm{Im}\right) \\
& \cdot \frac{G_{\uparrow\downarrow}}{\left(\sigma_\mathrm{N} + 2\lambda \coth \frac{t_\mathrm{N}}{\lambda} G_{\uparrow\downarrow}\right)} \frac{\cosh \frac{n-t_\mathrm{N}}{\lambda}}{\sinh \frac{t_\mathrm{N}}{\lambda}},
\end{aligned}
\tag{2.17}
$$

leading to the spin current distribution in N

$$
\begin{aligned}
\mathbf{j}_s^\mathbf{n}(n) = {} & J_{s0}^\mathrm{SH} \mathbf{t} \frac{\cosh \frac{2n-t_\mathrm{N}}{2\lambda} - \cosh \frac{t_\mathrm{N}}{2\lambda}}{\cosh \frac{t_\mathrm{N}}{2\lambda}} - 2\lambda J_{s0}^\mathrm{SH} \tanh \frac{t_\mathrm{N}}{2\lambda} \\
& \cdot \left(\mathbf{m} \times (\mathbf{m} \times \mathbf{t}) \, \mathrm{Re} + (\mathbf{m} \times \mathbf{t}) \, \mathrm{Im}\right) \frac{G_{\uparrow\downarrow}}{\sigma_\mathrm{N} + 2\lambda \coth \frac{t_\mathrm{N}}{\lambda} G_{\uparrow\downarrow}} \frac{\sinh \frac{n-t_\mathrm{N}}{\lambda}}{\sinh \frac{t_\mathrm{N}}{\lambda}}
\end{aligned}
\tag{2.18}
$$

The ISHE acting on the spin current components gives rise to longitudinal (along $\mathbf{j}$) and transverse (along $\mathbf{t}$) charge currents

$$
\frac{j_{q,\mathrm{long}}}{j_q^0} = 1 + \theta_\mathrm{SH}^2 \left(\frac{\cosh \frac{2n-t_\mathrm{N}}{2\lambda}}{\cosh \frac{t_\mathrm{N}}{2\lambda}} + (1 - m_t^2) \, \mathrm{Re} \frac{2\lambda G_{\uparrow\downarrow} \tanh \frac{t_\mathrm{N}}{2\lambda}}{\left(\sigma + 2\lambda \coth \frac{t_\mathrm{N}}{\lambda} G_{\uparrow\downarrow}\right)} \frac{\sinh \frac{n-t_\mathrm{N}}{\lambda}}{\sinh \frac{t_\mathrm{N}}{\lambda}}\right)
\tag{2.19}
$$

$$
\frac{j_{q,\mathrm{trans}}}{j_q^0} = \theta_\mathrm{SH}^2 \tanh \frac{t_\mathrm{N}}{2\lambda} (m_j m_t \mathrm{Re} - m_n \mathrm{Im}) \cdot \frac{2\lambda G_{\uparrow\downarrow}}{\left(\sigma + 2\lambda \coth \frac{t_\mathrm{N}}{\lambda} G_{\uparrow\downarrow}\right)} \frac{\sinh \frac{n-t_\mathrm{N}}{\lambda}}{\sinh \frac{t_\mathrm{N}}{\lambda}}
\tag{2.20}
$$

where $j_q^0 = \sigma_N E_j$ is the charge current driven by the external field.

In experiments, one commonly detects electrical resistivities. To determine the longitudinal and transverse components of the resistivity ρ, ρ_{long} and ρ_{trans}, we average the electrical current over the film thickness. The total longitudinal resistivity is governed by the applied charge current along $\mathbf{j}$. We expand ρ_{long} and ρ_{trans} to leading order in θ_{SH}^2 and obtain

$$\rho_{\text{long}} = \frac{1}{\sigma_{\text{long}}} = \left(\frac{\overline{j_{q,\text{long}}}}{E_j} \right)^{-1} \approx \rho_0 + \Delta\rho_0 + \Delta\rho_1 (1 - m_t^2) \tag{2.21}$$

for the longitudinal component where $\sigma_{\text{long}} = \sigma_N$ is the intrinsic electric conductivity of the bulk normal metal. We here used $\rho_0 = \sigma_N^{-1}$ and the abbreviations

$$\frac{\Delta\rho_0}{\rho_0} = -\frac{\theta_{\text{SH}}^2}{t_N} 2\lambda \tanh \frac{t_N}{2\lambda} \tag{2.22}$$

$$\frac{\Delta\rho_1}{\rho_0} = \frac{\theta_{\text{SH}}^2}{t_N} \lambda \text{Re} \frac{2\lambda G_{\uparrow\downarrow} \tanh^2 \frac{t_N}{2\lambda}}{\sigma + 2\lambda \coth \frac{t_N}{\lambda} G_{\uparrow\downarrow}}. \tag{2.23}$$

For the transverse resistivity, we end up with

$$\rho_{\text{trans}} = \frac{\sigma_{\text{long}}}{\sigma_{\text{trans}}^2} \approx \Delta\rho_1 m_j m_t + \Delta\rho_2 m_n \tag{2.24}$$

using

$$\frac{\Delta\rho_2}{\rho_0} = -\frac{\theta_{\text{SH}}^2}{t_N} \lambda \text{Im} \frac{2\lambda G_{\uparrow\downarrow} \tanh^2 \frac{t_N}{2\lambda}}{\sigma + 2\lambda \coth \frac{t_N}{\lambda} G_{\uparrow\downarrow}}. \tag{2.25}$$

Obviously, the longitudinal resistivity ρ_{long} is modulated by $(1 - m_t^2)$ and the proportionality factor $\Delta\rho_1/\rho_0$ depends on intrinsic properties of the N/FMI bilayer. In our geometry defined above, m_t is the projection of the magnetization vector $\mathbf{M}$ on the direction transverse to the applied current $\mathbf{j}_q \parallel \mathbf{j}$ in the film plane. m_t can be defined as the sine of the angle θ between the current direction $\mathbf{j}$ and the unity magnetization vector $\mathbf{m}$ (cf. Fig. 2.4). Therefore, we end up with a $\cos^2(\theta)$ modulation of ρ_{long},

$$\rho_{\text{long}} \approx \rho_0 + \Delta\rho_0 + \Delta\rho_1 (1 - \sin^2(\theta)) = \rho_0 + \Delta\rho_0 + \Delta\rho_1 \cos^2(\theta) \tag{2.26}$$

with a minimum signal for $m_t = 1$ ($\theta = \pi/2, 3\pi/2$) and a maximum signal for $m_t = 0$ ($\theta = 0, \pi$). The latter case can be achieved by both $m_j = 1, m_n = 0$ as well as $m_j = 0, m_n = 1$, corresponding to $\mathbf{M} \parallel \mathbf{j} \parallel \mathbf{j}_q$ and $\mathbf{M} \parallel \mathbf{n} \parallel \mathbf{s}$, respectively. In our experiments, the switching between those different boundary conditions will be realized by rotating the magnetization vector $\mathbf{M}$ of the FMI and therefore changing the projections of $\mathbf{m}$ on the coordinate axes $\mathbf{j}, \mathbf{t}$ and $\mathbf{n}$.

The evolution of the transverse resistivity ρ_{trans} shown in Eq. (2.24) also shows a modula-

tion proportional to $\Delta\rho_1$. However, the factor $m_j m_t$ can be transformed to $\sin(\theta)\cos(\theta)$ and thus the angular dependence of the signal[4] will be shifted by $\pi/4$ with respect to ρ_{long}. Additionally, the SMR theory provides the prediction of a spin current based modulation of the transverse resistivity in the out-of-plane configuration ($m_n \neq 0$) proportional to $\Delta\rho_2$. This phenomenon is called the *spin Hall anomalous Hall effect* [15] and will be discussed separately in Chapter 3.

2.1.7 Magnetic proximity magnetoresistance: an alternative model?

Before we start with the discussion of our experimental data, an alternative approach to explain a magnetization-orientation dependent modulation of a normal metal's resistivity will be introduced at this point. From the beginning of Chapter 2, we discussed charge and spin currents in so-called *non-magnetic* (normal) metals. The phrase non-magnetic was defined to represent materials without a ferromagnetic ordering. In terms of a two-spin-channel model [99], this implies that the number of occupied spin up and spin down states $n_\uparrow$ and $n_\downarrow$ in the conduction band are equal in the absence of an external magnetic field. However, around 50 years ago it has been proven that non-magnetic materials can adopt an induced magnetism, i.e. they show an imbalance of spin up and spin down states in their conduction band, if they are brought in direct contact with a ferromagnetic metal [100, 101]. Hereby, the strong hybridization of the N's orbitals with their ferromagnetic neighbors is responsible for this effect and thus the formation of a proximitized, "ferromagnetic" area in N is possible, but restricted to a few mono-layers at the N/F interface (cf. Fig. 2.5).

Within this ferromagnetic area, the response of the normal metal on an external magnetic field is affected by the proximity effect and one observes typical ferromagnetic fingerprints from the proximitized layer in N. In the simplest possible case, the magnetic response from the F layer can be neglected by assuming F to be electrically insulating. Therefore, a magnetic field dependent signal can be directly attributed to the magnetic properties of N. However, for N films with a finite thickness, the non-proximitized part of N will dominate the electrical signal and thus induced magnetoresistive effects will show a strong thickness dependence and will be suppressed in thick (thickness $t \gg a$, with a the thickness of one monolayer of the material) normal metal layers.

In the following, we will briefly discuss, what the electrical signal in a proximitized normal metal would look like. For this, we assume a ferromagnetic, conducting sample representing solely the proximitized area. It was found in 1856 by William Thomson [102], that the resistivity of a ferromagnetic material depends on the relative orientation between the

---

[4]$m_j m_t$ is a non-vanishing factor for so-called in-plane rotations, i.e. rotations of the unity magnetization vector **m** in the plane spanned by **j** and **t**.

current direction and an external magnetic field. In experiments, one usually observes $\rho_\parallel > \rho_\perp$ [103] in conductive ferromagnets, where the indices $\parallel$ and $\perp$ indicate the relative orientation between the direction $\mathbf{j}$ of the applied current and the external field direction $\mathbf{H}$. This is referred to as *anisotropic magnetoresistance* (AMR).

In a theoretical picture, this leads to [99]

$$\rho_{\text{long}} = \frac{\rho_\parallel + 2\rho_\perp}{3} + \left(\rho_\parallel - \rho_\perp\right)\left(m_j^2 - \frac{1}{3}\right). \tag{2.27}$$

Thus, similar to the SMR theory in Sec. 2.1.6, the AMR shows a quadratic dependence on one projection direction of $\mathbf{m}$. However, we want to emphasize, that the AMR is modulated by m_j^2, while the SMR shows a proportionality to m_t^2. This difference will be crucial to separate between AMR and SMR in the following.

For the transverse resistivity, the AMR reads

$$\rho_{\text{trans}} = \frac{\mathbf{E} \times \mathbf{j}_q}{|\mathbf{j}_q|^2} = \left(\rho_\parallel - \rho_\perp\right)\sin\left(\theta\right)\cos\left(\theta\right) = \left(\rho_\parallel - \rho_\perp\right)m_t m_j. \tag{2.28}$$

Again, Eq. (2.28) is similar to the expression for ρ_{trans} provided by the SMR theory (cf. Sec. 2.1.6). Both Eq. (2.28) and the first part of Eq. (2.24) are proportional to $m_t m_j$, making it impossible to differ between AMR and SMR in the transverse in-plane resistivity signal.

The formation of proximitized layers is detectable with techniques sensitive to the spin-orientation of an element, like polarized neutron reflectometry [104], X-ray magnetic circular dichroism (XMCD) [49, 105, 106], or X-ray resonant magnetic reflectivity (XRMR)
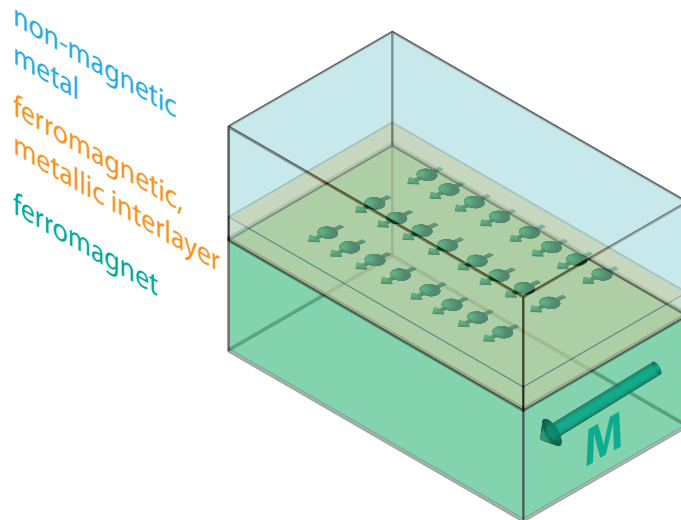

Figure 2.5: Formation of induced magnetic moments within a non-magnetic normal metal layer in direct contact to a ferromagnet due to the proximity effect.

[107]. Within the past 15 years, the proximity effect was reported in metallic multi-layer systems consisting of alternating layers of magnetic (inducting) and non-magnetic (induced) layers like Ni/Pt [105] or Fe/Pt [108]. In Sec. 2.3, we will present the investigation of induced magnetic moments in the material combination used in our experiments, i.e. platinum in direct contact with the ferromagnetic insulator yttrium iron garnet via XMCD [49, 106, 109]. Within that section, we will discuss the proximity-induced AMR (or proximity MR [47]) as a candidate for a contrary interpretation of our experimental results.

This concludes the theoretical introduction to the spin Hall magnetoresistance. In the following section, we present an overview of the samples used in our experiments and introduce the experimental setup.

2.2 Sample preparation and experimental setup

As shown in Sec. 2.1.5, for testing the SMR concept experimentally one needs a hybrid structure consisting of a normal metal with large spin orbit interaction (SOI) and an adjacent, insulating ferromagnet. In our experiments, we chose single-crystalline yttrium iron garnet ($Y_3Fe_5O_{12}$, YIG) thin films for the ferromagnetic insulating layer and platinum (Pt) for the normal metal. Certainly, the occurrence of the SMR is not restricted to the material combination YIG/Pt. Results for other FMI/N combinations utilizing Fe_3O_4 and $NiFe_2O_4$, tungsten and tantalum have been reported [46, 97, 98], showing that the SMR is a universal concept for normal metals with large spin orbit interaction in vicinity to a ferromagnetic insulator. This section provides a brief overview on the sample fabrication, a more detailed information on the sample growth and pre-characterization of our YIG/Pt hybrid systems can e.g. be found in Ref. [110]. An overview on the experimental setup and measurement techniques will conclude this section.

2.2.1 Sample growth

The samples used in our experiments are YIG/Pt thin film heterostructures deposited onto (111)-oriented gadolinium gallium garnet ($Gd_3Ga_5O_{12}$,GGG) or yttrium aluminum garnet ($Y_3Al_5O_{12}$,YAG) single crystal substrates as described in Ref. [106]. The YIG thin films with a thickness t_F ($4\,nm \leq t_F \leq 200\,nm$) were epitaxially grown via pulsed laser deposition from a stoichiometric polycrystalline target, utilizing a KrF excimer laser with a wavelength of $248\,nm$, at a repetition rate of $10\,Hz$ and a laser fluence of $2\,J/cm^2$. The deposition was carried out in an oxygen atmosphere at a pressure of $25 \times 10^{-3}\,mbar$ and a substrate temperature of $500°C$ (YAG) or $550°C$ (GGG), respectively. After cooling

the sample to room temperature, a polycrystalline Pt layer of thickness t_N was deposited in situ on top of the YIG film via electron beam evaporation. We applied high-resolution X-ray reflectometry (HR-XRR) as exemplarily shown in Fig. 2.8 to determine t_F, t_N and the interface roughness h for all samples, using the Software Package LEPTOS (Bruker AXS). The results of the reflectometry simulations for all samples discussed in this chapter are summarized in Tab. 6.2 .

2.2.2 Experimental setup for magnetotransport experiments

We patterned the YIG/Pt bilayers into Hall bar structures (width $w = 80\,\mu$m, contact separation $l = 600\,\mu$m) using optical lithography and subsequent argon ion beam milling [see Fig. 2.6(a)]. Each sample is glued to the copper base of a chip-carrier sample holder using GE Varnish [cf. Fig. 2.6(b)] and the contacts of the Hall bar structures are connected to the bonding frame of the sample holder using $30\,\mu$m thin aluminum wires via wedge bonding. The chip carrier is connected to the head of a dipstick, which may be used in the variable temperature insert (VTI) of either a superconducting split-coil magnet cryostat ("Moria", $\mu_0 H \leq 7\,$T) or a superconducting 3D vector magnet cryostat ("Chaos", $\mu_0 H \leq 2\,$T for rotations, see Sec. 6.2) for magnetoresistance measurements ($10\,$K $\leq T \leq 300\,$K). The "Moria" cryostat's VTI is equipped with a stepper motor, which allows a rotation of the sample with respect to the external magnetic field. Additionally, the dipstick offers different mounting stages for the chip carrier, enabling a sample mounting in different configurations with respect to the rotation axis and the magnetic field direction. For measurements in the "Chaos" cryostat, however, we rotate the external magnetic field, while the sample position inside the VTI is fixed. As the data taken for both methods (rotating the sample in an external magnetic field and vice versa) represents the same phenomenology, we do not separate between measurements taken in the "Moria" and the
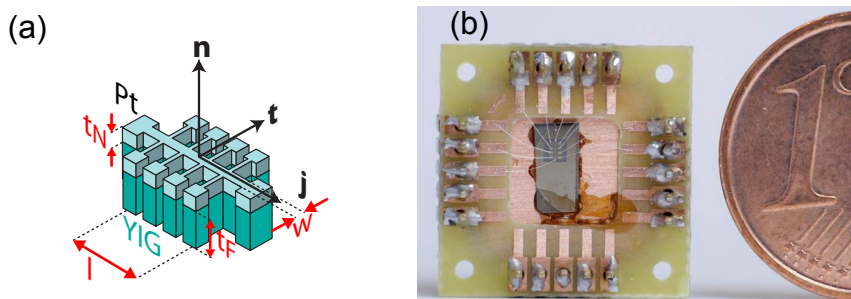
Figure 2.6: (a) Sketch of the Hall bar patterned YIG/Pt bilayer and definition of the coordinate system by **j**, **t**, and **n**. **(b)** Picture of a mounted and contacted YIG/Pt sample and a 1 Euro cent coin to serve as a rule. The photograph is provided by our former bachelor student Dominik Irber [111].

"Chaos" in the following. Additionally, for simplicity reasons, we speak of a rotation of the external magnetic field around the sample for both cases. In our experiments, we current bias the Hall bars with a j_q of up to $500\,\mu A$ and detect the longitudinal and transverse voltages V_{long} and V_{trans} as a function of the magnetization orientation $\mathbf{M}$. To manipulate the direction of $\mathbf{M}$, we define three different rotation planes as follows (cf. Fig. 2.7)

- *in-plane* (ip) rotations in the sample plane spanned by $\mathbf{j}$ and $\mathbf{t}$ ($m_n = 0$)

- *out of plane perpendicular* $\mathbf{j}$ (oopj) in the plane spanned by $\mathbf{n}$ and $\mathbf{t}$ ($m_j = 0$)

- *out of plane perpendicular* $\mathbf{t}$ (oopt) in the plane spanned by $\mathbf{n}$ and $\mathbf{j}$ ($m_t = 0$),

and took advantage of the concept of the angle-dependent magnetoresistance (ADMR) [46, 112, 113]. Therefore, an external magnetic field of constant magnitude $\mu_0 H \leq 7\,T$ is rotated in the rotation planes introduced above while we recorded the evolution of the sample's resistivity $\rho\,(\delta_H)$. Here, δ_H denotes the rotation angle α, β, or γ between the magnetic field $\mathbf{H}$ and the current direction $\mathbf{j}$ or the transverse direction $\mathbf{t}$, respectively. A definition of the rotation angles can be taken from Fig. 2.7. The magnitude of the magnetic field was intentionally chosen much larger than the anisotropy and demagnetizing fields of YIG, in order to ensure that the YIG magnetization $\mathbf{M}$ is always saturated and oriented along $\mathbf{H}$, $\delta_H = \delta$.

The longitudinal and transverse resistivities ρ_{long} and ρ_{trans} of the sample can be calculated from the voltage drop $V_{long}\,(\delta)$ along the direction of charge current flow, $V_{trans}\,(\delta)$ along $\mathbf{t}$ and the magnitude j_q of the charge current density:

$$\rho_{long}\,(\delta) = V_{long}\,(\delta) \cdot \frac{w t_N}{j_q l} \tag{2.29}$$

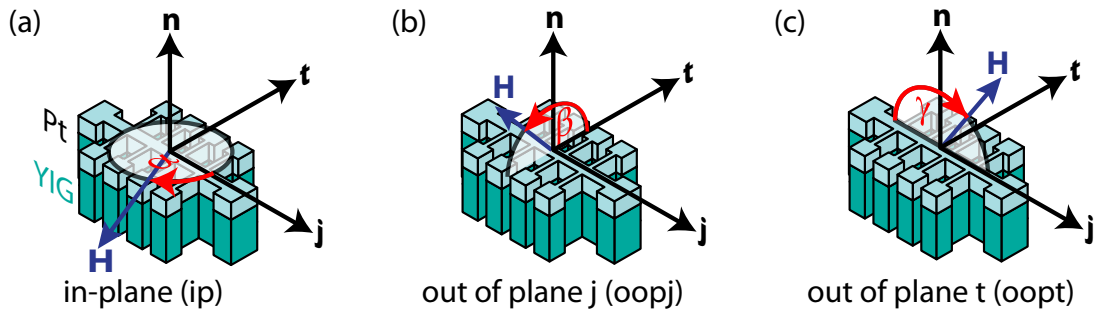$$\rho_{trans}\,(\delta) = V_{trans}\,(\delta) \cdot \frac{t_N}{j_q} \tag{2.30}$$

Figure 2.7: Definition of the rotation planes in-plane (ip, panel **a**), out of plane perpendicular **j** (oopj, panel **b**) and out of plane perpendicular **t** (oopt, panel **c**) including the respective rotation angles α, β and γ.

A slight misalignment of the contact leads of the Hall bar structure may result in a superposition of a small percentage of the longitudinal signal to the transverse voltage and vice versa. Since the longitudinal voltages taken in our experiments are orders of magnitude larger than the transverse signals, this is crucial especially in out of plane rotations. In detail, for oopj and oopt rotations, one expects a Hall signal from the Pt of the order of $-20\,\mathrm{p\Omega m/T}$ [114] (bulk value), whereas the longitudinal signal given by the sheet resistivity of Pt is about $200 - 700\,\mathrm{n\Omega m}$. Therefore, even a few per mill of ρ_{long} superimposing ρ_{trans} will distort the transverse signal.

The $\cos^2(\delta)$ shaped longitudinal signals taken in our measurement are periodic by $\delta = 180°$, $\rho^{\mathrm{symm}}(\delta) = \rho^{\mathrm{symm}}(\delta + 180°)$, whereas the $\sin(\delta)$ shaped Hall signature in the out of plane measurements is antisymmetric by $\delta = 180°$, $\rho^{\mathrm{antisymm}}(\delta) = -\rho^{\mathrm{antisymm}}(\delta + 180°)$. Here, the angle δ again stands for the out of plane rotation angles β and γ. We used the following equation to antisymmetrize the transverse out of plane data

$$\rho_{\mathrm{trans}}^{\mathrm{antisymm}} = \begin{cases} \frac{\rho_{\mathrm{trans}}(\delta) - \rho_{\mathrm{trans}}(\delta + 180°)}{2}, & \text{for } 0° \leq \delta \leq 180° \\ \frac{\rho_{\mathrm{trans}}(\delta) - \rho_{\mathrm{trans}}(\delta - 180°)}{2}, & \text{for } 180° < \delta \leq 360° \end{cases} \tag{2.31}$$

Additionally, a superimposing transverse component can be separated from the longitudinal signal via

$$\rho_{\mathrm{long}}^{\mathrm{symm}} = \begin{cases} \frac{\rho_{\mathrm{long}}(\delta) + \rho_{\mathrm{long}}(\delta + 180°)}{2}, & \text{for } 0° \leq \delta \leq 180° \\ \frac{\rho_{\mathrm{long}}(\delta) + \rho_{\mathrm{long}}(\delta - 180°)}{2}, & \text{for } 180° < \delta \leq 360° \end{cases} \tag{2.32}$$

Both equations were implemented in a Python based program written by Richard Schlitz [115] during his bachelor's thesis. In our experiments, we took $720°$ data sets ($360°$ rotation clockwise and counter-clockwise) and averaged the data taken in both rotation directions. We (anti-) symmetrized all ADMR raw data shown in this work using Eq. (2.31) and (2.32) after calculating ρ_{long} and ρ_{trans} according to Eq. (2.29) and (2.30).

2.2.3 Sheet resistivity in Pt thin films

Before starting the magnetoresistive experiments, we checked the temperature- and thickness dependence of the sheet resistivity ρ_0 of our Pt thin films, taken from measurements of the longitudinal resistivity ρ_{long} in the absence of an external magnetic field. We observe an increase of ρ_0 from $200\,\mathrm{n\Omega m}$ to more than $700\,\mathrm{n\Omega m}$ with decreasing Pt thickness t_{N}, which we attribute to the finite roughness of the YIG/Pt interface. Upon decreasing the temperature from room temperature to $10\,\mathrm{K}$, ρ_0 additionally decreases by an average factor of the residual resistance ratio $RRR = \rho_{300\,\mathrm{K}}/\rho_{10\,\mathrm{K}} \approx 1.5$ [cf. Fig. 2.8(a)] for all samples investigated. The residual resistance ratio can be understood as a measure for the number of impurities in a material. The higher the RRR value, the less impurities
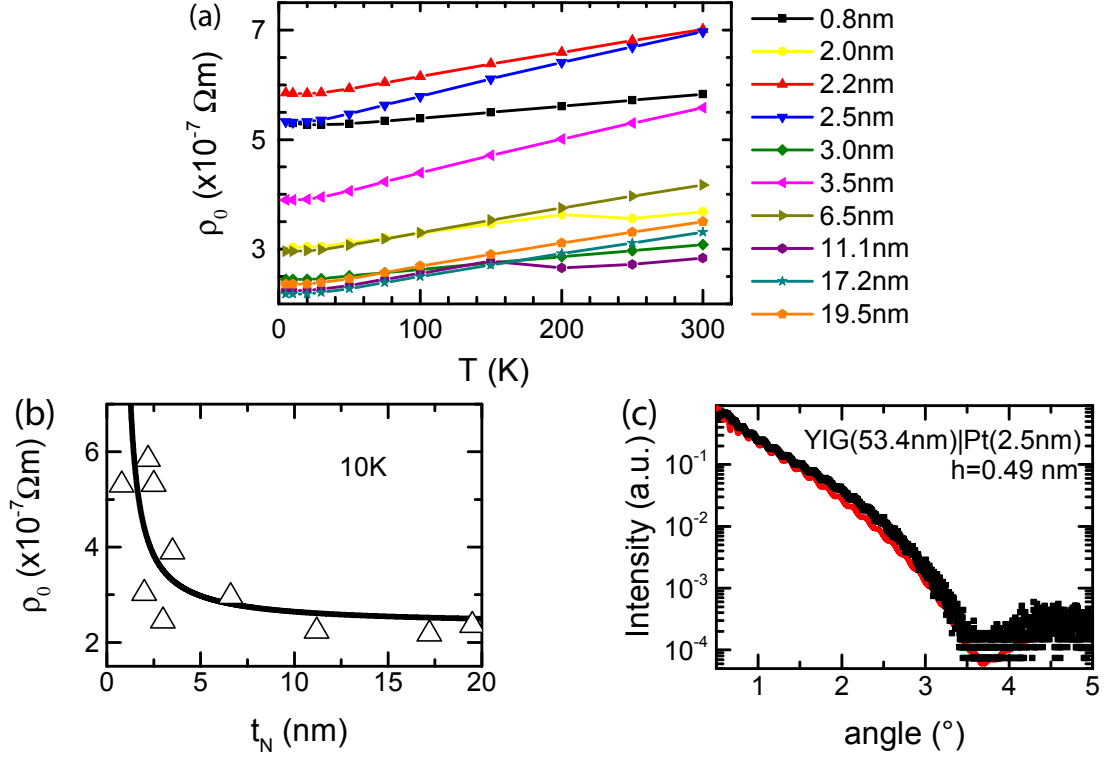
Figure 2.8: **(a)** Temperature dependence of the resistivity ρ for a set of YIG/Pt samples with different values t_{N} of the Pt thickness. **(b)** Thickness dependence of ρ_0 (symbols) for the 10 K data and a fit using Eq. (2.33) shown as a solid line. Panel **(c)** shows exemplary HR X-ray reflectometry (HR-XRR) data for a sample with a Pt thickness of $t_{\mathrm{N}} = 2.5\,\mathrm{nm}$. The red line shows a HR-XRR fit for a thickness of the YIG layer of $t_{\mathrm{YIG}} = 53.4\,\mathrm{nm}$ and a roughness of $h = 0.49\,\mathrm{nm}$.

are present. For Pt, RRR values of about 700 and higher have been reported [116] for wires with diameters of $250\,\mu\mathrm{m}$. While of course surface effects have to be taken into account for thin films, too, the investigation of our Pt nevertheless indicates a quite high impurity density. In order to take the film thickness and temperature dependence of ρ_0 into account, we use a thickness dependent resistivity $\rho_0(t_{\mathrm{N}}, T)$ as proposed by Fischer *et al.* [117]:

$$\rho_0(t_{\mathrm{N}}, T) = \rho_\infty(T) \left(1 + \frac{3}{8\,(t_{\mathrm{N}} - h)} \ell_\infty \,(1 - p) \right), \tag{2.33}$$

where ρ_∞ is the resistivity for $t_{\mathrm{N}} \to \infty$, h the interface roughness, ℓ_∞ the mean free path for $t_{\mathrm{N}} \to \infty$ and p the fraction of electrons scattered at the metal surface. Here, we assume a diffusive limit ($p = 0$) and choose $\rho_\infty(T) = \rho_0(16.9\,\mathrm{nm}, T)$ (assuming the 16.9 nm film to be bulk-like) and $\ell_\infty = 3\,\mathrm{nm}$ from a fit of Eq. (2.33) to the experimental data (cf. fit in Fig. 2.8 (b) to the 10 K data). In literature, $\ell_\infty \approx 12\,\mathrm{nm}$ has been reported for Pt [117], the difference to our value is supposed to be due to the increased number of impurities in our films (cf. RRR value). To enable a straightforward fit of the data as a function of the film thickness, i.e., across several samples, we use the same average

rms value of $h = 0.7$ nm for the interface roughness (derived from HR-XRR as listed in Tab. 6.2) for all samples in the following sections.

2.3 Magnetotransport experiments at room temperature

In Sec. 2.1.6, we theoretically described a novel magnetoresistive phenomenon in FMI/N bilayers, the spin Hall magnetoresistance. To experimentally test this conjecture, we start the experimental part of this chapter with a room temperature analysis of the magnetization orientation dependent magnetotransport in YIG/Pt bilayers. We show that the MR fingerprint is a unique feature and can be linked to the SMR theory presented above, while it is at odds with a magnetic proximity-based AMR assumption. Taking advantage of the SMR picture, we are able to extract the film anisotropy of the ferrimagnetic insulator YIG from magnetotransport measurements in Sec. 2.3.4. Afterwards, we discuss the magnetic field dependence of the SMR in Sec. 2.3.5. From a characteristic normal metal thickness dependence of the MR signal, we close this section with a calculation of spin transport parameters of the YIG/Pt bilayer using the SMR theory in Sec. 2.3.6. The room-temperature results presented in this section have been published in Physical Review B [46].

2.3.1 Magnetoresistive fingerprint in YIG/Pt

We start the evaluation of the MR in YIG/Pt bilayers with the analysis of ADMR measurements obtained from a YIG (53 nm)/Pt (8.5 nm) bilayer taken at $T = 300$ K with a magnetic field of $\mu_0 H = 1$ T applied. The experimental results are summarized in Fig. 2.9. For the ADMR experiments with an ip magnetic field rotation, as depicted in Fig. 2.9 (a), we observe an angular dependence with a period of 180° and a maximum in ρ_{long} for $\mathbf{H}$ parallel ($\alpha = 0°$) or anti-parallel ($\alpha = 180°$) to $\mathbf{j}$ and a minimum for $\mathbf{H}$ parallel ($\alpha = 90°$) or anti-parallel ($\alpha = 270°$) to $\mathbf{t}$. Due to the small in-plane magnetic anisotropy of the YIG layer, its magnetization is aligned with the external magnetic field in good approximation for all α. ρ_{long} shows a $\cos^2(\alpha)$ dependence with $-\Delta\rho/\rho_0 \approx 6.5 \times 10^{-4}$ in accordance to Eq. (2.21) [cf. green dashed lines in Fig. 2.9 (a)]. In addition, the transverse resistivity depicted in Fig. 2.9 (d) exhibits a $\cos(\alpha)\sin(\alpha)$ dependence. We observe a maximum in ρ_{trans} at $\alpha = 135°$ and $\alpha = 315°$, while the minima are located at $\alpha = 45°$ and $\alpha = 225°$. The amplitude of the modulation in ρ_{trans} in Fig. 2.9 (d) corresponds to the modulation in the longitudinal resistivity, and we observe $\rho_1 = -\rho_3$ as expected from the SMR theory.

In ip configuration, however, also a fit according to Eq. (2.27) provides a qualitative agreement to our experimental data. This is shown by means of the red dashed lines in Fig. 2.9
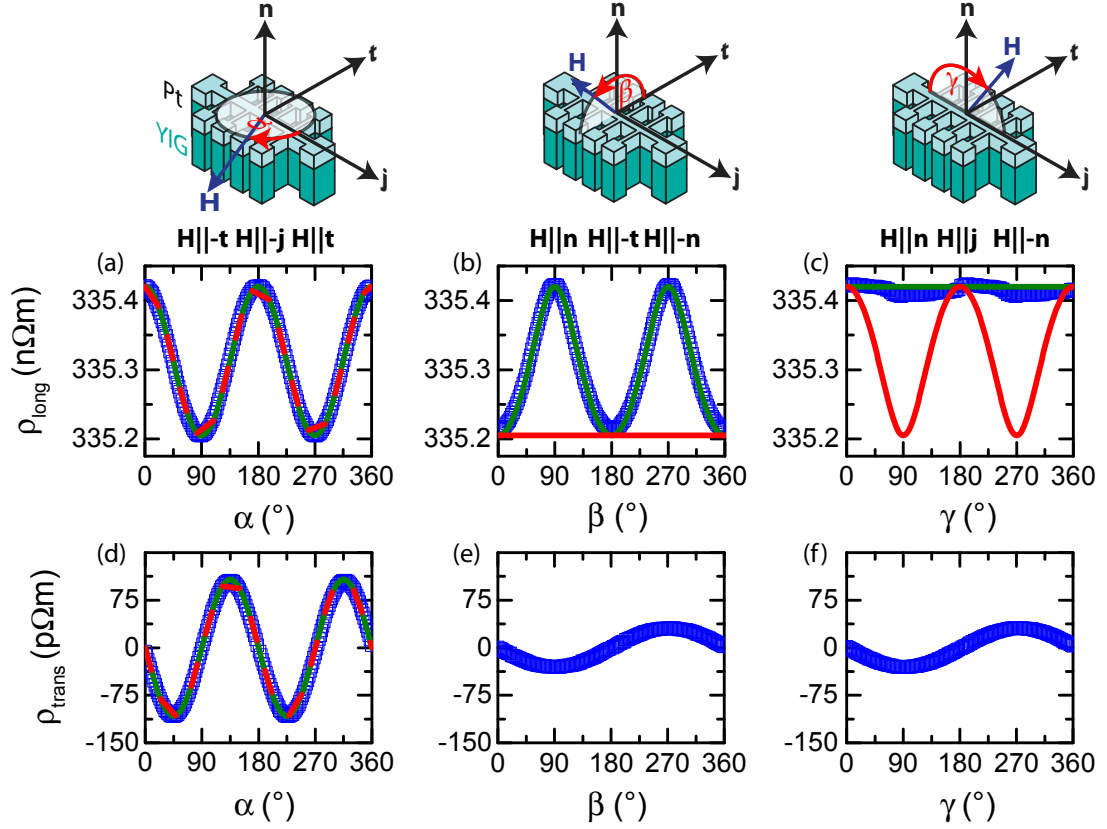
Figure 2.9: ADMR results for a YIG (53 nm)/Pt (8.5 nm) bilayer taken at $T = 300\,\text{K}$ by applying a magnetic field of $\mu_0 H = 1\,\text{T}$. **(a)** - **(c)** Evolution of the longitudinal resistivity ρ_{long} for rotations in ip **(a)**, oopj **(b)** and oopt **(c)** configuration. **(d)** -**(f)**: Dependence of the transverse resistivity ρ_{trans} on the magnetic field orientation for rotations in ip **(d)**, oopj **(e)** and oopt **(f)** configuration. The green dashed lines represent fits using the SMR theory. Fits taking advantage of the proximity MR model are depicted in red dashed lines.

(a) and (d). In ip configuration ($m_n = 0$), both Eq. (2.21) ($\rho_{\text{long}} \propto m_t^2$) and Eq. (2.27) ($\rho_{\text{long}} \propto m_j^2$) agree with our experimental findings and thus a qualitative distinction between the SMR and the proximity MR concept is not possible by performing experiments with magnetization orientations in the sample plane only.

In case of the oopj rotation plane [cf. Fig. 2.9 (b)], we observe maxima in ρ_{long} located at $\beta = 90°$ (**H** $\parallel$ **n**) and $\beta = 270°$ (**H** $\parallel$ $-$**n**). The minima in ρ_{long} occur at $\beta = 0°$ (**H** $\parallel$ **t**) and $\beta = 180°$ (**H** $\parallel$ $-$**t**). The longitudinal resistivity exhibits a $\sin^2(\beta)$ dependence and we again find $-\Delta\rho/\rho_0 \approx 6.5 \times 10^{-4}$. As shown by the green line in Fig. 2.9 (b), the SMR model again reproduces the characteristics of our experimental signal, while a fit using the AMR theory [red line in Fig. 2.9 (b)] suggests no dependence of ρ_{long} on the rotation angle β in this configuration ($m_j = 0$). For the transverse resistivity, we now observe a completely different angular dependence proportional to $\sin(\beta)$ with a period of 360°. ρ_{trans} has a minimum at $\beta = 90°$ (**H** $\parallel$ **n**) and a maximum at $\beta = 270°$ (**H** $\parallel$ $-$**n**). This is

the signature of the Hall effect in the Pt layer and will be discussed separately in Ch. 3. Interestingly, the angular dependence of $\rho_{\text{long}}(\gamma)$ vanishes for the oopt rotation plane [cf. Fig. 2.9(c)] in good approximation. Small wiggles on the longitudinal signal stem from a strong temperature dependence of the Pt sheet resistivity[5]. Thus, a small change in the environmental temperature is directly visible in the transport data[6]. A seemingly occurring 180° periodicity of the longitudinal signal can be attributed to the symmetrization during the data processing. The upper limit for the resistivity modulation in oopt geometry is 4×10^{-5} for this sample and thus is at least one order of magnitude smaller than the signal modulation found in ip and oopj. Using the Pt temperature coefficient $\tau_{\text{Pt}} \approx 3800\,\text{ppm}$ at room temperature [118], a modulation $\Delta\rho/\rho_0 = 4 \times 10^{-5}$ is correlated to a temperature imbalance of about $11\,\text{mK}$ in the Pt film. This value in good approximation corresponds to the temperature fluctuations $\Delta T \approx 8\,\text{mK}$ of the dipstick detected for this measurement.

The almost constant oopt signal is in contrast to the expected angular dependence of a proximity MR [cf. Eq. (2.27)], but is fully consistent with our SMR model [cf. Eq. (2.21)]. Thus, from a set of ADMR measurements taken in different rotation planes, we can exclude the proximity MR effect as the source of the observed MR. For ρ_{trans}, we again find a $\sin(\gamma)$ angular dependence, which dominantly stems from the ordinary Hall effect in Pt.

A MR in YIG/Pt bilayers with similar angular behavior was also reported by Huang *et al.* [43], but these authors attributed their findings to an AMR effect originating from an induced magnetism (proximity MR, cf. Sec. 2.1.7) in the Pt layer. As discussed in the context of Fig. 2.9, our results suggest that systematic measurements as a function of **M** orientation in out-of-plane geometries allow to distinguish between SMR and AMR. The angular dependence observed in YIG/Pt samples at the WMI as well as by Huang *et al.* [43] can be consistently explained by the SMR model presented in Sec. 2.1.5, while we can rule out a conventional AMR as an explanation for the observed magnetoresistance.

2.3.2 Reproducibility of the SMR

The characteristic SMR fingerprint in magnetotransport experiments on YIG/Pt bilayers was found in a set of more than 20 samples with variable Pt thickness t_{N}. In Figs. 2.10 and 2.11, we show a compilation of longitudinal and transverse ADMR data taken at $300\,\text{K}$ for three samples with different Pt thicknesses $t_{\text{N}} = 2.2\,\text{nm}$, $6.5\,\text{nm}$ and $16.9\,\text{nm}$

---

[5]Pt is known as a material with a strong temperature dependent resistance (temperature coefficient $\tau \approx 3800\,\text{ppm}$ at room temperature [118]), which led to a wide-spread use of Pt for thermometers, but challenges the noise level control in transport experiments.

[6]See Bachelor's thesis of Tobias Maier [119] for more details.

while applying an external magnetic field of $1\,\mathrm{T}$. We again find $\cos^2(\alpha)$ and $\sin^2(\beta)$ shaped signals in ρ_{long} for ip and oopj rotations with the corresponding modulation amplitude, while in good approximation the longitudinal signal is constant as a function of the external field orientation in oopt rotations. Small wiggles on ρ_{long} observed in this configuration were not reproducible in a repetition of the measurements and can be attributed to temperature fluctuations during the measurements.

Please note that we intentionally chose the Y-axes scales in Fig. 2.10 for all panels such that the full scale would indicate the same relative amplitude $-\Delta\rho_1/\rho_0$ of 1.8×10^{-3}. Therefore, the amplitudes of the $\cos^2(\delta)$ and $\sin^2(\delta)$ shaped signals for the different samples depicted in Fig. 2.10 can be directly compared to each other. The thickness dependence of the Pt sheet resistivity found in these samples was already discussed in Sec. 2.2.3.

Figure 2.10: Longitudinal SMR results for a set of YIG/Pt samples taken at $T = 300\,\mathrm{K}$ using $\mu_0 H = 1\,\mathrm{T}$. **(a)-(c)** Evolution of the longitudinal resistivity ρ_{long} for rotations in ip configuration for $t_{\mathrm{N}} = 2.2\,\mathrm{nm}$ **(a)**, $t_{\mathrm{N}} = 6.5\,\mathrm{nm}$ **(b)** and $t_{\mathrm{N}} = 16.9\,\mathrm{nm}$ **(c)**. **(d)-(f)** Evolution of the longitudinal resistivity for rotations in oopj configuration for $t_{\mathrm{N}} = 2.2\,\mathrm{nm}$ **(d)**, $t_{\mathrm{N}} = 6.5\,\mathrm{nm}$ **(e)** and $t_{\mathrm{N}} = 16.9\,\mathrm{nm}$ **(f)**. **(g)-(i)** Evolution of the longitudinal resistivity for rotations in oopt configuration for $t_{\mathrm{N}} = 2.2\,\mathrm{nm}$ **(g)**, $t_{\mathrm{N}} = 6.5\,\mathrm{nm}$ **(h)** and $t_{\mathrm{N}} = 16.9\,\mathrm{nm}$ **(i)**.

We find a strong Pt thickness dependence of the SMR amplitude. The largest modulation amplitude $-\Delta\rho_1/\rho_0 = 1.2 \times 10^{-3}$ occurs in the sample with the thinnest Pt layer of this set [$t_N = 2.2$ nm, panel(a,d,g)] and the signal decreases to $-\Delta\rho_1/\rho_0 = 7.2 \times 10^{-4}$ for $t_N = 6.5$ nm (panel b,e,h). The sample with the thickest Pt layer of this set [$t_N = 16.9$ nm, panel(c,f,i)] shows an even lower SMR with $-\Delta\rho_1/\rho_0 = 2.9 \times 10^{-4}$. This thickness dependent behavior again can be explained by the SMR theory and will be discussed in detail in Sec. 2.3.6.

Taking a look at the transverse data depicted in Fig. 2.11, again a $\cos(\alpha)\sin(\alpha)$ dependence is found in all samples for ip rotations (panel a-c) and the absolute amplitudes
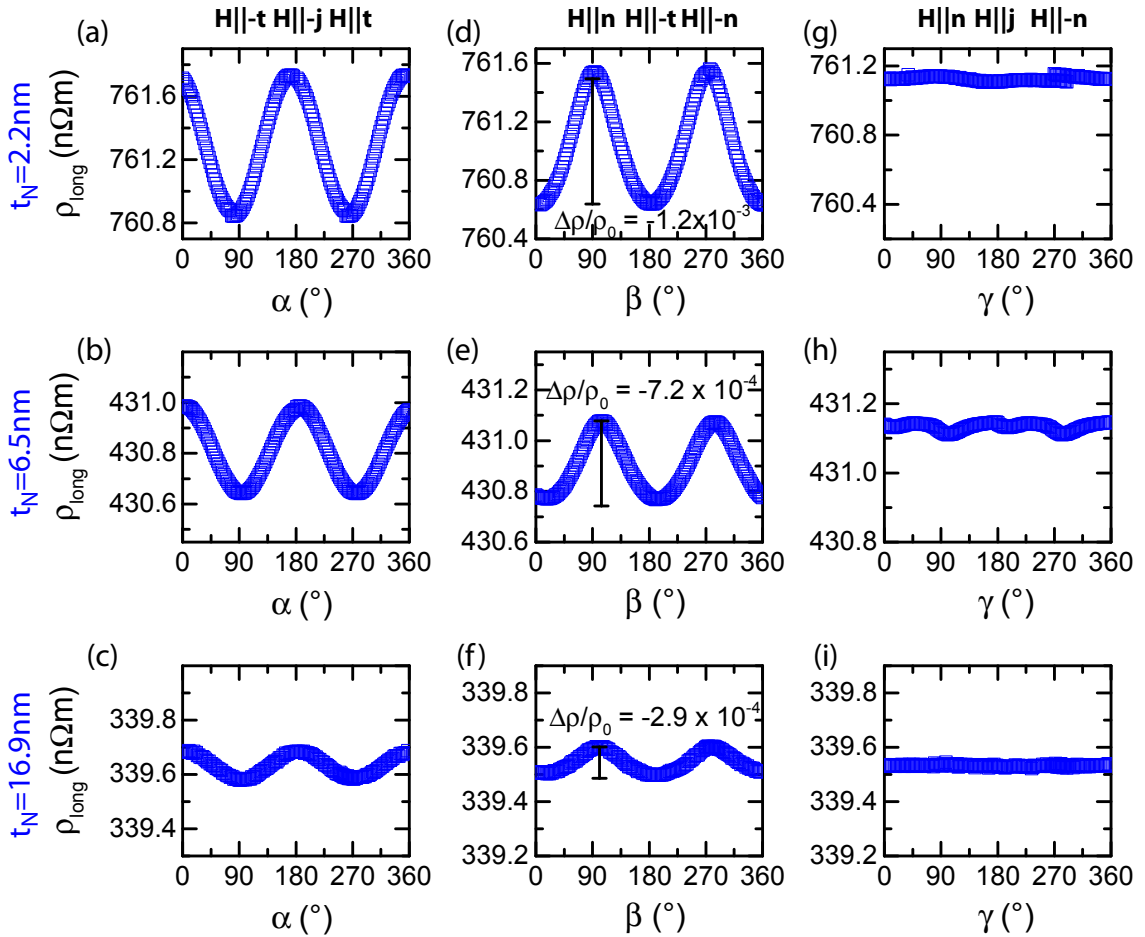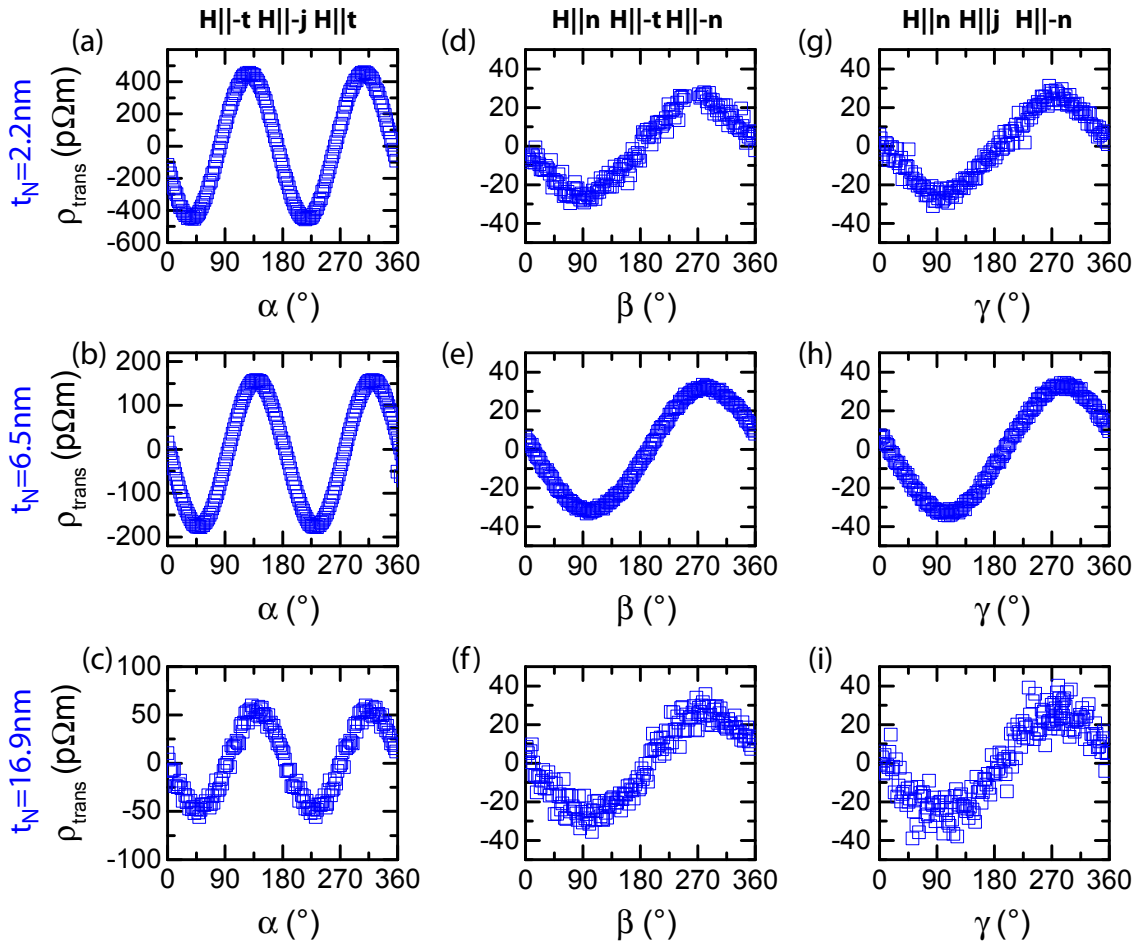

Figure 2.11: Transverse SMR results for a set of YIG/Pt samples taken at $T = 300$ K using $\mu_0 H = 1$ T. **(a)-(c)** Evolution of the transverse resistivity ρ_{trans} for rotations in ip configuration for $t_N = 2.2$ nm **(a)**, $t_N = 6.5$ nm **(b)** and $t_N = 16.9$ nm **(c)**. **(d)-(f)** Evolution of the transverse resistivity for rotations in oopj configuration for $t_N = 2.2$ nm **(d)**, $t_N = 6.5$ nm **(e)** and $t_N = 16.9$ nm **(f)**. **(g)-(i)** Evolution of the transverse resistivity for rotations in oopt configuration for $t_N = 2.2$ nm **(g)**, $t_N = 6.5$ nm **(h)** and $t_N = 16.9$ nm **(i)**. The different noise levels are due to different measurement ranges of the nanovoltmeter used in the respective experiment.

of the modulation correspond to the longitudinal ip and oopj data in Fig. 2.10 for each sample. In both out of plane rotation planes, we again find $\sin(\delta)$ shaped Hall signals in all samples. The amplitudes of the signals are around $25\,\text{p}\Omega\text{m}$, which correspond to the literature value for the conventional (ordinary) Hall effect in bulk Pt [65]. A detailed discussion of field and temperature dependent contributions to the transverse Hall signals (not shown here) will be the postponed to Chapter 3.

2.3.3 XMCD

Besides magnetotransport experiments, X-ray magnetic circular dichroism (XMCD) measurements (cf. Sec. 2.1.7) on YIG/Pt bilayers have been carried out to investigate a possibly induced magnetic moment in the Pt layer[7]. In our experiments, we used a set of YIG/Pt bilayers grown on YAG substrates[8] under the conditions described above (see Sec. 2.2). The XMCD measurements have been performed at the European Synchrotron Radiation Facility (ESRF) in Grenoble. We took X-ray absorption near-edge spectra (XANES) at the Pt L_3 edge for an external magnetic field of $\pm 60\,\text{mT}$ applied in the sample plane. The XMCD signal is calculated from these spectra for corresponding measurements with either opposite sign of the external magnetic field or opposite polarity of the X-ray beam. Even by integrating the XMCD signal in the sample with the thinnest Pt layer studied ($t_\text{N} = 1.6\,\text{nm}$), an average over 30 XMCD spectra showed that the induced magnetic moment in Pt – if present at all – is small in our samples. We estimated an upper limit of $(0.003 \pm 0.001)\,\mu_\text{B}$ per Pt atom for the induced total magnetic moment in Pt, which is at least 30 times smaller than the induced magnetic moment resolved in a Fe/Pt reference sample [106, 109]. A detailed analysis of the XMCD data was published in Ref. [106].

We have to admit that our XMCD results are in strong contrast to the findings published by Lu et al.. These authors reported an AMR-like transport in Pt thin films on YIG, exhibiting the same magnetic field orientation dependent signatures as our measurements presented above. In their experiments, they used a several μm thick, single-crystalline YIG film grown via liquid-phase epitaxy (LPE) on (111)-oriented GGG substrates, with a $1.5\,\text{nm}$ Pt thin film deposited *ex situ* via sputtering. From their XMCD data, they calculated an average induced magnetic moment of $0.054\,\mu_\text{B}$ per Pt atom. However, by

---

[7]X-ray absorption energies indicate relative energetic levels of an atom's electronic shell. These energy differences are characteristic for each element. For atoms with a finite magnetic moment, the absorption of X-rays additionally is sensitive to the helicity of the photons. In XMCD experiments, one therefore calculates the absorption difference for e.g. left and right circular polarized waves to get information on the (element-specific) spin moment of the valence band.

[8]As the absorption energy of Ga ($10.3671\,\text{keV}$) is close to the Pt L_3 edge ($11.5637\,\text{keV}$), and therefore might affect the results of X-ray absorption near-edge spectra (XANES) at the Pt L_3 edge, it is recommended to use YAG substrates instead of GGG ($\text{Gd}_3\text{Ga}_5\text{O}_{12}$) for XMCD experiments.

comparing the corresponding X-ray absorption near edge spectra (XANES) from Lu *et al.* with the ones taken in Ref. [106], one finds distinct discrepancies that might indicate a contamination and non-metallic behavior in the sputtered Pt film used by Lu *et al.*, that might be the origin of their reported induced magnetic moment. A more detailed analysis of this issue can be found in Ref. [109].

2.3.4 Anisotropy extraction

The concept of the spin Hall magnetoresistance is based on the interplay of the magnetization orientation of the FMI layer and the spin current in N. Therefore, the SMR effect should not, in good approximation, be influenced by the strength of the external magnetic field, as long as the magnetization aligns[9] with $\mu_0 H$. However, by reducing the external magnetic field strength to values close to the anisotropy fields of the FMI, the SMR allows for electrical anisotropy characterizations of ferromagnetic insulators (here: YIG), in a similar fashion as it was established for conducting ferromagnets by Limmer *et al.* [112, 113, 120].

On the basis of Fig. 2.12 and 2.13, we now discuss ADMR data for the YIG/Pt(2.2 nm) sample for different external magnetic field strengths between 1 T and 100 mT. Upon reducing the external magnetic field strength, the angular dependence of the ip signals in ρ_{long} and ρ_{trans} are approximately not affected by the amplitude of $\mu_0 H$, while we observe a slight decrease of the offset value ρ_0 with decreasing $\mu_0 H$ for the longitudinal resistivity. The observation of a $\cos^2(\alpha)$ shaped signal in ρ_{long} even at the lowest field investigated is due to a very small in-plane anisotropy in the (111)-oriented YIG, such that the magnetization is oriented parallel to the external magnetic field even for the data set with the smallest external field.

In the oopj configuration, however, the shape anisotropy influences the orientation of the magnetization in YIG for $\mu_0 H \leq 500$ mT, which results in a deviation from the $\sin^2(\beta)$ dependence in ρ_{long}.

For oopt orientations, where no $\cos^2(\gamma)$ shaped signal is visible, we find abrupt changes in ρ_{long} for $\mu_0 H \leq 100$ mT. These spikes can be explained by an abrupt in-plane reorientation of the magnetization, when the magnetic field orientation is close to $\gamma = 90°(\mathbf{H} \parallel \mathbf{n})$ and $\gamma = 270°(\mathbf{H} \parallel -\mathbf{n})$.

The transverse signal in both out-of-plane configurations, that will be discussed in Ch. 3 in more detail, reflects the dominance of the conventional Hall effect on ρ_{trans} and thus shows a direct proportionality between the sinusoidal modulation of the signal and the the external magnetic field strength. Abrupt changes in ρ_{trans}, visible for $\mu_0 H \leq 100$ mT,

---

[9]The high field dependence for $\mu_0 H \geq 1$ T will be discussed in Sec. 2.3.5.

Figure 2.12: Longitudinal SMR results for a YIG/Pt ($t_N = 2.2$ nm) sample taken at $T = 300$ K using $\mu_0 H = 1$ T(blue), $\mu_0 H = 0.5$ T(green), and $\mu_0 H = 0.1$ T(red) in the rotation planes ip **(a-c)**, oopj **(d-f)** and oopt **(g-i)**. The solid, colored lines represent fits using the SMR theory.

again originate from an in-plane re-orientation of the magnetization if **H** is almost parallel or anti-parallel to the film normal **n**.

For a quantitative analysis, we combine the SMR theory with a simulation technique successfully used for ADMR in ferromagnetic, conductive materials like (Ga,Mn)As [112, 113, 120, 121] and Heusler compounds [122]. Starting from a ferromagnetic single domain model, we calculate the free enthalpy of the ferromagnetic system,

$$G_M(\mathbf{m}) = -\mu_0 H(\mathbf{h} \cdot \mathbf{m}) + B_n m_n^2. \tag{2.34}$$

Here, $\mathbf{h} = \mathbf{H}/|H|$ is a unity vector pointing along the external field orientation **H** and B_n represents the uniaxial contribution of the shape anisotropy. In our model, we neglect possibly occurring uniaxial anisotropies as well as the cubic anisotropy. However, these additional terms can easily be added to Eq. (2.34) and our simulation routine, while fits to
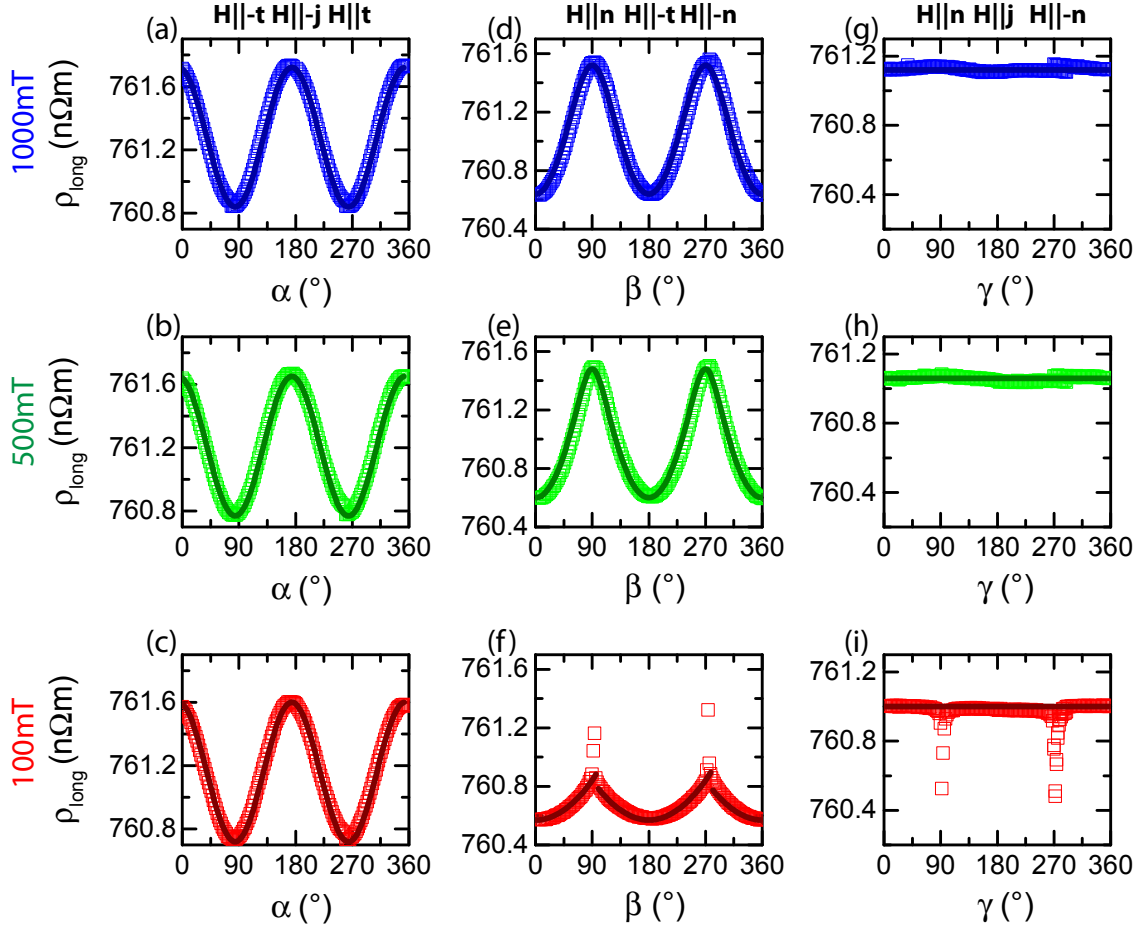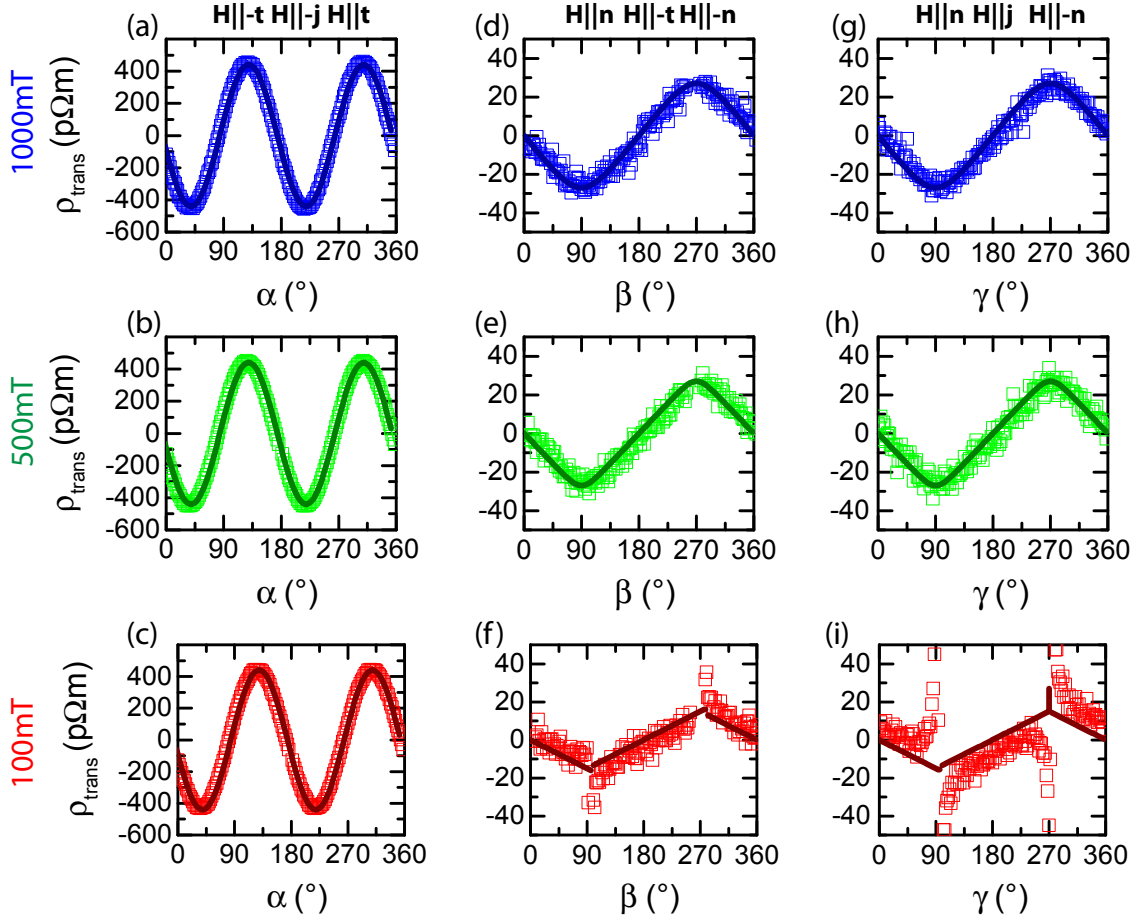
Figure 2.13: Transverse SMR results for a YIG/Pt ($t_N = 2.2$ nm) sample taken at $T = 300$ K using $\mu_0 H = 1$ T(blue), $\mu_0 H = 0.5$ T(green), and $\mu_0 H = 0.1$ T(red) in the rotation planes ip **(a-c)**, oopj **(d-f)** and oopt **(g-i)**. The solid, colored lines represent fits using the SMR theory.

our experimental data as discussed below support that the anisotropy observed in SMR measurements on YIG/Pt are dominated by B_n.

In a LabView based simulation (see Ref. [120] and [110] for details), we choose a starting value for the anisotropy constant B_n and determine the magnetization direction **m** for every magnetic field orientation by numerically minimizing the free enthalpy. From the obtained **m** vector, we calculate ρ_{long} and ρ_{trans} using a set of ρ_i parameters given by Eqs. 2.21 and 2.24. An iterative optimization process of B_n and the ρ_i parameters is carried out, until we achieve a satisfactory agreement between experiment and simulation for all rotation planes and $\mu_0 H$ magnitudes with one single set of B_n and ρ_i. Therefore, we take all ρ_i parameters except ρ_2 independent of the external magnetic field strength. A slight field dependence of the offset value ρ_0, however, is taken into account. In Figs. 2.12 and 2.13, the simulation curves obtained this way are depicted as solid, colored lines. Obviously, the simulation is in good agreement with the experimental data for all external

fields.

In Tab. 6.2, we summarized the respective ρ_i and $B_\mathbf{n}$ parameters for all samples investigated in this work. The extracted $B_\mathbf{n}$ values spread from $50\,\mathrm{mT}$ to $150\,\mathrm{mT}$ with an average value of $79.5\,\mathrm{mT}$. From ferromagnetic resonance (FMR) experiments on a GGG/YIG ($25\,\mathrm{nm}$) film performed by M. Althammer, we extracted an uniaxial anisotropy of $B_\mathrm{n} = 184.4\,\mathrm{mT}$ close to the literature value $179\,\mathrm{mT}$ [123]. Obviously, the extracted value for $B_\mathbf{n}$ is more than a factor of two smaller than the expectation from literature. One might attribute this mismatch to the fact that the FMR value for $B_\mathbf{n}$ is extracted from a YIG film with a width of about $2\,\mathrm{mm}$ and a length of $5\,\mathrm{mm}$, but the anisotropy values extracted via SMR are taken on Hall bar structured samples (width $80\,\mu\mathrm{m}$ and length $600\,\mu\mathrm{m}$), while the YIG film thicknesses are comparable. As the aspect ratio of the edge length $w : l : h$ enters the demagnetization tensor $\hat{N}_\mathrm{demag}$ for the shape anisotropy using

$$E_\mathrm{m} = \frac{\mu_0}{2} \int \mathbf{M} \cdot \hat{N}_\mathrm{demag} \cdot \mathbf{M} dV, \tag{2.35}$$

a change in the ratio between the in-plane edge length and the out-of-plane edge length changes the magnetostatic energy E_m of the system. For the FMR sample, we can approximate theses aspect ratios with $w : l : h \propto \infty : \infty : 0$ along the $\mathbf{j}$, $\mathbf{t}$ and $\mathbf{n}$ direction, which results in a demagnetization tensor

$$\hat{N}_\mathrm{demag,thin\ film} \propto \begin{pmatrix} 0 & 0 & 0 \\ 0 & 0 & 0 \\ 0 & 0 & 1 \end{pmatrix}, \tag{2.36}$$

while for the Hall bar the ratio between the $\mathbf{j}$ and $\mathbf{t}$ directions and the $\mathbf{n}$ direction decreases, leading to

$$\hat{N}_\mathrm{demag,Hall\ bar} \propto \begin{pmatrix} \epsilon_x & 0 & 0 \\ 0 & \epsilon_y & 0 \\ 0 & 0 & 1 - (\epsilon_x + \epsilon_x) \end{pmatrix}. \tag{2.37}$$

With this, the energetic landscape in Eq. (2.34) changes with aspect ratio and one expects a decrease in the uniaxial component B_n for the Hall bar compared to the "infinitely extended" sample, which is reproduced by the B_n value extracted from our measurements.

2.3.5 Magnetic field dependence

In Sec. 2.3.4, we discussed the influence of the external magnetic field strength on the amplitude of the SMR signal in YIG/Pt hybrids. Taking a closer look at this issue from a different angle, we now discuss the field dependence of the SMR for higher fields
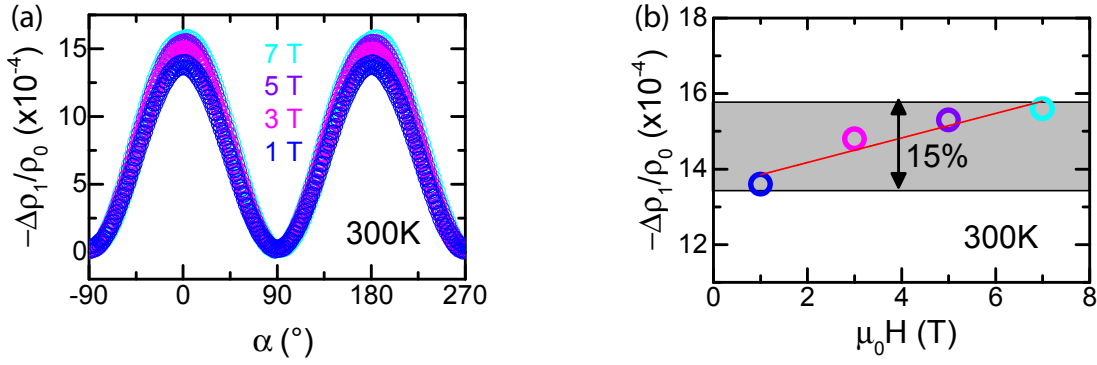
(a)

(b)

Figure 2.14: **(a)** Longitudinal SMR signal $-\Delta\rho_1/\rho_0$ in ip configuration for a YIG/Pt (3.1 nm) sample grown on YAG taken at 300 K for various magnetic fields (see legend). **(b)** Magnetic field dependence of the longitudinal SMR signal shown in panel **(a)**.

($\mu_0 H \geq 0.5$T). Figure 2.14 (a) shows ADMR rotations as a function of $\mu_0 H$ for the YIG/Pt (3.1 nm) sample grown on YAG taken at 300 K. Since the amplitudes of the $\cos^2(\delta)$ modulations have been proven to be identical for ip and oopj rotations at 300 K for $\mu_0 H \geq 500$ mT, we again focus on one rotation plane (ip). To allow for a simple reading of the $-\Delta\rho_1/\rho_0$ values from Fig. 2.14, we normalize the longitudinal resistivities to the respective minimum values, using

$$-\frac{\Delta\rho_1}{\rho_0} = \frac{\rho_{\text{long}} - \rho_{\text{long,min}}}{\rho_{\text{long,min}}}. \tag{2.38}$$

As indicated by the colored symbols in Fig. 2.14 (a), the longitudinal SMR amplitude $-\Delta\rho_1/\rho_0$ increases slightly with increasing field. The extracted $-\Delta\rho_1/\rho_0$ values as a function of $\mu_0 H$ are depicted in Fig. 2.14 (b). Obviously, an increase of about 15% is visible by increasing the field from 1 T to 7 T. From a linear fit to the field dependent $-\Delta\rho_1/\rho_0$ signal (cf. red line in Fig. 2.14 (b)), we find a slope of 0.325×10^{-4}/T with an offset value of 13.525×10^{-4}.

At first sight, this observation is at odds with the concept of the spin Hall magnetoresistance. In Sec. 2.1.5 we discussed that the SMR stems from the variation of the boundary conditions at the FMI/N interface. In this model, one expects that only the presence of a magnetization in the ferromagnetic layer is necessary to observe the SMR. In a theoretical description, the longitudinal SMR is governed by the real part of the spin mixing conductance G_r, which in a very basic picture integrates the number of spin transport channels across the interface and therefore is proportional to the number of magnetic moments in the FMI layer located at the interface. The observation of an increase of the SMR with increasing external magnetic field, in the present interpretation, corresponds to an effective increase of G_r. This can be interpreted as a gain of the number of magnetic
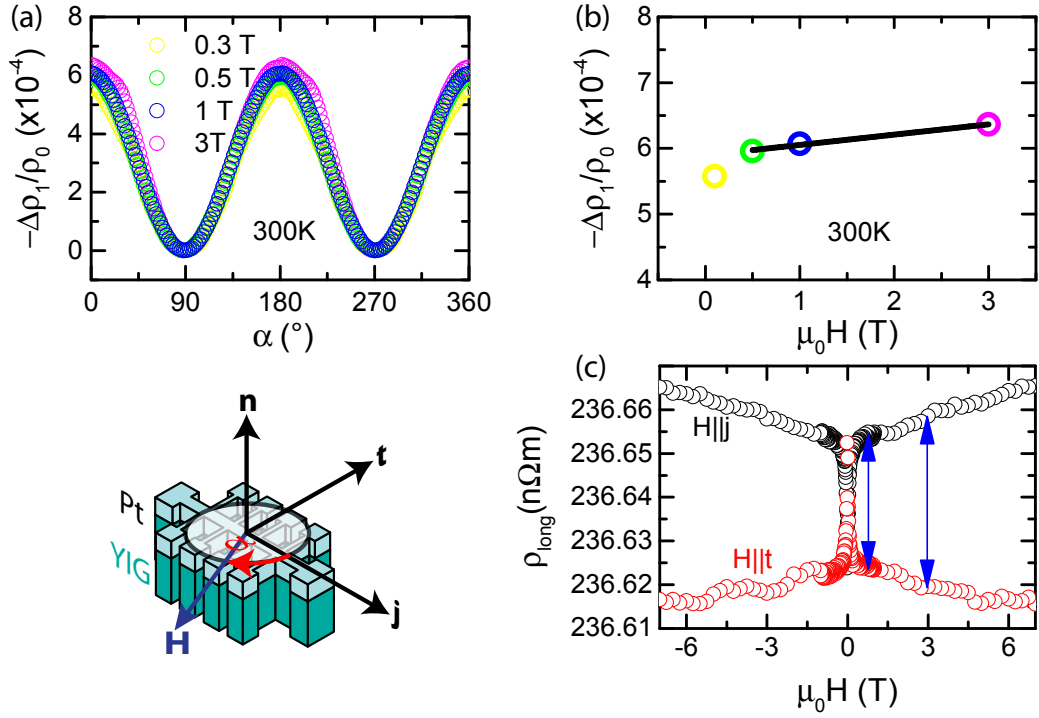
Figure 2.15: (a) Longitudinal SMR signal $-\Delta\rho_1/\rho_0$ in ip configuration for a YIG/Pt (6.1 nm) sample grown on GGG taken at 300 K for various magnetic fields (see legend). The additional shoulder for the 3 T measurement at $\alpha \approx 40°$ and $\alpha \approx 220°$ stems from a temperature instability during the measurement. The periodicity of this feature is caused by the symmetrization of the data according to Eq. (2.32). **(b)** Magnetic field dependence of the longitudinal SMR signal shown in panel (a). **(c)** Longitudinal resistivity ρ_{long} as a function of the external magnetic field strength for $\mathbf{H} \parallel \mathbf{j}$ (black) and $\mathbf{H} \parallel \mathbf{t}$ (red).

moments per unit area contributing to G_r.

In our experiments, we observe a linear increase of the SMR amplitude up to $\mu_0 H = 7$ T, which is the highest possible field accessible in the magnet cryostat "Moria" used for our experiments[10]. This phenomenon may be explained by a certain amount of pinned or "locked" magnetic moments at the FMI/N interface. These moments can only be activated (i.e. aligned with the external magnetic field) if the energy provided by the externally applied magnetic field overcomes the pinning energy. Thus, by increasing $\mu_0 H$ in our experiments, one increases the number of contributing moments in this interpretation, which is reflected in an effective increase of G_r. The linear field dependence observed in Fig. 2.14 therefore might hint to a homogeneous distribution of pinning energies.

For the sample shown in Fig. 2.14, we used yttrium aluminum garnet (YAG) as a substrate. For this substrate material, the lattice mismatch to the YIG lattice is about 3%,

---

[10]Recent experiments carried out at the high field laboratory in Grenoble confirmed a linear increase of the SMR signal up to at least 28 T for YIG/Pt (2.0 nm) [124].

which leads to a strain in the first YIG monolayers grown on top of the YAG substrate. This is observable e.g. from rocking curves around a YIG reflection in X-ray spectroscopy measurements, where we found a small peak with full width at half maximum (FWHM) of 0.04° ascribed to the relaxed film on top of a broader background peak (FWHM =0.4°) stemming from strained layers at the YAG/YIG interface [125]. Even if we assume that the strain in the YIG film relaxes with increasing distance from the substrate, we suggest that for the thin films ($t_{\mathrm{F}} \approx 60\,\mathrm{nm}$) used in our experiments, a full relaxation has not taken place at the top YIG layer close to the interface, which causes the pinning. Additionally, due to by relaxation processes, defects in the crystalline structure occur. These defects again can influence the magnetic properties of the material.

However, we also observe a magnetic field dependent increase of the SMR signal for YIG films grown on GGG (cf. Fig. 2.15). Again, we find a linear field dependence in ip rotations with a slope of $0.157 \times 10^{-4}/\mathrm{T}$, which is about a factor of two smaller than the fit results achieved for YAG/YIG/Pt[11]. External magnetic field dependent measurements performed in two configurations at $0°(\mathbf{H} \parallel \mathbf{j})$ and $90°(\mathbf{H} \parallel \mathbf{t})$ [cf. Fig. 2.15(c)] confirm this observation. In the latter representation, the SMR amplitude is proportional to the difference of the resistivity values obtained for both configurations, which is indicated by the blue arrows in Fig. 2.15(c).
GGG has a lattice mismatch of about 0.03% to YIG, which is a factor of 100 smaller than the lattice mismatch for YAG. Thus, one expects that the strain at the GGG/YIG interface relaxes within a reduced number of layers compared to YAG substrates, which is also confirmed by the absence of a broad background in the rocking curve around the YIG (444) reflection (FWHM 0.04°) [110]. The magnetic field dependence of the SMR in YIG/Pt bilayers grown on GGG might stem from pinning effects, too, as these samples again have a YIG thickness of about 60 nm.

On the other hand, the field dependence of the SMR could also be caused by a pinning induced by the finite surface roughness of the YIG/Pt interface. However, as compiled in Tab. 6.2 in the appendix, the surface roughnesses for films grown on GGG and YAG inferred from HR-XRR are comparable. Thus, a roughness introduced pinning may not explain the difference in field dependence obtained for the different substrate materials. To confirm the pinning model experimentally, it is suggested to perform e.g. magnetic force microscopy to map the magnetic surface of YIG thin films grown on GGG and YAG. Therefore, microscopy experiments taken at a set of samples with different thicknesses of the YIG layers should give further insight to a strain-induced pinning of magnetic

---

[11] For performing the linear fit to the field dependence in Fig. 2.15 (b) we neglect the data point taken at 300 mT as it seems that there is a different slope for $\mu_0 H \leq 0.5\,\mathrm{T}$ caused by anisotropy effects.

moments as well as surface defects. Unfortunately, such measurements were not possible during this thesis. They should be object of further investigations.

2.3.6 Dependence on t_N

Utilizing the data presented in Fig. 2.10, we noticed, that the longitudinal SMR signal $-\Delta\rho_1/\rho_0$ decreases for increasing Pt thickness. This is in accordance with ascribing the MR observed in FMI/N bilayers to an interface phenomenon. In Fig. 2.16(a), an overview of the detected $-\Delta\rho_1/\rho_0$ ratios for a set of 21 YIG/Pt samples grown on YAG and GGG is depicted as a function of the Pt layer thickness t_N. All data presented in this graph was taken at identical conditions at $T = 300\,\mathrm{K}$ using an external magnetic field of $1\,\mathrm{T}$ in oopj configuration. We clearly observe a maximum SMR in our samples at a Pt thickness of around $t_N^{\mathrm{max}} \approx 3\,\mathrm{nm}$. The different substrate materials used in our experiments are encoded in the black (for GGG) and green (for YAG) symbols in Fig. 2.16(a). Within an experimental error of 5×10^{-5}, the choice of the substrate material does not affect the SMR amplitude.

By fitting the experimental data to the SMR theory for $-\Delta\rho_1/\rho_0$ [cf. Eq. (2.23)], we are able to reproduce the thickness dependence. In other words, we can extract the material parameters represented by the spin diffusion length λ, the spin Hall angle θ_{SH} and the real part of the spin mixing interface conductance G_r from the fit using Eq. (2.23). As already discussed in Sec. 2.2.3, we take into account the thickness dependence of the sheet resistivity ρ_0. This limits the applicability of Eq. (2.23) to film thicknesses larger than the interface roughness h. In our simulation, we additionally use the assumption
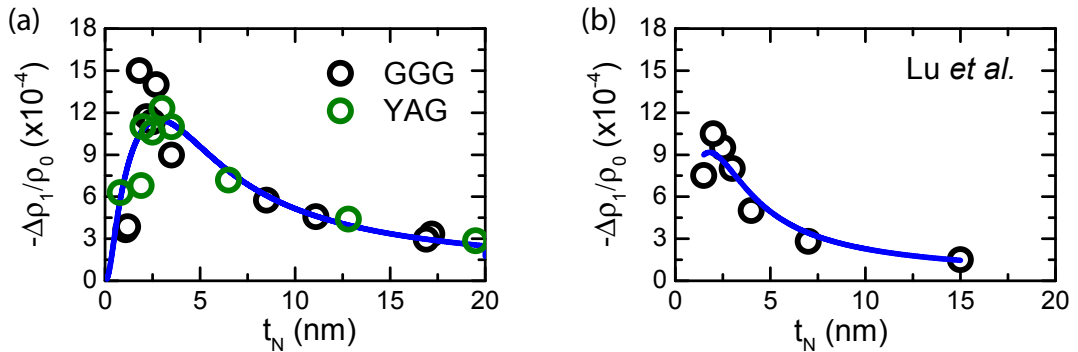
Figure 2.16: **(a)** Thickness dependence of the longitudinal SMR amplitude $-\Delta\rho_1/\rho_0$ for a set of YIG/Pt samples grown at the WMI on GGG (black symbols) and YAG (green symbols) substrates. All data taken at $300\,\mathrm{K}$ in oopj configuration using $\mu_0 H = 1\,\mathrm{T}$. The solid blue line represents a fit using the SMR theory [cf. Eq. (2.39)]. In panel **(b)**, the same SMR-based fit is performed for the data published by Lu *et al.* [47].

$G_r \gg G_i$ [126] to rewrite Eq. (2.23) as

$$\frac{\Delta\rho_1}{\rho_0} = \frac{\theta_{\mathrm{SH}}^2}{t_{\mathrm{N}}}\lambda\mathrm{Re}\frac{2\lambda G_{\uparrow\downarrow}\tanh^2\frac{t_{\mathrm{N}}}{2\lambda}}{\sigma + 2\lambda\coth\frac{t_{\mathrm{N}}}{\lambda}G_{\uparrow\downarrow}} \approx \frac{\theta_{\mathrm{SH}}^2}{t_{\mathrm{N}}}\lambda\frac{2\lambda G_r\tanh^2\frac{t_{\mathrm{N}}}{2\lambda}}{\sigma + 2\lambda\coth\frac{t_{\mathrm{N}}}{\lambda}G_r}. \qquad (2.39)$$

To extract the experimental values for λ, θ_{SH} and G_r, we fitted Eq. (2.39) to the data points depicted in Fig. 2.16(a) (the fit is represented by the blue solid line) and extracted $\lambda = 1.5\,\mathrm{nm}$, $\theta_{\mathrm{SH}} = 0.11$ and $G_r = 4\times 10^{14}\Omega^{-1}\mathrm{m}^{-2}$.

The value achieved for G_r is in good agreement with both theoretical calculations [126] and spin pumping experiments [127]. The MR effect in YIG/Pt hybrids, attributed either to the SMR or the magnetic proximity MR, was experimentally observed by different groups utilizing hybrid structures deposited by different methods [43, 45, 47, 96, 128, 129]. All of them observed the characteristic fingerprint ($\cos^2(\alpha)$ and $\sin^2(\beta)$ shaped modulations on ρ_{long} in ip and oopj configuration, but no MR in oopt configuration) in magnetotransport experiments performed at room temperature. In Tab. 2.1, we summarized the results for the spin transport parameters obtained from fits using Eq. (2.39), either performed by the respective authors themselves or calculated in Ref. [46] and the present work, respectively.

Interestingly, the Pt thickness dependent data interpreted within the proximity magnetoresistance framework published by Lu *et al.* can be reproduced with the SMR theory [cf. blue solid line in Fig. 2.16(b)] by using almost the same spin transport parameters for a fixed value of $G_r = 4.0\times 10^{14}\Omega^{-1}\mathrm{m}^{-2}$, $\lambda = (1.0\pm 0.2)\mathrm{nm}$ and $\theta_{\mathrm{SH}} = (0.12\pm 0.01)$. The spin diffusion length λ extracted from SMR measurements spreads from $0.8\,\mathrm{nm}$ for the data obtained in [43] to $2.5\,\mathrm{nm}$ for Pt on top of the LPE-YIG films discussed in [46], while the analysis of our data suggests $\lambda = 1.5\,\mathrm{nm}$. These values are comparable to earlier results [130]. However, since the spin diffusion strongly depends on the density and type

YIG	Pt	λ(nm)	θ_{SH}	$G_r(\Omega^{-1}\mathrm{m}^{-2})$	reference
PLD	evap.	(1.5 ± 0.2)	(0.11 ± 0.01)	4.0×10^{14}	present work and [46]
LPE	sputt.	2.5	0.03	4.0×10^{14}	Althammer *et al.* [46]
LPE	sputt.	0.8	0.11	4.0×10^{14}	Huang *et al.* [43], in [46]
LPE	sputt.	n.a.	0.03	6.4×10^{13}	Hahn *et al.* [96]
LPE	evap.	1.5	0.08	1.2×10^{14}	Vlietstra *et al.* [45]
RF-sputt.	sputt.	0.5	0.044	7.57×10^{14}	Marmion *et al.* [128]
LPE	sputt.	1.5	0.10	1.1×10^{14}	Uchida *et al.* [129]
LPE	sputt.	(1.0 ± 0.2)	(0.12 ± 0.01)	4.0×10^{14}	data from Lu *et al.* [47]

Table 2.1: Spin diffusion length λ, spin Hall angle θ_{SH} and real part of the spin mixing interface conductance G_r obtained from YIG/Pt hybrids grown under different conditions. All data was taken at $300\,\mathrm{K}$.

of impurities in the N, a significant difference of values for λ spreading from $1.25\,\mathrm{nm}$ [130] to $10\,\mathrm{nm}$ [131] and $(14 \pm 6)\,\mathrm{nm}$ [132] have been reported to the literature in the past.

A similar variance can be obtained for the values for the spin Hall angle θ_{SH} of platinum. θ_{SH} was found to be in the range from 0.03 to 0.12 obtained from SMR fits. The values for θ_{SH} in Pt reported from spin pumping experiments spread from 0.0037 [133] up to 0.08 [134] and 0.113 [135]. We attribute these large differences in λ and θ_{SH} to the different deposition techniques for the Pt layer. Additionally, *ab initio* calculations by Gradhand *et al.* [136] suggest that the presence of impurities substantially changes the magnitude of θ_{SH}, while they only slightly alter the spin diffusion length in Pt.

The values obtained for the real part of the spin mixing conductance also show a spread of one order of magnitude from $6.4 \times 10^{13}\,\Omega^{-1}\mathrm{m}^{-2}$ in Ref. [96] to $7.57 \times 10^{14}\,\Omega^{-1}\mathrm{m}^{-2}$ in Ref. [128]. However, the values obtained for G_r from the SMR measurements listed in Tab. 2.1 are in good agreement with the theoretically calculated order of magnitude of $10^{14}\,\Omega^{-1}\mathrm{m}^{-2}$ [126]. The spread in G_r, which is related to the number of spin transport channels per unit area, might origin from both, the various deposition techniques for the YIG film and the fact that the Pt top layer was deposited either *in situ* (i.e. without breaking the vacuum between the deposition processes for YIG and Pt) or *ex situ*.

In summary, the discussion of the thickness dependence of the SMR in FMI/N material systems enables a detailed characterization of the spin transport parameters in N as well as the interface between the FMI and N. In the next section, this powerful tool will be used to acquire further insight to the spin transport as a function of temperature.

2.4 Temperature dependence of the SMR in YIG/Pt

As already shown in the previous section, the spin Hall magnetoresistance enables the determination of spin transport properties of normal metals from electrical measurements. A detailed knowledge of these material parameters is of key importance in spintronics. Up to now, this work discussed the SMR at room temperature. However, since spin transport in a normal metal is not linked to a certain temperature, the SMR concept should also work at changed environmental conditions[12].

This section deals with the temperature dependence of the SMR effect in YIG/Pt bilayers. In a first step, we discuss the temperature evolution of the spin transport material characteristics of this material combination. The main results of this chapter have already been published in Ref. [50]. Within this context, we additionally discuss the magnetic field dependence of the SMR signal at low temperatures in Sec. 2.4.2. We will close this chapter with the study of an additional, magnetoresistive signal occurring in oopt

---

[12]On the other hand, the SMR of course should be strongly linked to the ferromagnetism of the FMI
    layer and therefore, an upper limit in temperature is given by the Curie temperature T_{c}.

configuration at low temperatures in Sec. 2.4.3.

2.4.1 Temperature dependent spin transport properties of Pt inferred from spin Hall magnetoresistance

In this section, we take advantage of the SMR framework to access the spin transport parameters θ_{SH}, λ and G_r for a wide temperature range between 10 K and room temperature. Before we start the discussion of the temperature dependent spin transport in platinum, we begin with a general investigation of the magnetoresistance in YIG/Pt at lower temperatures. Therefore, we look at the magnetoresistance data taken for the YIG $(t_{\mathrm{F}} = 53\,\mathrm{nm})/\mathrm{Pt}(t_{\mathrm{N}} = 8.5\,\mathrm{nm})$ sample, the very same sample we used for the experimental discussion of the SMR concept, at $T = 100\,\mathrm{K}$ and $T = 10\,\mathrm{K}$.

In Fig. 2.17, ADMR data taken at $\mu_0 H = 1\mathrm{T}$ is depicted for all three rotation planes at $T = 300\,\mathrm{K}$, $100\,\mathrm{K}$ and $10\,\mathrm{K}$, where the $T = 300\,\mathrm{K}$ data is identical with the one shown in Fig. 2.9. To allow for a simple comparison of the $-\Delta\rho_1/\rho_0$ ratios, we again normalize the longitudinal resistivity to the minimum value [cf. Eq. 2.38]. This enables a direct reading of $-\Delta\rho_1/\rho_0$ from the y-axes in Fig. 2.17. Obviously, the $\cos^2(\alpha)$ like behavior of the longitudinal resistivity in in-plane rotations [panel (a), (d), (g)] does not change qualitatively with decreasing temperature, while its absolute value of $-\Delta\rho_1/\rho_0$ for this particular sample drops from 6.5×10^{-4} at room temperature to 2.5×10^{-4} at 10 K. These amplitudes are in agreement with the $-\Delta\rho_1/\rho_0$ modulation extracted from oopj rotations [panel (b), (e), (h)]. Again, the qualitative shape of the curve in oopj configuration does not change with decreasing temperature. However, we find a more and more pronounced deviation from the $\sin^2(\beta)$ dependence with decreasing temperature: at $\beta = 90°$ and $\beta = 270°$ the curve gets narrower, while at $\beta = 0°$ and $\beta = 180°$ the curve gets broader. We attribute this to an increase of the saturation magnetization and therefore to an increase of the shape anisotropy at low T. The temperature dependence of the anisotropy values extracted from our simulation for this data set (cf. Tab. 6.1) confirms this assumption.

For the oopt configuration [panel (c), (f), (i)], where no resistance modulation is visible at $300\,\mathrm{K}$[13], we also find no angular dependence at 100 K. However, for the 10 K data set, a small $\cos^2(\gamma)$ dependence with maxima at $\gamma = 90°$ ($\mathbf{H} \parallel \mathbf{n}$) and $270°$ ($\mathbf{H} \parallel -\mathbf{n}$) becomes visible [cf. Fig. 2.17 (i)] and we extract a modulation amplitude of 2.4×10^{-5} for this oopt data set. At first sight, this observation of a magnetoresistance in oopt configuration is at odds with the SMR theory (cf. Sec. 2.1.5) and needs to be investigated in more detail. This discussion will take place in Sec. 2.4.3.

---

[13]Please note that the wiggles in the 300 K oopt data are attributed to thermal instabilities, cf. Sec. 2.3.

We choose the oopj rotation geometry for the following discussion of the temperature dependence of the longitudinal SMR in YIG/Pt. In this configuration, the SMR signal can be directly separated from an anisotropic magnetoresistance[14]. In particular, one would not expect a magnetization orientation dependence of the resistivity in this configuration stemming from an AMR-like contribution as discussed in Sec. 2.3, as well as in Ref. [46]. We observe an increase of ρ_0 with decreasing N thickness t_N, which we attribute to the finite roughness of the YIG/Pt interface as already discussed in Sec. 2.2.3. In order to take the film thickness and temperature dependence of ρ_0 into account, we use the thickness dependent resistivity from Eq. (2.33).   As evident from Fig. 2.17, the magnitude

---

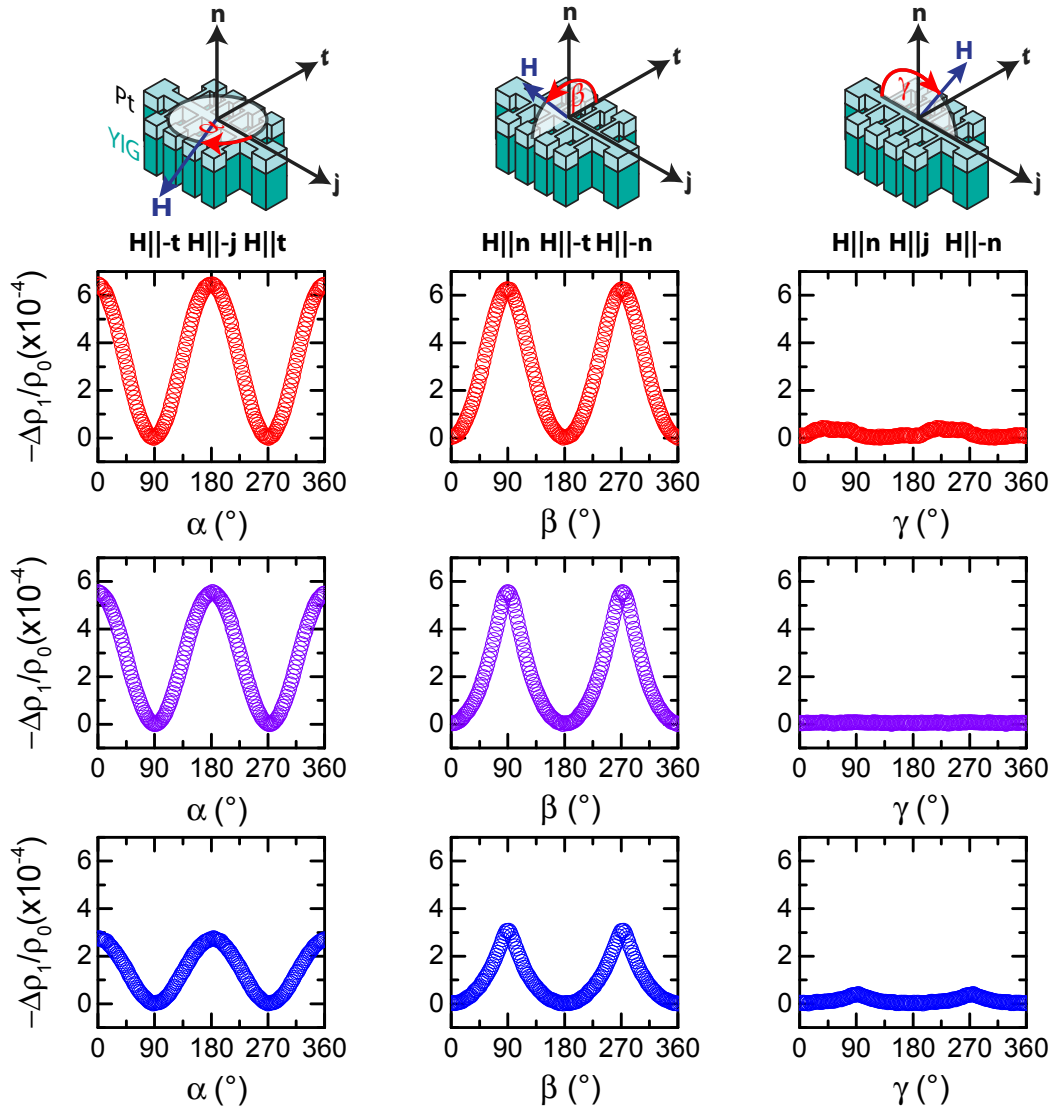[14]All data presented in this section is taken at $\mu_0\mathbf{H} = 1\,\text{T}$.

Figure 2.17: Temperature dependence of the longitudinal ADMR signal in ip, oopj and oopt configuration for a YIG/Pt (8.5 nm) sample taken at 300 K [red, panel **(a)**-**(c)**], 100 K [purple, panel **(d)**-**(f)**] and 10 K [blue, panel **(g)**-**(i)**], using $\mu_0 H = 1\,\text{T}$.
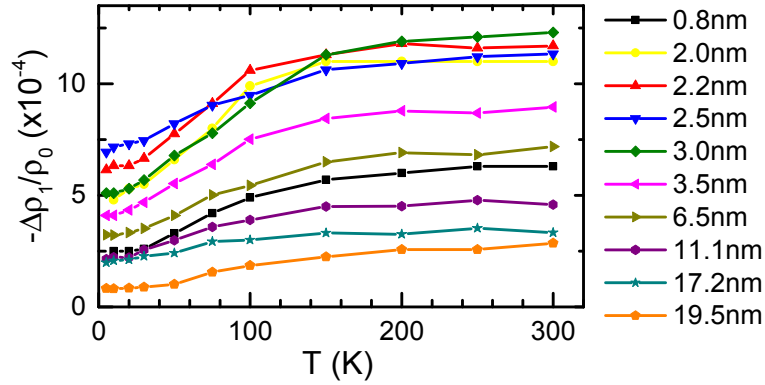
Figure 2.18: Temperature dependence of the longitudinal SMR amplitude $-\Delta\rho_1/\rho_0$ in oopj configuration ($\mu_0 H = 1\,\text{T}$) for a set of YIG/Pt samples with variable Pt thickness t_N (see legend).

of the SMR signal $-\Delta\rho_1/\rho_0$ decreases with decreasing temperature. This behavior was found in all YIG/Pt bilayers investigated. The temperature dependence of the extracted $-\Delta\rho_1/\rho_0$ values is compiled in Fig. 2.18. Upon plotting $-\Delta\rho_1/\rho_0$ as a function of t_N for different, constant temperatures T as shown in Fig. 2.19(a)-(c), a clear maximum in the SMR signal magnitude at around $t_N \approx 3\,\text{nm}$ becomes evident. Note that according to
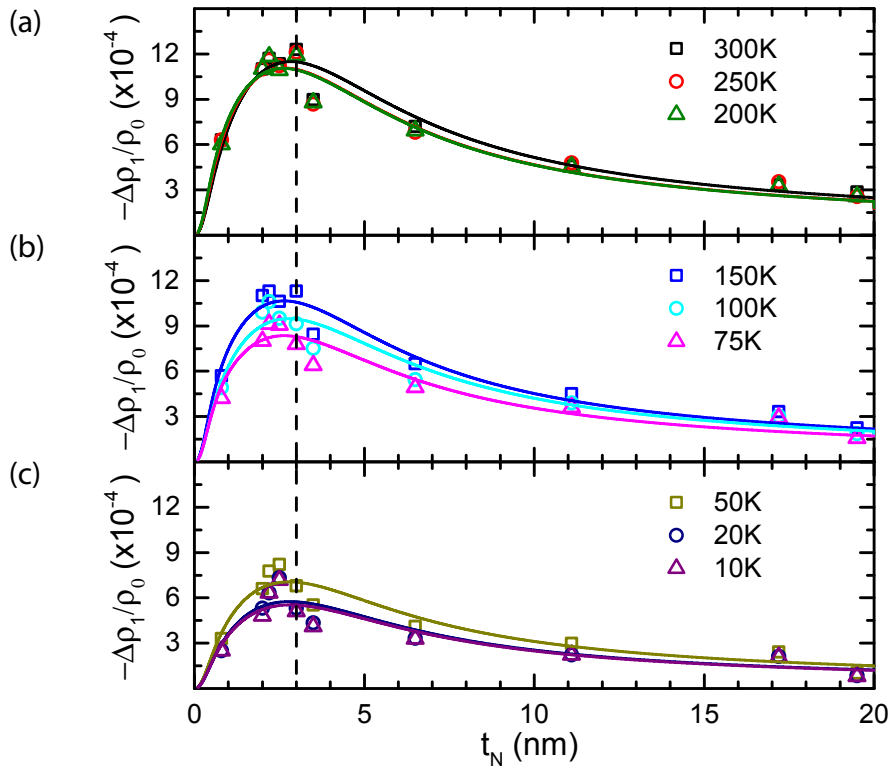

Figure 2.19: Thickness dependence of the longitudinal SMR amplitude $-\Delta\rho_1/\rho_0$ for a set of YIG/Pt samples taken at various temperatures in oopj configuration using $\mu_0 H = 1\,\text{T}$. Symbols represent data, lines fits to the data using Eq. (2.39).

Eq. (2.23) the SMR should show a maximum at $t_N \approx 2\lambda$. Fig. 2.19 reveals that this maximum appears at the same t_N value of about $3\,\text{nm}$ for all temperatures within the accuracy of our measurements, suggesting that the spin diffusion length λ is only weakly temperature dependent.

Finally, we use Eq. (2.23) to extract the Pt spin transport parameters from our set of experimental data. As discussed above, Eq. (2.23) depends on four parameters: $\theta_{\text{SH}}(T)$, $\lambda(T)$, $\rho(t_N, T)$ and $G_r(T)$. Since we use $\rho_0(t_N, T)$ calculated from Eq. (2.33), this leaves $\theta_{\text{SH}}(T)$, $\lambda(T)$, and $G_r(T)$ as free parameters. Fitting the data yields $\theta_{\text{SH}}(T)$, $\lambda(T)$ and $G_r(T)$, shown as full symbols in Fig. 2.20(a-c). These parameters consistently describe our entire set of experimental data, as depicted by the solid lines in Fig. 2.19.
As the temperature dependence of G_r and λ is rather weak and comparable to the fitting error, we perform a second analysis with temperature independent $\bar{G}_r = 4.0 \times 10^{14}\,\Omega^{-1}\text{m}^{-2}$ and $\bar{\lambda} = 1.5\,\text{nm}$ values (cf. Fig. 2.20). The $\theta_{\text{SH}}(T)$ values obtained from this simple analysis [cf. red open symbols in Fig. 2.20(a)] are very similar to the ones obtained from the full fit. This suggests that the real part of the spin mixing interface conductance G_r is almost independent of temperature, as one might naively expect considering that the
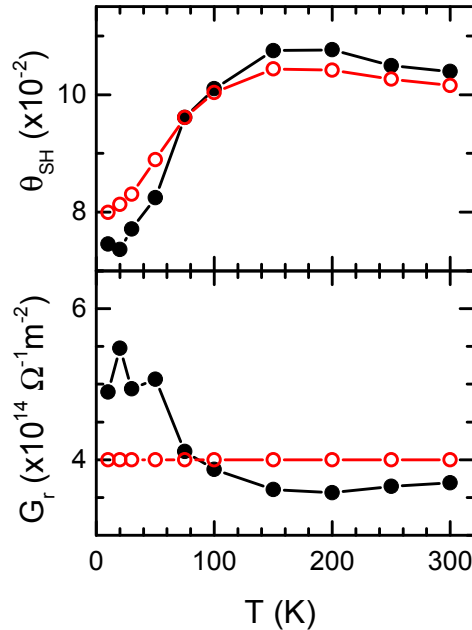
Figure 2.20: Temperature dependence of **(a)** the spin Hall angle θ_{SH}, **(b)** the spin diffusion length λ and **(c)** the real part of the spin mixing conductance G_r for Pt extracted from a fit to our SMR data. Full black symbols represent the values obtained using three free parameters $\theta_{\text{SH}}(T)$, $G_r(T)$ and $\lambda(T)$, red open symbols indicate simulations with constant $\bar{G}_r = 4 \times 10^{14}\,\Omega^{-1}\text{m}^{-2}$ and $\bar{\lambda} = 1.5\,\text{nm}$. Panel **(d)** shows σ_{spin} calculated using the temperature dependent resistivity $\rho_0(T)$ from our experimental data for a sample with $t_N = 3\,\text{nm}$.

density of states in Pt does not significantly change with T. The spin diffusion length $\bar{\lambda}$ obtained from our fit is comparable to earlier results [130]. However, since the spin diffusion strongly depends on the density and type of impurities in the N, a significant difference of the values for λ spreading from $1.25\,\mathrm{nm}$ [130] to $(14\pm6)\,\mathrm{nm}$ [132] is reported in the literature.

From the relation $\theta_{\mathrm{SH}} = \sigma_{\mathrm{spin}}/\sigma_{\mathrm{N}}$, we can calculate the temperature dependent spin Hall conductivity $\sigma_{\mathrm{spin}}(T)$ using the temperature dependent $\theta_{\mathrm{SH}}(T)$ from the simulation and the measured electrical conductivity $\sigma(t_{\mathrm{N}}, T) = \rho_0^{-1}(t_{\mathrm{N}}, T)$. Figure 2.20(d) shows $\sigma_{\mathrm{spin}}(T)$ for the $t_{\mathrm{N}} = 3\,\mathrm{nm}$ sample [the $\rho_0(T)$-evolution is very similar in all samples studied, see Fig. 2.8(a)]. From both simulation approaches, we obtain a $\sigma_{\mathrm{spin}}(T)$ dependence that does not substantially change within the temperature range investigated, with a magnitude $\sigma_{\mathrm{spin}} = (3.6\pm0.3)\times10^5\,\Omega^{-1}\mathrm{m}^{-1}$ quantitatively consistent with other measurements [133].

2.4.2 Magnetic field dependence at low temperatures

The magnetic field dependence of the SMR at $T = 10\,\mathrm{K}$ is investigated in Fig. 2.21. In the same fashion as used for the discussion of the magnetic field dependence at $300\,\mathrm{K}$ shown in Fig 2.14, we extract the relative modulation amplitude $-\Delta\rho_1/\rho_0$ from ADMR measurements in ip geometry taken at various fields $1\,\mathrm{T} \leq \mu_0 H \leq 7\,\mathrm{T}$ [panel (a)]. The results are compiled in Fig. 2.21 (b). Again, we find an increase of about 13% by increasing the external magnetic field from $1\,\mathrm{T}$ to $7\,\mathrm{T}$, almost comparable to the field dependence obtained at room temperature for the same sample (cf. Sec. 2.3.5). We again attribute this field dependence to the pinning effect discussed in Sec. 2.3.5. This interpretation combined with our experimental results at $10\,\mathrm{K}$ and $300\,\mathrm{K}$ implies that the pinning of magnetic moments is independent of temperature in good approximation.
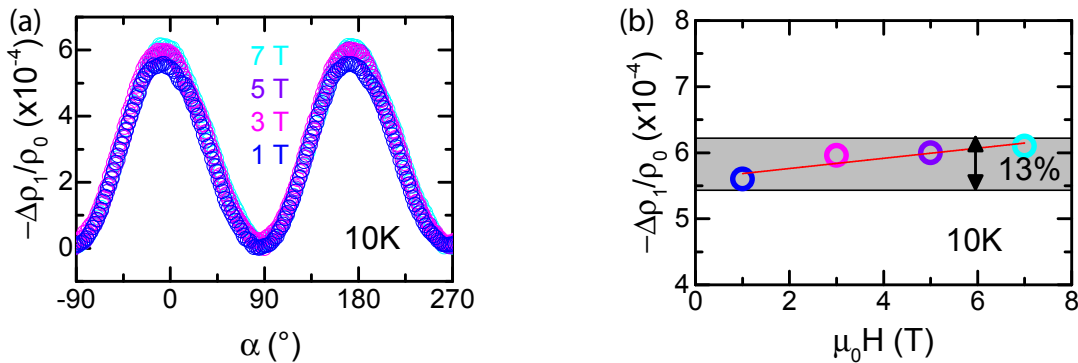
Figure 2.21: **(a)** Longitudinal SMR signal $-\Delta\rho_1/\rho_0$ in ip configuration for a YIG/Pt $(3.1\,\mathrm{nm})$ sample taken at $10\,\mathrm{K}$ for various magnetic fields (see legend). **(b)** Magnetic field dependence of the longitudinal SMR signal shown in panel **(a)**.

2.4.3 Oopt signal at low temperatures

In the previous section, we found a finite magnetoresistive behavior in oopt configuration for a YIG/Pt (8.5 nm) film at 10 K. At first sight, this result contradicts the SMR interpretation of the magnetotransport data at low temperatures. To investigate the origin of this feature in more detail, we took oopt rotations of this particular sample for temperatures below 100 K, with an external magnetic field of 1 T applied. The results of this temperature dependent study are depicted in Fig. 2.22. For a simple extraction of the resistivity modulation $\Delta\rho/\rho_0$ from Fig. 2.22, we again normalized the data sets to the respective minimum of ρ_{long}. Obviously, a $\sin^2(\gamma)$ shaped behavior is visible for $T < 100$ K with a strong temperature dependence of $\Delta\rho/\rho_0$. We observe a maximum signal at $\gamma = 90°$, where the external magnetic field is aligned perpendicular to the film plane. At all temperatures, the maxima exhibit sharp spikes, indicating a strong influence of the shape anisotropy. At some temperatures ($T = 15$ K and $T = 25$ K), the resistive signal drops to a lower level at $\gamma = 90°$ and $\gamma = 270°$, which might be due to a spontaneous in-plane re-orientation of the magnetization at these angles.

To extract the anisotropy as a function of temperature, we took advantage of our ADMR-based simulation introduced above. From a fit to the experimental data, we found a good agreement for the shape anisotropy field used for the oopt data (AMR-like) and the corresponding oopj data set [see Fig. 2.17(h)] taken at 10 K, $B_{\mathrm{n}} = 400$ mT. Furthermore, our data suggests a decrease of B_{n} with increasing temperature (cf. Tab. 6.1), which coincides with the decrease of the saturation magnetization in YIG as a function of temperature.

In Fig. 2.23(a), we compiled the $\Delta\rho/\rho_0$ modulation amplitudes of the oopt signals as a function of temperature. For temperatures lower than 30 K, we find an almost constant MR amplitude, $\Delta\rho/\rho_0 \approx 4 \times 10^{-5}$ with a slight decrease for decreasing T. For $T > 30$ K, the signal amplitude decreases and vanishes at $T = 100$ K. An exponential fit of the form

$$\Delta\rho/\rho_0 = A + B\exp\left(-T/T_0\right) \tag{2.40}$$

can describe this part of the data with $T_0 = 22.41$ K, $A = 6.9 \times 10^{-6}$ and $B = 1.5 \times 10^{-4}$. We can exclude a "direct" AMR stemming from a conductive YIG thin film, since the sheet resistivity of YIG was determined to be higher than 1×10^7 Ωm [137], which is about four orders of magnitude lower than the literature value for bulk YIG [138], but still about 14 orders of magnitude higher than the Pt sheet resistivity. These values were determined at room temperature, it can be assumed that the insulating properties of YIG increase with decreasing temperature.

Additionally, we checked the magnetic field dependence of the MR signal in oopt. By

Figure 2.22: Temperature dependence of the longitudinal ADMR signal in oopt configuration for a YIG/Pt (8.5 nm) sample taken at temperatures between 5 K and 100 K (see legend) using $\mu_0 H = 1$ T.

Figure 2.23: (**a**) Temperature dependence of the longitudinal ADMR signal in oopt configuration for the YIG/Pt (8.5 nm) sample using $\mu_0 H = 1$ T. The gray line represents an exponential fit to the temperature regime above 25 K. (**b**) Field dependence of the longitudinal ADMR signal in oopt configuration for the YIG/Pt (8.5 nm) sample taken at 15 K, using $\mu_0 H = 0.5$ T, 1 T and 2 T (see legend).
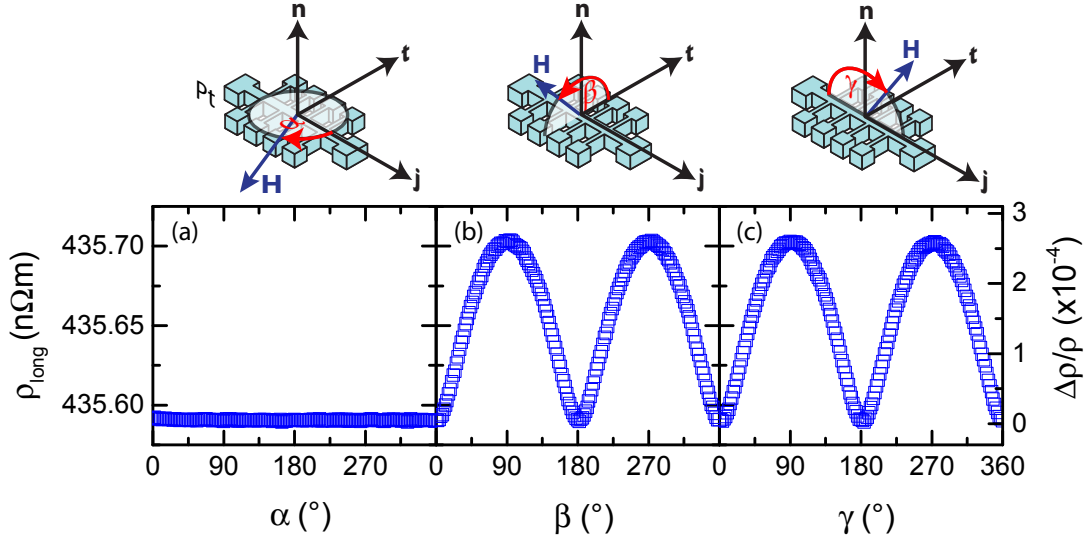
Figure 2.24: Longitudinal ADMR results for a Pt ($t_N = 3.5\,\text{nm}$) sample on YAG substrate taken at $T = 10\,\text{K}$ using $\mu_0 H = 1\,\text{T}$ in **(a)** ip, **(b)** oopj and **(c)** oopt configuration.

reducing the external magnetic field to $500\,\text{mT}$, the MR amplitude decreases by a factor of two to 2×10^{-5}. On the other hand, the signal amplitude for a rotation taken at $\mu_0 H = 2\,\text{T}$ almost showed the same $\Delta\rho/\rho_0$ ratio as the data taken at $1\,\text{T}$ [see Fig. 2.23(b)]. We thus conclude that the MR found in oopt configuration at low temperatures does not stem from a reorientation of the magnetization to an in-plane axis, as found above for $300\,\text{K}$ rotations with small external fields, even though the saturation magnetization amplitude of YIG and the in-plane anisotropy increase with decreasing temperature.

In a second step of our analysis, we investigate a thin Pt film ($t_N = 3.5\,\text{nm}$) directly deposited onto a YAG substrate for reference. At low temperatures (here: $10\,\text{K}$), we find a magnetoresistive behavior in this sample as well, see Fig. 2.24. Interestingly, the $\sin^2(\delta)$ shaped MR is only visible in out of plane rotations, while the signal shows no modulation if the external magnetic field $\mu_0 H = 1\,\text{T}$ is rotated in the sample plane. For oopj and oopt rotations, the modulation is of comparable amplitude and we extract $\Delta\rho/\rho_0 \approx 2.6 \times 10^{-4}$. The absence of a magnetoresistive signal modulation in in-plane rotations suggests that this MR can neither be attributed to a conventional anisotropic magnetoresistance in a ferromagnetic metal, nor to a positive magnetoresistance in a non-ferromagnetic metal [99].

For the following discussion, we focus on the oopt data taken at the YAG/Pt reference sample. Again, the MR signal taken in oopt at $\mu_0 H = 1\,\text{T}$ decreases with decreasing temperature [cf. Fig. 2.25(a) and (b)] and vanishes at $T \approx 30\,\text{K}$. In this sample, we find a strong magnetic field dependence of the oopt signal, which is depicted in Fig. 2.25(c). The $\Delta\rho/\rho_0$ ratio increases by a factor of two by increasing the external magnetic field

Figure 2.25: Magnetotransport at low temperatures for the YAG/Pt(3.5 nm) reference sample.
(a) Temperature dependence of the longitudinal ADMR signal in oopt configuration taken at temperatures between 10 K and 30 K (see legend) using $\mu_0 H = 1$ T.
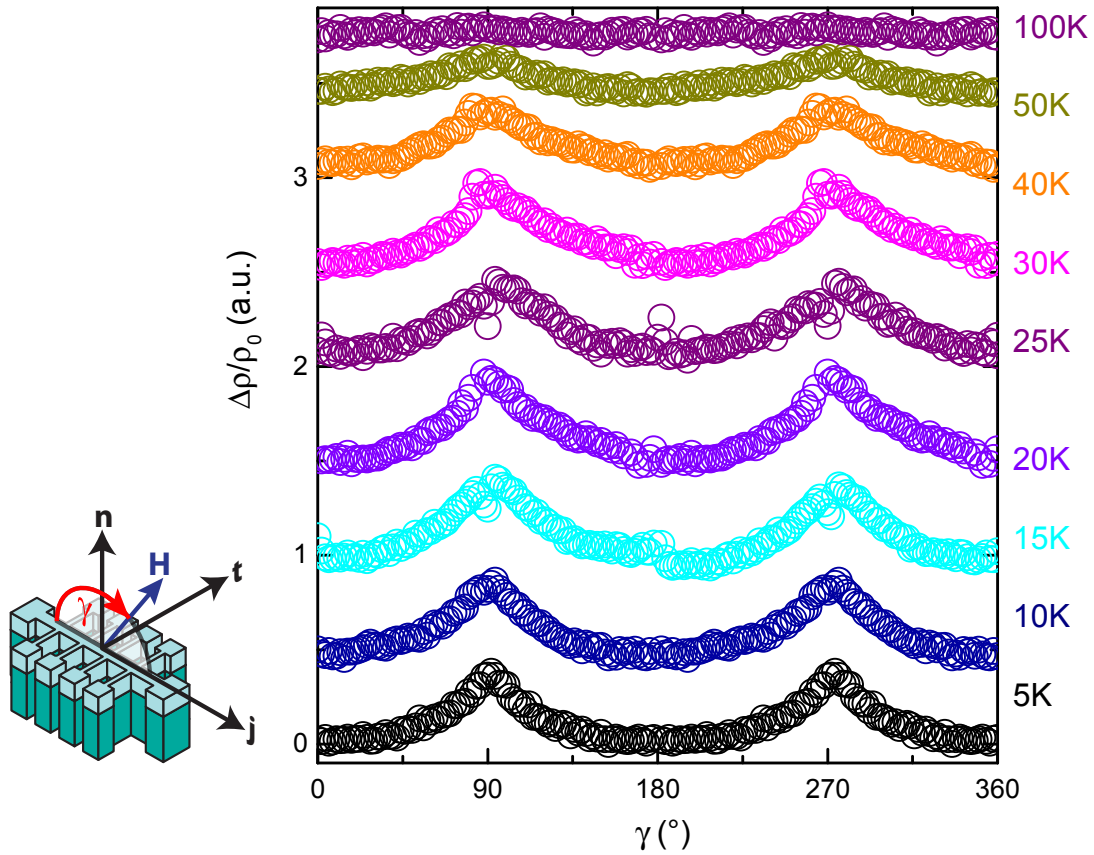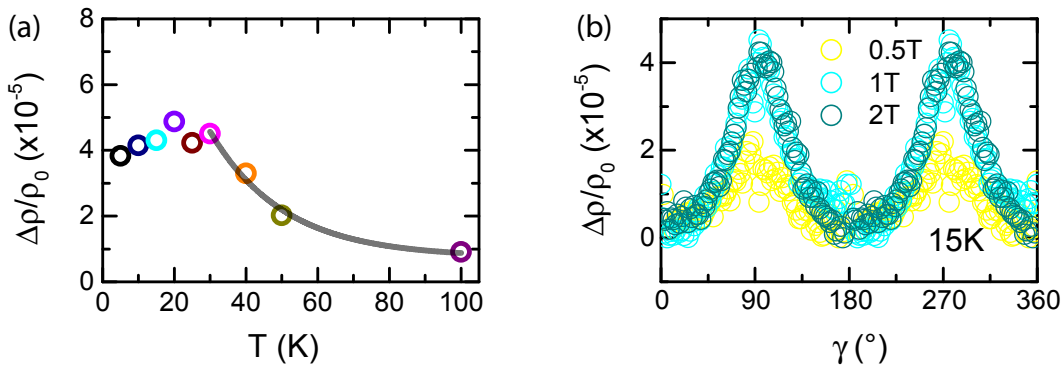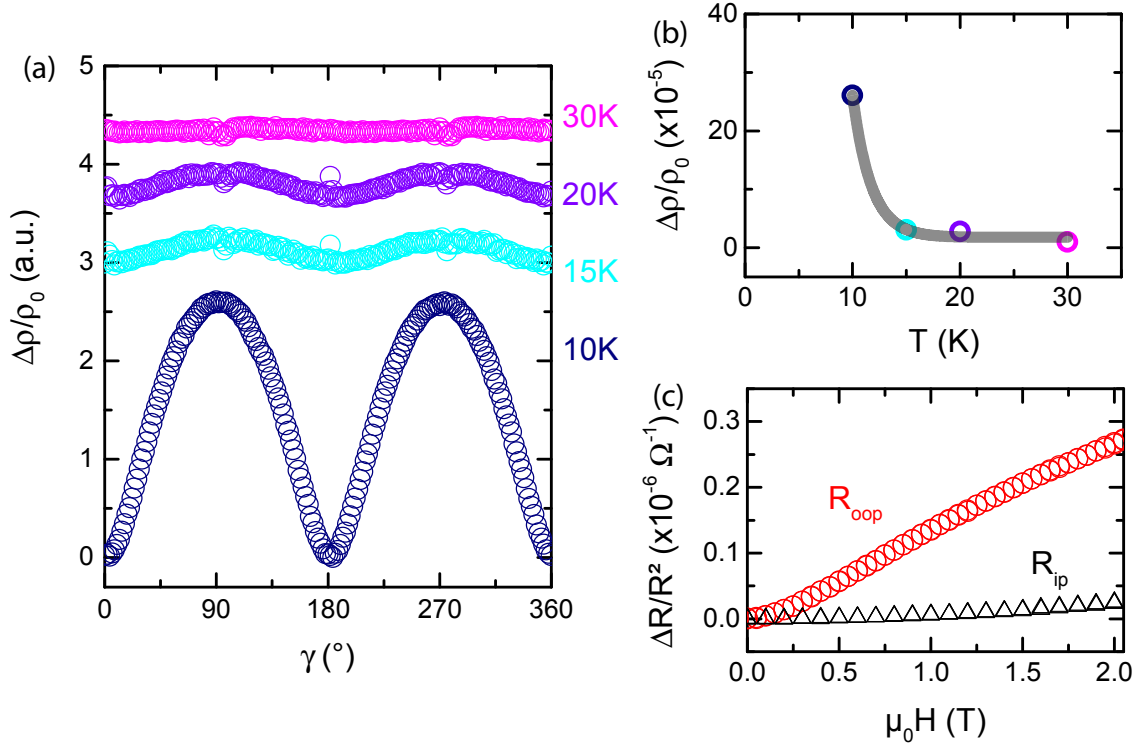**(b)** Temperature dependence of the longitudinal ADMR signal in oopt configuration for the YAG/Pt (3.5 nm) sample taken at various temperatures using $\mu_0 H = 1$ T. The gray line represents an exponential fit to the data. **(c)** Field dependence of the longitudinal ADMR signal taken at 15 K for $\mathbf{H} \parallel \mathbf{n}$ (red) and $\mathbf{H} \perp \mathbf{n}$ (black).

from 1 to 2 T, indicating a linear connection between $\Delta\rho/\rho_0$ and the external field. In contrast to the oopt data taken in YIG/Pt, we find no temperature regime with almost constant MR ratio at low temperatures. However, an exponential decay fit according to Eq. (2.40) enables a good agreement with the experimental data using $T_0 = 1.73$ K, $A = 1.78 \times 10^{-4}$ and $B = 0.078$ [see Fig. 2.25(b)].

We also find a comparable MR signal in out of plane rotations in a second reference sample consisting of 15.6 nm Pt on a YAG substrate (cf. Fig. 2.26). However, the $\Delta\rho/\rho_0$ ratio at 10 K is about one order of magnitude smaller than the one obtained for YAG/Pt (3.5nm), but still comparable to the MR in oopt configuration found in YIG/Pt. A similar positive magnetoresistance in Pt thin films was also reported by Hoffmann, Hofmann and Schoepe [139]. These authors compared their magnetic field dependent resistivity in Pt to the weak localization theory [140] as well as to a different model based on electron-electron interactions [141], but found no indication to ascribe the magnetoresistance in Pt to neither weak localization, nor electron interactions.
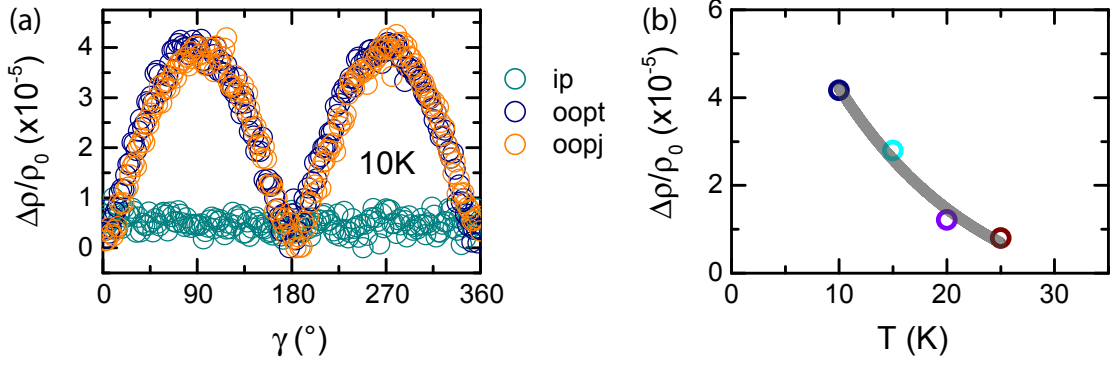
Figure 2.26: Magnetotransport at low temperatures for YAG/Pt(15.6 nm). **(a)** Longitudinal ADMR signal in ip, oopj and oopt configuration taken at 10 K, using $\mu_0 H = 1\,\mathrm{T}$ (see legend). **(b)** Temperature dependence of the longitudinal ADMR signal in oopt configuration for the YAG/Pt(15.6 nm) sample taken at various temperatures using $\mu_0 H = 1\,\mathrm{T}$. The gray line represents an exponential fit to the data.

We conclude, that this magnetoresistive behavior is a general phenomenon in our Pt thin films. Thus, we attribute the occurrence of a MR signal in oopt in our YIG/Pt to this Pt-MR instead of a magnetic proximity effect. The mechanism behind this low-temperature MR in Pt thin films is still unknown. As it vanishes for increasing temperature, we exclude ferromagnetic impurities in the Pt film[15] to be the origin of this phenomenon. However, we would neither expect an out of plane easy axis for a contamination with e.g. nickel or iron.

2.5 SMR dependence on t_{F}

Up to now, the SMR in YIG/Pt was discussed utilizing bilayers consisting of almost the same thickness $t_{\mathrm{F}} \approx 60\,\mathrm{nm}$ of the ferrimagnetic insulator YIG with different thicknesses t_{N} of the platinum layer deposited on top. At this point, we investigate the influence of t_{F} on the SMR amplitude. To enable a good comparability of the data achieved from different samples, we fabricate YIG films with various thickness t_{F} on top of (111)-oriented GGG substrates as described in Sec. 2.2.1. As the lattice mismatch between GGG and YIG is two orders of magnitude smaller than the one between YAG and YIG, we intentionally choose the paramagnetic substrate GGG for this part of the analysis. After PLD growth of YIG, we *in situ* deposit Pt thin films with comparable thickness $t_{\mathrm{N}} \approx 3\,\mathrm{nm}$ to rule out the influence of the Pt thickness discussed above. For reference, we directly deposit $t_{\mathrm{N}} = 3.5\,\mathrm{nm}$ of platinum on top of a YAG substrate[16]. All samples of this series

---

[15]As the electron beam evaporation chamber used for the Pt deposition is also used for ferromagnetic metals like iron, nickel and cobalt, we can not exclude a finite contamination of the Pt thin film with these materials, even though we found no hint for a contamination in XRD measurements.

[16]Here, we consciously chose the YAG substrate for the Pt reference film, since atomic force microscope measurements performed by Felix Schade during his Bachelor's thesis indicated, that the GGG sub-
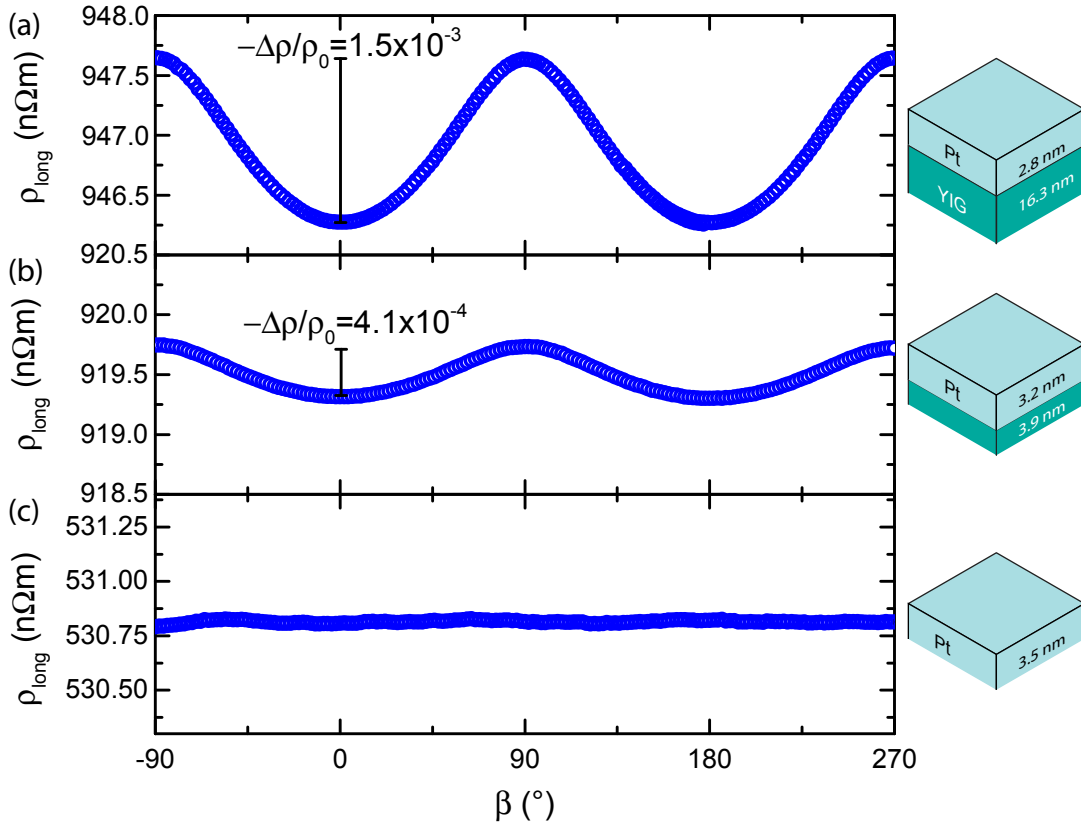
Figure 2.27: Longitudinal SMR signal for a set of YIG/Pt samples with YIG thicknesses **(a)** $t_F = 16.3$ nm, **(b)** $t_F = 3.9$ nm and **(c)** $t_F = 0$ nm. All Data taken in oopj configuration at 300 K for $\mu_0 H = 1$ T.

again are patterned into Hall bar structures and we detect the change of the longitudinal resistivity as a function of the magnetic field orientation in oopj rotations at $T = 300$ K and $\mu_0 H = 1$ T.

In Fig. 2.27, we exemplarily compile the ADMR results for two YIG/Pt bilayer samples with $t_F = 16.3$ nm, $t_F = 3.9$ nm and the reference sample ($t_F = 0$ nm). The Pt thicknesses of these samples are in the range of 2.8 nm $\leq t_N \leq 3.5$ nm and therefore are located around the thickness value for the maximum SMR signal, $t_N^{max} \approx 2\lambda \approx 3$ nm. The relative amplitude $-\Delta\rho_1/\rho_0 = 1.5 \times 10^{-3}$ for the sample with $t_F = 16.3$ nm is in good agreement with SMR experiments taken on samples with thicker ferromagnetic layers (cf. Sec. 2.3.6). However, by decreasing the thickness of F down to $t_F = 3.9$ nm [Fig. 2.27 (b)], the $-\Delta\rho_1/\rho_0$ decreases to 4.1×10^{-4} and vanishes for the reference sample without ferromagnetic layer [cf. Fig. 2.27 (c)].

For a more detailed analysis of the t_F dependence of the SMR signal, we plot the $-\Delta\rho_1/\rho_0$ values for a set of samples with 0 nm $\leq t_F \leq 200$ nm in Fig. 2.28. Again, the Pt thicknesses were determined to spread around $t_N^{max} \approx 3$ nm, with 2.8 nm $\leq t_N \leq 3.5$ nm. The relative

---

strate surfaces has a larger rms surface roughness ($h_{GGG} \geq 0.5$ nm) than YAG ($h_{YAG} \geq 0.3$ nm) [142].
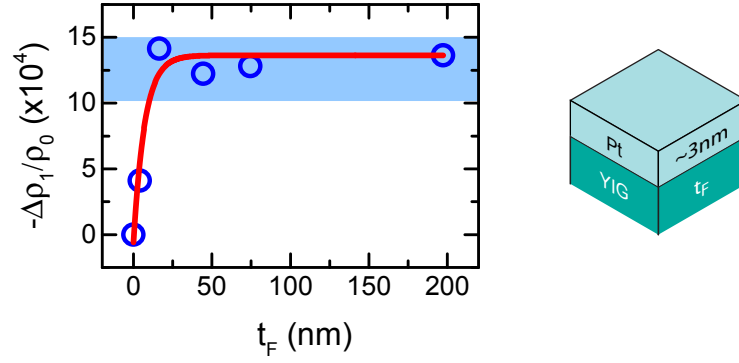
Figure 2.28: Thickness dependence of the longitudinal SMR amplitude $-\Delta\rho_1/\rho_0$ for a set of YIG/Pt samples with various YIG thicknesses t_F. Data taken in oopj configuration at 300 K for $\mu_0 H = 1$ T. The light blue area indicates the expected $-\Delta\rho_1/\rho_0$ regime from the SMR theory for Pt thicknesses 2.8 nm $\leq t_N \leq 3.5$ nm. The red line indicates an exponential decay fit of the form $y = A\exp\left(-t_F/t_1\right)$ to the data.

SMR signal expected for this range of t_N from Sec. 2.3.6 is highlighted by the colored area in Fig. 2.28. As already indicated in the discussion above, the $-\Delta\rho_1/\rho_0$ values for samples with $t_F \geq 16.3$ nm are found in the expected range $1.0 \times 10^{-3} \leq -\Delta\rho_1/\rho_0 \leq 1.5 \times 10^{-3}$ deduced from Fig. 2.16.

Within the experimental accuracy, we find no thickness dependence of the SMR in this regime, which is in good agreement with the intuitive picture of the SMR given in Sec. 2.1.5. Naively speaking, the presence of the ferromagnetic insulator merely models the boundary conditions for the spin transfer torque at the FMI/N interface. Therefore, only the direction of the FMI's magnetization **M** (controlled by the external magnetic field **H**), but not its amplitude M is relevant for the SMR effect.

This picture changes for very thin t_F values, where we find a signal drop down to 4.1×10^{-4} for $t_F = 3.9$ nm as already indicated in Fig. 2.28(b). For this particular sample, the thickness of the FMI layer is reduced to less than 2 monolayers, taking into account the monolayer thickness d_{111} calculated from the YIG lattice constant a, $d_{111} = \sqrt{3}a = 2.1436$ nm for (111) oriented YIG films.

We model the experimental data with an exponential decay fit of the form $-\Delta\rho_1/\rho_0 = A\exp\left(-t_F/t_0\right)$. Using $A = -1.42 \times 10^{-3}$ and $t_0 = 7.1$ nm, we are able to reproduce the thickness dependence of $-\Delta\rho_1/\rho_0$. From this, we conclude that an influence of the thickness of the FMI (in the case of YIG) is only present for ultra-thin films.

Unfortunately, the paramagnetic background of GGG hampers the examination of the influence of the saturation magnetization of the YIG in the monolayer thin sample via SQUID magnetometry, such that no analysis on M is possible. In literature, d'Allivy Kelly *et al.* estimated a decrease of the saturation magnetization M_{sat} of about 20% for a decreasing YIG film thickness from 7 nm to 4 nm [143]. An other approach to study the magnetization of a FMI would be (broadband) ferromagnetic resonance (FMR). How-

ever, in this particular film we found no YIG specific FMR line at various frequencies in a range from 20 to 40 GHz [144], indicating that the magnetization M might indeed be reduced dramatically in this ultra thin FMI film. In contrast to the findings on (111) oriented YIG presented above, we admit that for bilayers consisting of ultra-thin YIG films ($1 \leq t_F \leq 5$ unit cells) and approximately 5 nm Pt grown on (100) and (110) oriented GGG substrates, we neither find a t_F dependence of $-\Delta\rho_1/\rho_0$ within the experimental error, nor a strong influence of the YIG film termination on the SMR signal [145, 146]. Therefore, the estimation deduced above also serves as an upper limit to the t_F dependence of the spin Hall magnetoresistance and the applicability of the theory presented in Sec. 2.1.6.

2.6 Spin Hall magnetoresistance: A summary

In this chapter, we have quantitatively investigated a novel magnetoresistive effect in YIG/Pt bilayers. In literature, two contrary interpretations of this MR have been reported during the past years. In our work we showed that the concept of the spin Hall magnetoresistance effect (SMR) [15, 44–46, 48] based on the interconversion of a charge current to a spin current (cf. Sec. 2.1.5 and Sec. 2.1.6) and vice versa is in excellent agreement with our experimental data, whereas the framework of a magnetic proximity magnetoresistance (cf. Sec. 2.1.7 and Ref. [43, 47, 49]) does not coincide with our findings. The SMR effect characteristically depends on the absorption of a spin current at the FMI/N interface, which can be modulated via the orientation of the magnetization of the FMI with respect to the spin polarization of the spin current in N. The SMR effect thus enables a remote sensing of the magnetization direction in the FMI by simply measuring the resistance of the adjacent N layer. In Sec. 2.3.1 we showed that the signature of the SMR qualitatively differs from the magnetic proximity magnetoresistance, in particular when the magnetization of the YIG layer has a component perpendicular to the Pt film plane. Thus, we took advantage of magnetotransport measurements as a function of the magnetization orientation to disentangle AMR and SMR. Moreover, the excellent quantitative agreement between the SMR theory and our experimental data for more than 20 YIG/Pt bilayer samples, as exemplarily discussed in Sec. 2.3.2, clearly shows that a static magnetic proximity effect is not the origin of the observed MR in FMI/N hybrids. Besides, this conclusion is supported by the absence of indications for induced magnetic moments in the Pt layer inferred from X-ray magnetic circular dichroism experiments reported in Sec. 2.3.3. This led us to a variety of applications for the SMR, enabling us e.g. to study the anisotropy of a ferromagnetic insulator from electric transport measurements on YIG/Pt bilayers discussed in Sec. 2.3.4. We found that the SMR reflects the magnetic landscape of the YIG if one reduces the external magnetic field strength

applied in magnetotransport measurements. Thus, from a simulation based on both the SMR theory and a minimization of the free enthalpy of the magnetic system, we were able to extract the shape anisotropy $B_n \approx 79\,\mathrm{mT}$ for our YIG thin films.

We also studied the SMR as a function of high magnetic fields $1\,\mathrm{T} \leq \mu_0 H \leq 7\,\mathrm{T}$ in Sec. 2.3.5. While the present SMR theory is formulated in terms of an interface effect and thus only depends on the presence of a magnetization (modulated by a non-vanishing spin mixing interface conductance $G_{\uparrow\downarrow}$), we found a linear increase of about 15 % in the $-\Delta\rho_1/\rho_0$ signal from $1\,\mathrm{T}$ to $7\,\mathrm{T}$ for YIG/Pt grown on YAG (3 % lattice mismatch between YIG and the substrate), suggesting that the number of transport channels per unit area, described by $G_{\uparrow\downarrow}$, is field dependent. This behavior was also found in YIG thin films grown on GGG (0.03 % lattice mismatch), and the field dependence in the sample grown on YAG is about a factor of two higher than the one on GGG. We interpreted this external magnetic field dependence of the longitudinal SMR with a formation of pinned magnetic moments in the YIG layer close to the interface, stemming from an unavoidable lattice mismatch in the YIG thin ($\approx 60\,\mathrm{nm}$) film. However, to clarify this in more detail, a study of the magnetic surface of YIG thin films grown on YAG and GGG by magnetic force microscopy is recommended for the future. Additionally, the influence of the magnetization amplitude M in the FMI layer has to be included to the SMR theory. In a subsequent set of normal metal layer thickness dependent measurements, we utilized the SMR for a temperature resolved determination of the spin transport characteristics in Pt. Starting from measurements at room temperature in Sec. 2.3.6, the analysis of the thickness dependence of the resistivity modulation $-\Delta\rho_1/\rho_0$ characteristic for the SMR enabled the determination of the spin transport parameters in Pt. Our investigation led to a set of parameters for the real part of the spin mixing conductance G_r for the YIG/Pt interface, as well as the spin Hall angle θ_SH and the spin diffusion length λ in Pt. Our results are close to the values reported by other groups (cf. Tab. 2.1) obtained either from SMR experiments or spin pumping [17, 18, 22, 24]. This motivated a temperature dependent study of the SMR in YIG/Pt, presented in Sec. 2.4. We observed a decrease of the SMR at low temperatures for all samples investigated (cf. Sec. 2.4.1) and utilized the SMR theory to extract the temperature dependence of the spin transport characteristics in Pt. From the temperature-independent maximum in the thickness dependence of $-\Delta\rho_1/\rho_0$ we concluded that the spin diffusion length λ in Pt is almost temperature-independent. Additionally, from a simulation of the SMR theory to the $-\Delta\rho_1/\rho_0$ data, we found that G_r is almost T-independent, too. On the other hand, the temperature dependent decrease of the signal suggests a decrease of θ_SH from 0.11 at room temperature to 0.075 at $10\,\mathrm{K}$.

For low temperature angle dependent magnetoresistance experiments, we additionally resolved a feature that is not compatible with the SMR theory. By rotating the external

magnetic field in the plane defined by the current direction $\mathbf{j}$ and the film normal $\mathbf{n}$ (oopt), we found a non-zero magnetoresistive contribution proportional to $\cos^2(\gamma)$, although the SMR model suggests no magnetic field orientation dependence in this configuration (cf. Sec. 2.4.3). However, this signal, observable at temperatures $T \leq 50\,\mathrm{K}$ and decreasing with increasing temperature, was also found in Pt thin films directly deposited on YAG substrates. Even though we could not clarify the origin of this Pt-magnetoresistance within the present work, we attribute this effect to an intrinsic feature of Pt in the thin film regime, which should not be confused with a magnetic proximity effect (cf. Sec. 2.1.7). However, a FMI thickness dependent study of the SMR in YIG/Pt bilayers in Sec. 2.5 suggests that the SMR effect decreases for reducing t_F down to $3.9\,\mathrm{nm}$. Even though this seams feasible, since for $t_\mathrm{F} = 0\,\mathrm{nm}$ (plain Pt film, $M_\mathrm{YIG} = 0$) the SMR vanishes, the present SMR theory does not include the magnetic properties of the FMI layer with exception of the presence of a finite magnetization $\mathbf{M}$. Even here, not the magnitude M of $\mathbf{M} = M\mathbf{m}$, but merely its direction $\mathbf{m}$ enters the SMR equations (cf.Sec. 2.1.6). Taken together with the anisotropy characterization and indications for pinned magnetic moments discussed above, we showed that SMR can also be used to sense magnetic properties in ferromagnetic insulators. In this context, our results advocate for a deeper characterization of "spin-transparent" interfaces in terms of the spin mixing interface conductance $G_{\uparrow\downarrow}$ from both theoretical and experimental point of view in the future, including for example information on the magnonic system of the FMI.

In conclusion, it is not astonishing that during the past two years, the SMR became an established tool to determine a full set of spin transport parameters from magneto-transport experiments, namely the spin Hall angle, the spin diffusion length and the real part of the spin mixing interface conductance. The simple electrical detection technique led to numerous publications reporting on the temperature dependent spin transport not only in YIG/Pt bilayers [45, 50, 128, 129], but also utilizing other normal metals like tantalum [96] or palladium [147]. In addition to that, the SMR recently was reported in material combinations based on the conductive ferromagnet CoFeB [97, 98]. These authors utilized tungsten and tantalum for N. Both materials show a significantly increased spin Hall angle compared to Pt, which led to a *large* [97] resp. *giant* [98] SMR in their material combinations. Although using a conductive ferromagnet in these experiments, the anisotropic magnetoresistance from the F layer was found to be small compared to the SMR stemming from the CoFeB/N interface. Therefore, the SMR concept is not restricted to insulating ferromagnets. By utilizing the SMR as a novel characterization tool, also new F/N material combinations can be tested electrically for their suitability in spintronic applications.

3 Spin Hall anomalous Hall effect

Historically, most magnetotransport experiments were performed in a longitudinal geometry, e .g. by detecting the potential difference along an applied charge current as a function of the external magnetic field amplitude. However, additional material properties can be extracted from transverse magnetotransport experiments. In the context of magnetoresistance, we use *transverse* to describe experiments in a setup where we apply a charge current along the sample (e.g. in **j** direction) and take the transverse voltage drop perpendicular to the initial charge current (here along **t**). These type of experiments, first performed by E. Hall in 1879, provides information on the internal properties of a material like the charge carrier density [66].

As already shown from a theoretical perspective in Sec. 2.1.6, the spin Hall magnetoresistance (SMR) based on the simultaneous action of SHE and ISHE includes a contribution in transverse geometry [c.f. Eq. (2.24)]. Recently, it has been suggested [15, 44, 95] that the transverse component of the SMR, referred to as spin Hall anomalous Hall effect (SH-AHE) [15], allows for quantifying the imaginary part G_i of the spin mixing interface conductance of an FMI/N hybrid from measurements of anomalous Hall-type effects (AHE) [15]. During the past 15 years, merely the real part G_r linked to an in-plane magnetic field torque [92, 93] was accessible experimentally e.g. from spin pumping experiments [17, 24, 85, 86, 94]. On the other hand, the imaginary part G_i describing an arbitrary phase shift between the spin current in the N and the one in the FMI up to now remained a theoretical concept. For YIG/Au hybrids, e.g., it was calculated $G_i/G_r \approx 1/10$ [126], but a detailed experimental testing of this concept remained open.

In this chapter, we present an experimental study of ordinary and anomalous Hall-type signals observed in YIG/Pt bilayers. We discuss the film thickness and temperature dependence of the AHE signals in terms of the SH-AHE and extract G_i as a function of temperature. Therefore, we start with a theoretical introduction of the ordinary and anomalous Hall effect in Sec. 3.1, followed by a discussion of the theoretical predictions of the spin Hall anomalous Hall effect. The experimental setup will be introduced in Sec. 3.2. In our experiments shown in Sec. 3.3, we compare the observation of a strong thickness and temperature dependence in both the ordinary and the anomalous Hall effect in YIG/Pt with reference experiments performed on thin Pt films deposited directly onto

diamagnetic substrates. The results of this chapter have been published in Ref. [148].

3.1 Theoretical overview

While the concept of the ordinary and anomalous Hall effect is fundamental and widely used, the spin Hall anomalous Hall effect was predicted about two years ago [15] and represents a new concept in spintronics. Therefore, this chapter starts with a brief introduction to the conventional and anomalous Hall effects. In a second step, we will illuminate the phenomenology of the SH-AHE in FMI/N hybrids from a theoretical perspective to pave the way for the discussion of the experimental data in Sec. 3.3.

3.1.1 Conventional Hall effect

Charged particles moving in an external magnetic field $\mathbf{B}$ are subject to the Lorentz force $\mathbf{F}_\mathrm{L} = q(\mathbf{v} \times \mathbf{B})$. For electrons ($q = -e$), the resulting force is given by

$$\mathbf{F} = -e(\mathbf{E} + \mathbf{v} \times \mathbf{B}) \tag{3.1}$$

where $q = -e$ is the electric charge of the electron ($e = |e|$), $\mathbf{v}$ its velocity and $\mathbf{E} = E_j\mathbf{j}$ an electrical field applied along $\mathbf{j}$. In the following, the electrons of a (non-magnetic) metal are assumed to move opposite to the technical current direction along $-\mathbf{j}$ and the external magnetic field is applied perpendicular to the film surface, $\mathbf{H} \parallel \mathbf{n}$. This results in a deflection of the electrons along the $-\mathbf{t}$ direction, perpendicular to both the initial direction of motion and the magnetic field. Thus, due to this charge accumulation, a transverse electric field $\mathbf{E}_\mathrm{t}$ builds up along $-\mathbf{t}$. In steady state, $\mathbf{E}_\mathrm{t}$ is compensated by
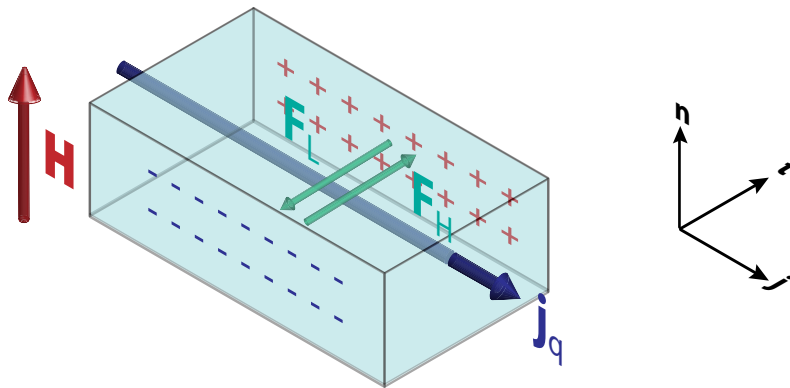
Figure 3.1: Concept of the ordinary Hall effect: electrons are assumed to move opposite to the technical current direction $\mathbf{j}_\mathrm{q}$ along $-\mathbf{j}$. The Lorentz force $\mathbf{F}_\mathrm{L}$ leads to a deflection of the electrons along $-\mathbf{t}$, resulting in an electric field $\mathbf{E}_\mathrm{t}$ along $-\mathbf{t}$. In steady state, $\mathbf{F}_\mathrm{L}$ is compensated by the Hall field $\mathbf{F}_\mathrm{H} \parallel \mathbf{t}$. Illustration in analogy to [70].

the so-called Hall field $\mathbf{E}_H = -1/e\mathbf{F}_H$. This is known as the *conventional* (ordinary) Hall effect (OHE) [66]. Here, we discuss the electric transport in the framework of Sommerfeld's theory. The transverse electric field E_t reads

$$E_t = -\frac{eB\tau}{m}E_j \tag{3.2}$$

with τ the average time between two scattering events and E_j the electrical field due to $\mathbf{j}_q$. This defines the transverse (Hall) voltage

$$V_H = \frac{\alpha_{OHE}J_q}{t} \tag{3.3}$$

along $\mathbf{t}$. Here, J_q is the electric current applied along the $\mathbf{j}$ direction, t the thickness of the sample (along $\mathbf{n}$) and $\alpha_{OHE} = \frac{B}{nq}$ the Hall resistivity, containing the charge carrier density n. Thus, a measurement of α_{OHE} yields information of the density of charge carriers in conductive materials. This feature became a standard characterization technique in solid state physics. In general, the discussion of the Hall effect has to take into account the band structure of the material. A detailed information can be found e.g. in Ref. [70]. As shown above, the conventional Hall effect depicts the influence of an external magnetic field on propagating charge carriers. Therefore, the OHE does not depend on an existing magnetization in the sample and thus is also present in non-ferromagnetic conductive materials.

3.1.2 Anomalous Hall effect

In the previous section, the conventional Hall effect in a metallic (non-magnetic) material was presented. In the description given above, the spin degree of freedom was not taken into account. This picture is valid for non-ferromagnetic materials, where $n_\uparrow = n_\downarrow$ (cf. Sec. 2.1.1). As in ferromagnetic metals the numbers of spin-up and spin-down charge carriers at the Fermi edge are different, spin-dependent contributions become visible. Historically, the discovery of this spin-dependent effect by E. Hall took place only two years after the discovery of the ordinary Hall effect [149]. Hall observed that for ferromagnetic materials, the transverse (Hall-effect) voltage shows a step around $\mu_0 H = 0$ (see e.g. Fig. 3.2(b)) and called this the *anomalous Hall effect* (AHE). However, the microscopic explanation by Karplus and Luttinger was given more than 70 years later [57]. Like the spin Hall effect introduced in Sec. 2.1.2, the anomalous Hall effect is based on the spin orbit interaction and can have both intrinsic (Berry curvature [59]) and extrinsic (skew scattering [57] and side jump effect [58]) contributions. A detailed overview can e.g. be found in [64]. As introduced earlier, the SOI in ferromagnets leads to a spin-sensitive scattering of the conduction electrons, resulting in a spin-polarized current perpendicular
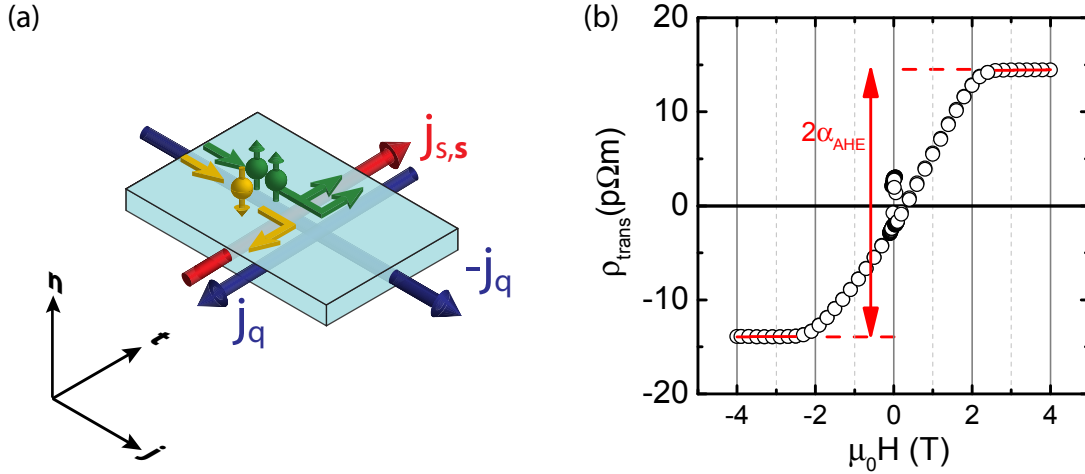
(a)

(b)

Figure 3.2: (a): Concept of the anomalous Hall effect: the spin orbit interaction in ferromagnetic metals leads to a spin polarized current perpendicular to the initial charge current. Figure in analogy to [54]. **(b)**: Transverse resistivity ρ_{trans} along **t** as a function of the external magnetic field amplitude $\mu_0 H$ at a fixed orientation of the external magnetic field, $\mathbf{H} \parallel \mathbf{n}$ for a 20 nm thick ferromagnetic film (here: Permalloy, $\text{Ni}_{0.80}\text{Fe}_{0.20}$ on MgO). The red solid lines represents a linear fit to the data in the high field limit ($\mu_0 H \geq 2.5\,\text{T}$) to extract the ordinary Hall coefficient α_{OHE} from the slope. The abscissa from a back extrapolation of the linear fit to $\mu_0 H = 0\,\text{T}$ (dashed line) defines the anomalous Hall coefficient α_{AHE}. The additional structure around $0\,\text{T}$ can be interpreted as a re-orientation of the magnetization in the sample plane in zero field and might stem from a slight misalignment of the **n** direction.

to the initial charge current [c.f. Fig. 3.2(a)]. Again, this scattering process only depends on the spin orientation (here $|\uparrow\rangle$ and $|\downarrow\rangle$ along **n**) and is not affected by an external magnetic field. Hall-type experiments on a ferromagnetic sample therefore result in two regimes as a function of the external magnetic field ([see Fig. 3.2(b)]. The ordinary Hall coefficient can be read from the slope of a linear fit to the transverse voltage in the saturation regime [cf. Eq. 3.3], while the anomalous Hall coefficient α_{AHE} corresponds to the abscissa from a back extrapolation of the linear fit to $\mu_0 H = 0\,\text{T}$ [dashed line in Fig. 3.2(b)].

3.1.3 Spin Hall anomalous Hall effect

In contrast to the ordinary and anomalous Hall effect presented above, an other "Hall-like" effect was postulated in 2013. In Sec. 2.1.6, we introduced the theory of the spin Hall anomalous Hall effect that is part of the SMR theory published by Chen *et al.* [15]. Like before, we define $\mathbf{m} = (m_j, m_t, m_n)^{\text{T}}$ as the unity magnetization vector expressed with respect to the coordinate system introduced in Fig. 2.4. Focusing on the contribution

that scales with m_n, we find from Eq. (2.24)

$$\rho_{\text{trans}} \approx \Delta\rho_2 m_n. \tag{3.4}$$

This term obviously should appear for a non-vanishing magnetization contribution pointing along the film normal. Of course, the conventional Hall effect in N has to be taken into account, too, but it will be superimposed by an anomalous Hall-like contribution, stemming from a spin current based transverse resistivity component. This is called the spin Hall anomalous Hall effect (SH-AHE).

The prefactor $\Delta\rho_2$ can be approximated using $G_r >> G_i$, leading to [15]

$$\begin{aligned}
\frac{\Delta\rho_2}{\rho} &\approx \frac{2\lambda^2\theta_{\text{SH}}^2}{t_{\text{N}}} \frac{\sigma G_i \tanh^2 \frac{t_{\text{N}}}{2\lambda}}{(\sigma + 2\lambda G_r \coth \frac{t_{\text{N}}}{\lambda})^2 + (2\lambda G_i \coth \frac{t_{\text{N}}}{\lambda})^2} \\
&\approx \frac{2\lambda^2\theta_{\text{SH}}^2}{t_{\text{N}}} \frac{\sigma G_i \tanh^2 \frac{t_{\text{N}}}{2\lambda}}{(\sigma + 2\lambda G_r \coth \frac{t_{\text{N}}}{\lambda})^2}.
\end{aligned} \tag{3.5}$$

Thus, similar to the (longitudinal) SMR, a strong t_{N} dependence is expected for the SH-AHE contribution in FMI/N hybrids. At this point, we want to emphasize that the SH-AHE, although it is named after the anomalous Hall effect, unlike the "classical" AHE also occurs in non-ferromagnetic metals. The name of this effect only expresses the analogy of the *fingerprint* of the SH-AHE with the AHE. Thus, the SH-AHE is not to be confused with the ferromagnetic AHE effect that would also be visible in the framework of the proximity MR introduced in Sec. 2.1.7.

3.2 Experimental setup

In this chapter, we investigate two types of thin film structures, YIG/Pt bilayers and single Pt thin films on yttrium aluminum garnet ($Y_3Al_5O_{12}$, YAG) substrates. The YIG/Pt bilayers again are obtained by growing epitaxial YIG thin films with a thickness of $t_{\text{F}} \approx 60$ nm on single crystalline YAG or gadolinium gallium garnet ($Gd_3Ga_5O_{12}$,GGG) substrates using pulsed laser deposition [46,106]. In an *in situ* process, we then deposit a thin polycrystalline Pt film onto the YIG via electron beam evaporation. We hereby systematically vary the Pt thickness from sample to sample in the range 1 nm $\leq t_{\text{N}} \leq 20$ nm. In this way, we obtain a series of YIG/Pt bilayers with fixed YIG thickness, but different Pt thicknesses. For reference, we furthermore fabricate a series of YAG/Pt bilayers, depositing Pt thin films with thicknesses 2 nm $\leq t_{\text{N}} \leq 16$ nm directly onto YAG substrates. We employ X-ray reflectometry and X-ray diffraction to determine t_{N} and to confirm the polycrystallinity of the Pt thin films. A detailed information on the film thicknesses for both types of thin film structures used in our study are listed in Tab. 6.2 and Tab. 6.5. The
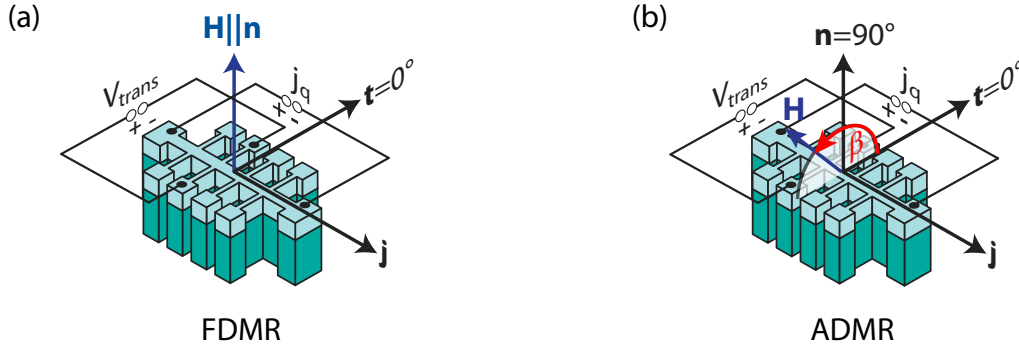
Figure 3.3: Measurement geometry for **(a)** field dependent magnetoresistance experiments (FDMR) at a fixed orientation of the external magnetic field (**H** ∥ **n**) and **(b)** angle dependent magnetoresistance experiments (ADMR) in oopj configuration as defined in Sec. 2.2.2.

parameter h again represents the surface roughness of Pt obtained from high-resolution X-ray reflectometry. For YIG/Pt bilayers, we determine an averaged surface roughness of $h = (0.7 \pm 0.2)$ nm, while for plain Pt on diamagnetic substrate, we obtain a slightly lower value of $h = (0.5 \pm 0.1)$ nm. However, within the estimated errors, the interface roughnesses of both types of samples are comparable and thus we expect no influence of the surface roughnesses on our data except size effects for $t_{Pt} \approx h$.

For electrical transport measurements, the samples are patterned into Hall bar mesa structures (width $w = 80\,\mu$m, contact separation $l = 600\,\mu$m) [50] [c.f. Fig. 3.3(a)]. We current bias the Hall bars with j_q of up to $500\,\mu$A and measure the transverse (Hall like) voltage V_{trans} either as a function of the magnetic field orientation (angle dependent magnetoresistance, ADMR [46,112]) or of the magnetic field amplitude $\mu_0 H$ (field dependent magnetoresistance, FDMR), for sample temperatures T between $10\,$K and $300\,$K. For all FDMR data reported below, the external magnetic field was applied perpendicular to the sample plane [$\mu_0 \mathbf{H} \parallel \mathbf{n}$, c.f. Fig. 3.3(a)]. For the ADMR measurements, we rotate an external magnetic field of constant magnitude $1\,$T $\leq \mu_0 H \leq 7\,$T in the plane perpendicular to the current direction $\mathbf{j}$ [oopj, see Fig. 2.7(b) and 3.3(b)].

Here, β again is defined as the angle between the transverse direction $\mathbf{t}$ and the magnetic field $\mathbf{H}$. In all ADMR experiments, we choose $\mu_0 H$ larger than the anisotropy and the demagnetization fields of the YIG film. As a result, the YIG magnetization $\mathbf{M}$ is always saturated and oriented along $\mathbf{H}$ in good approximation. The transverse resistivity $\rho_{trans}(\beta, H) = V_{trans}(\beta, H)\, t_N / j_q$ of the Pt layer is calculated from the voltage $V_{trans}(\beta)$ along $\mathbf{t}$. Again, we antisymmetrisize the transverse ADMR data with respect to $\sin(\beta) = -\sin(\beta + 180°)$ according to Eq. (2.31) to avoid influences from superpositions of the longitudinal voltages.

3.3 Experimental results

At first, we focus on magnetotransport experiments at room temperature. Figure 3.4(a), (c), (e) show FDMR measurements carried out at $300\,\mathrm{K}$ in YIG/Pt bilayers with $t_\mathrm{N} = 2.0, 6.5$ and $19.5\,\mathrm{nm}$. Extracting the ordinary Hall coefficient $\alpha_\mathrm{OHE} = \partial\rho_\mathrm{trans}(H)/\partial(H)$ from the slope, we obtain $\alpha_\mathrm{OHE}(19.5\,\mathrm{nm}) = -25.5\mathrm{p\Omega m/T}$ for the thickest Pt layer [see Fig. 3.4(e)], close to the literature value for bulk Pt [150]. Additionally, we observe a small superimposed S-like feature around $\mu_0 H = 0\,\mathrm{T}$, indicating the presence of an AHE like contribution. To quantify this contribution, we extract the full amplitude of the S-shape corresponding to an AHE like contribution α_AHE from linear fits to $\mu_0 H = 0\,\mathrm{T}$,
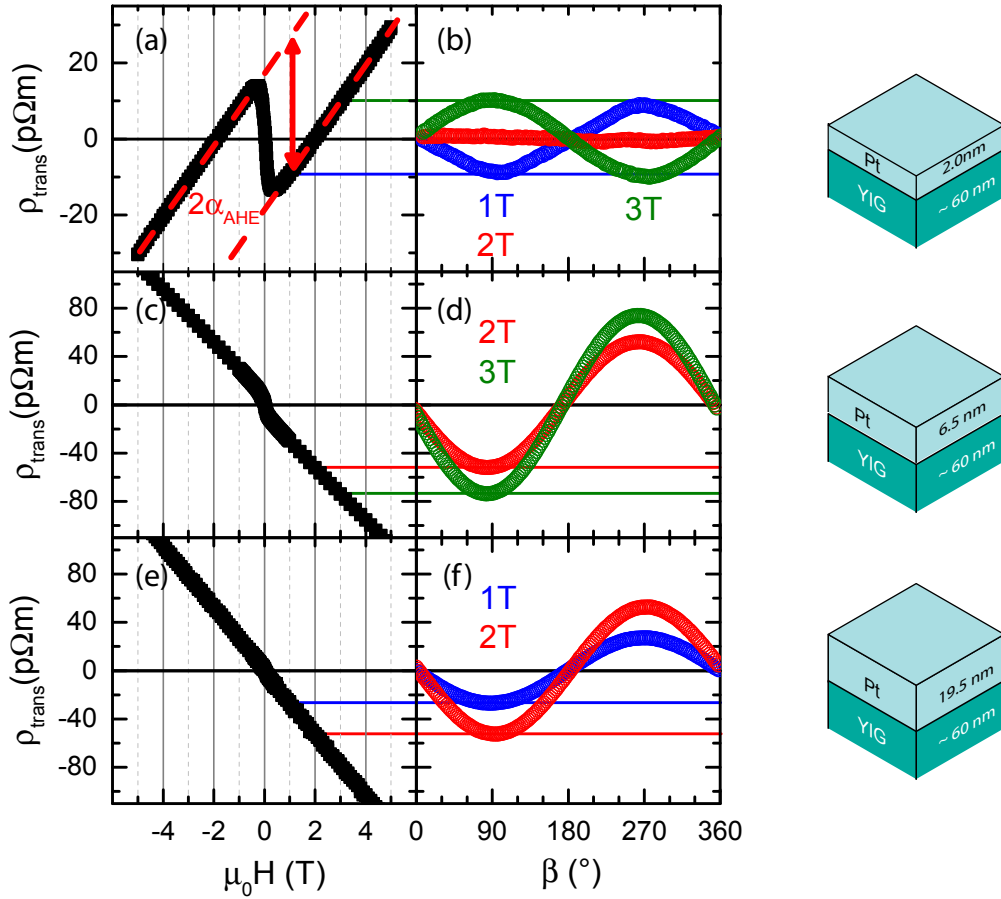
Figure 3.4: **(a)**, **(c)**, **(e)**:Transverse resistivity ρ_trans taken from FDMR measurements for YIG/Pt bilayers with **(a)** $t_\mathrm{N} = 2.0\,\mathrm{nm}$, **(c)** $6.5\,\mathrm{nm}$ and **(e)** $19.5\,\mathrm{nm}$, respectively. All data are taken at $300\,\mathrm{K}$. The dashed red lines in panel **(a)** indicate the extraction of α_AHE from linear fits to $\rho_\mathrm{trans}(H)$ extrapolated to $\mu_0 H = 0\,\mathrm{T}$. **(b)**, **(d)**, **(f)**: corresponding ADMR data taken in oopj configuration at $300\,\mathrm{K}$ at various constant external magnetic fields (see legends). The colored, horizontal lines in panels (a,b), (c,d) and (e,f) are intended as guides to the eye, to show that the ρ_trans values inferred from FDMR and ADMR are consistent for identical magnetic field configurations.

as indicated in Fig. 3.4(a). In the sample with $t_N = 6.5\,\text{nm}$ [Fig. 3.4(c)], α_{OHE} decreases to $-23.1\text{p}\Omega\text{m/T}$ and we find an increased $\alpha_{\text{AHE}}(t_N = 6.5\,\text{nm}) = (-6 \pm 1)\text{p}\Omega\text{m}$. For $t_N = 2.0\,\text{nm}$ [see Fig. 3.4(a)], we observe $\alpha_{\text{OHE}} = 7\,\text{p}\Omega\text{m/T}$, i.e. an inversion of the sign of the OHE. Additionally, we find α_{AHE} equal to $(-12 \pm 1)\,\text{p}\Omega\text{m}$. The presence of an AHE like behavior in YIG/Pt samples coincides with recent reports [43, 68, 95, 151–153]. However, our study of α_{AHE} as a function of platinum thickness and temperature in addition reveals a pronounced thickness dependence of α_{AHE} for $t_N \leq 10\,\text{nm}$ that will be addressed below [c.f. Fig. 3.4(b)].

Complementary to the FDMR experiments, we investigate ρ_{trans} as a function of the magnetic field orientation (ADMR). Here, the OHE is expected to depend only on the component $H_\perp = H\sin(\beta)$, i.e., $\rho_{\text{trans}}(\beta) \propto \sin(\beta)$. The experimental data shown in Figs. 3.4(b), (d) and (f) confirm this expectation. Information of the AHE and OHE coefficients can also be obtained form these experiments: Taking ADMR data at different magnetic field amplitudes, a linear fit to the amplitudes of the sine shaped signal again reveals α_{OHE} from the slope and α_{AHE} from the abscissa at $\mu_0 H = 0$, respectively. As indicated from the colored horizontal lines in Fig. 3.4, the data obtained from ADMR and FDMR are indeed consistent.

For reference, we also performed FDMR measurements on Pt thin films deposited directly on single-crystalline diamagnetic yttrium aluminum garnet (YAG) substrates. Figures 3.5(b),(d),(f) show the characteristic linear behavior for $\rho_{\text{trans}}(H) \propto H$, i.e., an ordinary Hall effect, without any AHE contribution. Extracting the ordinary Hall coefficient $\alpha_{\text{OHE}} = \partial\rho_{\text{trans}}(H)/\partial(H)$ from the slope, we obtain $\alpha_{\text{OHE}}(t_N = 2.0\,\text{nm}) = -3.1\,\text{p}\Omega\text{m/T}$, $\alpha_{\text{OHE}}(t_N = 3.5\,\text{nm}) = -15.9\,\text{p}\Omega\text{m/T}$, and $\alpha_{\text{OHE}}(t_N = 15.6\,\text{nm}) = -23.1\,\text{p}\Omega\text{m/T}$ with a systematic error of $\Delta\alpha_{\text{OHE}} = 0.1\,\text{p}\Omega\text{m/T}$. While α_{OHE} of the thickest Pt film with $t_N = 15.6\,\text{nm}$ is consistent with the literature value $\alpha_{\text{OHE}} = -24.4\,\text{p}\Omega\text{m/T}$ [150], we find significantly smaller OHE coefficients for the 3.5 nm and the 2.0 nm thick Pt film. This behavior in the thin film regime ($t_N \leq 10\,\text{nm}$) agrees with earlier reports [114]. Measurements of $\alpha_{\text{OHE}}(T)$ show a T independent α_{OHE} and the absence of any AHE like contribution. We also investigate ρ_{trans} as a function of the magnetic field orientation (ADMR) for this set of samples. As evident from Fig. 3.5(c) and (e), we obtain that the OHE depends only on the component $H_\perp = H\sin(\beta)$, i.e., $\rho_{\text{trans}}(\beta) \propto \sin(\beta)$. To conclude, in these reference samples, we find a similar thickness dependence of the ordinary Hall-effect (OHE), but no AHE-type signal. Thus, the sign inversion of the OHE in YIG/Pt hybrids is expected to be intimately connected to the Pt thin film regime [95].

We further investigate the temperature dependence of ρ_{trans} as a function of the magnetic field orientation (ADMR). In Fig. 3.6(a) we show ADMR data for a YIG/Pt(2.0 nm) hy-

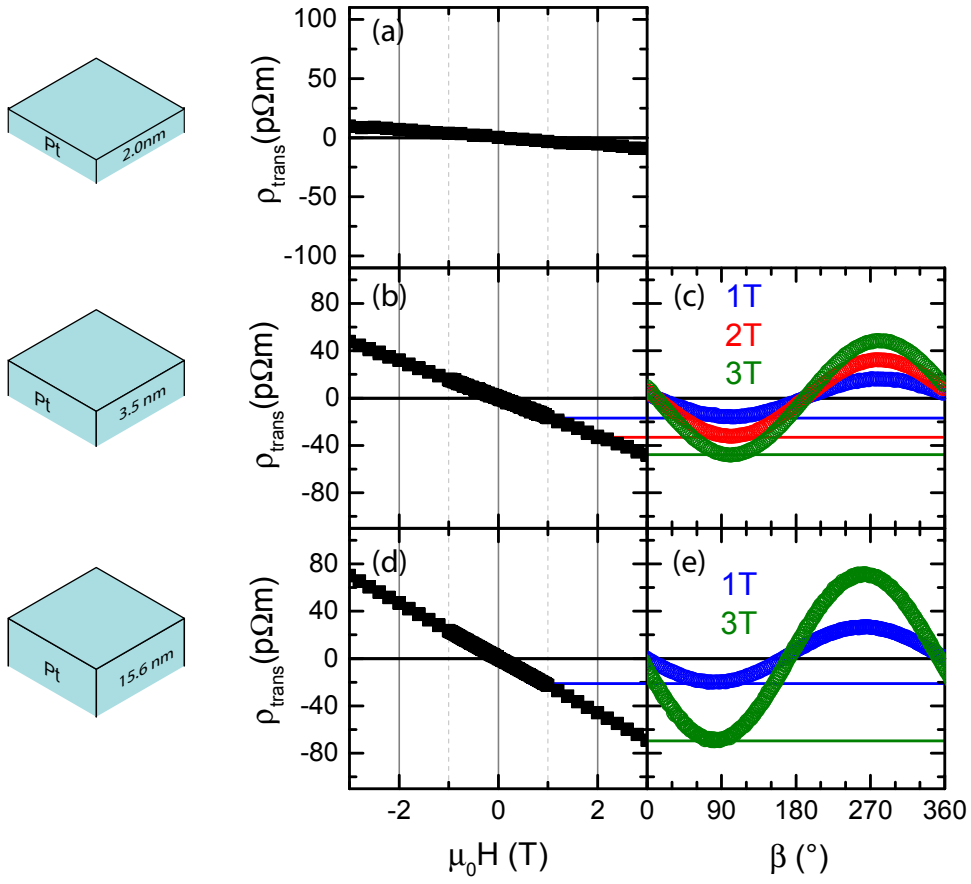**Figure 3.5:** **(a)** Transverse resistivity ρ_{trans} taken from a FDMR measurement for YAG/Pt (2.0 nm). **(b)** ρ_{trans} taken from a FDMR measurement for YAG/Pt (3.5 nm). **(c)** ρ_{trans} as a function of β for YAG/Pt (3.5 nm). **(d, e)**: FDMR and ADMR measurements for $t_{\text{N}} = 15.6$ nm on YAG. The colored, horizontal lines in panels (b, c) and (d, e) are intended as guides to the eye, to show that the ρ_{trans} values inferred from FDMR and ADMR are consistent for identical magnetic field configurations. All data taken at 300 K.

brid recorded at 10 K. As discussed above, in ADMR experiments, the OHE is expected to depend only on the component $H_{\perp} = H \sin(\beta)$. Therefore, one expects, $\rho(\beta) \propto \sin(\beta)$ for the angular dependence of the transverse resistivity. However, our experimental data reveals additional higher than linear order contributions of the form $V_{\text{trans}} \propto M_{\perp}^n$, with $\rho_{\text{trans}} \propto A \sin(\beta) + B \sin^3(\beta) + \cdots$. A fast Fourier transformation [c.f. Fig. 3.6(c)] of the ADMR data suggests the presence of $\sin^n(\beta)$ contributions up to at least $n = 5$. We admit that a quantitative determination of corresponding higher order coefficients is difficult, since the amplitudes of the contributions for $n \geq 5$ are below our experimental resolution of $1 \, \text{p}\Omega\text{m}$. A behavior similar to that shown in Fig. 3.6(a) is found in all YIG/Pt samples with $t_{\text{N}} \leq 5$ nm [see reference data in Fig. 3.7 (a)], but not in plain Pt films on YAG.
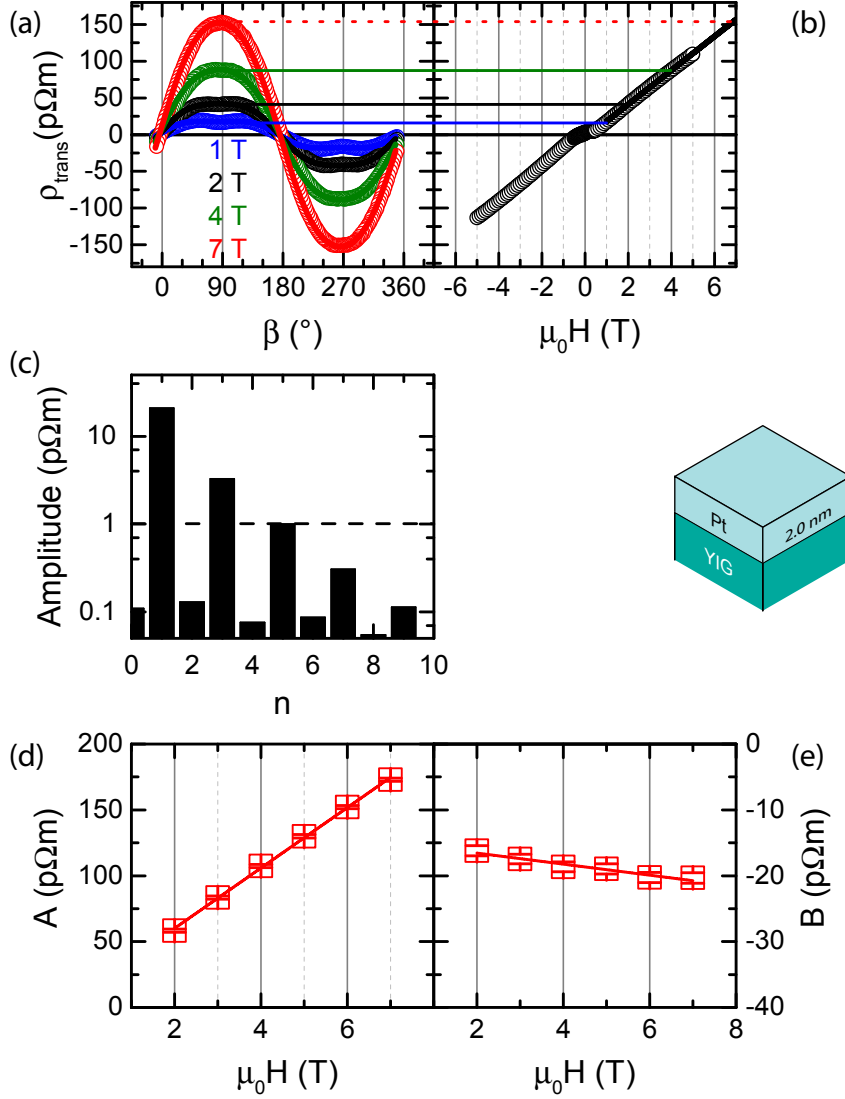
Figure 3.6: (a) ADMR and **(b)** FDMR data for a YIG/Pt sample with $t_N = 2.0\,\mathrm{nm}$, taken at $10\,\mathrm{K}$ for different $\mu_0 H$ (open symbols). The horizontal lines in panel (a,b) are intended as guides to the eye, to show that the ρ_{trans} values inferred from FDMR and ADMR are consistent for identical magnetic field configurations. Fits of Eq. (3.6) to the ADMR data in **(a)** are shown as solid lines. **(c)** Fast Fourier transform (FFT) results in terms of $\sin^n(\beta)$ for the ADMR data taken at $T = 10\,\mathrm{K}$ with $\mu_0 H = 7\,\mathrm{T}$ for the YIG/Pt(2.0 nm) sample shown in **(a)**. The dashed line indicates the experimental noise level of $1\,\mathrm{p\Omega m}$. Panels **(d)** and **(e)** show the fit parameters A and B obtained from Eq. (3.6) for YIG/Pt(2.0 nm) at $T = 10\,\mathrm{K}$ to the data in (a). Linear fits to the magnetic field dependence of A and B are shown as solid lines.

To allow for simple analysis, we use

$$\rho_{\mathrm{trans}} = A\sin(\beta) + B\sin^3(\beta) \tag{3.6}$$

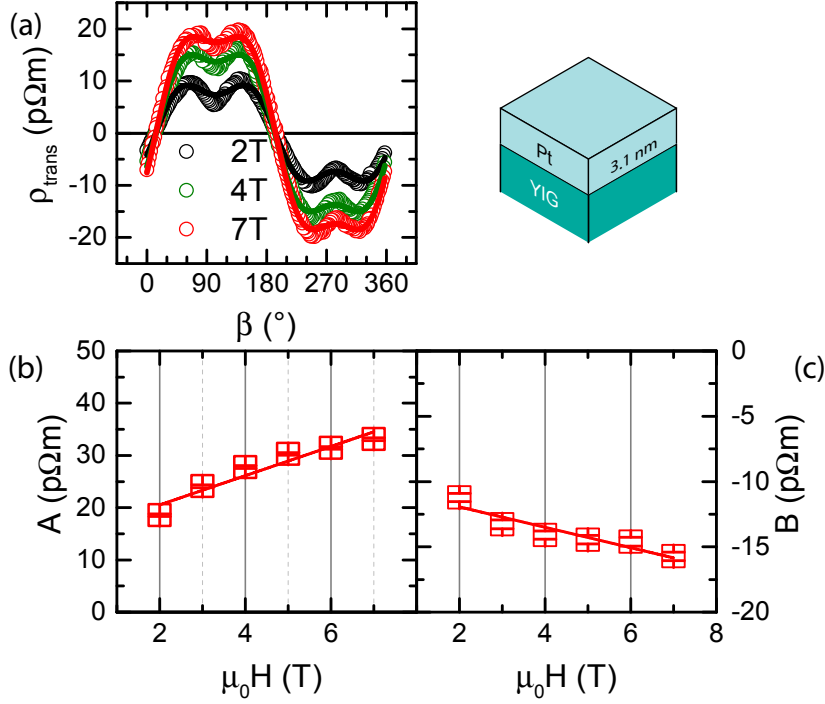in the following. Fits of the ADMR curves measured at different field magnitudes ac-

Figure 3.7: **(a)** ADMR data for a YIG/Pt sample with $t_N = 3.1\,\text{nm}$, taken at $10\,\text{K}$ for different $\mu_0 H$ (open symbols). The fits of Eq. (3.6) to the data are shown as solid lines. **(b)** and **(c)** show the fit parameters A and B obtained from Eq. (3.6) for YIG/Pt(3.1 nm) at $T = 10\,\text{K}$. Linear fits to the magnetic field dependence of A and B are shown as solid lines.

cording to Eq. (3.6) are shown as solid lines in Figs. 3.6(a) and 3.7(a). The magnetic field dependence of the fit parameters A and B is shown in Fig. 3.6(d),(e) for the sample with $t_N = 2.0\,\text{nm}$ and in Fig. 3.7(b),(c) for $t_N = 3.1\,\text{nm}$. We disentangle magnetic field dependent (OHE like) and "field independent" (AHE like) contributions to A by fitting the data to $A(\mu_0 H) = A_{\text{OHE}} \cdot \mu_0 H + A_{\text{AHE}}$. As evident from Figs. 3.6 and 3.7, the α_{OHE} and α_{AHE} values derived from FDMR and ADMR measurements are quantitatively consistent[1].

A_{OHE} as a function of t_N is shown in Fig. 3.8(a). Obviously, A_{OHE} deviates from the bulk OHE literature value [150] in YIG/Pt bilayers with $t_N \leq 10\,\text{nm}$ and also exhibits a temperature and thickness-dependent sign change for small t_N. A thickness-dependent behavior of the OHE without sign change has also been reported in Ref. [95]. However, these authors found an increase of the OHE coefficient in the thin film regime, which could be due to the formation of a thin, non-conductive "dead" Pt layer at the interface as, e.g., reported for Ni/Pt [154]. In contrast, we attribute the thickness dependence of the OHE in our samples solely to a modification of the Pt properties in the thin film regime. We additionally suggest to interpret the sign change of the OHE to a transition from electron-like transport to hole-like transport in the very thin film regime. A calcula-

---

[1]We want to emphasize that, by neglecting higher order contributions in our analysis, A and B can not straightforwardly be read from the ADMR data in Figs. 3.6(a) and 3.7(a).

tion of the bandstructure of Pt could give deeper insight into this phenomenon. Together with a theoretical discussion, further experiments will be required in the future to clarify the origin of the temperature dependence of the OHE in YIG/Pt hybrids.

The anomalous Hall coefficient A_{AHE}, present only in YIG/Pt hybrids, i.e., when a magnetic insulator is adjacent to the N, is depicted in Fig. 3.8(b). We observe a strong dependence of A_{AHE} on t_{N} similar to the thickness dependent magnetoresistance obtained from longitudinal transport measurements reported earlier [46], but with a sign change in A_{AHE} between 100 K and 10 K. This observation agrees with recent reports of $A_{\text{AHE}} = 54\,\text{p}\Omega\text{m}$ for YIG/Pt(1.8 nm) [153] and $A_{\text{AHE}} = 6\,\text{p}\Omega\text{m}$ for YIG/Pt(3 nm) [152], both taken at 10 K. Our study suggests a maximum in A_{AHE} around $t_{\text{N}} = 3\,\text{nm}$, compatible with a complete disappearance of A_{AHE} for $t_{\text{N}} \to 0$. This observation however is at odds with the attribution of the AHE in YIG/Pt to a proximity MR as postulated in Ref. [152]. In this case, one would expect a monotonous increase of the AHE signal with decreasing Pt layer thickness, and eventually a saturation when the entire nonmagnetic layer is spin polarized. The absence of a proximity MR in our Hall data is consistent with XMCD data on similar YIG/Pt samples [106] as well as other ferromagnetic insulator/N hybrids [155].

We now model our experimental findings in terms of the SH-AHE theory [15] using Eq. (3.5). To fit the nonlinear behavior of $A_{\text{AHE}}(t_{\text{N}})$, we combine this expression with the thickness dependence of the sheet resistivity for thin Pt films [117] as discussed in Ref. [50] and Sec. 2.2.3. We use the parameters $\lambda = 1.5\,\text{nm}$, $G_{\text{r}} = 4 \times 10^{14}\Omega^{-1}\text{m}^{-2}$, $\theta_{\text{SH}}(300\,\text{K}) = 0.11$ and $\theta_{\text{SH}}(10\,\text{K}) = 0.075$ obtained from longitudinal SMR measurements on similar YIG/Pt bilayers (c.f. Sec. 2.4.1). As obvious from the solid lines in Fig. 3.8(b), Eq. (3.5) reproduces our thickness dependent AHE data upon using $G_{\text{i}} = 1 \times 10^{13}\,\Omega^{-1}\text{m}^{-2}$ for 300 K and $G_{\text{i}} = -3 \times 10^{13}\,\Omega^{-1}\text{m}^{-2}$ for 10 K. For 300 K, the value for G_{i} nicely coincides with earlier reports [46] as well as theoretical calculations [126]. In the SH-AHE model, the only parameter allowing to account for the sign change in ρ_{trans} as a function of temperature is G_{i}. In this picture, our AHE data thus indicate a sign change in G_{i} between 300 K and 10 K.

We finally address the thickness and temperature dependence of the $\sin^3(\beta)$ contribution parametrized by $B = B_{\text{AHE}} + B_{\text{OHE}}\mu_0 H$, that cannot straightforwardly be explained in a conventional Hall scenario. As evident from the linear fits in Figs. 3.6(e) and 3.7(c), B is nearly field independent. A slight field dependence $B_{\text{OHE}} \leq 1\,\text{p}\Omega\text{m/T}$ might arise due to fitting errors caused by neglected higher order terms ($n \geq 5$). Therefore, we focus our discussion on the field independent part B_{AHE} in the following. B_{AHE} exhibits a
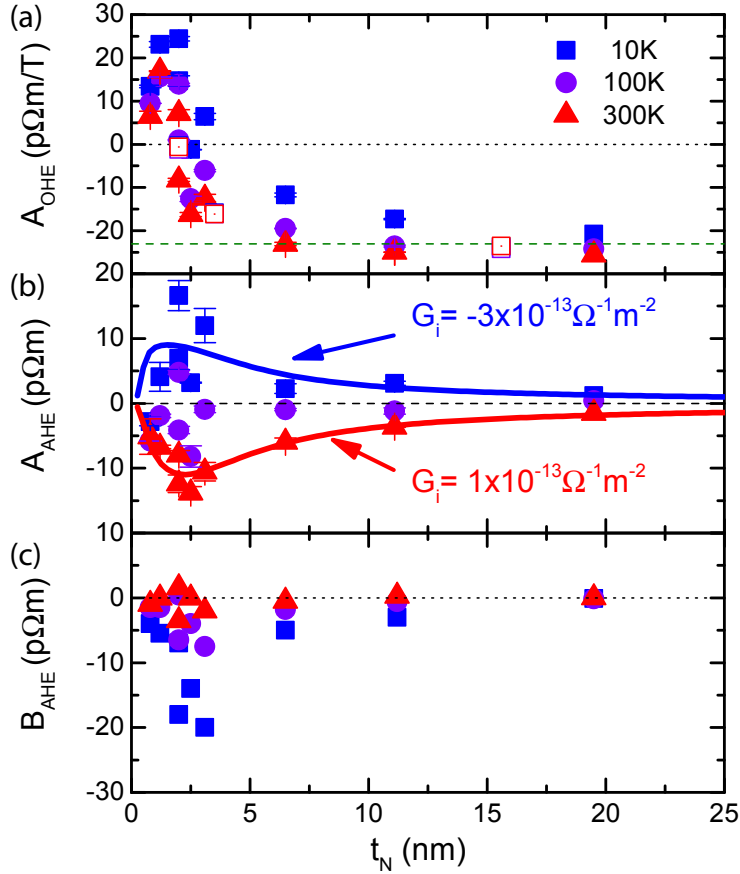
Figure 3.8: (a)-(c) Field dependent (OHE-like) and field independent (AHE-like) Hall coefficients A and B proportional to $\sin(\beta)$ and $\sin^3(\beta)$, respectively, plotted versus the Pt thickness for $T = 300\,\mathrm{K}$ (red), $T = 100\,\mathrm{K}$ (purple) and $T = 10\,\mathrm{K}$ (blue). The data is obtained from ADMR measurements for YAG/Pt (open symbols) and YAG/YIG/Pt (full symbols). A_{OHE} depicted in **(a)** describes the conventional Hall effect, the olive dashed line corresponds to the literature value for bulk Pt [150]. **(b)** Thickness dependence of A_{AHE}. The solid lines show fits to the SH-AHE theory using $G_i = 1 \times 10^{13}\,\Omega^{-1}\mathrm{m}^{-2}$ for $T = 300\,\mathrm{K}$ (red) and $G_i = -3 \times 10^{13}\,\Omega^{-1}\mathrm{m}^{-2}$ for $T = 10\,\mathrm{K}$ (blue). Panel **(c)** shows the thickness dependence of the field independent coefficient B_{AHE} of the $\sin^3(\beta)$ term.

strong temperature and thickness dependence as shown in Fig. 3.8(c), suggesting a close link to A_{AHE} and therefore the SH-AHE. However, we do not observe a temperature-dependent sign change in B_{AHE}. Expanding the SMR theory [15] to include higher order contributions of the magnetization directions m_i $(i = j, t, n)$ in analogy to the procedure established for the AMR of metallic ferromagnets [112,113], $\sin^3(\beta)$ terms appear in ρ_{trans}, but with an amplitude proportional to θ_{SH}^4. Assuming $\theta_{\mathrm{SH}}(\mathrm{Pt}) \approx 0.1$, this would lead to $B_{\mathrm{AHE}}/A_{\mathrm{AHE}} \approx 0.01$, which disagrees with our experimental finding $B_{\mathrm{AHE}}/A_{\mathrm{AHE}} \geq 0.2$. Additionally, we study the influence of the longitudinal resistivity on ρ_{AHE}. For metallic ferromagnets, one usually considers $\rho_{\mathrm{AHE}} \propto M(H)\rho_{\mathrm{long}}^{\alpha}$ with $1 \leq \alpha \leq 2$ [57,58]. Applying this approach to V_{trans} of the YIG/Pt samples discussed here is not possible: Since the

longitudinal resistance is modulated by the SMR with $\rho_1/\rho_0 \leq 10^{-3}$ [46], $\rho_{\mathrm{AHE}} \propto \rho^\alpha$ would imply $B_{\mathrm{AHE}}/A_{\mathrm{AHE}} \leq 10^{-3}$. This is in contrast to our experimental findings. Thus, a dependence of the form $\rho_{\mathrm{AHE}} \propto \rho_{\mathrm{long}}^\alpha$ cannot account for our experimental observations. Finally, a static magnetic proximity effect [43, 47, 49] (see Sec. 2.1.7) also cannot explain B_{AHE}, since the thickness dependence of B_{AHE} shown in Fig. 3.8 (c) clearly indicates a decrease for $t_{\mathrm{N}} \leq 2.5\,\mathrm{nm}$. Consequently, within our present knowledge, neither a spin current related phenomenon (SMR, SH-AHE), nor a proximity based effect can explain the origin or the magnitude of this anisotropic higher order anomalous Hall effect. We also would like to point out that the higher order $\sin^3(\beta)$ term can be resolved only in ADMR measurements. In conventional FDMR experiments, such higher order contributions cannot be discerned.

3.4 Spin Hall anomalous Hall effect: A summary

In summary, we have investigated the ordinary and anomalous Hall effect in YIG/Pt heterostructures for different Pt thicknesses, comparing magnetization orientation dependent (ADMR) and magnetic field magnitude dependent (FDMR) measurements at temperatures between $10\,\mathrm{K}$ and $300\,\mathrm{K}$.

In reference experiments performed on Pt thin films on diamagnetic (YAG) substrates, we observe a Pt thickness dependent ordinary Hall effect (OHE) only. This thickness dependence is in agreement with earlier results [114] and suggests a change in the band structure of Pt, more precisely a transition from electron-like to hole-like transport in the ultra-thin film regime. Therefore, theoretical calculations of the band structure of ultra-thin Pt should give deeper insights to the (magneto)transport in Pt.

In contrast, in YIG/Pt bilayers, an AHE like signal is present in addition. The AHE contribution changes sign as a function of temperature and is subject to a strong dependence on the Pt layer thickness. The extracted AHE signal as a function of t_{N} can be modeled using a spin Hall magnetoresistance-type formalism for the transverse transport coefficient for all temperatures studied within this work. This further substantiates the theoretical model of the SMR and the fact that within this framework, spin transport can become visible in electrical measurements. However, we need to assume a temperature dependent sign change in the imaginary part of the spin mixing interface conductance to describe the sign change in the anomalous Hall signal observed experimentally. The absolute values of the experimental extracted numbers $-3 \times 10^{13}\,\Omega^{-1}\mathrm{m}^{-2}$ at $10\,\mathrm{K}$ and $1 \times 10^{13}\,\Omega^{-1}\mathrm{m}^{-2}$ at $300\,\mathrm{K}$ for G_i furthermore coincides with earlier theoretical calculations. Thus, a link of our experimental findings to the theoretical prediction given by the SMR theory is indeed possible and supports the validity of this framework with respect to the proximity MR model.

On the other hand, a clear, simple to understand picture of the concept of the imaginary spin mixing interface conductance is still missing. This represents a future challenge for both experimentalists and theorists in *spintronics*. If the temperature dependence of G_i is a uniform feature in FMI/N bilayers, which should be validated experimentally for other material combinations in the future, this implies that the phase shift between the FMI and N changes as a function of temperature. This is not taken into account in the present Landauer-Büttiker-like picture of $G_{\uparrow\downarrow}$, in principle summing up the number of spin transport channels at the interface. Our findings additionally indicate that both temperature dependent properties, the magnetic structure of the FMI as well as the spin transport in N have to be considered in describing interface characteristics. For a check of theoretical concepts to come, experiments may also be considered to be based on easier to calculate material combinations, e.g. ferromagnetic insulators with a reduced number of atoms per unit cell compared to YIG (80 atoms).

Additionally, in our analysis we find contributions proportional to $\sin^3(\beta)$ and higher orders in the ADMR data for YIG/Pt. The physical mechanism responsible for this behavior could not be clarified within this work and will be subject of further investigations. The $\sin^3(\beta)$ contribution is not observed in Pt thin films directly deposited on a diamagnetic substrate, indicating that this is not a pure Pt effect like the one we reported for the longitudinal transport in Sec. 2.4.3. This higher order feature could neither be explained by a higher order SMR contribution proportional to θ_{SH}^4, nor by the influence of the longitudinal resistivity modulation on the transverse signal like $\rho_{\mathrm{AHE}} \propto \rho_{\mathrm{long}}^\alpha$ ($1 \leq \alpha \leq 2$). However, the presence of higher order contributions in ρ_{trans} for YIG/Pt indicates the importance of the FMI/N interface in magnetoresistive experiments. Even though only the first order contribution can be ascribed to the SH-AHE, the thickness dependence of the parameter B_{AHE} indicates a strong correlation between the SMR concept and the $\sin^3(\beta)$ contribution in YIG/Pt. Here, it may be suggested to consider a possible anisotropy in the spin transport parameters, which might be the origin of this anisotropic AHE in YIG/Pt. At this point, again G_i should come into focus, since this parameter governs the main difference between the longitudinal and the transverse SMR formulas in Eqs. 2.21 and 2.24. Additionally, no higher order contributions were found in the previous section discussing the longitudinal SMR, indicating that the set of spin transport parameters responsible for the formation of $-\Delta\rho_1/\rho_0$ are isotropic in good approximation.

In the end, the observation of higher order contributions to the AHE in angle dependent magnetotransport measurements in YIG/Pt not only denotes the presence of a wide range of non-understood features in a quite "traditional" material combination, but also confirms the usefulness of magnetization orientation dependent experiments. Clearly,

magnetotransport measurements as a function of the magnetic field magnitude only, i.e. for a single magnetic field orientation (perpendicular field), as usually performed to study Hall effects, are not sufficient to access all transverse transport features.

4 Observation of the spin Nernst effect in platinum

A pure spin current, as defined in Sec. 2.1.1, is the direct transport of spin angular momentum, without an associated net transport of electric charge. The concept of a pure spin current triggered a novel field in electronics known as spintronics, in which the electron's spin degree of freedom is utilized instead of its electric charge. By transferring concepts of *electronics* to *spintronics*, a wide field with novel effects and possible applications has opened. During the last decade, fundamentally important electronic devices like the transistor have been adapted for spin current effects [8, 156–158]. Additionally, transport effects describing pure spin current flows like the spin Seebeck effect [34–36], or the spin Peltier effect [159, 160] have been discovered, but up to now, one major pure spin current transport effect still only is a theoretical conjecture. The thermal relative of the spin Hall effect, the so-called spin Nernst effect, has been discussed on theoretical grounds during the past years [161–164], but was not observed experimentally. This is surprising, considering that the spin Nernst effect is the last missing link for a complete spin current transport picture.

In this chapter, we report on the experimental observation of the spin Nernst effect (SNE), i.e. the generation of a spin current perpendicular to a heat current. We demonstrate the existence of this thermally generated spin current in platinum by attaching a YIG thin film to the Pt. The YIG layer works as a switchable spin current detector. We modulate the spin transfer into the YIG layer by controlling its magnetization orientation. This leads to a presence vs. suppression of the spin current reflected at the YIG/Pt interface. By action of the inverse spin Hall effect, the spin current contributions in N are subsequently converted into charge currents along the initial heat current. This allows for a detection of the spin Nernst spin current in the charge channel on top of the longitudinal thermopower voltage. We refer to this as the spin Nernst magneto-thermopower.

This section starts with a brief motivation of the spin Nernst effect in Sec. 4.1, followed by a gedankenexperiment based introduction to the concept of the spin Nernst magneto-thermopower (SNMTP). This part will be closed by a theoretical calculation of the SNMTP. In Sec. 4.2, we present the measurement setup including the development of a new

dipstick for low-noise magneto-thermopower measurements. The experimental data will be discussed in Sec. 4.3. Our experiments allow to compare the spin Hall angle in Pt and its thermal analog, the spin Nernst angle. The discussion of this first experimental determination of the spin Nernst angle in Sec. 4.3.7 is corroborated by first principles calculations preformed by Sebastian Wimmer [165]. The results presented in this chapter will be submitted for publication [166].

4.1 Theory

In this Section, we develop the theoretical background of the spin Nernst magneto-thermopower. At first, we introduce the Seebeck effect (thermoelectric effect) and compare electrically and thermally driven transverse response effects to introduce the phenomenology of the spin Nernst effect in Sec. 4.1.2. Afterwards, we combine the thermal spin current generation via the spin Nernst effect with the inverse spin Hall effect, leading to the concept of the Spin Nernst magneto-thermopower. After introducing this in a very intuitive gedankenexperiment in Sec. 4.1.3, we present a theoretical calculation based on the spin diffusion theory in Sec. 4.1.4.

4.1.1 Thermopower and Seebeck effect

Charge transport is inevitably connected to a particle transport of electrons or holes. In electronics, the charge transport is usually driven by an electric field $\mathbf{E} = -\nabla\Phi$, leading to a charge flow along the gradient of the electrical potential Φ. However, also a thermal imbalance along a sample can drive a flow of (charged) particles.

To be more specific, we consider a metallic beam of length l in the following [Fig. 4.1(a)].
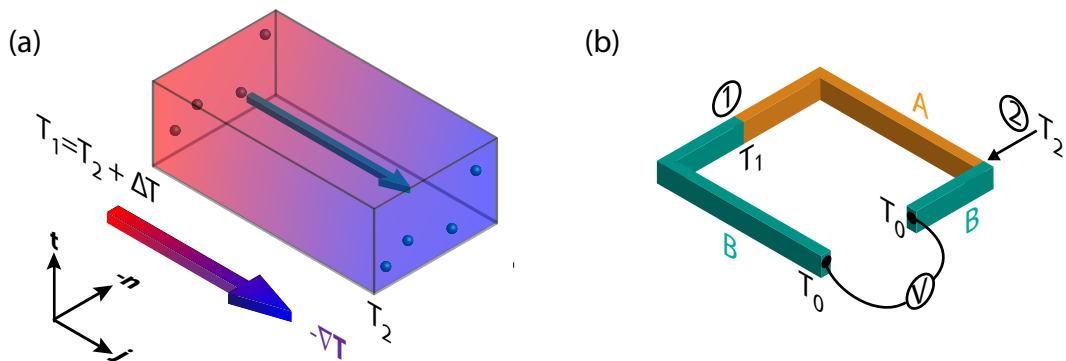

Figure 4.1: **(a)** Concept of thermopower: particles located at the left side of a metallic beam with local temperature $T_1 = T_2 + \Delta T$ exhibit a higher entropy than particles at the right side $(T = T_2)$. This leads to a particle flow from the hot to the cold end of the beam. **(b)** Geometry of a thermocouple to measure the Seebeck effect between two metals A and B. For details, see text.

The right side of this beam is in thermal contact with a heat reservoir T_2, while the left side is connected to a heat reservoir $T_1 = T_2 + \Delta T$. The temperature difference ΔT leads to a difference in entropy, with particles located at the left end of the sample exhibiting a higher entropy than particles on the right end. Thus, particles from the left have an increased tendency to propagate to the right end than the other way around. If we assume the material to be metallic and the particles carrying an electric charge $-e$, this thermally driven particle transport is accompanied with a charge transport along the direction $\mathbf{j}$ of the temperature gradient $\nabla T = \mathbf{j} \partial_j T$, leading to an electric field building up along this direction. The proportionality factor between the electric field $\mathbf{E}_{\text{thermal}}$ and a temperature gradient ∇T given by

$$\mathbf{E}_{\text{thermal}} = \hat{S} \nabla T \tag{4.1}$$

is called the thermopower tensor $\hat{S}$. $\hat{S}$ is connected to the energy dependence of the electrical conductivity at the Fermi surface. Starting from Boltzmann's equation, one can derive [70]

$$\hat{S} = \frac{\pi^2}{3} \frac{k_{\text{B}} T}{e} \left[\frac{\partial \ln(\hat{\sigma}_{\text{N}}(E))}{\partial E} \right]_{E = E_{\text{F}}}. \tag{4.2}$$

Here, E is the charge particle's energy, E_{F} the Fermi energy, k_{B} Boltzmann's constant and $\hat{\sigma}_{\text{N}}(E)$ the conductivity tensor, taking into account material properties and geometry specific anisotropy of the electric transport. In a different, widely-used notation, the thermopower $\hat{S}$ is also called the Seebeck coefficient and, for a specific definition of the directions of $\mathbf{E}_{\text{thermal}}$ and ∇T, the matrix form of $\hat{S}$ is simplified to a scalar S.

To experimentally measure the thermopower, one usually forms a closed electric circle with two metals A and B, where the two contact areas 1 and 2 are at different temperatures T_1 and T_2 [see Fig. 4.1(b)]. One detects the potential difference along this construction via a voltmeter connected to both open ends. The voltmeter as well as both open ends of metal B must be at the same, arbitrary temperature T_0. The potential difference V_{thermal} detected at the voltmeter is given by the integral over the electric field along the circuit and thus we end up with

$$V_{\text{thermal}} = \int_{T_1}^{T_2} (S_{\text{A}} - S_{\text{B}}) \, dT \tag{4.3}$$

where S_{A} and S_{B} are the scalar thermopowers of material A and B, respectively. The generation of this potential difference is called the Seebeck effect (thermoelectric effect), while the measurement device depicted in Fig. 4.1(b) is referred to as a thermocouple.

4.1.2 Transverse transport phenomena

In 1879, Edwin Hall [66] discovered that a transverse charge current density arises in a conductive material, if a magnetic field $\mathbf{H}$ and a charge current density $\mathbf{j}_q$ are simultaneously applied and $\mathbf{H}$, $\mathbf{j}_q$ and the detection direction of ρ_{trans} form a trihedron. This so-called Hall effect, which has already been discussed in Ch. 3, is sketched in Fig. 4.2(a). Intuitively, the Hall effect can be understood in terms of the Lorentz force $F_{\mathrm{L}} = q(\mathbf{E} + \mathbf{v} \times \mu_0\mathbf{H})$ acting on a charged particle moving perpendicular to the magnetic field. Here, $\mathbf{E}$ again represents the electric field, q is the particle's charge and $\mathbf{v}$ it's velocity. This leads to a charge current density $\mathbf{j}_q^{\mathrm{Hall}} = \sigma_{\mathrm{N}}R_{\mathrm{H}}\mu_0\mathbf{H} \times \mathbf{j}_q$ perpendicular to both the initial charge current and the magnetic field. Here, $R_{\mathrm{H}} = 1/nq$ represents the Hall constant which is sensitive to the sign of q and the charge carrier density n. In the following, we discuss the transverse effects for electrons, carrying a charge $q = -e$ ($e > 0$), in non-ferromagnetic samples. In our picture, $\mathbf{j}_q$ represents the direction of positive charged particles (technical current flow). Thus, electrons propagate in the opposite direction along $-\mathbf{j}$ (see definition of the coordinate system in Fig. 4.2) and are deflected by the Lorentz force along $\mathbf{n}$. The resulting Hall current $\mathbf{j}_q^{\mathrm{Hall}}$ thus points along $\mathbf{n}$.

The thermal analogue of the Hall effect, the so-called Nernst effect, arises when the charge current bias is substituted with a thermal drive. The temperature gradient $-\nabla T$ applied along $\mathbf{j}$ leads to a heat current $\mathbf{j}_h = -\kappa\nabla T$ with κ being the thermal conductivity. Like the Seebeck coefficient, κ in general (for anisotropic solid states) is a tensor. In a free electron gas model, which in good approximation holds for metals, κ can be used as a scalar function with $\kappa = \frac{\pi^2}{3m}nk_{\mathrm{B}}^2\tau T$, where n is the electron density, m the electron mass, k_{B} Boltzmann's constant, τ the scattering time and T the temperature. κ can be linked to the electrical conductivity σ_{N} via Wiedemann-Franz's law [70]:

$$\frac{\kappa}{\sigma_{\mathrm{N}}} = \frac{\pi^2}{3}\frac{k_{\mathrm{B}}^2}{e^2}T. \tag{4.4}$$

The heat current is accompanied with a particle flow due to the difference in entropy between the hot and the cold end of the sample, allowing for an effective particle motion from the hot side with higher entropy to the cold end. In analogy to the Hall effect depicted in Fig. 4.2(a), we here discuss electrons propagating along the thermal drive in the following. The combined action of a temperature gradient ∇T and an applied magnetic field $\mathbf{H}$, again pointing along the $\mathbf{t}$ direction, leads to a transverse charge current $\mathbf{j}_q^{\mathrm{Nernst}} = -(N\mu_0\sigma_{\mathrm{N}}/\kappa)\,\mathbf{H} \times \mathbf{j}_h$ [70]. This is referred to as the Nernst current (Nernst effect) [167], cf. Fig. 4.2(b). The proportionality factor N is called the Nernst constant. The sign of N is material specific and we in the following assume $N < 0$ [168]. Owing to their fundamental importance from both a basic research and a device perspective, the
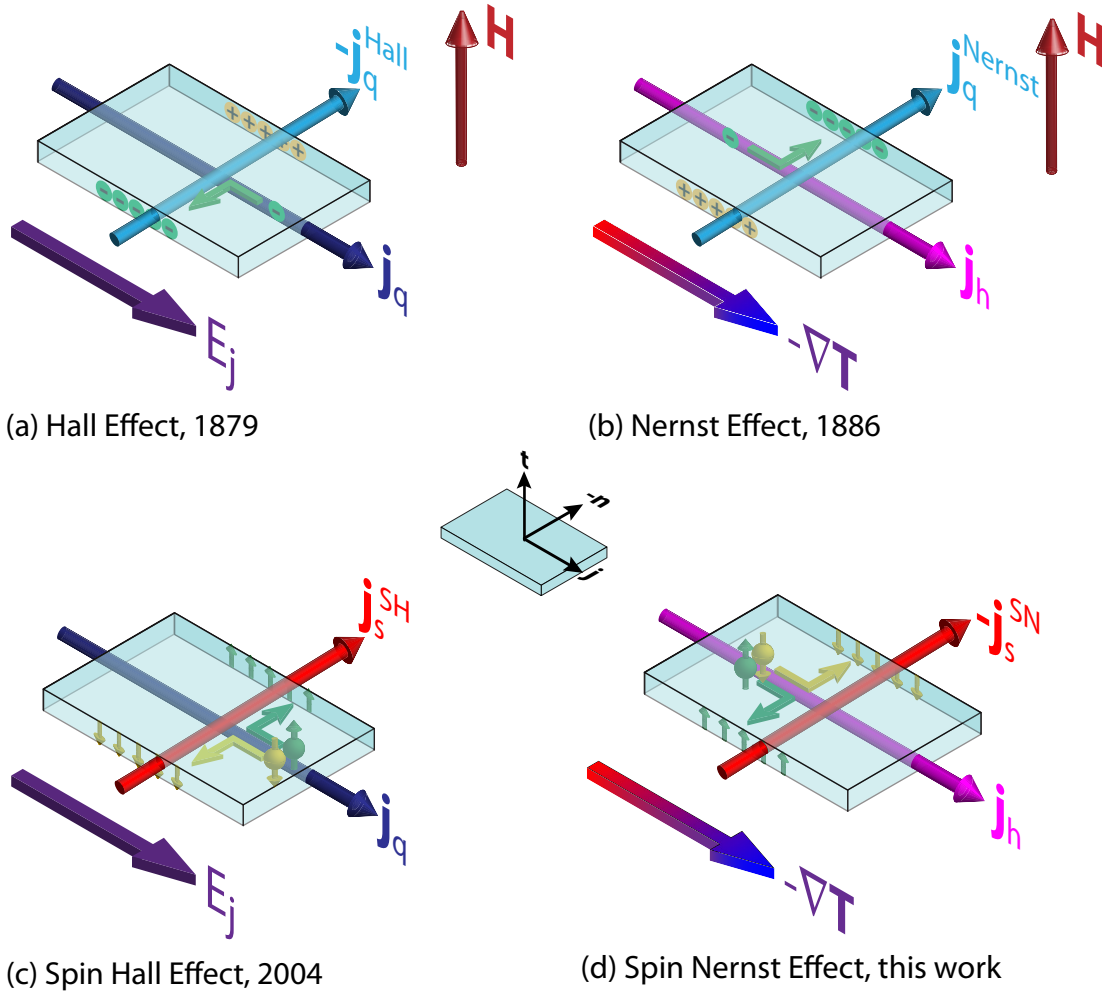
(a) Hall Effect, 1879   (b) Nernst Effect, 1886

(c) Spin Hall Effect, 2004   (d) Spin Nernst Effect, this work

Figure 4.2: **(a)** Conventional Hall effect: Electrons in a metallic sample move opposite to the (technical) current direction $\mathbf{j}_q$ along $-\mathbf{j}$. The presence of an external magnetic field along $\mathbf{t}$ leads to a deflection of the electrons along $\mathbf{n}$, which can be interpreted as a transverse charge current $\mathbf{j}_q^{\text{Hall}}$ along $\mathbf{n}$. **(b)** Nernst effect: A heat current $\mathbf{j}_h$ driven by a temperature gradient $\nabla T \parallel -\mathbf{j}$ gives rise to a particle motion along $\mathbf{j}$. Due to the magnetic field along $\mathbf{t}$, a transverse electric current along $-\mathbf{n}$ arises. **(c)** Spin Hall effect: A charge current $\mathbf{j}_q$ is applied along $\mathbf{j}$. Electrons carrying $|\!\uparrow\rangle$ or $|\!\downarrow\rangle$ spin are deflected due to the spin-orbit interaction. This gives rise to a spin current $\mathbf{j}_s^{\text{SH}} \parallel -\mathbf{n}$. **(d)** Spin Nernst effect: A temperature gradient $\nabla T \parallel -\mathbf{j}$ drives a motion of $|\!\uparrow\rangle$ and $|\!\downarrow\rangle$ electrons along $\mathbf{j}$. The SOI leads to a deflection of $|\!\uparrow\rangle$ electrons along $\mathbf{n}$ and vice versa, resulting in a spin current $\mathbf{j}_s^{\text{SN}}$ along $\mathbf{n}$.

Hall and the Nernst effects have been extensively studied in electrical conductors. The Hall and Nernst effects are prototypical examples of transverse transport phenomena, in which the direction of transport induced by an external drive is orthogonal to the latter.

Transverse transport phenomena are not limited to the charge channel. In analogy to the transverse charge currents arising in the Hall or Nernst effects, it also is possible to induce transverse pure spin currents (cf. Sec. 2.1.1) in metals. We already intro-

duced in Sec. 2.1.2 that in electrical conductors, conventional charge currents can induce transverse spin currents via spin-orbit interaction (SOI) [55, 56]. One speaks of the spin Hall effect [56] when the transverse spin current is driven by a charge current $\mathbf{j}_q$, see Fig. 4.2(c). This phenomena arises in the absence of magnetic fields, since it is based on spin dependent scattering processes (cf. Sec. 2.1.2). Thus, the spin polarization axis $\mathbf{s}$ takes the role of the magnetic field. In the following, we assume a charge current density $\mathbf{j}_q$ along $\mathbf{j}$. Without loss of generality, we define the spin polarization along the $\mathbf{t}$ axis, $\mathbf{s} \parallel \mathbf{t}$. Spin dependent scattering now leads to a deflection of $|\uparrow\rangle$ electrons along $-\mathbf{n}$ and $|\downarrow\rangle$ electrons along $\mathbf{n}$. This results in a net flow of angular momentum[1] along $-\mathbf{n}$, and we can express the resulting spin current density[2] as $\mathbf{j}_s^{\mathrm{SH}} = \theta_{\mathrm{SH}} \left(\hbar/2e\right) \left(\mathbf{s} \times \mathbf{j}_q\right)$. As already defined in Sec. 2.1.2, the spin Hall angle θ_{SH} here characterizes the charge-to-spin conversion efficiency.

In analogy to the Nernst effect, we now replace the charge current with a temperature gradient [cf. Fig. 4.2(d)]. We define the direction of $-\nabla T \parallel \mathbf{j}$ in accordance to Fig. 4.2(b) and choose $\mathbf{s} \parallel \mathbf{t}$. The temperature difference along the sample again causes a particle motion along $\mathbf{j}$ and we assume electrons as the majority charge carriers. Again, due to the SOI, $|\uparrow\rangle$ electrons are deflected along $\mathbf{n}$ and vice versa. This transverse spin current arising in a direction transverse to an applied temperature gradient is called the spin Nernst spin current [cf. Fig. 4.2(d)] and can be written as $\mathbf{j}_s^{\mathrm{SN}} = \theta_{\mathrm{SN}} \left(\hbar/2e\right) \left(-S/(\kappa\rho)\right) \left(\mathbf{s} \times \mathbf{j}_h\right)$. Here, S is the (scalar) Seebeck coefficient, κ the (scalar) thermal conductivity, ρ the (scalar) resistivity of the metal to which the thermal drive is applied, and θ_{SN} the spin Nernst angle [161–164], i.e. a heat-to-spin current conversion efficiency.

While the spin Hall effect has been very vividly investigated both theoretically and experimentally in the last decade [67, 157, 158] and has provided a pathway for the electrical generation and detection of spin currents, the spin Nernst effect has remained a theoretical conjecture. The key outcome of this thesis is the experimental observation of the spin Nernst effect in Pt.

4.1.3 Concept of the spin Nernst magneto-thermopower

In the following section, we introduce the idea behind our experimental approach to detect the spin Nernst effect. To describe the mechanism behind the detection of the spin Nernst effect in a very intuitive picture, we start with a gedankenexperiment. Consider a free standing N thin film with large SOI like Pt in a plane spanned by orthogonal vectors $\mathbf{j}$ and $\mathbf{n}$ (cf. Fig. 4.3). We connect one end of the sample to a heat reservoir and the other side to a heat sink to apply a temperature gradient $-\nabla T$ along $\mathbf{j}$. If one now measures the voltage

---

[1]In our notation, a positive spin current is defined as the propagation direction of $|\uparrow\rangle$ particles.
[2]Please note that this chapter assumes a charge transport carried by electrons.

drop along the sample, a thermal voltage due to the charge Seebeck effect will be visible (cf. Sec. 4.1.1). The temperature difference along the film additionally induces a spin current $\mathbf{j}_s^{SN}$ due to the spin Nernst effect. That spin current propagates in the direction of $\mathbf{n}$ with a spin polarization $\mathbf{s} \parallel \mathbf{t}$ [cf. Fig. 4.3(a)]. In a free standing film, this leads to a spin accumulation, comparable to the charge accumulation in the conventional (charge) Hall effect. In equilibrium, a spin current back flow $\mathbf{j}_s^b = -\mathbf{j}_s^{SN}$ will arise in steady state, compensating the initial spin current $\mathbf{j}_s^{SN}$. $\mathbf{j}_s^b$ will then be converted into a charge current
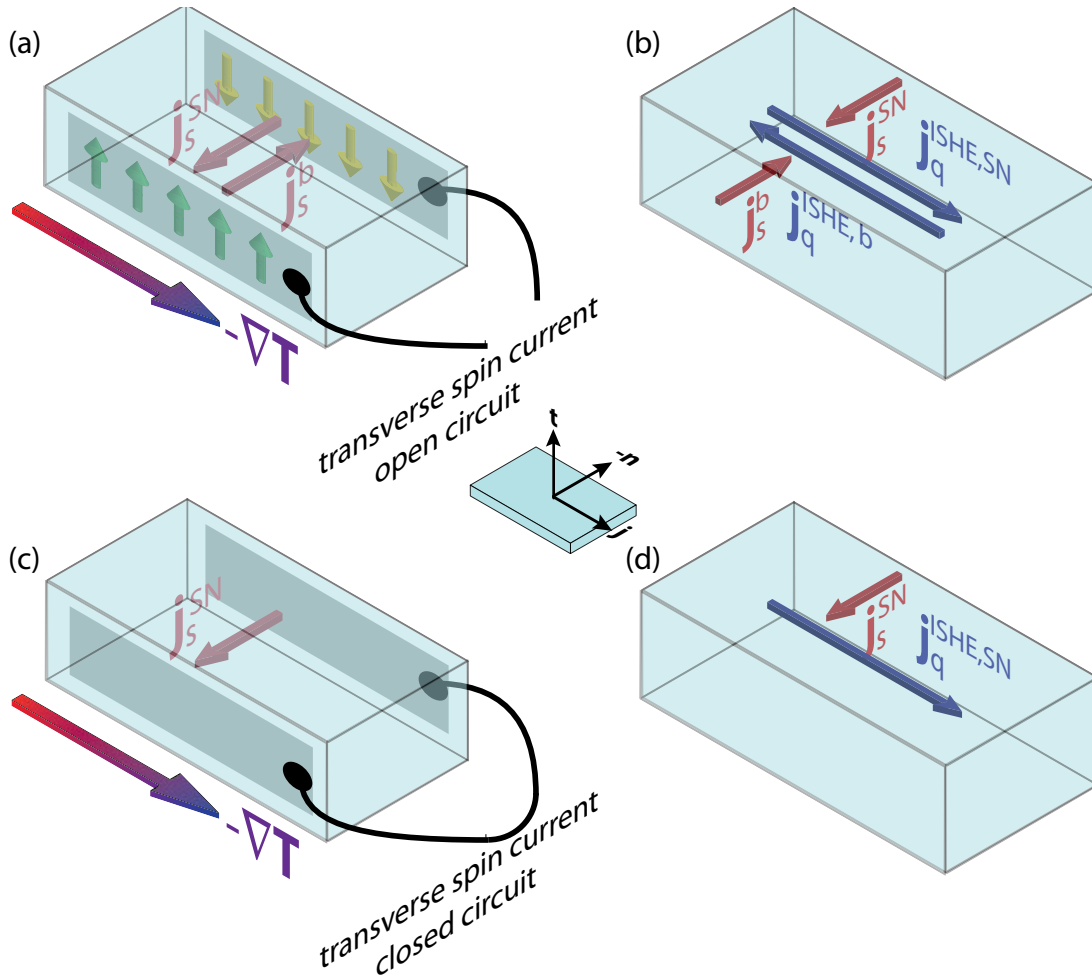

Figure 4.3: Concept of the spin Nernst magneto-thermopower (SNMTP): **(a)**: A temperature gradient ∇T applied along $-\mathbf{j}$ evokes a spin current $\mathbf{j}_s^{SN}$ along $\mathbf{n}$ via the SNE. Therefore, a gradient of the spin chemical potential will build up along $-\mathbf{n}$. For *transverse spin current open circuit boundary conditions* depicted in **(a)**, a spin current back flow $\mathbf{j}_s^b$ propagating opposite to the initial spin current $\mathbf{j}_s^{SN}$ is generated. **(b)** Both spin currents $\mathbf{j}_s^{SN}$ and $\mathbf{j}_s^b$ give rise to charge current contributions $\mathbf{j}_q^{ISHE,SN}$ and $\mathbf{j}_q^{ISHE,b}$ via the ISHE, which are of the same magnitude but opposite in sign. **(c)** If one short circuits the boundaries along $\mathbf{n}$ for spin current flow, no spin chemical potential builds up and thus the generation of $\mathbf{j}_s^b$ is suppressed. We call this the *transverse spin current closed circuit boundary condition.* **(d)** The absence of $\mathbf{j}_s^b$ also leads to a suppression of the charge current contribution stemming from $\mathbf{j}_s^b$.

$\mathbf{j}_{q}^{\mathrm{ISHE,b}} = \theta_{\mathrm{SH}} \left(\frac{2e}{\hbar} \right) \left(\mathbf{s} \times \mathbf{j}_{s}^{b} \right)$ parallel to ∇T via the inverse spin Hall effect (ISHE) [17]. In the same fashion, $\mathbf{j}_{s}^{\mathrm{SN}}$ leads to a charge current contribution along $-\mathbf{j}$ via the ISHE, which we can formulate as $\mathbf{j}_{q}^{\mathrm{ISHE,SN}} = \theta_{\mathrm{SH}} \left(\frac{2e}{\hbar} \right) \left(\mathbf{s} \times \mathbf{j}_{s}^{\mathrm{SN}} \right)$ [see Fig. 4.3(b)]. However, the latter charge currents are of equal magnitude but opposite in sign, $\mathbf{j}_{q}^{\mathrm{ISHE,SN}} = -\mathbf{j}_{q}^{\mathrm{ISHE,b}}$, such that they also cancel. There thus is no net charge current, viz. no SNMTP, in this case. We call this case the *transverse spin current open circuit boundary condition.*

If we now assume a spin current short between both sides of the sample along $\mathbf{n}$ [cf. Fig. 4.3(c)], the spin chemical potential built up along $\mathbf{n}$ will be removed and thus, the spin current back flow $\mathbf{j}_{s}^{b}$ anti-parallel to $\mathbf{j}_{s}^{\mathrm{SN}}$ will be suppressed. We refer to this as the *transverse spin current closed circuit boundary condition.* In this case, the conversion of $\mathbf{j}_{s}^{b}$ into a charge current will also be suppressed. Thus, merely $\mathbf{j}_{s}^{\mathrm{SN}}$ will contribute to the charge current flow along $\mathbf{j}$ via the ISHE [see Fig. 4.3(d)].

Taken together, the combination of the spin Nernst and the inverse spin Hall effect induces a thermopower contribution along the temperature gradient direction. The magnitude of this additional thermopower depends on the transverse spin current boundary conditions. The SNMTP thus can be detected if these boundary conditions can be modulated in situ, in one and the same sample. In our experiments, we use the spin transfer torque (STT) at a ferromagnetic insulator (FMI, here: YIG)/N (here: Pt) interface to controllably go back and forth between these two different boundary conditions. This concept is in close analogy to the spin Hall magnetoresistance (cf. Sec. 2.1.5) [15, 44–46, 96]. We manipulate the spin angular momentum exchange between $\mathbf{j}_{s}^{\mathrm{SN}}$ in the N layer and the magnetization $\mathbf{M}$ of the FMI via spin transfer torque (cf. Sec. 2.1.4) by controlling the orientation of $\mathbf{M}$. As this effect is based on the thermal generation of spin currents by the SNE, we refer to this as the *spin Nernst magneto-thermopower* (SNMTP).

4.1.4 Theory of the spin Nernst magneto-thermopower

The gedankenexperiment given above introduced the SNMTP in a simple picture. For quantitative modeling it is necessary to again invoke the diffusive nature of transport as well as spin dissipation in the metallic film. Using spin diffusion theory [169] and quantum mechanical boundary conditions in terms of the spin-mixing interface conductance $G_{\uparrow\downarrow}$ [27, 88, 126], we develop a theoretical framework to describe the SNMTP in FMI/N bilayers. This concept based on theoretical calculations performed by Yan-Ting Chen can be considered as a generalization of the spin Hall magnetoresistance [15, 41, 43–46, 96] introduced in Sec. 2.1.6. We want to note that, like in Sec. 2.1.6, spin currents are written in units of charge currents ($[j_{s}] = A/m^{2}$) in our theoretical calculations.

We consider a FMI/N bilayer as shown in Fig. 4.4, and calculate the spin accumulation

stemming from a thermally driven spin current via the spin Nernst effect. In analogy to Eq. (2.5), the spin current density in the non-relativistic limit is given by

$$\mathbf{j}_s = qn\frac{<\mathbf{v}\times\Sigma+\Sigma\times\mathbf{v}>}{2} = (\mathbf{j}_{s,j},\mathbf{j}_{s,t},\mathbf{j}_{s,n})^T = \left(\mathbf{j}_s^j,\mathbf{j}_s^t,\mathbf{j}_s^n\right). \tag{4.5}$$

$\mathbf{j}_s$ is a second-order tensor (in units of charge current density $\mathbf{j}_q = qn<\mathbf{v}>$), where q is the particle's charge, n is the density of the particles, $\mathbf{v}$ is the velocity operator, Σ is the spin operator represented by Pauli spin matrices, and $<...>$ denotes the mathematical expectation value. The row vectors $\mathbf{j}_{s,i}$ represent spin currents with a spin polarization pointing along the $\mathbf{i}$ direction, while the column vectors $\mathbf{j}_s^k$ denote the spin current densities with polarization $\mathbf{s}$ propagating along the $\mathbf{k}$ direction. We define the heat current $\mathbf{j}_h = n<(\epsilon-\epsilon_F)\mathbf{v}>$ as the energy current density. Here, ϵ stands for the energy of the particle, and ϵ_F represents the Fermi energy. The relation between thermodynamic driving forces and currents can be summarized by [15, 169]

$$\begin{pmatrix}\mathbf{j}_q\\\mathbf{j}_h\\\mathbf{j}_{s,j}\\\mathbf{j}_{s,t}\\\mathbf{j}_{s,n}\end{pmatrix} = \sigma_N \begin{pmatrix} 1 & ST & \theta_{SH}\mathbf{j}\times & \theta_{SH}\mathbf{t}\times & \theta_{SH}\mathbf{n}\times \\ ST & L_0T^2 & ST\theta_{SN}\mathbf{j}\times & ST\theta_{SN}\mathbf{t}\times & ST\theta_{SN}\mathbf{n}\times \\ \theta_{SH}\mathbf{j}\times & ST\theta_{SN}\mathbf{j}\times & 1 & 0 & 0 \\ \theta_{SH}\mathbf{t}\times & ST\theta_{SN}\mathbf{t}\times & 0 & 1 & 0 \\ \theta_{SH}\mathbf{n}\times & ST\theta_{SN}\mathbf{n}\times & 0 & 0 & 1 \end{pmatrix} \begin{pmatrix} -\nabla\mu_0/q \\ \nabla T/T \\ -\nabla\mu_{sj}/(2q) \\ -\nabla\mu_{st}/(2q) \\ -\nabla\mu_{sn}/(2q) \end{pmatrix}. \tag{4.6}$$

Equation (4.6) reflects Onsagers reciprocity [170, 171] by the symmetry of the response matrix. Furthermore, we use $\boldsymbol{\mu}_s = (\mu_{sj},\mu_{st},\mu_{sn})^T - \mu_0\mathbf{1}$ for the spin accumulation, i.e. the spin-dependent chemical potential relative to the charge chemical potential μ_0, σ_N for the electric conductivity, S for the Seebeck coefficient, $L_0 = (\pi^2/3)(k_B/e)^2$ for the Lorenz constant with the Boltzmann constant k_B, and $\theta_{SH}(\theta_{SN})$ for the spin Hall (Nernst) angle. We additionally define $\mathbf{j}_{q,0} = \sigma_N S\nabla T$ for the charge current contribution arising from the Seebeck effect. Equation 4.6 is a thermoelectric generalization of Eq. (2.6). In Eq. (4.6), the lower non-diagonal elements generate spin currents in the presence of an applied electric field (thermal gradient), i.e. these matrix elements represent the direct spin Hall
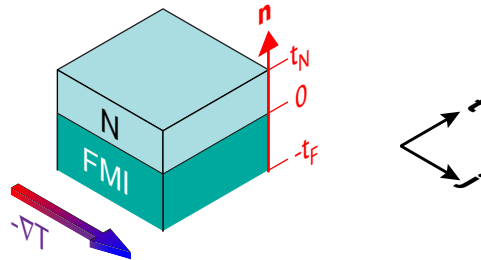

Figure 4.4: Definition of the geometry for SNMTP calculations.

(Nernst) effect. On the other hand, elements above the diagonal provide a connection between gradients of the spin accumulations and the charge (heat) current density, i.e. the inverse spin Hall (Nernst) effects. To study the spin Nernst effect, we focus on the spin current generated by an external thermal gradient. Therefore, we choose the temperature gradient in the $\mathbf{j}$ direction $\nabla T = \mathbf{j}\partial_j T$ for the driving force. Additionally, we assume an open spin current circuit configuration, such that the output can be formulated as a thermal voltage expressed in terms of an electric field $\mathbf{E}_{\text{th}}$.

The spin accumulation $\boldsymbol{\mu}_{\text{s}}$ is given by the spin-diffusion equation in N,

$$\nabla^2 \boldsymbol{\mu}_{\text{s}} = \frac{\boldsymbol{\mu}_{\text{s}}}{\lambda^2}. \tag{4.7}$$

As already introduced in Sec. 2.1.3, the spin-diffusion length $\lambda = \sqrt{D\tau_{\text{sf}}}$ can be expressed in terms of the charge diffusion constant D and the spin-flip relaxation time τ_{sf} [172]. For N films with thickness t_{N} (cf. Fig. 4.4), the general solution of Eq. (4.7) is given by

$$\boldsymbol{\mu}_{\text{s}}(z) = \mathbf{A}e^{-n/\lambda} + \mathbf{B}e^{n/\lambda}. \tag{4.8}$$

In this context, $\mathbf{A}$ and $\mathbf{B}$ represent constant column vectors that are determined by the boundary conditions at the interfaces. The spin current in N is a sum of diffusion and spin Hall drift contributions, cf. Eq. (4.6). For simplicity, we assume the FMI/N bilayer depicted in Fig. 4.4 to be homogeneous in the $(\mathbf{j}, \mathbf{t})$ plane. This allows us to focus on the spin current density flowing in the $\mathbf{n}$ direction, given by

$$\mathbf{j}_{\text{s}}^{\text{n}}(n) = -\frac{\sigma_{\text{N}}}{2q}\partial_n \boldsymbol{\mu}_{\text{s}} - j_{\text{s0}}^{\text{SN}}\mathbf{t}, . \tag{4.9}$$

We here define $j_{\text{s0}}^{\text{SN}} = \theta_{\text{SN}}\sigma_{\text{N}}S\partial_j T = \theta_{\text{SN}}j_{\text{q,0}}$ for the bare spin Nernst current. This is the spin current generated directly by the action of the SNE. $\mathbf{j}_{\text{s}}^{\text{n}}(n)$ has to be continuous at the interfaces $n = t_{\text{N}}$ and $n = 0$. The spin current at the N/vacuum ($n = t_{\text{N}}$) interface vanishes, $\mathbf{j}_{\text{s}}(t_{\text{N}}) = 0$. On the other hand, the spin current density $\mathbf{j}_{\text{s}}^{\text{(F)}}$ at the FMI/N interface is governed by the spin accumulation and the spin-mixing interface conductance: [27, 88]

$$q\mathbf{j}_{\text{s}}^{\text{(F)}}(\mathbf{m}) = G_{\text{r}}\mathbf{m} \times (\mathbf{m} \times \boldsymbol{\mu}_{\text{s}}) + G_{\text{i}}(\mathbf{m} \times \boldsymbol{\mu}_{\text{s}}). \tag{4.10}$$

We here use $\mathbf{m} = (m_j, m_t, m_n)^T$ parametrizing a unit vector pointing along the magnetization direction. In accordance to Sec. 2.1.4, $G_{\uparrow\downarrow} = G_r + iG_i$ represents the complex spin-mixing interface conductance per unit area. The sign of Eq. (4.10) defines the direction of the spin current $\mathbf{j}_{\text{s}}^{\text{(F)}}$ and in this context, a positive current corresponds to up spins flowing from the FMI towards N. Taking advantage of these boundary conditions,

we calculate $\mathbf{A}$ and $\mathbf{B}$ from Eq. (4.7). In a next step, we calculate the spin accumulation $\boldsymbol{\mu}_\mathrm{s}(n)$ from $\mathbf{A}$ and $\mathbf{B}$, resulting in

$$\boldsymbol{\mu}_\mathrm{s}(n) = -\mathbf{t}\mu_s^0 \frac{\sinh\frac{2n-t_\mathrm{N}}{2\lambda}}{\sinh\frac{t_\mathrm{N}}{2\lambda}} + \mathbf{j}_\mathrm{s}^{(\mathrm{F})}(\mathbf{m})\frac{2q\lambda}{\sigma_\mathrm{N}}\frac{\cosh\frac{n-t_\mathrm{N}}{\lambda}}{\sinh\frac{t_\mathrm{N}}{\lambda}}. \tag{4.11}$$

The abbreviation $\mu_s^0 = (2q\lambda/\sigma_\mathrm{N})j_{s0}^{\mathrm{SN}}\tanh(t_\mathrm{N}/2\lambda)$ represents the spin accumulation at the interface in the absence of spin transfer, i.e., when $G_{\uparrow\downarrow} = 0$. Carrying out the calculations in analogy to Sec. 2.1.6 and Ref. [15], we determine the spin accumulation

$$\begin{aligned} \frac{\boldsymbol{\mu}_\mathrm{s}(n)}{\mu_s^0} &= -\mathbf{t}\frac{\sinh\frac{2n-t_\mathrm{N}}{2\lambda}}{\sinh\frac{t_\mathrm{N}}{2\lambda}} \\ &+ [\mathbf{m}\times(\mathbf{m}\times\mathbf{t})\mathrm{Re} + (\mathbf{m}\times\mathbf{t})\mathrm{Im}]\frac{2\lambda G_{\uparrow\downarrow}}{\sigma_\mathrm{N}+2\lambda G_{\uparrow\downarrow}\coth\frac{t_\mathrm{N}}{\lambda}}\frac{\cosh\frac{n-t_\mathrm{N}}{\lambda}}{\sinh\frac{t_\mathrm{N}}{\lambda}} \end{aligned} \tag{4.12}$$

and the spin current in the N

$$\begin{aligned} \frac{\mathbf{j}_\mathrm{s}^n(n)}{j_{s0}^{\mathrm{SN}}} &= \mathbf{t}\frac{\cosh\frac{2n-t_\mathrm{N}}{2\lambda} - \cosh\frac{t_\mathrm{N}}{2\lambda}}{\cosh\frac{t_\mathrm{N}}{2\lambda}} \\ &- [\mathbf{m}\times(\mathbf{m}\times\mathbf{t})\mathrm{Re} + (\mathbf{m}\times\mathbf{t})\mathrm{Im}]\frac{2\lambda G_{\uparrow\downarrow}\tanh\frac{t_\mathrm{N}}{2\lambda}}{\sigma_\mathrm{N}+2\lambda G_{\uparrow\downarrow}\coth\frac{t_\mathrm{N}}{\lambda}}\frac{\sinh\frac{n-t_\mathrm{N}}{\lambda}}{\sinh\frac{t_\mathrm{N}}{\lambda}}. \end{aligned} \tag{4.13}$$

In our geometry, the action of the inverse spin Hall effect leads to a charge current in the $(\mathbf{j},\mathbf{t})$ plane. To be more specific, the total longitudinal (along $\mathbf{j}$) and transverse (along $\mathbf{t}$) charge currents read

$$\frac{j_{\mathrm{q,long}}(n)}{j_{\mathrm{q,0}}} = 1 + \theta_\mathrm{SH}\theta_\mathrm{SN}\left[\frac{\cosh\frac{2n-t_\mathrm{N}}{2\lambda}}{\cosh\frac{t_\mathrm{N}}{2\lambda}} + (1-m_t^2)\mathrm{Re}\frac{2\lambda G_{\uparrow\downarrow}\tanh\frac{t_\mathrm{N}}{2\lambda}}{\sigma_\mathrm{N}+2\lambda G_{\uparrow\downarrow}\coth\frac{t_\mathrm{N}}{\lambda}}\frac{\sinh\frac{n-t_\mathrm{N}}{\lambda}}{\sinh\frac{t_\mathrm{N}}{\lambda}}\right] \tag{4.14}$$

and

$$\frac{j_{\mathrm{q,trans}}(n)}{j_{\mathrm{q,0}}} = \theta_\mathrm{SH}\theta_\mathrm{SN}(m_j m_t\mathrm{Re} - m_n\mathrm{Im})\frac{2\lambda G_{\uparrow\downarrow}\tanh\frac{t_\mathrm{N}}{2\lambda}}{\sigma_\mathrm{N}+2\lambda G_{\uparrow\downarrow}\coth\frac{t_\mathrm{N}}{\lambda}}\frac{\sinh\frac{n-t_\mathrm{N}}{\lambda}}{\sinh\frac{t_\mathrm{N}}{\lambda}}. \tag{4.15}$$

In our experiments, we detect (thermal) voltages along $\mathbf{j}$ and $\mathbf{t}$. These voltages can be expressed as an electric field $\mathbf{E}_\mathrm{th} = E_\mathrm{th,j}\mathbf{j} + E_\mathrm{th,t}\mathbf{t}$ compensating $j_\mathrm{q,long}$ and $j_\mathrm{q,trans}$ in steady state:

$$E_\mathrm{th,j} = -\left[1 + \theta_\mathrm{SH}\theta_\mathrm{SN}\left[\frac{\cosh\frac{2n-t_\mathrm{N}}{2\lambda}}{\cosh\frac{t_\mathrm{N}}{2\lambda}} + (1-m_t^2)\mathrm{Re}\frac{2\lambda G_{\uparrow\downarrow}\tanh\frac{t_\mathrm{N}}{2\lambda}}{\sigma_\mathrm{N}+2\lambda G_{\uparrow\downarrow}\coth\frac{t_\mathrm{N}}{\lambda}}\frac{\sinh\frac{n-t_\mathrm{N}}{\lambda}}{\sinh\frac{t_\mathrm{N}}{\lambda}}\right]\right]S\partial_j T \tag{4.16}$$

$$E_{\text{th,t}} = -\theta_{\text{SH}}\theta_{\text{SN}}(m_j m_t \text{Re} - m_n \text{Im})\frac{2\lambda G_{\uparrow\downarrow}\tanh\frac{t_{\text{N}}}{2\lambda}}{\sigma_{\text{N}} + 2\lambda G_{\uparrow\downarrow}\coth\frac{t_{\text{N}}}{\lambda}}\frac{\sinh\frac{n-t_{\text{N}}}{\lambda}}{\sinh\frac{t_{\text{N}}}{\lambda}}S\partial_j T. \qquad (4.17)$$

Thus, by averaging the electric field over the total film thickness along **n** in analogy to Eq. (2.22) and Eq. (2.24) we obtain

$$\overline{E_{\text{th,j}}} = -[S + \Delta S_0 + \Delta S_1(1 - m_t^2)]\partial_j T \qquad (4.18)$$

$$\overline{E_{\text{th,t}}} = [-\Delta S_1 m_j m_t + \Delta S_2 m_n]\partial_j T, \qquad (4.19)$$

using

$$\Delta S_0 = S\theta_{\text{SH}}\theta_{\text{SN}}\frac{2\lambda}{t_{\text{N}}}\tanh\frac{t_{\text{N}}}{2\lambda} \qquad (4.20)$$

$$\Delta S_1 = -S\theta_{\text{SH}}\theta_{\text{SN}}\frac{\lambda}{t_{\text{N}}}\text{Re}\frac{2\lambda G_{\uparrow\downarrow}\tanh^2\frac{t_{\text{N}}}{2\lambda}}{\sigma_{\text{N}} + 2\lambda G_{\uparrow\downarrow}\coth\frac{t_{\text{N}}}{\lambda}} \qquad (4.21)$$

$$\Delta S_2 = -S\theta_{\text{SH}}\theta_{\text{SN}}\frac{\lambda}{t_{\text{N}}}\text{Im}\frac{2\lambda G_{\uparrow\downarrow}\tanh^2\frac{t_{\text{N}}}{2\lambda}}{\sigma_{\text{N}} + 2\lambda G_{\uparrow\downarrow}\coth\frac{t_{\text{N}}}{\lambda}}. \qquad (4.22)$$

The voltages detected in our experiments are linked to the electric field components in Eq. (4.18) and Eq. (4.19) via $V_{\text{thermal,long}} = \int \overline{E_{\text{th,j}}}(\mathbf{j})d\mathbf{j}$ and $V_{\text{thermal,trans}} = \int \overline{E_{\text{th,t}}}(\mathbf{t})d\mathbf{t}$. Thus, the spin current generated by the SNE generates an additional contribution ΔS_1 to the Seebeck coefficient. For longitudinal thermopower measurements, we therefore expect an magnetization orientation dependent contribution to S and thus to the thermopower voltage $V_{\text{thermal,long}}$ proportional to $\Delta S_1(1 - m_t^2)$. This is caused by the spin transport across the FMI/N interface described mainly by G_r. Comparing Eq. (4.18) with the longitudinal SMR [cf. Eq. (2.21)], we find the same magnetization orientation dependence proportional to m_t^2. We thus expect that the SNMTP has a very similar fingerprint as the SMR, with modulations in $V_{\text{thermal,long}}$ when the magnetization of the FMI (the YIG) is rotated in planes spanned by **j** and **t** (ip) as well as in planes spanned by **n** and **t** (oopj), while we expect no modulations in $V_{\text{thermal,long}}$ when the magnetization of the FMI is rotated in oopt configuration with the magnetization in (**j**,**n**) plane. Additionally, the prefactor ΔS_1 shows a very close analogy to Eq. (2.23). Thus, like the SMR, the SNMTP characteristically depends on the spin transport parameters in N. However, the SMR equation [Eq. (2.23)] is proportional to θ_{SH}^2, while Eq. (4.21) is proportional to $\theta_{\text{SH}}\theta_{\text{SN}}$. Therefore, the SNMTP can be used to quantify the concept of the spin Nernst angle experimentally.

According to Eq. (4.19), one also expects a magnetization orientation dependent modulation in the transverse thermopower voltage $V_{\text{thermal,trans}}$. We expect a $\sin\alpha\cos\alpha$ dependence when the magnetization of the FMI is rotated in planes spanned by **j** and **t** (ip). On the other hand, the term proportional to ΔS_2 (caused mainly by G_i) is expected to

contribute only when there is a magnetization component normal to the film plane. This can be achieved for magnetization rotations in the planes spanned by **j** and **n** (oopt) and **t** and **n** (oopj). The second part of Eq. (4.19) can be understood as an anomalous Nernst effect like contribution caused by the spin Nernst effect. In analogy to the spin Hall anomalous Hall effect discussed in Ch. 3, we refer to this phenomenon as the *spin Nernst anomalous Nernst effect.*

4.2 Experimental setup

Caloritronic experiments require a precise control of the (local) sample temperature. In the following section, we introduce the development of the experimental setup and the sample layout to control the environmental temperature and to minimize thermal noise.

4.2.1 Dipstick for thermopower experiments

In Sec. 2.2.2, we introduced a measurement setup for magnetotransport experiments in a
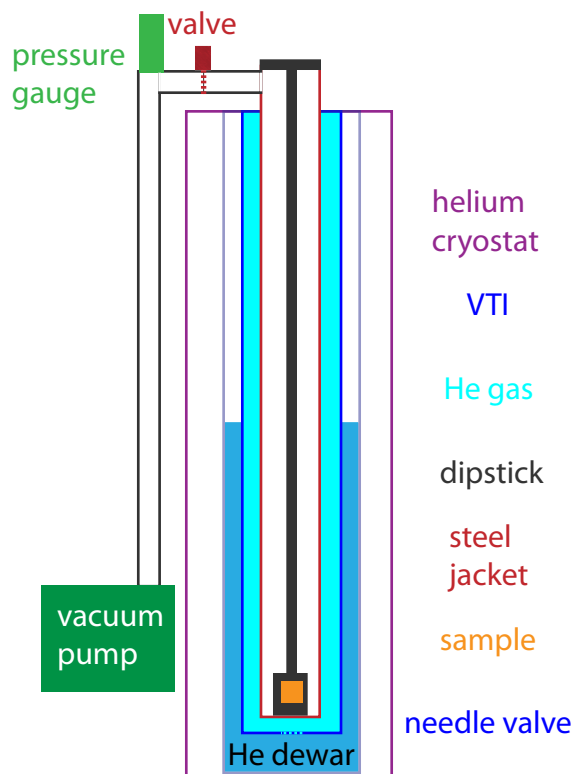
Figure 4.5: Experimental setup for caloritronic experiments in a helium cryostat. Components see legend.

magnet cryostat. Using a magnet cryostat generally implies that the sample is mounted to a dipstick that is placed in the variable temperature insert (VTI) of the cryostat. The VTI is filled with Helium gas that provides the cooling of the dipstick, while the dipstick's temperature is actively controlled by an electric heater combined with a temperature sensor. Caloritronic experiments, however, require that the measurements are performed in the absence of an exchange gas. This is necessary to optimize the control of the temperature gradient direction, and especially to avoid out-of-plane components of the temperature gradient [120]. Therefore, we developed a new dipstick design that enables magnetotransport measurements in high vacuum. In this approach, the whole sample space

from the bottom of the dipstick up to the entrance of the cryostat's VTI is enclosed with a steel jacket that can be connected to a vacuum pump (cf. Fig. 4.5). In this way, the pressure inside the jacket can straightforwardly be reduced to 10^{-6} mbar. The vacuum pump was permanently connected to the dipstick during the caloritronic experiments to achieve a constant pressure during the measurements. A detailed description of the dipstick design can be found in Sec. 6.3.

4.2.2 Sample and sample layout

The sample used for SNE experiments is a yttrium iron garnet (YIG)/Pt thin film hybrid structure. We epitaxially grew a 40 nm thick YIG film on a 5×5 mm sized and 500μm thick, single crystalline (111) - oriented GGG substrate via pulsed laser deposition with the parameters used in Sec. 2.2.2. Following the YIG growth, 4.1 nm of polycrystalline Pt were deposited *in situ* on top of the YIG film via electron beam evaporation at room temperature. High-resolution X-ray diffraction (HR-XRD) measurements confirmed the polycrystallinity of the Pt thin film and revealed no secondary phases. The thicknesses of the YIG and Pt layers were determined by high-resolution X-ray reflectometry (HR-XRR) to $t_{\mathrm{F}} = (40 \pm 2)$ nm and $t_{\mathrm{N}} = (4.1 \pm 0.2)$ nm, respectively. As we pointed out in Sec. 4.1.4, the SNMTP effect crucially depends on the spin transport in N, and the maximum signal is expected for t_{N} close to twice the spin diffusion length λ. With this, we expect the sample with $t_{\mathrm{N}} = 4.1$ nm to show a significant SNMTP signal.

For caloritronic experiments, the control of temperature is of crucial importance. In the present work, we generate spin currents by applying a temperature gradient. The amount of spin current generated via the spin Nernst effect (cf. Sec. 4.1.2) will be (in linear response) proportional to the temperature difference along the sample. Thus, the larger the temperature differences can be made, the easier the detection of the spin current will be. We therefore developed a new sample design where a resistive heater is located directly on the sample in close vicinity to the Hall bar. To achieve this, the resistive heater (consisting of an additional thin strip next to one end of the Hall bar) and the Hall bar itself are patterned to the YIG/Pt bilayer in a single step [cf. Fig. 4.6 (a)]. By using this on chip heater, one avoids heat resistances (Kapitza resistances) at material junctures, e.g. between a heater placed on the sample holder and the substrate. Secondly, we can control the direction of ∇T to be along and not perpendicular the Hall bar. This is of great importance to avoid parasitic effects, e.g. the anomalous Nernst effect [60,173–175]. We will call this heating strip the on chip heater (OCH) in the following.

In detail, the sample is patterned to a Hall bar structure with an additional strip along the transverse **t** direction via photo-lithography and argon ion beam milling. A sketch of
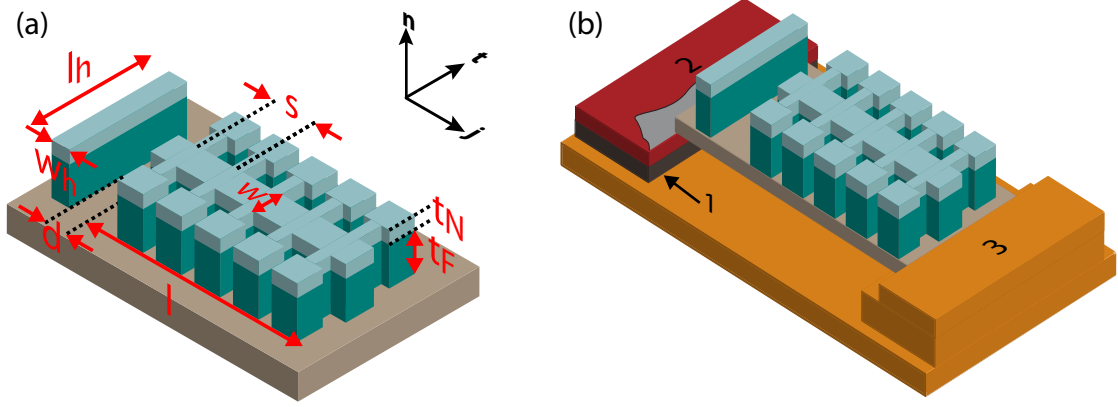
Figure 4.6: (a) Sample layout for SNMTP experiments. A YIG($t_F = 40\,\text{nm}$)/Pt($t_N = 4.1\,\text{nm}$) sample is patterned into a Hall bar geometry (width $w = 250\,\mu\text{m}$, length $l = 3150\,\mu\text{m}$). On the top end of the Hall bar, an additional heater strip (OCH, width $w_h = 250\,\mu\text{m}$, length $l_h = 1175\,\mu\text{m}$) is patterned along **t** with distance $d = 250\,\mu\text{m}$ to the Hall bar. **(b)** Experimental setup: The sample is mounted on a copper based sample holder. The OCH side of the sample is connected to a stack consisting of a vespel block providing thermal isolation ("1") and an additional resistive heater ("2"). The Hall bar side of the sample is in thermal contact with the sample holder, mediated by a massive copper block ("3"). By applying an electric power P_{heater} to the OCH, one end of the Hall bar is heated, while the other side is connected to the heat bath provided by the sample holder.

the sample geometry is shown in Fig. 4.6 (a). The Hall bar has a width of $w = 250\,\mu\text{m}$ and a length of $l = 3150\,\mu\text{m}$, the distance between two adjacent transverse contact pairs is $s = 625\,\mu\text{m}$. The heating strip along **t** is $w_h = 250\,\mu\text{m}$ wide and $l_h = 1175\,\mu\text{m}$ long, the distance between the Hall bar and the heating strip is $d = 250\,\mu\text{m}$. The sample is mounted to a sample holder made of copper (Cu) [cf. sketch in Fig. 4.6 (b)] using GE 7031 thermally conductive varnish. The sample holder consists of a massive Cu block (labeled as number "3" in the sketch) on the Hall bar side acting as a heat sink. The OCH side of the sample is connected to an additional $100\,\Omega$ resistive heater (labeled as number "2", not used in the set of experiments presented here). The $100\,\Omega$ resistor is placed on top of a vespel (a special kind of plastic) block ("1"). Here, we intentionally chose vespel to minimize thermal conductivity between the sample and the sample holder in this direction. All bonding pads at the Hall bar as well as the heater strip are connected to a copper bonding frame with $30\,\mu\text{m}$ thick Al wires via wedge bonding.

4.2.3 Thermopower handling

The copper-based sample holder is mounted at the bottom end of a dipstick that is enclosed by the steel jacket. During our measurements, we evacuate the steel jacket using a Pfeiffer Hi cube 80 eco turbo pump; the pressure within the sample space reached a

minimum of $(5 \pm 1) \times 10^{-6}$ mbar and was kept constant at this value during the experiments.

The dipstick is mounted into the variable temperature insert (VTI) of an Oxford Instruments liquid He flow cryostat with 3D vector magnet (cf. Sec. 6.2). The base temperature of the dipstick was chosen to 220 K[3] and stabilized by a LakeShore LS340 temperature controller. We determined the temperature fluctuations of this heat bath to ± 3 mK after a thermalization time of at least six hours, coinciding with fluctuations in the thermal voltage along the Pt thin film smaller than 10 nV when no temperature gradient is applied. By applying currents of up to 20 mA to the heater strip (OCH) next to the Hall bar via an Agilent B2900A Precision Source Measure Unit, we heat up one side of the sample and thus create a temperature gradient along the Hall bar direction $\mathbf{j}$. We additionally checked our sample for a possible electric connection between the OCH and the Hall bar. The resistance between the OCH and the Hall bar was found to be larger than 10 GΩ.

The temperature profile along the Hall bar is determined by the method of resistive thermometry along two transverse Hall bar contact separated by a distance of $l_1 = 2500\,\mu$m (see Fig. 4.7). Using two Keithley K2400 Source Measure Units, we applied currents of $10\,\mu$A to both sets of transverse contact pads (current along $\mathbf{t}$) at the hot and cold end of the Hall bar. The electric power applied is smaller than 2×10^{-7} W, and we thus expect no noticeable influence of Joule heating. To determine the local temperatures, we first stabilize the sample temperature to 220 K ($P_{\text{heater}} = 0$) and measure $R_{\text{i}}(T)(i = 1, 2)$ at both ends of the Hall bar while sweeping the sample temperature up to 270 K using the temperature control of the dipstick provided by the LS340 [cf. Fig. 4.7(a)]. By setting a slow warm up rate of 6 K/h, we ensure that the dipstick is in thermal equilibrium with the sample and thus T_{dipstick} represents the sample temperature.

The temperature dependent resistance curves, shown in Fig. 4.7(c), are used as calibration curves. In a second step [cf. Fig. 4.7(b)], we again stabilize the sample at the base temperature of 220 K and determine the local transverse resistivities R_1 and R_2 while applying different heating powers up to 286 mW to the OCH. Comparing $R_1(P_{\text{heat}})$ and $R_2(P_{\text{heat}})$ with the calibration curves taken before [cf. Fig. 4.7 (c)] leads to a sensitive temperature profile of the sample with an experimental error of $\Delta T_{\text{local}} \approx 0.1$ K.

As expected, we find a linear dependence of the temperature difference along the Hall bar on the applied heating power, leading to an almost linear scaling between thermopower and applied heater power. Slight deviations from the linearity can be explained by the temperature dependence of the Seebeck coefficient [176]. The results for $\Delta T(P_{\text{heater}})$ are

---

[3]The VTI of the magnet cryostat is designed to operate at temperatures up to 300 K. Since we intend to heat one end of the sample, we chose a temperature distinctly lower than 300 K to avoid a damage of measurement equipment. On the other hand, the temperature dependence of the thermopower in Pt [176] as well as the spin Hall angle in Pt (cf. Sec. 2.4) advocate for temperatures around room temperature.
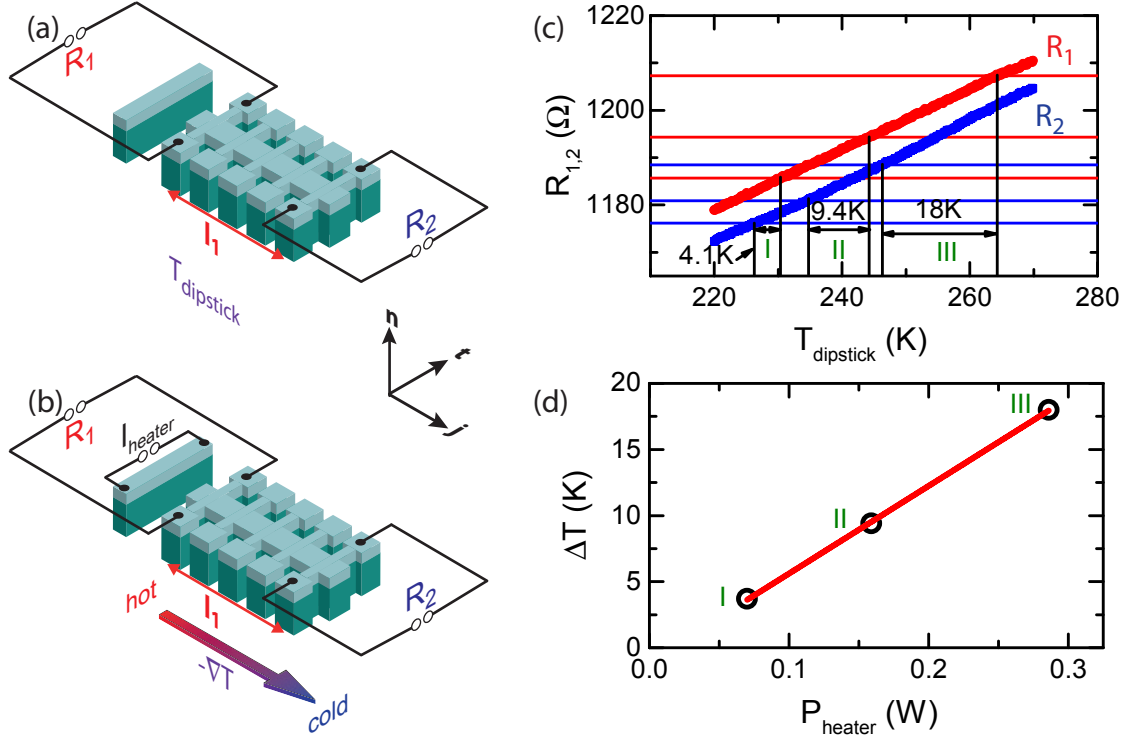
Figure 4.7: (a,b) Concept of the resistive thermometry: In a first step **(a)**, the resistances $R_1(T)$ and $R_2(T)$ along two transverse contact pairs are detected as a function of the sample temperature T, while no power is applied to the heater. Here, the sample temperature is homogeneous and given by the dipstick temperature T_{dipstick}. $R_1(T)$ and $R_2(T)$ serve as calibration curves for the thermometry. Afterwards **(b)**, the dipstick temperature is kept constant ($T_{\mathrm{base}} = 220\,\mathrm{K9}$ while I_{heater} is increased stepwise. R_1 and R_2 are now taken as a function of P_{heater}. Panel **(c)** shows both the calibration curves $R_1(T)$ and $R_2(T)$ and the heater power dependent resistivities (horizontal lines). From those calibration curves, the local temperatures can be calculated as a function of P_{heater}. Here, we show three different heater powers (I) $P_{\mathrm{heater}} = 70\,\mathrm{mW}$, (II) $P_{\mathrm{heater}} = 159\,\mathrm{mW}$ and (III) $P_{\mathrm{heater}} = 286\,\mathrm{mW}$. The extracted temperature differences ΔT along the Hall bar as a function of P_{heater} are shown in **(d)**.

depicted in Fig. 4.7 (d). The maximum generated temperature difference between the contacts separated by the distance l_1 was found to be $18.0\,\mathrm{K}$ for $P_{\mathrm{heater}} = 286\,\mathrm{mW}$.

In Fig. 4.8, we finally show the thermopower voltages taken along the Hall bar direction ($V_{\mathrm{thermal,long}}$) and perpendicular to the Hall bar direction ($V_{\mathrm{thermal,trans}}$) for different, constant heating currents applied to the OCH. For this measurement, no (transverse) charge current was fed to the Hall bar and a magnetic field of $1\,\mathrm{T}$ was applied along **j**. The presence of a magnetic field is not necessary for the determination of the thermoelectric effect. However, by orienting the magnetization of the YIG film, we control the contribution given by the SNMTP in this experiment. We find an increase in the absolute value of $V_{\mathrm{thermal,long}}$ with increasing I_{heater} as one would expect from $V_{\mathrm{therm}} = -S\Delta T$. For the
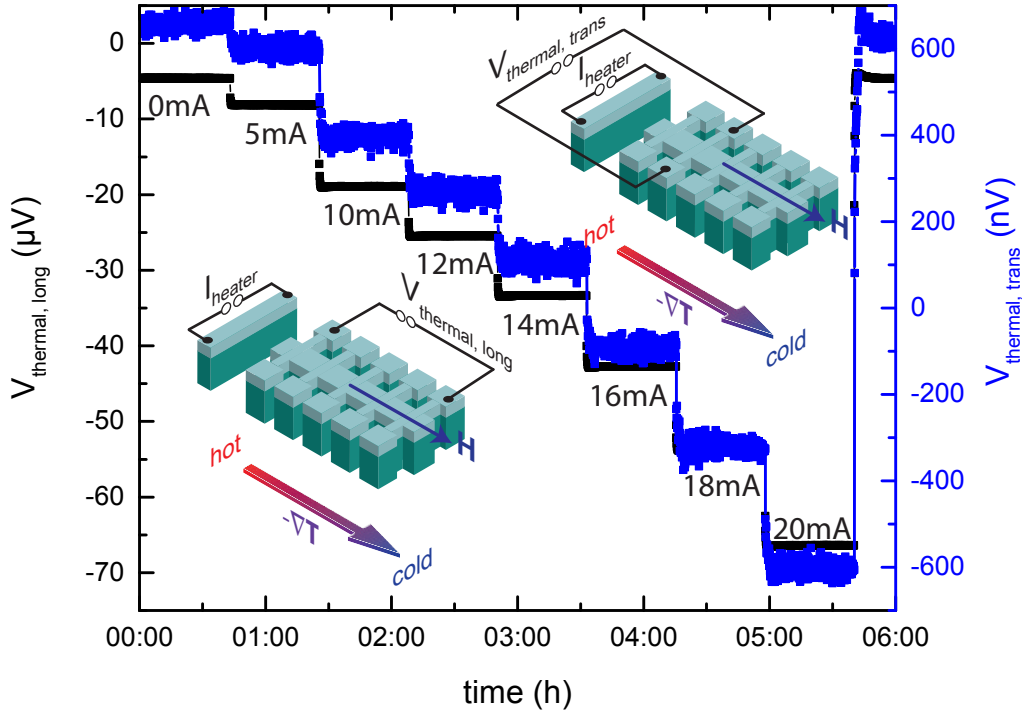
Figure 4.8: Longitudinal (black) and transverse (blue) thermal voltages taken for a stepwise increase of I_{heater} applied to the OCH. $20\,\text{mA}$ correspond to $P_{\text{heater}} = 286\,\text{mW}$.

highest current applied, we extract $S = -3.7\mu\text{V/K}$ using $\Delta T = 18.0\,\text{K}$. With respect to the average sample temperature $\bar{T} = (T_{\text{hot}} - T_{\text{cold}})/2 = 255.4\,\text{K}$ extracted from the resistive thermometry shown above, S is in excellent agreement with the literature value for Pt, $S(260\,\text{K}) = -3.8\mu\text{V/K}$ [176].

However, we can not rule out a small contribution of the longitudinal signal to the transverse thermopower, owing to small fabrication induced misalignments between the contacts, as already mentioned in the discussion of the SMR measurements in Sec. 2.2.2. We therefore also observe thermal voltages of about $2\,\%$ of $V_{\text{thermal,long}}$ along the transverse ($\mathbf{t}$) direction. The presence of $V_{\text{thermal,trans}}$ may also indicate a slight tilt of the OCH with respect to the Hall bar direction, leading to a non-vanishing component of the temperature gradient along $\mathbf{t}$. From Fig. 4.8, we estimate a tilt of the OCH with respect to $\mathbf{t}$ of $\alpha' = 1°$ (see also Fig. 4.11).

4.2.4 Control of the magnetization orientation

In Sec. 4.1.3, we discussed that spin transport stemming from the spin Nernst effect can be detected in FMI/N hybrids via a control of the spin transfer across the interface. For electrically generated spin currents, a magnetization orientation based detection has already successfully been used in the framework of the spin Hall magnetoresistance discussed in

Ch. 2. Here, we take advantage of a similar technique to switch between transverse spin current open and closed circuit conditions (cf. Sec. 4.1.3). To control the magnetization orientation of the YIG layer, we apply external magnetic fields $\mu_0 H_{\text{ext}} \geq 500\,\text{mT}$ using the 3D vector magnet introduced in Sec. 6.2. We intentionally choose $\mu_0 H_{\text{ext}}$ to exceed the saturation field $M_{\text{Sat}}^{\text{YIG}} \approx 170\,\text{mT}$ of the YIG by far, such that the magnetization vector $\mathbf{M}$ of the ferromagnetic layer is always aligned parallel to $\mu_0 H_{\text{ext}}$ in good approximation. Like in the SMR experiments, we rotate the external magnetic field in certain planes with respect to the Hall bar. To keep a constant definition of the rotation planes for in-plane (ip), out of plane perpendicular $\mathbf{j}$ (oopj) and out of plane perpendicular $\mathbf{t}$ (oopt), we again use the rotation geometries introduced in Sec. 2.2.2 and Fig. 2.7.

4.2.5 Constant thermopower for on chip heating

To generate large temperature differences along the Hall bar, we developed an on chip heating method introduced in Sec. 4.2.2. However, this method contains an additional complexity that should be kept in mind during the SNMTP experiments: Since our heating strip consists of the same YIG/Pt hybrid structure as the Hall bar, we observe a SMR - modulation of the heating power $P_{\text{heater}} = R_{\text{heater}} \times I_{\text{heater}}^2$. The conventional SMR of this sample was determined to be $-\Delta\rho_1/\rho_0 = (1.05 \pm 0.10) \times 10^{-3}$ (cf. Sec. 4.3.5). Please note that the heater is oriented with its long side along the $\mathbf{t}$ direction and therefore rotated by 90° with respect to the Hall bar. This has to be taken into account for the discussion of $P_{\text{heater}}(\delta)$ in the different rotation geometries, too: For ip rotations [cf. Fig. 4.9(a)], the modulation of the heater resistance thus is rotated by 90° with respect to the SMR signal of a Hall bar oriented along $\mathbf{j}$. Rotating the magnetic field in the oopj geometry (Hall bar definition) can be interpreted as a rotation in the plane spanned by $\mathbf{n}$ and the long side of the heater (along the applied heater current) and thus this is similar to an oopt rotation in a conventional Hall bar[cf. Fig. 4.9(b)]. Otherwise, for rotating the magnetic field in the oopt geometry (Hall bar definition), the magnetization of the YIG below the heater strip is rotated in an oopj like configuration [cf. Fig. 4.9(c)]. Our experimental data depicted in Fig. 4.9(a) confirms this SMR-like resistance modulation of the OCH.

To avoid a SMR based modulation of the heater power, we use a LabView based closed-loop control to re-modulate the applied heater current and provide a constant heater power of $P_{\text{heater}} = 286\,\text{mW}$ instead of a constant heater current. Therefore, we re-modulate I_{heater} in a SMR like fashion to balance the modulation of R_{heater} (cf. black data points in Fig. 4.9). Using this method, we are able to suppress the SMR modulation of the heater power at least by a factor of 20. Please note that the $\sin^2(\delta)$ signal of R_{heater} depicted in Fig. 4.9 is already reduced by a factor of $\sqrt{2}$ with respect to the original SMR
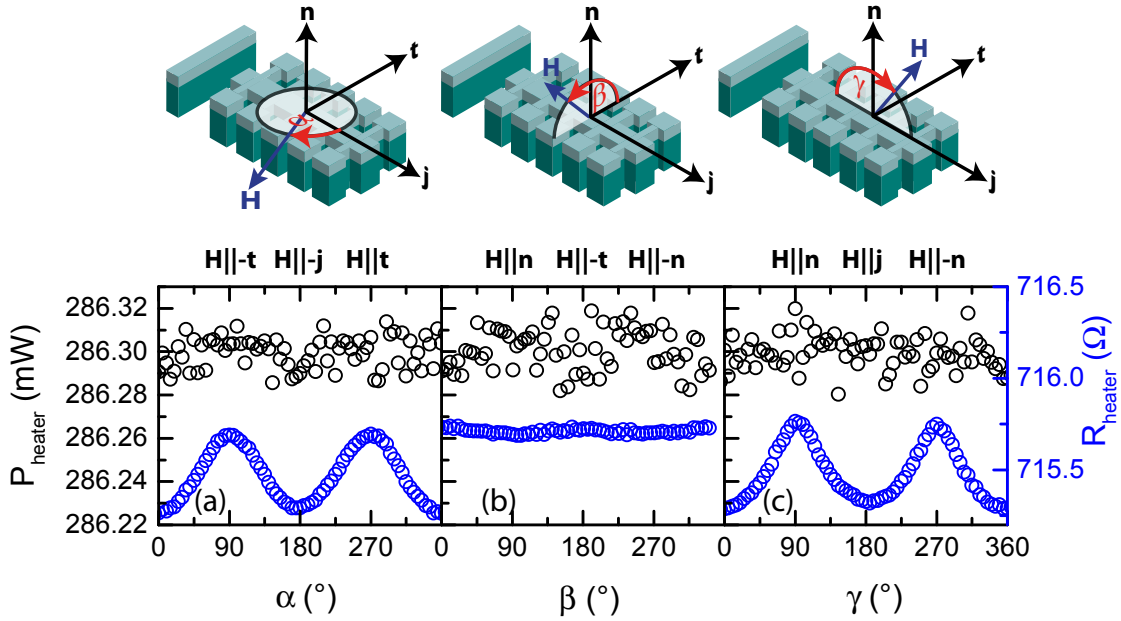
Figure 4.9: Heater power P_{heater} (black symbols) and resistance R_{heater} (blue symbols) as a function of the YIG magnetization orientation in **(a)** ip, **(b)** oopj and **(c)** oopt configuration for $\mu_0 H = 1\,\text{T}$. During this measurement, we modulated the current I_{heater} applied to the OCH to keep the heating power constant.

amplitude due to the regulation of I_{heater}.

4.3 Experimental results

The following section contains the experimental results obtained from our spin Nernst magneto-thermopower measurements. We start with the discussion of a full set of magnetic field rotations for one heater power. A generalization of this fingerprint including the heater power and magnetic field dependence follows in Sec. 4.3.2 and 4.3.3. All SN-MTP measurements shown in this section are obtained using the constant power on chip heating method including the feedback-regulation introduced in Sec. 4.2.5. We (anti-) symmetrized the data with respect to $\delta = 180°$ according to Eq. (2.31) and Eq. (2.32) to dispel the influence of possible thermal drifts of the system during the measurement of a set of ip, oopj and oopt rotations, which approximately takes 8 h.

4.3.1 Fingerprint of the SNMTP

For SNMTP experiments, we remove all current sources from the Hall bar ($I_{\text{q}} = 0$) and thermalize the sample to $T_{\text{base}} = 220\,\text{K}$. To apply a temperature gradient along **j** as a driving force, we bias the OCH with a modulated current with an average value of $\bar{I}_{\text{heater}} = 20\,\text{mA}$, leading to a constant heater power of $P_{\text{heater}} = 286\,\text{mW}$ independent of
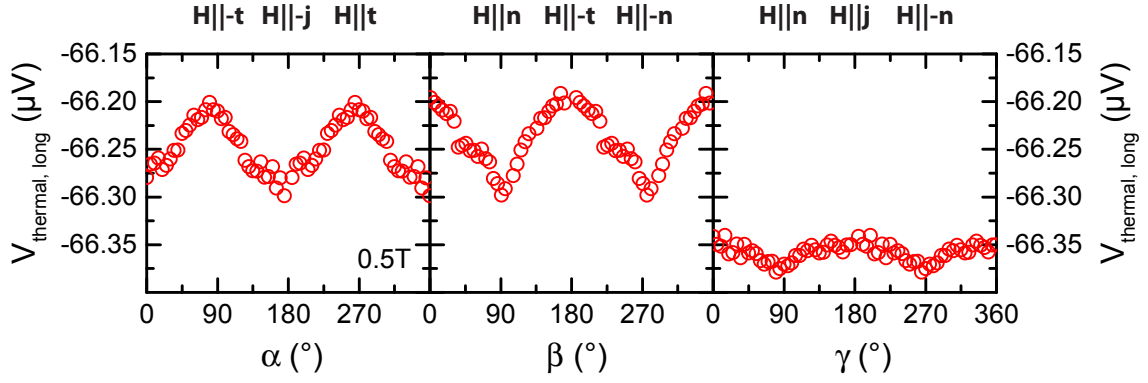
Figure 4.10: Longitudinal spin Nernst magneto-thermopower experiments on a YIG/Pt(4.1 nm) hybrid: A modulated charge current with an average value of $\bar{I}_{\text{heater}} = 20\,\text{mA}$ is applied to the OCH to provide a constant heater power of $286\,\text{mW}$. This generates a temperature difference of $\Delta T = 18\,\text{K}$ along the Hall bar. The longitudinal voltage drop $V_{\text{thermal,long}}$ is detected as a function of the magnetization orientation (see sketches), while an external magnetic field of $0.5\,\text{T}$ is rotated in ip **(a)**, oopj **(b)** and oopt **(c)**.

the magnetic field orientation (cf. Sec. 4.2.5). We rotate a constant external magnetic field $\mu_0 H = 0.5\,\text{T}$ around the sample and detect the longitudinal and transverse thermal voltages using and an Agilent 34420A and a Keithley K2182A nanovoltmeter, respectively. We use a digital filtering of the detected signal and averaged over 100 power line cycles using the internal filtering functions of the nanovoltmeters. Therefore, we are able to reduce the fluctuations of our voltage measurements to around $\pm 5\,\text{nV}$ which is close to the resolution limit given by the thermal stability of the nanovoltmeters.

Figure 4.10 shows the evolution of the longitudinal thermal voltage $V_{\text{thermal,long}}$ as a function of the magnetization orientation while rotating an external magnetic field $\mu_0 H = 0.5\,\text{T}$ in ip (panel a), oopj (panel b) and oopt (panel c) configuration. For the ip data [cf. Fig. 4.10(a)], we find a $\sin^2(\alpha)$ shaped modulation $\Delta V_{\text{thermal}}$ of about $-80\,\text{nV}$ on top of the thermal voltage $V_{\text{thermal,long}} = -66.20\,\mu\text{V}$ given by the thermopower effect. This modulation reaches its minimum for $\mathbf{H} \parallel \mathbf{j}$ and $\mathbf{H} \parallel -\mathbf{j}$, while maxima are obtained for $\mathbf{H} \parallel \mathbf{t}$ and $\mathbf{H} \parallel -\mathbf{t}$.

In oopj rotation geometry [cf. Fig. 4.10(b)], we find a similar, $\cos^2(\beta)$ shaped modulation on top of the thermal voltage $V_{\text{thermal,long}} = -66.20\,\mu\text{V}$ with a modulation amplitude $\Delta V_{\text{thermal,long}} \approx 100\,\text{nV}$ slightly increased compared to the ip rotation. Again, a maximum signal is recorded for $\mathbf{H} \parallel \mathbf{t}$ and $\mathbf{H} \parallel -\mathbf{t}$ and the level in good approximation coincides with the one detected for the ip rotation. For this oopj geometry, the minima are located at $\mathbf{H} \parallel \mathbf{n}$ and $\mathbf{H} \parallel -\mathbf{n}$ and the voltage level for $\mathbf{H} \parallel \mathbf{n}$ almost coincides with the signal detected at $\mathbf{H} \parallel \mathbf{j}$ in ip rotations.

For the oopt rotation [cf. Fig. 4.10(c)], however, $\Delta V_{\text{thermal}}$ reduces to a value smaller than
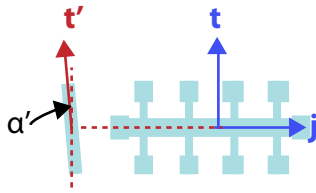
Figure 4.11: Definition of the tilt angle α' between the direction $\mathbf{t}$ and the long side of the on
chip heater (along $\mathbf{t}'$).

25 nV. We also find that the voltage levels for $\mathbf{H} \parallel \mathbf{j}$ and $\mathbf{H} \parallel \mathbf{n}$ do not perfectly coincide
with the levels obtained in ip and oopj rotation. We attribute this to the fact that the
oopt data was obtained prior the oopj and ip measurements. In the oopt data we find
a slight linear thermal drift of about 30 nV between the first ($\gamma = 0°$ for the clockwise
rotation) and the last data point ($\gamma = 0°$ for the counter- clockwise rotation) on the
full 720° data set (not shown here). This drift did not occur in further (oopj and ip)
rotations, indicating that the thermalization of the sample took about 2 h longer than
estimated. This thermal drift, even though it cancels out by symmetrizing the data, gives
an additional offset on $V_{\text{thermal,long}}$, which can be found in Fig. 4.10(c).

Despite the slight thermal instability of the system in oopt, the data set shown in Fig. 4.10
can be understood in terms of the spin Nernst magneto-thermopower: In our geometry,
the temperature gradient along $\mathbf{j}$ induces a spin Nernst spin current along $\mathbf{n}$ with spin
polarization $\mathbf{s} \parallel \mathbf{t}$. Thus, $\mathbf{H} \parallel \mathbf{t}$ and $\mathbf{H} \parallel -\mathbf{t}$ correspond to the spin current open circuit
boundary condition, since a spin transfer towards the YIG is prohibited for $\mathbf{H} \parallel \mathbf{s} \parallel \mathbf{t}$.
On the other hand, both $\mathbf{H} \parallel \pm\mathbf{j}$ and $\mathbf{H} \parallel \pm\mathbf{n}$ correspond to perfect spin current closed
circuit boundary conditions, since they allow for a spin transfer. This is also in excellent
agreement with Eq. (4.18) discussed in Sec. 4.1.4. We have to admit that the finite mod-
ulation $\Delta V_{\text{thermal}}^{\text{oopt}} \leq 25$ nV in the oopt rotation geometry can not be straightforwardly
understood in terms of the SNMTP picture. However, a slight tilt of the direction of
∇T in the sample plane (see Fig. 4.11) could cause a component of ∇T along $\mathbf{t}$. This
would result in additional SNMTP signals for ip and oopt rotations. Estimating the tilt
angle α' from the ratio of the modulation voltages in oopj and oopt, we end up with
$\alpha' = \arcsin\left((25 \pm 5)\,\text{nV}/(80 \pm 5)\,\text{nV}\right) \approx (18 \pm 4)°$. This tilt is at odds with our calcula-
tion of α' from Fig. 4.8 and it is also too large to directly stem from imperfect fabrication
(geometric offset of contact leads). However, we can not exclude an anisotropy of the
thermal conductivity along the sample, which might also result in a ∇T component along
$\mathbf{t}$. This anisotropy is already included to our estimation of α'.

  Now, we turn to the transverse thermopower depicted on Fig. 4.12. For ip rota-
tions [see Fig. 4.12(a)], we find a $\sin(\alpha)\cos(\alpha)$ modulation on top of an offset voltage
$V_{\text{thermal,trans}} \approx 620$ nV. This offset voltage stems from a small superposition of the lon-
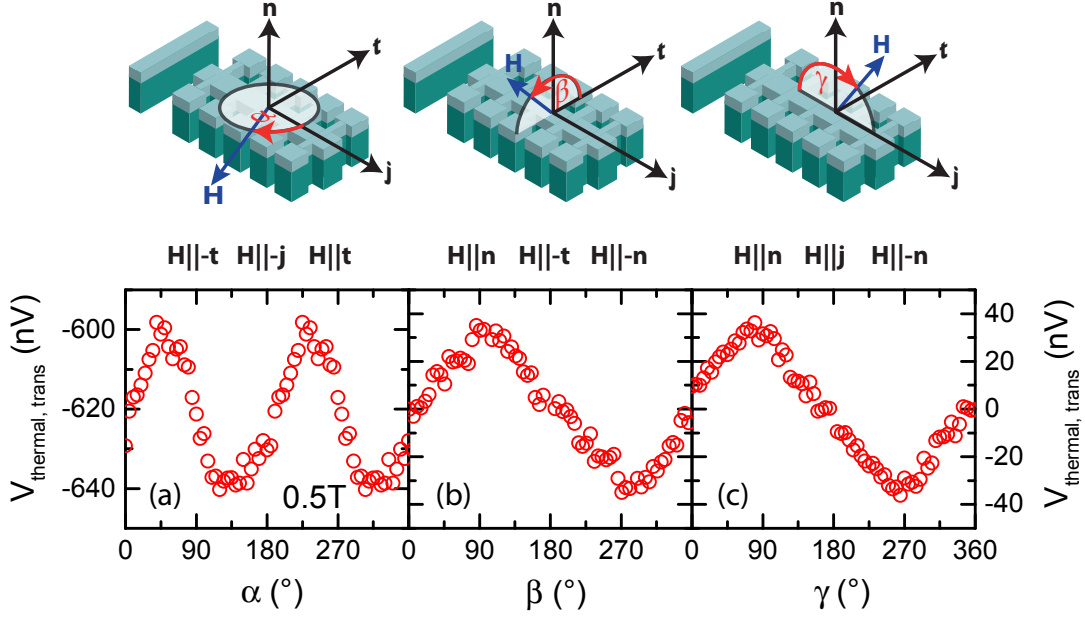
Figure 4.12: Transverse SNMTP experiments on a YIG/Pt(4.1 nm) hybrid: A modulated charge current with an average value of $\bar{I}_{\text{heater}} = 20\,\text{mA}$ is applied to the OCH to provide a constant heater power of 286 mW. This generates a temperature difference of $\Delta T = 18\,\text{K}$ along the Hall bar. The transverse voltage drop $V_{\text{thermal,trans}}$ is detected as a function of the magnetization orientation (see sketches), while an external magnetic field of 0.5 T is rotated in ip **(a)**, oopj **(b)** and oopt **(c)**.

gitudinal thermal voltage. The modulation $\Delta V_{\text{thermal,trans}}$ can be interpreted with the first part of Eq. (4.19) and thus consolidates the SNMTP theory. In both out of plane rotations, however, we find $\sin(\delta)$ shaped responses to the magnetic field orientation [cf. Fig. 4.12(b,c)]. We interpret these signals as a conventional Nernst effect in platinum. To investigate this in further detail, the magnetic field amplitude dependence of the out of plane signal has to be studied. This will be postponed to Sec. 4.3.3.

To conclude, the longitudinal and transverse data shown above change in the characteristic fashion expected from Eq. (4.18) and Eq. (4.19). We therefore interpret our results as the experimental observation of the spin Nernst effect in platinum.

4.3.2 Power and field dependence

On the same sample, we repeat the angle dependent magneto-thermopower measurements for different heating powers between 100 mW and 286 mW resulting in temperature differences between 7.7 K and 18.0 K along the Hall bar, as well as for two different magnetic fields at 0.5 T and 1 T. To extract the modulation amplitudes $\Delta V_{\text{thermal,long}}$ and ratios $\Delta V_{\text{thermal,long}}/V_{\text{thermal,long}}$ from our experimental data, we symmetrized the raw data taken for each rotation plane and magnetic field amplitude and performed $\cos^2(\delta)$ fits. As already shown in Fig. 4.8, the absolute value of the longitudinal thermopower voltage
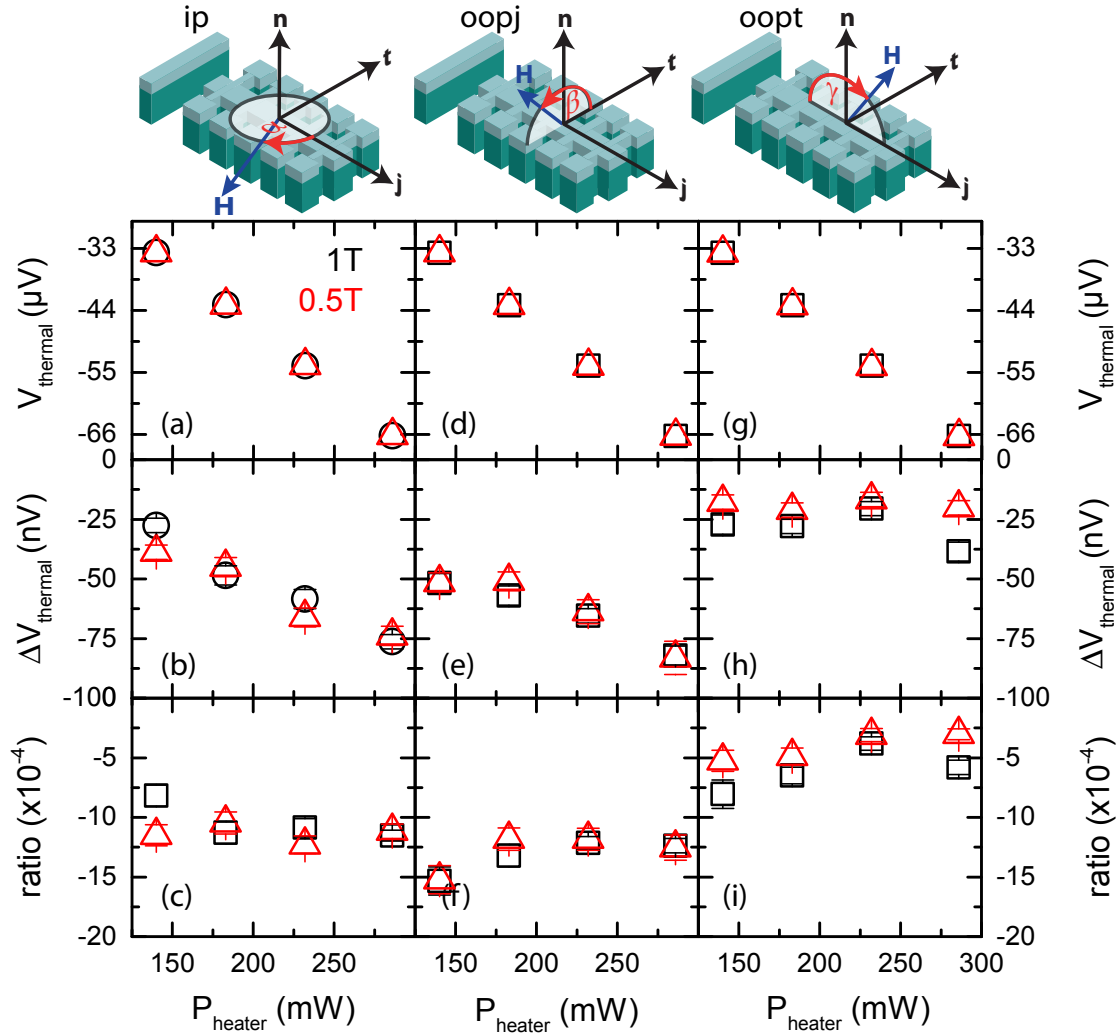
Figure 4.13: Power dependence of the longitudinal thermal voltage $V_{\text{thermal,long}}$ (first row), the voltage modulation amplitude $\Delta V_{\text{thermal,long}}$ (second row) and the ratio of both (third row) for rotations in ip (left column), oopj (middle) and oopt rotations (right column) for a base temperature of $T = 220\,\text{K}$ and magnetic field strength of $0.5\,\text{T}$ (red triangles) and $1\,\text{T}$ (black squares), respectively.

$V_{\text{thermal,long}}$ scales with the amplitude of the power applied to the heater strip and thus with the temperature difference building up along the Hall bar. This is of course independent of the presence of a magnetic field and we observe a linear connection between $V_{\text{thermal,long}}$ and P_{heater} in all three rotation planes [cf. Fig. 4.13(a,d,g)].

However, we observe an increase in the modulation voltage $\Delta V_{\text{thermal,long}}$ with increasing P_{heater} in ip and oopj rotations. This is shown in Fig. 4.13(b) and (e) for two different magnetic field amplitudes. For both $0.5\,\text{T}$ (red triangles) and $1\,\text{T}$ (black squares), $\Delta V_{\text{thermal,long}}$ increases with increasing P_{heater} and the difference between the $0.5\,\text{T}$ and $1\,\text{T}$ data points is within the experimental error of $\pm 5\,\text{nV}$ given by the thermal stability of the nanovoltmeters. The ratios $\Delta V_{\text{thermal,long}}/V_{\text{thermal,long}}$ for ip and oopj rotations

are depicted in Fig. 4.13(c) and (f). As the SNMTP can be interpreted as a modulation on the thermal voltage due to a spin current flow across the YIG/Pt interface, the relative amplitude of the modulation of the longitudinal voltage is expected to be independent of both heating power and external magnetic field, as long as a thermally driven spin current is generated. This is confirmed experimentally in Fig. 4.13(c) and (f). Again, within the experimental error, the ratio (which can be seen proportional to the factor $\theta_{\mathrm{SH}}\theta_{\mathrm{SN}}$) is almost constant as a function of both P_{heater} and $\mu_0 H$ for ip and oopj, $\Delta V_{\mathrm{thermal,long}}/V_{\mathrm{thermal,long}} \approx 1.2 \times 10^{-3}$. For the temperature range depicted here (the average sample temperature rises with increasing P_{heater}, see Fig. 4.7), θ_{SH} was determined to be almost independent of temperature [50]. Thus, the temperature dependence of the spin Nernst angle θ_{SN} is suggested to be rather weak according to Fig. 4.13(c) and (f).

The power dependence of the longitudinal oopt signal is depicted in Fig. 4.13(g-i). As stated by Eq. (4.18), we expect a constant SNMTP signal as a function of the magnetization orientation in this geometry. While $V_{\mathrm{thermal,long}}$ scales with P_{heater} [cf. Fig. 4.13(g)], we find that the modulation amplitude observed in oopt is almost constant, $\Delta V_{\mathrm{thermal,long}}^{\mathrm{oopt}} \approx -25\,\mathrm{nV}$, cf. Fig. 4.13(h). We thus assume that the origin of the modulation in oopt rotations is not related to the spin Nernst magneto-thermopower. This power independence is at odds with the interpretation of $\Delta V_{\mathrm{thermal,long}}^{\mathrm{oopt}}$ with a non-vanishing $\mathbf{t}$ component of ∇T. Additionally, $|\Delta V_{\mathrm{thermal,long}}^{\mathrm{oopt}}|$ rises with increasing magnetic field. The decrease of $\Delta V_{\mathrm{thermal,long}}^{\mathrm{oopt}}(P_{\mathrm{heater}})$ also results in a negative power dependence of the ratio $\Delta V_{\mathrm{thermal,long}}^{\mathrm{oopt}}/V_{\mathrm{thermal,long}}$, as depicted in Fig. 4.13(i). With increasing heater power, the voltage modulation in oopt decreases slightly. This again is at odds with the results found for ip and oopj rotations depicted in Fig. 4.13(c) and (f). In conclusion, due to its power dependence, the modulation found in oopt can not be attributed to the SNMTP concept for $\nabla T \cdot \mathbf{t} \neq 0$. This issue will be subject of future investigations.

4.3.3 Nernst effects

In analogy to the power dependence of the longitudinal thermopower, we now investigate the transverse thermopower signal. As already discussed above, the ip signal of $V_{\mathrm{thermal,trans}}$ reflects the modulation of the longitudinal ip signal with an angular shift by 45°. For the out of plane rotations, however, this picture changes. We already postulated in Sec. 4.1.4, that a conventional Nernst effect [cf. Fig. 4.2(b)] occurs in $\mathbf{t}$ direction, if the magnetization $\mathbf{M}$ has a component perpendicular to the sample plane ($m_n \neq 0$) and perpendicular to the direction of the temperature gradient applied along $\mathbf{j}$. In Fig. 4.14 (a,b), we show two sets of out of plane rotations taken at $P_{\mathrm{heater}} = 286\,\mathrm{mW}$ and at external magnetic fields of $0.5\,\mathrm{T}$ (red symbols) and $1\,\mathrm{T}$ (black symbols) in oopj (a) and oopt (b) geometry. The signals shown in Fig. 4.14 (a,b) are anti-symmetrized with respect
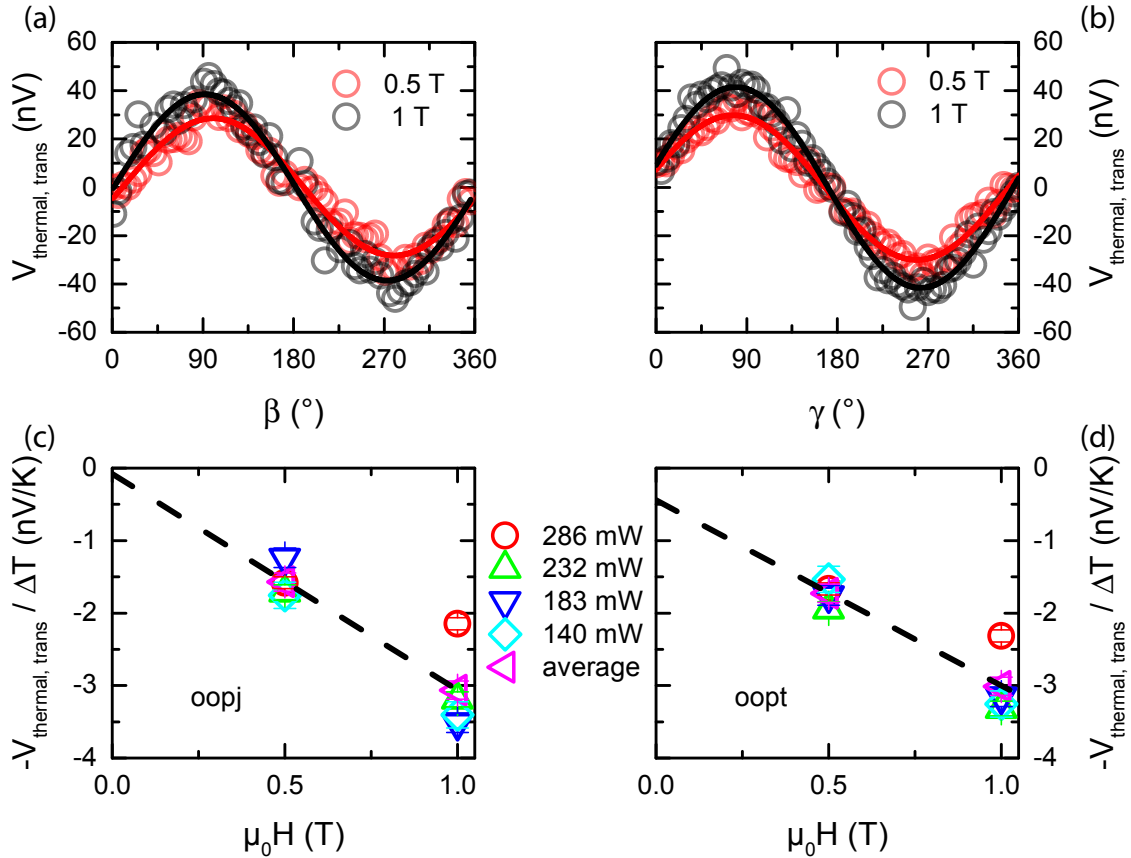
Figure 4.14: **(a,b)** Evolution of the transverse thermal voltage $V_{\text{thermal,trans}}$ in **(a)** oopj and **(b)** oopt configuration taken at $P_{\text{heater}} = 286\,\text{mW}$ and external magnetic fields of $0.5\,\text{T}$ (red symbols) and $1\,\text{T}$ (black symbols). The colored, solid lines represent $\sin(\delta)$ fits to the data. **(c,d)** Magnetic field dependence of the signal amplitude of $V_{\text{thermal,trans}}/\Delta T$ for a set of heater powers (see legend) are depicted in **(c)** for oopj and **(d)** for oopt geometry. The pink triangles represent average values of the heater dependent signals. Linear fits to the field dependence of these average values are shown as black dashed lines.

to $\delta = 180°$. We find a sinusoidal dependence of $V_{\text{thermal,trans}}$ that exhibits a slight field dependent increase.

Performing this field dependent rotation sets for several heater powers P_{heater} leads to Fig. 4.14 (c,d). As encoded by the colored symbols, we find a similar field dependence in both rotation planes for all heater powers. The data points depicted in Fig. 4.14 (c,d) represent the amplitudes of $\sin(\delta)$ taken from fits to the experimental data [cf. solid lines in Fig. 4.14 (a,b)]. We divided the values of $V_{\text{thermal,trans}}$ by the heater dependent values of ΔT. The $-V_{\text{thermal,trans}}/\Delta T$ ratio (i.e., the amplitude of the Nernst coefficient N) seems to be almost independent of the amplitude of P_{heater}; we thus average the heater power dependent data taken for each field. This results in the pink triangle symbols in Fig. 4.14 (c,d). The dashed black lines in the same graphs represent linear fits to those

average values. From the slope of the linear fits, we extract $N_{\mathrm{oopj}} = -2.98\,\mathrm{nV/(KT)}$ and $N_{\mathrm{oopt}} = -2.56\,\mathrm{nV/(KT)}$. These values can be interpreted as the Nernst coefficient of platinum. As the Nernst coefficient is expected to be independent of the rotation geometry, we thus conclude the averaged value $N_{\mathrm{av}} = -2.77\,\mathrm{nV/(KT)}$ for our estimation of N, which is comparable with earlier reports [168]. Furthermore, we can estimate an upper limit of the spin Nernst anomalous Nernst effect contribution (cf. Sec. 4.1.4) to the field dependent transverse voltages from the abscissa in Fig. 4.14 (c) and (d). Our data suggests that this feature, if present at all, is smaller than $0.5\,\mathrm{nV/K}$ and thus within the resolution limit of our experimental setup.

4.3.4 Parasitic effects

We can exclude that the thermopower modulations observed in oopt geometry (cf. Sec. 4.3.1) are generated by the spin Seebeck effect (SSE), which has been reported for ferromagnetic conductors [35], semiconductors [36]) and insulators [34] covered with normal metals like Pt. Here, we discuss the longitudinal SSE scenario for a YIG/Pt bilayer. A temperature gradient ∇T is applied along the $-\mathbf{n}$ direction, i.e. parallel to the film normal [34]. Additionally, the magnetization $\mathbf{M}$ of the YIG layer is aligned in-plane along $\mathbf{t}$ via an externally applied magnetic field. The presence of ∇T drives a spin current $\mathbf{j}_s$ along $\mathbf{n}$ with a spin polarization $\mathbf{s}$ along $\mathbf{t}$. This spin current is then transformed into a charge current in N via the ISHE and one detects a so-called spin Seebeck voltage $V_{\mathrm{SSE}} \propto \mathbf{j}_s \times \mathbf{s}$ along $\mathbf{j}$ (see Fig. 4.15). In this geometry, a $\cos{(\alpha)}$ shaped voltage signal along $\mathbf{j}$ was reported for ip magnetic field rotations [34]. This signature of course differs from our $\sin^2{(\alpha)}$ shaped SNMTP signals observed in Sec. 4.3.1.

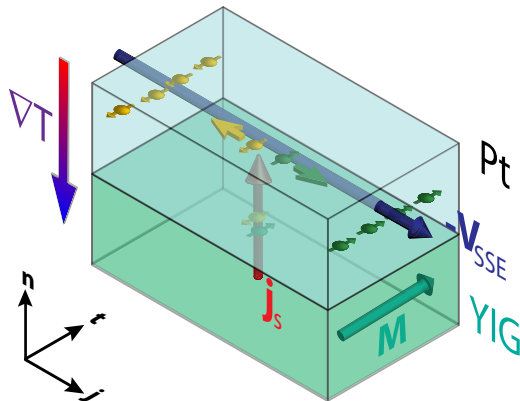One could of course assume an SSE contribution stemming from the temperature gra-

Figure 4.15: Concept of the longitudinal spin Seebeck effect in YIG/Pt: a temperature gradient ∇T applied along the $-\mathbf{n}$ direction drives a spin current $\mathbf{j}_s$ along $\mathbf{n}$ with spin polarization $\mathbf{s} \parallel \mathbf{t}$. In the Pt layer, $\mathbf{j}_s$ is transformed into a voltage V_{SSE} via the ISHE.
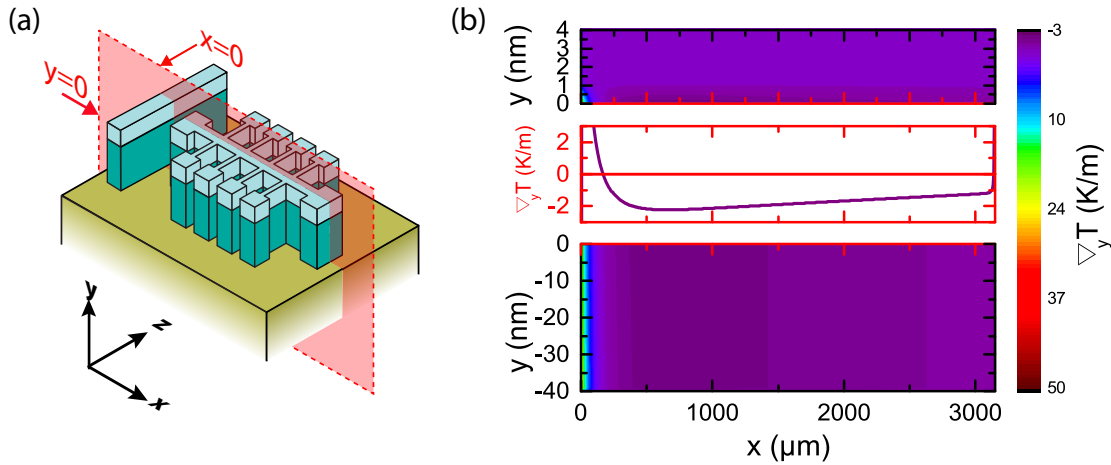
Figure 4.16: Simulation results for the temperature profile: **(a)** Sketch (not to scale) of the sample used in the experiments. The red shaded plane indicates the cut for which the simulation was done. The point $(x = 0, y = 0)$ corresponds to the YIG/Pt interface at the left end (facing the heater) of the Hall bar. **(b)** Simulation result for the out of plane thermal gradient $\nabla_y T$. The upper and lower panel show the result for the Pt and YIG layer, respectively. The middle one gives $\nabla_y T(x)$ at $y = 0$, the interface between the Pt and the YIG. Only close to the ends of the Hall bar does $\nabla_y T$ differ significantly from 0, however, without ever exceeding a crucial magnitude which would influence the experiment. Figure provided by M. Schreier.

dient along **j** in our experiments, too. The longitudinal Seebeck effect in this case would result in a spin current parallel to ∇T that can be generated into a voltage along **t** via the ISHE. This, however, is at odds with our observation of the $\sin^2(\alpha)$ and $\cos^2(\beta)$ shaped longitudinal thermal voltages in ip and oopj rotations. While the thermal gradient in our sample lies dominantly in the film plane, the different thermal conductances of the bulk substrate and the thin YIG and Pt films will unavoidably introduce small out of plane components in the thermal gradient. Such out of plane components may lead to parasitic contributions from the spin Seebeck or anomalous Nernst effect.

To quantify the magnitude of the out of plane thermal gradients and thus the contributions from spin Seebeck and anomalous Nernst effects[4], we conduct a finite elements simulation of the temperature profiles in our sample. Exploiting the symmetry of the sample, we set up the experimental geometry as described in the Sec. 4.2.2 and simulate the steady state temperature profile for a 2D cross-section of the sample, indicated by the red plane in Fig. 4.16(a). Here, we fix the heater temperature to a constant value of $270\,\mathrm{K}$ and couple the sample to a heat sink ($T_{\mathrm{heatsink}} = 220\,\mathrm{K}$) via a phenomenologically

---

[4]We are aware that the anomalous Nernst effect requires a conductive ferromagnetic material. Since we found no indication for such an interlayer at the YIG/Pt interface via XMCD, we assume that both anomalous Nernst effect and the anisotropic magnetoresistance are not responsible for the features found in our experiments on YIG/Pt.

determined thermal boundary conductance of $3 \times 10^3 \, \text{W}/(\text{m}^2\text{K})$. The value of the latter reproduces the $18 \, \text{K}$ temperature drop along the Hall bar measured in the experiment. Thermal radiation of the Pt Hall bar is taken into account using $\epsilon = 0.1$ for the emissivity of the Pt [177]. With the material parameters tabulated in Tab. 6.4 in Sec. 6.1.4, we obtain a mean value of the out of plane thermal gradient of $\nabla_\mathbf{n} T = \nabla_\text{y} T \approx 1 \, \text{K}/\text{m}$ [Fig. 4.16(b)]. This corresponds to $|V_\text{SSE}| = S\Delta T \leq 2 \, \text{nV}$, which is far beyond our experimental detection limit. Our experiments can therefore be considered as effectively free from contributions from the spin Seebeck effect.

Similarly, for any reasonable value $N_\text{ANE}^\text{Pt} \lesssim 1 \, \mu\text{V}/(\text{KT})$, cf. $N_\text{ANE}^\text{Ni} = 0.5 \, \mu\text{V}/(\text{KT})$ (Ref. [178]) for the anomalous Nernst coefficient N_ANE of an assumed proximity magnetized Pt one would only obtain values in the few nanovolt to sub nanovolt regime, again much smaller than the ΔV observed in our experiment.

This is not withstanding that both spin Seebeck and anomalous Nernst effect do exhibit a different behavior with respect to the orientation of the external magnetic field than the one observed in our experiments anyway.

4.3.5 Reference SMR measurements

In an additional set of experiments, we perform ADMR measurements on the YIG/Pt Hall bar to measure the SMR effect in analogy to Ch. 2. The temperature of the heat bath was stabilized to $220 \, \text{K}$ and we applied a constant heating power of $286 \, \text{mW}$ to the heating strip to ensure the averaged sample temperature to be comparable to the thermopower experiments presented earlier. We use a Keithley K2400 Source Measure Unit to apply a constant current $j_\text{q} = 500 \, \mu\text{A}$ along the Hall bar and rotate an external magnetic field $\mu_0 H = 1 \, \text{T}$ around the sample. For each rotation geometry (see definitions in Fig. 2.7) we detect the longitudinal and transverse voltage drops using an Agilent 34420A nanovoltmeter and a Keithley K2182A nanovoltmeter.

At first, we focus on the longitudinal signal depicted in Fig. 4.17. In agreement with the SMR theory shown in Sec. 2.1.6 and earlier experiments on YIG/Pt Hall bars (cf. Sec. 2.3.1), we observe a $\cos^2(\alpha)$ modulation of V_long for rotations in ip [cf. Fig. 4.17 (a)] and a $\sin^2(\beta)$ shaped modulation in oopj geometry [cf. Fig. 4.17 (b)]. In both cases, the minima appear at $\mathbf{H}||\mathbf{M}||\mathbf{t}$, i.e. when the magnetization $\mathbf{M}$ of the YIG is parallel to the spin polarization $\mathbf{s}$ and thus no spin transfer at the YIG/Pt interface is possible (cf. Sec. 2.3.1). The relative amplitude $\Delta V_\text{long}/V_\text{long}$ corresponds to the SMR amplitude $-\Delta\rho_1/\rho_0$ and is determined to be $(1.05 \pm 0.10) \times 10^{-3}$, which is in good agreement with earlier results for a similar thickness of the Pt layer (cf. Sec. 2.3.6). In oopt geometry, $\mathbf{M}$ is always perpendicular to $\mathbf{s} \parallel \mathbf{t}$ and thus no orientation dependent modulation of V_long
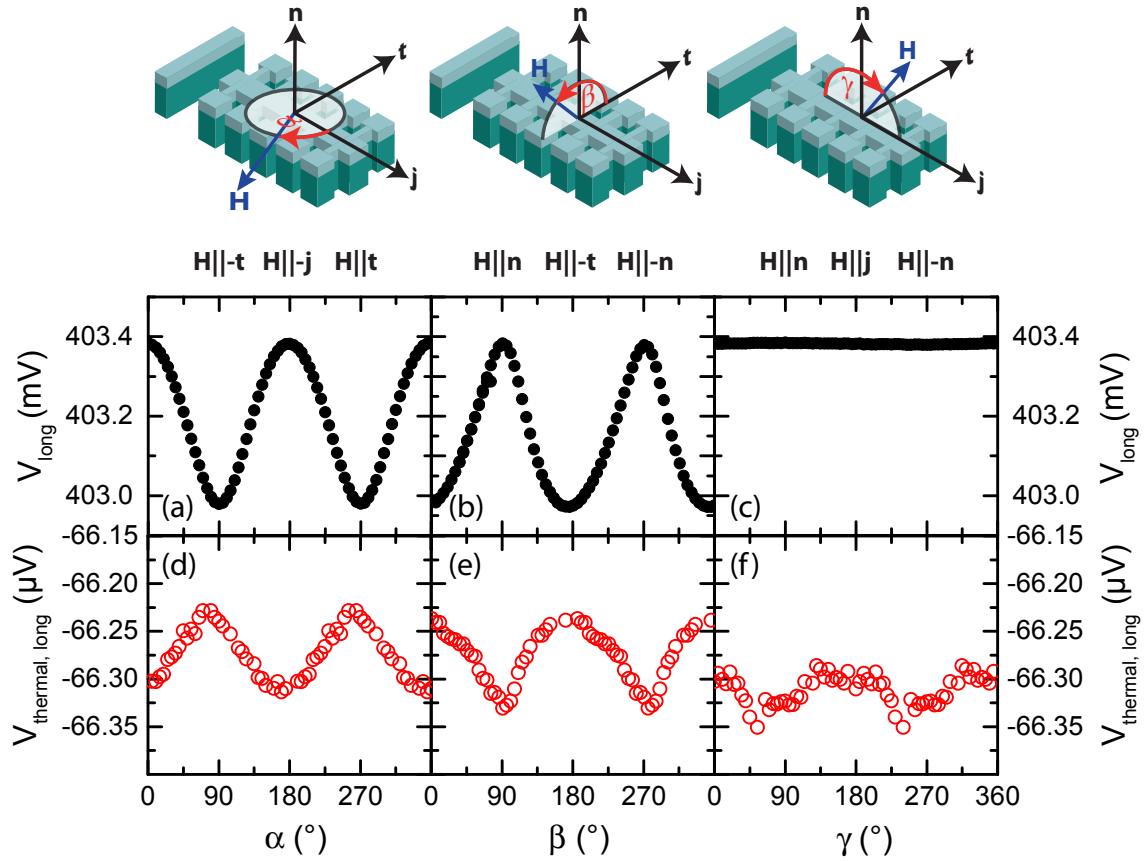
Figure 4.17: Spin Hall magnetoresistance experiments on the Hall bar used in Sec. 4.3.1. A charge current $j_q = 500\,\mu$A is applied along the Hall bar and the longitudinal voltage drop V_{long} is detected as a function of the magnetization orientation (cf. Ch. 2), while an external magnetic field of $1\,$T is rotated in **(a)** ip, **(b)** oopj and **(c)** oopt configuration. $P_{heater} = 286\,$mW is applied to the heater strip to provide the same (average) sample temperature as for the SNMTP experiments. For comparison, the longitudinal SNMTP signals achieved at $\mu_0 H = 1\,$T from this sample are shown in panel**(d)**-**(f)** for corresponding rotation planes.

is observed [see Fig. 4.17 (c)]. For comparison, the longitudinal SNMTP signals achieved from the same sample are shown in Fig. 4.17 (d)-(f) for corresponding rotation planes. This data - except the negative modulation amplitude - is in good qualitative agreement with the SMR data. Thus, the SNMTP can be seen as a thermal analog of the SMR. The opposite signs of the modulation amplitudes correspond to the interplay of heat and spin currents in the SNMTP and will be discussed in Sec. 4.3.7.

Furthermore, the transverse voltage V_{trans} shown in Fig. 4.18 (a)-(c) is in good agreement with the SMR theory, resulting in a $\sin(\alpha)\cos(\alpha)$ signal in ip and Hall-like $\sin(\beta)$ and $\sin(\gamma)$ - contributions in oopj and oopt rotations with maxima observed when **M** is perpendicular to the film plane.

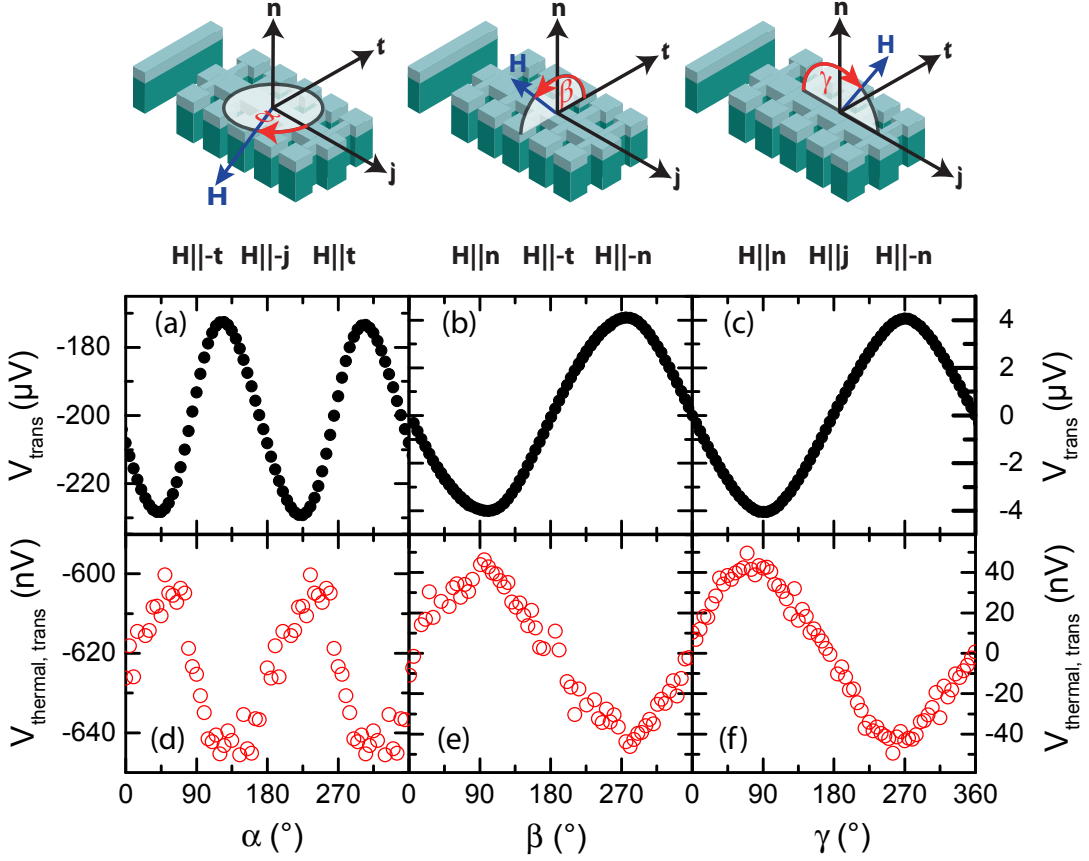As discussed earlier (cf. Sec. 2.3.1), we observe no evidence for an anisotropic magnetore-

Figure 4.18: Transverse Spin Hall magnetoresistance experiments: While $j_q = 500\,\mu A$ is applied along the Hall bar, the transverse voltage drop V_{trans} is detected as a function of the magnetization orientation (cf. Ch. 2), while an external magnetic field of $1\,T$ is rotated in **(a)** ip, **(b)** oopj and **(c)** oopt configuration. $P_{heater} = 286\,mW$ is applied to the heater strip to provide the same (average) sample temperature as for the SNMTP experiments. For comparison, the transverse SNMTP signals achieved at $\mu_0 H = 1\,T$ from this sample are shown in panel**(d)**-**(f)** for corresponding rotation planes.

sistance (AMR) within our polycrystalline Pt layer which would result e.g. in a $\cos^2(\gamma)$ dependence of the longitudinal voltage in the oopt rotation. Again, this indicates that our signal cannot be attributed to a proximity induced MR due to induced magnetic moments in the N layer [47], but it is based on the interplay of spin and charge currents in the framework of the SHE and ISHE. Therefore, we do not expect proximity effects to influence our thermopower measurements as well.

4.3.6 Reproducibility

The same sets of SMR and SNMTP measurements are also performed on a reference sample with $t_F = (51 \pm 2)\,nm$ and $t_N = (3.9 \pm 0.2)\,nm$ grown on yttrium aluminum garnet ($Y_3Al_5O_{12}$, YAG) under growth conditions presented in Sec. 2.2.1. Although using a

different substrate material here, the thermal properties of both samples are quite similar (thermal conductivity for YAG (GGG) $14(8)\frac{\text{W}}{\text{kgK}}$ [179, 180]). Therefore, we expect no influence from the choice of the substrate material on our SNMTP experiments. The sample was patterned in the same fashion as the first one discussed in Sec. 4.3.1. The experimental setup remained unchanged, and the heat bath was stabilized to $250\,\text{K}$ while applying heater powers of up to $440\,\text{mW}$ to the on chip resistive heater. This led to a temperature difference of up to $23.6\,\text{K}$ along the Hall bar and an average sample temperature $\bar{T} \approx 297.0\,\text{K}$ determined by the on-chip thermometry procedure described above.

Magnetization orientation dependent SMR measurements for $\mu_0 H_{\text{ext}} = 1\,\text{T}$ and $j_{\text{q}} = 500\,\mu\text{A}$ applied along the **j** direction are shown in Fig. 4.19(a-f) . Here, we observe the same angular dependencies in the longitudinal and transverse voltages as reported for conventional SMR measurements (cf. Sec. 2). From the longitudinal voltage modulations in oopj rotation [cf. Fig. 4.19 (b)], we read a SMR amplitude of $-\Delta V/V = 1.1 \times 10^{-3}$. For this sample, however, we notice a slight misalignment in the rotation planes. This can easily be seen in the evolution of the longitudinal voltages in Fig. 4.19 (a,b) by comparing the levels obtained from ip (a) and oopj (b) rotations. Additionally, due to this tilt of the rotation planes, we find a finite modulation signal also in the longitudinal voltage obtained from the oopt rotation with $\Delta V_{\text{long}}/V_{\text{long}}^{\text{oopt}} \approx 1 \times 10^{-4}$. The transverse signal [see Fig. 4.19 (d-f)] also reproduces the expectations for a SMR measurement in YIG/Pt. Especially in both out of plane rotations [cf. Fig. 4.19 (e,f)] we find hints for the misalignment in the shape of the Hall-like transverse signals deviating from a perfect $\sin(\delta)$. Additionally, for oopt measurements, we find hint for an ip re-orientation of the magnetization for $\gamma = 90°(270°)$ in both V_{long} [cf. Fig. 4.19 (c)] and V_{trans} [cf. Fig. 4.19 (f)].

Here, we intentionally use this misalignment of the rotation planes to test its influence on SNMTP experiments. In thermally driven SNMTP measurements with $P_{\text{heater}} = \text{const.} = 440\,\text{mW}$, we therefore use the same alignment of **j**, **t** and **n** as described above. The result of the longitudinal voltage evolution obtained from thermal measurements can be read from Fig. 4.19(g-i). The thermal voltage due to the thermopower effect was found to be $V_{\text{thermal,long}} \approx -76.6\,\mu\text{V}$. For ip and oopj rotations, we find $\sin^2(\alpha)$ and $\cos^2(\beta)$ modulations with $|\Delta V_{\text{thermal,long}}/V_{\text{thermal,long}}| \approx 110\,\text{nV}$ and $120\,\text{nV}$, respectively. The evolution of $V_{\text{thermal,long}}$ for ip and oopj thus qualitatively reproduces the fingerprint of the SNMTP observed in the first sample. However, for this set of measurements, the signal levels of ip and oopj measurements do not coincide. This feature is also visible in the SMR data [cf. Fig. 4.19(a,b)], and (partially) is due to the misalignment of the rotation planes. In oopt geometry [cf. Fig. 4.19(i)], we find a reduced modulation compared to the first two rotation planes, $|\Delta V_{\text{thermal,long}}/V_{\text{thermal,long}}| \approx 40\,\text{nV}$. For the corresponding SMR signal, we find a modulation ratio about $\Delta V_{\text{oopt}}/\Delta V_{\text{oopj}} \approx 0.1$. The evolution of $V_{\text{thermal,long}}$
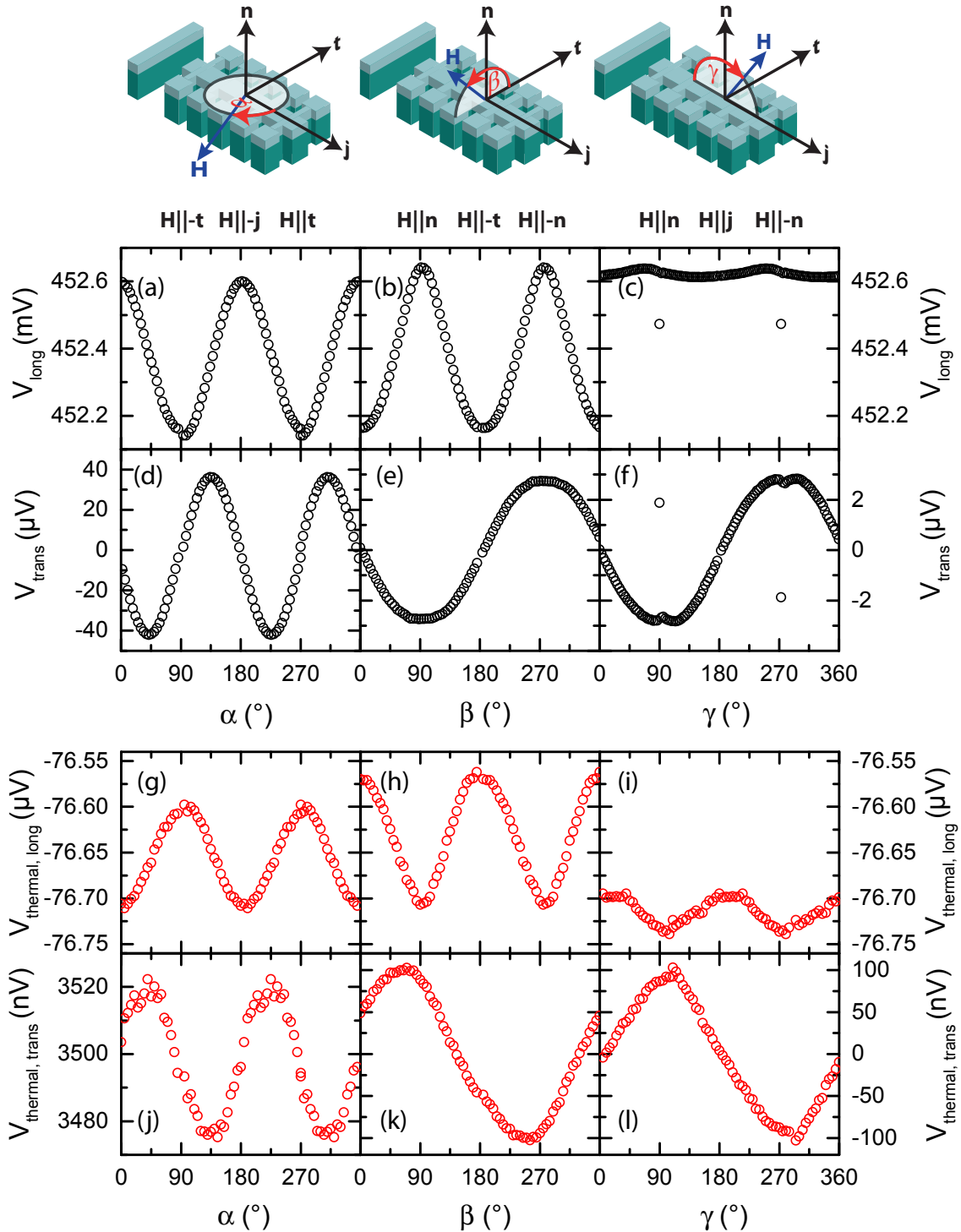
Figure 4.19: SMR (**a-f**, black) and SNMTP (**g-l**, red) measurements for a YAG/YIG ($t_{\mathrm{F}} = 51\,\mathrm{nm}$)/Pt ($t_{\mathrm{N}} = 3.9\,\mathrm{nm}$) reference sample. All measurements taken for $P_{\mathrm{heater}} = \mathrm{const.} = 440\,\mathrm{mW}$ and $\mu_0 H = 1\,\mathrm{T}$. The experimental setup and the sample layout is equivalent to Fig. 4.6.

quantitatively disagrees with this value, and we find $\Delta V_{\text{thermal}}^{\text{oopt}}/\Delta V_{\text{thermal}}^{\text{oopj}} \approx 0.23$. Thus, the signal modulation observed for $V_{\text{thermal,long}}$ in oopt geometry can not be directly attributed to improperly aligned rotation planes. However, as already discussed above for the first sample, a modulation of the thermopower in oopt might also indicate a tilt between the $\mathbf{t}$ direction of the Hall bar and the long side of the resistive heater, leading to a non-vanishing component of ∇T along the $\mathbf{t}$ direction. For the case of the second sample, after subtracting 10% of $V_{\text{thermal,long}}^{\text{oopj}}$ due to the misalignment found in the SMR, we use the remaining thermopower signal $\tilde{V}_{\text{thermal,long}}^{\text{oopt}} \approx (28 \pm 5)\,\text{nV}$ to estimate the tilt angle $\alpha' \approx 13° \pm 3°$. This value is comparable to the angle estimated for the first sample (cf. Sec. 4.3.1). We thus assume that the modulation in $V_{\text{thermal,long}}$ found in oopt for both samples has the same origin. On these grounds, we conclude that the SNMTP experiments performed on second sample reproduces the findings found in Sec. 4.3.1. Again, parasitic thermal effects like the spin Seebeck effect are not responsible for the oopt thermopower signal. However, the occurrence of a $\cos^2(\gamma)$ shaped longitudinal thermopower signal found in oopt experiments advocates for further examination of this feature in the future.

The transverse SNMTP signal [cf. Fig. 4.19(j-l)] also reproduces the shape obtained from the transverse SMR measurement [cf. Fig. 4.19(d-f)]. In both out of plane rotations, we find similar deviations from a perfect $\sin(\delta)$ shape in $V_{\text{thermal,trans}}$. The ip re-orientation of the magnetization in oopt rotations is not observed in the SNMTP data. This may be attributed to the finite resolution of the nanovoltmeters. Thus, in conclusion, we find the SNMTP reproducible within the experimental limit given by the signal to noise ratio of the nanovoltmeters. This is of great importance with regard to possible applications of the SNMTP.

4.3.7 Spin Nernst angle of Pt

The previous sections showed that the SNMTP concept is in good qualitative agreement with the signals obtained from thermopower experiments performed on two samples. Now, we utilize the SNMTP theory presented in Sec. 4.1.4 to extract the heat to spin conversion efficiency for Pt, the spin Nernst angle θ_{SN}. Therefore, we calculate the relative thermopower ratio between open and closed spin current boundary conditions,

$$\frac{\Delta V_{\text{thermal,long}}}{V_{\text{thermal,long}}} = \frac{V_{\text{thermal,long}}(\mathbf{H} \parallel \mathbf{t}, \text{open}) - V_{\text{thermal,long}}(\mathbf{H} \perp \mathbf{t}, \text{closed})}{V_{\text{thermal,long}}(\mathbf{H} \parallel \mathbf{t}, \text{open})}. \tag{4.23}$$

Via the equations for the thermopower voltage given in Eq. (4.3) and Eq. (4.18), the definitions of $V_{\text{thermal,long}}(\mathbf{H} \parallel \mathbf{t}, \text{open})$ and $V_{\text{thermal,long}}(\mathbf{H} \perp \mathbf{t}, \text{closed})$ read

$$V_{\text{thermal,long}}(\mathbf{H} \parallel \mathbf{t}, \text{open}) = -\left(S + \Delta S_0\right)\Delta T \tag{4.24}$$

and

$$V_{\text{thermal,long}}(\mathbf{H} \perp \mathbf{t}, \text{closed}) = -\left(S + \Delta S_0 + \Delta S_1\right)\Delta T \tag{4.25}$$

with $\Delta T = T_{\text{cold}} - T_{\text{hot}} < 0$. Thus, $\Delta V_{\text{thermal,long}}/V_{\text{thermal,long}}$ corresponds to $-\Delta S_1/\tilde{S}$ with $\tilde{S} = S + \Delta S_0$.

For the first sample used in this chapter (cf. Fig. 4.10), we find $\Delta V_{\text{thermal,long}}/V_{\text{thermal,long}} = -100\,\text{nV}/66.2\,\mu\text{V} = -1.5 \times 10^{-3}$. Based on Eq. (4.21), we can calculate the spin Nernst angle θ_{SN} via

$$\theta_{\text{SN}} \approx -\frac{\Delta S_1}{S}\frac{t_{\text{N}}}{\theta_{\text{SH}}\lambda}\frac{\sigma_{\text{N}} + 2\lambda G_r \coth\frac{t_{\text{N}}}{\lambda}}{2\lambda G_r \tanh^2\frac{t_{\text{N}}}{2\lambda}}. \tag{4.26}$$

We use $\bar{G}_r = 4.0 \times 10^{14}\,\Omega^{-1}\text{m}^{-2}$, $\bar{\lambda} = 1.5\,\text{nm}$ and $\theta_{\text{SH}} = 0.11$ determined in Sec. 2.4.1 for YIG/Pt hybrids at $T = 250\text{K}$ comparable to $\bar{T} = 255\text{K}$ used in our thermopower measurements for this sample. With these parameters, we obtain $\theta_{\text{SN}} = -0.202$ from Eq. (4.26). For reference, we find $\Delta V_{\text{thermal,long}}/V_{\text{thermal,long}} = -120\,\text{nV}/76.57\,\mu\text{V} = -1.6 \times 10^{-3}$ for the second sample (cf. Fig. 4.19) with $\bar{T} = 297\text{K}$. As discussed in Sec. 2.4.1, G_r, λ and θ_{SH} do not vary much in the temperature range between 150K and 300K. Thus, we use the same parameters as for the first sample and obtain $\theta_{\text{SN}}(\text{reference}) = -0.203$. This value perfectly agrees with the one obtained from the first sample, indicating that the SNMTP concept is a precise technique to obtain the spin Nernst angle θ_{SN}.

Besides this nice agreement, the sign of θ_{SN} does not seem intuitive at first sight. For its charge driven relative, the spin Hall angle θ_{SH}, positive values for Pt have been reported in the literature. Even though the SMR concept utilized to obtain θ_{SH} in this work (see e.g. Sec. 2.3.6) is not sensitive to the sign of θ_{SH} since the relative SMR modulation is proportional to θ_{SH}^2, the sign of the spin Hall angle can be obtained e.g. from spin pumping measurements [24].

However, as suggested in a theoretical first-principle calculation in Ref. [163], the sign of θ_{SN} is determined by the interplay of two different contributions to the extrinsic skew scattering mechanism. Besides the term given directly by the presence of the temperature gradient, the spin Nernst effect is additionally influenced by the spin Hall effect, which is present due to the electric field induced by the Seebeck effect [163]. These authors found that, depending on the sign of the thermopower, this second term can be positive or negative. The first term, however, has the same order of magnitude but the opposite sign in comparison to the spin Hall angle.

Further calculations of the ratio between θ_{SH} and θ_{SN}, again based on first principles,

have been performed by the group of Hubert Ebert [165]. For platinum, they found $\theta_{\mathrm{SH}}/\theta_{\mathrm{SN}} \approx -0.9$ at $250\,\mathrm{K}$. This not only confirms our experimental result of an opposite sign between θ_{SH} and θ_{SN}, but also is in rough agreement with the ratio $\theta_{\mathrm{SH}}/\theta_{\mathrm{SN}} \approx -0.5$ found in our experiments.

In conclusion, the thermopower experiments presented in this chapter are in excellent agreement with the concept of the spin Nernst magneto-thermopower. This enables a first experimental determination of the heat to spin conversion efficiency for Pt, called the spin Nernst angle θ_{SN}. Our experiments suggest $\theta_{\mathrm{SN}} = -0.20$. This efficiency is larger than the charge current to spin current efficiency (given by the spin Hall angle), implying the importance of the SNE in future spin(calori)tronic applications.

4.3.8 Observation of the spin Nernst effect in Pt: A summary

This chapter reported on the first experimental observation of the spin Nernst effect. The close analogy of spintronics and electronics was already stated experimentally by the discovery of the spin Hall effect, a spintronic relative of the conventional Hall effect, in 2004 by Kato *et al.* [67]. However, an even more fundamental relation between electrics and thermoelectrics is given by the phenomenology of the Hall and Nernst effects in normal metals. All three of these charge and spin effects result in a response transverse to its driving force. Thus, combining the equivalence of electrical and thermal drives and the close analogy of charge and spin currents revealed one missing link, i.e. the generation of spin currents perpendicular to a temperature gradient. This spin Nernst effect, already studied in detail on theoretical grounds, is one of the fundamental principles of spin caloritronics.

To detect a spin current generated from an applied in-plane temperature gradient in a normal metal, we developed the concept of the spin Nernst magneto-thermopower (SNMTP). Within this framework, we visualize the spin Nernst spin current as a characteristic modulation of the thermopower voltage in a ferromagnetic insulator/normal metal bilayer. In our model, the ferromagnetic insulator (YIG) attached to the normal metal (Pt) serves as a spin current detector based on the absorption and reflection of spin currents at the interface via spin transfer torque. The absorption (reflection) of spin currents at such a FMI/N interface depends on the relative orientation of the current polarization flowing towards the interface and the magnetization orientation $\mathbf{M}$ of the YIG layer. To manipulate this boundary condition *in situ*, we modulate the orientation of $\mathbf{M}$ by the rotation of an external magnetic field.

In our experiments based on this concept, the fingerprint of the thermal voltage observed experimentally in three different rotation geometries is in excellent qualitative and quantitative agreement with the phenomenological concept of the spin Nernst magneto-

thermopower (cf. Sec. 4.1.3) as well as theoretical considerations based on spin diffusion theory (cf. Sec. 4.1.4).

We additionally studied the behavior of the SNMTP effect as a function of the heater power and the external magnetic field strength $\mu_0 H$. In particular, the framework of the SNMTP implies that the magnitude of $\mu_0 H$ does not affect the modulation of the thermopower due to a spin Nernst spin current, as long as the magnetization of the YIG is aligned to the external field in good approximation. Furthermore, except a temperature dependence of the spin transport parameters, the SNMTP is expected to be independent of the heating power applied. Our experimental data confirms both, the independence of the SNMTP on the external magnetic field strength as well as the independence of the heating power (cf. Sec. 4.3.2). Thus, the results of our thermopower experiments show that the signal measured in YIG/Pt hybrids is directly related to the application of an in-plane temperature gradient and therefore shows the experimental generation of a spin current via the spin Nernst effect. This leads to the first report of an experimental determination of the heat to spin conversion efficiency for Pt, called the spin Nernst angle θ_{SN}. Our experiments suggest $\theta_{SN} = -0.20$. Motivated by the particular importance of the spin Nernst effect as one of the last hidden jigsaw pieces in spin caloritronics, our results will soon be submitted for publication [166].

This chapter also contains a detailed study of the control of temperature gradients in caloritronics experiments. During the past years, various groups showed that the handling of temperature gradients is a crucial element in spin caloritronics. One has to avoid possible contributions of the temperature gradient along other directions, as they might lead to the occurrence of other effects that may provide a similar phenomenology. To especially avoid out of plane components of ∇T that may give rise to the spin Seebeck effect, we developed a new experimental setup for caloritronic experiments in the absence of an exchange gas. Additionally, the introduction of a novel sample layout allowed us to deposit the heater power directly onto the sample substrate and in close vicinity to the Hall bar. A COMSOL based simulation of the sample's temperature profile revealed the suppression of out of plane gradients by about three orders of magnitude. In our experiments, this setup enables us to exclude possible parasitic effects like the spin Seebeck effect as the origin of our thermopower signal. We admit that a finite contribution of ∇T along the transverse Hall bar direction can not be excluded in our experiments and might result in an oopt component of the thermopower modulation. However, a study of the power- and field dependence of $V_{thermal,long}$ in this rotation geometry did not confirm this suspicion.

In summary, the measurements presented in this chapter confirm the theory of the spin

Nernst magneto-thermopower and therefore reveal the existence of thermally driven spin currents in Pt. Within this context, we here reported on the first experimental observation of the spin Nernst effect. Uncovering this effect results in a new approach on the thermal generation of spin currents. We anticipate that the spin Nernst effect as well as the novel spin Nernst magneto-thermopower will play an eminent role in the emerging field of spin caloritronics, in particular concerning the development of spintronic devices utilizing inevitable existing thermal gradients e.g. from waste heat for spin current generation.

5 Summary and outlook

Controlling the generation, propagation and detection of pure spin currents are fundamentals in the field of spin caloritronics. In this work, we investigated spin caloritronic effects in yttrium iron garnet (YIG) /platinum (Pt) hybrid structures, driven by both charge currents and temperature gradients. Here, we summarize the key results of the previous chapters to conclude this thesis. Motivated by the importance of the obtained results, we highlight their influence on the field of spin caloritronics and provide an outlook to future experiments.

5.1 Summary

In Chapter 2, we studied the spin Hall magnetoresistance (SMR) in YIG/Pt heterostructures. Our results show that the ferrimagnetic and insulating YIG layer acts as a controllable drain for spin currents in the adjacent normal metal layer. Based on an interplay of the spin Hall effect and its inverse, the SMR can be interpreted as an all-electrical generation and detection of spin currents in the normal metal, providing full access to the spin transport properties in the charge channel. The magnetoresistive effect arising from the interaction of spin currents and the magnetization orientation of the FMI layer (controlled by an external magnetic field) is in excellent agreement with both the phenomenological and theoretical framework developed in a collaboration between the WMI, the Institute for Materials Research (IMR) Tohoku and TU Delft. In a comprehensive study, we measured the SMR effect in a set of more than 25 hybrid structures consisting of YIG crystalline thin films grown by pulsed layer deposition and a platinum capping layer deposited via electron beam evaporation. An investigation of the SMR effect as a function of the platinum layer thickness enabled the extraction of the temperature dependence of a set of spin transport parameters for platinum, in particular, the spin Hall angle θ_{SH}, the spin diffusion length λ, and the real part of the spin mixing interface conductance G_r (cf. Fig. 2.20). These results were also published in Ref. [50]. Furthermore, from magnetic field amplitude dependent experiments, we showed that the SMR enables a remote sensing of the anisotropy behavior of a ferromagnetic insulator.

By studying magnetotransport effects in YIG/Pt heterostructures in a transverse (Hall-

like) geometry in Chapter 3, we were able to experimentally confirm the theory of the spin Hall anomalous Hall effect (SH-AHE) proposed by Chen *et al.* [15]. The SH-AHE describes the generation of a spin current based resistivity contribution transverse to an applied charge current. This effect manifests itself in an anomalous Hall like signature and is governed by the imaginary part of the spin mixing conductance, G_i. Our analysis of a set of YIG/Pt hybrids with varying platinum layer thickness not only enabled the first experimental detection of G_i for a normal metal/ferromagnetic insulator interface, but also revealed a strong temperature dependence of G_i including a sign change at around 100 K. While the SH-AHE itself can be observed in magnetic field amplitude dependent experiments, i.e. by applying a magnetic field in a fixed geometry with respect to the hybrid structure, magnetization orientation dependent experiments performed on the same set of samples revealed an additional, fascinating feature (cf. Fig. 3.7). In this experiment, the conventional Hall effect manifests itself in a characteristic, $\sin(\beta)$ shaped curve, if one detects the transverse resistivity of a normal metal while rotating an external magnetic field in the plane perpendicular to the direction of the longitudinally applied current. While this picture holds for platinum thin films directly deposited on a diamagnetic substrate, we found an additional $\sin^3(\beta)$ contribution in Pt deposited on YIG. This effect exhibits both a strong temperature and Pt thickness dependence and by now can not be attributed either to a static magnetic proximity effect nor to a known spin current phenomenon. The results of Chapter 3 have been published in Ref. [148].

In Chapter 4, we reported on the first experimental observation of the spin Nernst effect. Pure spin currents can be generated from spin orbit interactions in heavy-ion metals. This can be achieved by driving a flow of conduction electrons e.g. by applying a charge current to the metal (spin Hall effect). In analogy, the generation of a pure spin current from a thermal gradient was predicted as the spin Nernst effect (SNE). We demonstrated the existence of a spin current generated transverse to an applied temperature gradient in a Pt thin film by attaching a YIG thin film used as a spin current detector. The presence of the YIG layer enables the manipulation of the spin current flow across the YIG/Pt interface. In our experiments, we control the spin transfer into the YIG layer by rotating the magnetization orientation of the ferromagnetic insulator. This allows for the detection of the spin Nernst spin current in the charge channel as a magnetization-orientation dependent thermopower voltage, taking advantage of the inverse spin Hall effect. We refer to this as the spin Nernst magneto-thermopower (SNMTP). In a collaboration with theory groups from IMR Tohoku, TU Delft and LMU München, a theoretical framework of the SNMTP was developed. The excellent agreement between our experiments and the theory enabled a first experimental estimation of the spin Nernst angle in Pt, i.e. a heat to spin conversion efficiency. We find that the efficiency of a spin current generation from

a heat current exceeds the one from charge current drives, but shows an opposite sign (cf. Sec. 4.3.7). This is also corroborated by first principle calculations recently performed at the LMU München. The results of Chapter 4 will be submitted for publication [166].

5.2 Outlook

The interplay of spin currents, spin accumulation and spin dissipation gives rise to the spin Hall magnetoresistance and the spin Nernst magneto-thermopower in FMI/N hybrid systems. In this work, we studied local interactions of a spin current in N and the magnetization vector of the FMI, resulting in characteristic modulations of the longitudinal (Chapter 2) and transverse (Chapter 3) resistivity of N as well as on its thermopower (Chapter 4). Very recently, Cornelissen *et al.* [181] showed, that in this context fascinating phenomena not only happen in local structures, i.e. directly at the normal metal/ferromagnetic insulator interface. These authors used a non-local measurement geometry to demonstrate the electrical excitation and detection of spin wave excitations in magnetically ordered systems (magnons). This experiment has a close link to the spin Hall magnetoresistance discussed in the present work. In the SMR, the spin current in N leads to a spin accumulation at the N/FMI interface. This spin accumulation exerts a torque on the magnetization of the FMI. However, a spin accumulation in N also induces a magnon accumulation in the FMI. This non-equilibrium magnon accumulation diffuses in the FMI and gives rise to the so-called magnon-mediated resistance (MMR) [182] in FMI/N hybrids with two spatially separated N stripes N_1 and N_2 [cf. Fig. 5.1(a)]:

By applying a charge current to the first normal metal strip (N_1), a spin current with spin polarization $\mathbf{s} \parallel \mathbf{t}$ propagating towards the FMI layer F is generated via the spin Hall effect. The resulting spin accumulation at the N/FMI interface generates a local excitation of a magnon population in the FMI layer. This magnon accumulation decays with increasing distance form the N/FMI interface. If one now places a second normal metal strip N_2 within the range of the magnon decay length, the magnons can excite a spin current in N_2 propagating along $\mathbf{n}$. That spin current can be detected in the charge channel utilizing the inverse spin Hall effect, generating a voltage along the $\mathbf{j}$ direction in N_2.

The presence of these magnons in the FMI, however, is limited by the magnon relaxation length λ_{m}. By varying the distance d between both normal metal stripes, Cornelissen *et al.* extracted $\lambda_{\mathrm{m}} \approx 10\,\mu\mathrm{m}$ for YIG thin films ($t_{\mathrm{F}} \approx 200\,\mathrm{nm}$) at room temperature. This length scale is up to three orders of magnitude higher than the spin diffusion length λ in normal metals. The observation of this magnon-mediated effect can be seen as the latest step on the pathway towards spin information processing. The efficiency of this effect can be parameterized by a generalization of the spin mixing interface conductance
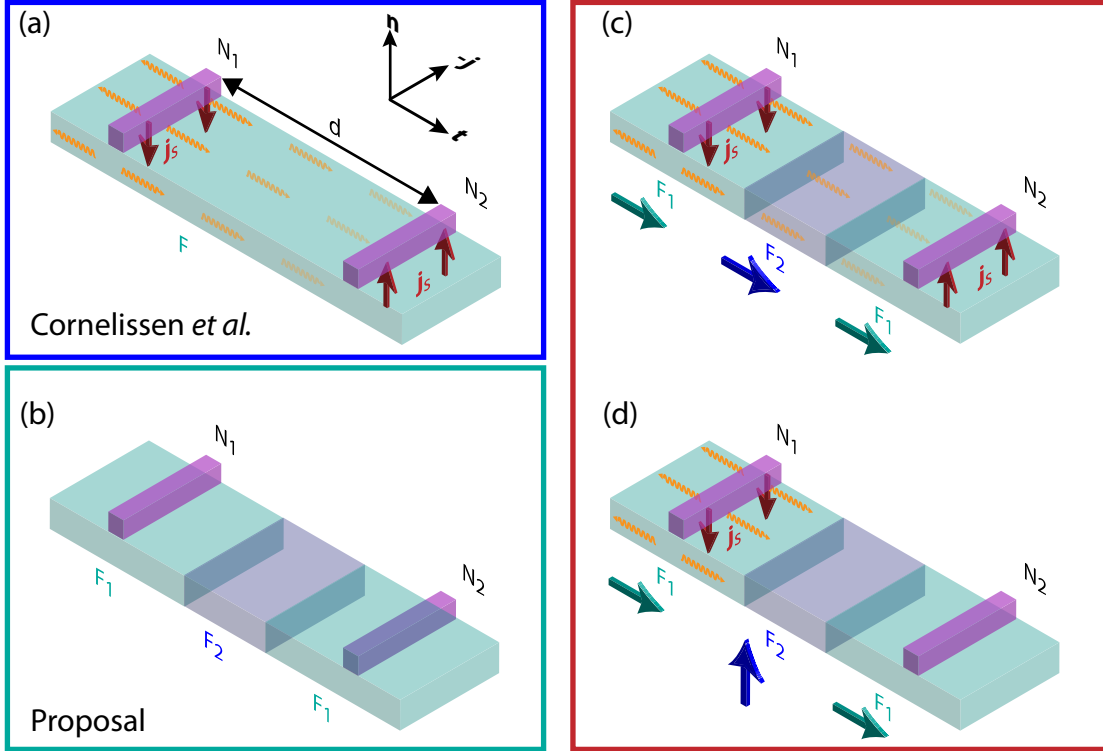
Figure 5.1: Non-local transport in FMI/N hybrids: **(a)** By driving a charge current in a normal metal strip N_1, a spin current $\mathbf{j}_s$ with spin polarization $\mathbf{s} \parallel \mathbf{t}$ is generated, propagating along $-\mathbf{n}$. The spin accumulation in N induces a local magnon accumulation in the FMI layer (orange arrows). The magnon accumulation decays with increasing distance to the FMI/N_1 interface. If a second normal metal strip N_2 is placed on top of the FMI and its distance d to N_1 is within the magnon decay length, the magnon accumulation below N_2 indues a spin current $\mathbf{j}_s$ in N_2. **(b)** Assuming that the FMI layer in panel **(a)** consists of two different ferromagnetic materials F_1 and F_2, the non-local structure acts as a magnon current switch. **(c)** If the magnetizations of F_1 and F_2 are aligned parallel, magnons can travel from the first F_1 region to the second one. This situation is in analogy to **(a)**. **(d)** By rotating the magnetization of F_2 by 90° with respect to F_1, the magnon propagation and thus the spin injection to N_2 is suppressed. Therefore, F_2 acts as a gate for the magnon propagation.

$G_{\uparrow\downarrow}$. At this point, we want to note that in the present SMR model used in this work, MMR-related effects are not explicitly taken into account. However, this again indicates the importance of $G_{\uparrow\downarrow}$. As we already pointed out in the summary of Chapter 2, further investigations on internal properties like anisotropy and magnetization dependence of $G_{\uparrow\downarrow}$ are crucial for spintronics in hybrid systems.

Against the background of the recently published MMR effect, we here suggest a new architecture based on the interplay of spin currents and magnons. The basic idea behind this magnon current switch (MCS) is sketched in Fig. 5.1(b). The main difference to the sample layout used by Cornelissen *et al.* is the integration of a second ferromagnetic, not necessarily insulating layer (F_2) between N_1 and N_2. F_2 divides the initial F layer in

two F_1 parts. We here assume no exchange coupling between F_1 and F_2, which can be achieved experimentally by additional, thin, non-magnetic buffer layers between F_1 and F_2. By applying a charge current to N_1, magnons can be generated in F_1 in accordance to the first part of the MMR effect. This can be seen as the source of the magnon current switch. The F_2 layer now acts as a gate on the magnon propagation in the FMI stack. If the magnetizations $\mathbf{M}_1$ and $\mathbf{M}_2$ of F_1 and F_2 are aligned parallel [cf. Fig. 5.1(c)], the magnons can propagate towards the second F_1/N_2 interface, where they excite a spin current in N_2 (drain). If, however, $\mathbf{M}_1$ and $\mathbf{M}_2$ are oriented perpendicular [cf. Fig. 5.1(d)], the magnons can not cross the F_1/F_2 interface and are restricted to F_1. In this case, the spin current injection at the drain is prohibited.

To realize the magnon current switch, we propose two possible scenarios: If one uses a metal oxide layer for N, the MCS could be realized in an all-oxide structure. Recently, Qiu *et al.* published spin Seebeck effect measurements obtained in a YIG/IrO$_2$ hybrid structure with $\theta_{\mathrm{SH}}^{\mathrm{IrO_2}} \cdot \lambda^{\mathrm{IrO_2}} = 0.15\,\mathrm{nm}$ [183]. The size of this product is comparable to the values for Pt obtained in Sec. 2.3.6 in this work. This makes metals oxides (one may also think of e.g. rubidium oxide and ruthenium oxide) to possible candidates for spintronics. Another advantage is that rutile-structured IrO$_2$ and its relatives can also be grown epitaxially [184] via pulsed laser deposition. One therefore can assume a MCS structure consisting of a metal oxide bottom layer N_1 ($t_{N_1} \approx 2\,\lambda_{N_1}$), followed by a $F_1/F_2/F_1$ tri-layer and a second N layer [cf. Fig. 5.2(a)][1]. To switch the MCS, the coercive fields of F_1 and F_2 have to be different. Taking advantage of materials already available from the PLD system at the WMI, yttrium iron garnet (YIG, $\mu_0 H_c^{\mathrm{YIG}} \approx 5\,\mathrm{mT}$) and gadolinum iron garnet (GdIG, $\mu_0 H_c^{\mathrm{GdIG}} \approx 50\,\mathrm{mT}$) may be proper candidates [185, 186]. To avoid exchange coupling between YIG and GdIG, another garnet structure with diamagnetic properties like yttrium aluminum garnet (YAG) may be used as a thin buffer layer (not shown here). The thicknesses of F_1 and F_2 should be chosen in a way that the total thickness of the garnet stack does not exceed λ_m. In this all-oxide structure, a second metal oxide can be used as a top layer with $t_{N_2} \approx 2\,\lambda_{N_2}$. In an initial state, the magnetizations $\mathbf{M}_{\mathrm{YIG}}$ and $\mathbf{M}_{\mathrm{GdIG}}$ are assumed to be oriented parallel to an external magnetic field $\mu_0 H < -\mu_0 H_c^{\mathrm{GdIG}}$. By applying a charge current to N_1, a magnon population can be induced in the lower GdIG layer, propagating through the ferromagnetic stack in this configuration and thus injecting a spin current to N_2. By increasing the external field to a value $\mu_0 H_c^{\mathrm{YIG}} \leq \mu_0 H \leq \mu_0 H_c^{\mathrm{GdIG}}$ and subsequently rotating the magnetic field by 90° in the film plane, the magnetization of the YIG layer can be rotated, while the magnetization orientations of the GdIG layers are pointing along the initial direction. In this

---

[1]Platinum does not serve as a proper candidate in this case, since Felix Schade and Dominik Irber showed during their Bachelor's theses, that both the electrical properties of Pt and the magnetic properties of the YIG layer change crucially if one deposits a YIG film via PLD on top of a thin Pt layer [111, 142].
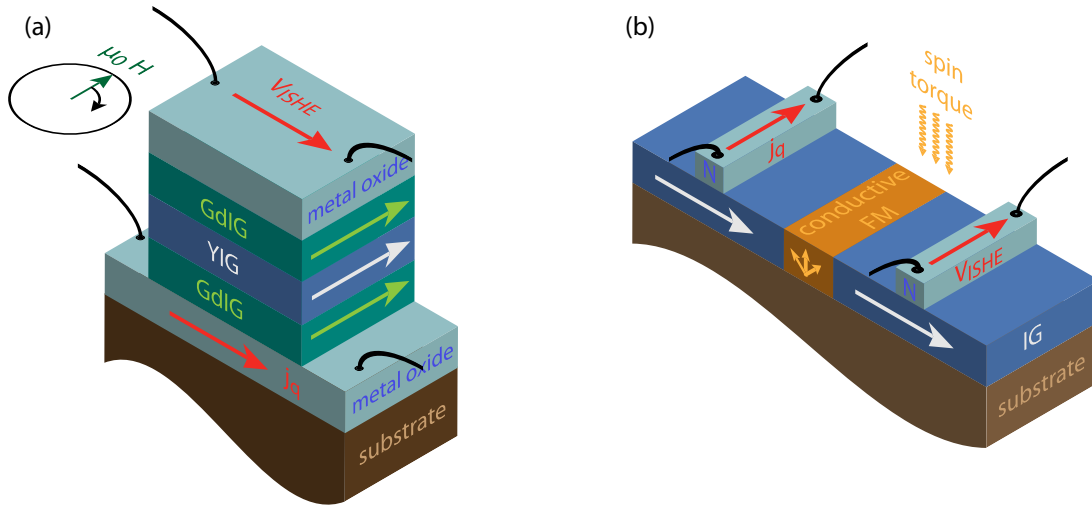
Figure 5.2: Two possible architectures for the MCS: **(a)** In an all-oxide version, the MCS structure (consisting of a metal oxide and a stack of rare earth iron garnets with different coercive field strength, e.g. YIG and GdIG) can be epitaxially grown *in situ* via pulsed laser deposition. In this geometry, the two different operation modes can be achieved via an external magnetic field. **(b)** The second geometry includes the inset of a ferromagnetic conductive layer between two parts of a ferromagnetic insulator [e.g. an iron garnet (IG)]. In this case, the switching of the magnetization orientation of the conductive ferromagnet can e.g. be realized via current driven spin torque.

configuration, no magnon transport through the YIG layer is possible and thus no spin current is injected to N_2.

However, a second approach can be realized by a more complex sample patterning via electron beam evaporation. We here assume a sample geometry like the one used in Cornelissen *et al.* [181] and Goennenwein *et al.* [182] [cf. Fig. 5.2(b)]. In this configuration, we start from an Iron Garnet (IG) thin film (F_1, $t_{IG} \approx 100$ nm, 1d transport regime) with two normal metal (e.g. platinum) stripes ($t_{N_1} = t_{N_2} \approx 2\lambda$) with distance $d \leq \lambda_m$ on top. A part of the IG thin film between N_1 and N_2 can be removed via e.g. argon ion beam milling and re-filled with a conductive ferromagnet like nickel (F_2, $\mu_0 H_c^{IG} > \mu_0 H_c^{F_2}$) by electron beam evaporation. For the following discussion, we assume the sample to be initially placed in an external magnetic field $\mu_0 H$ applied in plane perpendicular to the N stripes, that is increased from $\mu_0 H < -\mu_0 H_c^{IG}$ to $\mu_0 H_c^{F_2} < \mu_0 H < \mu_0 H_c^{IG}$ and subsequently rotated out of plane, such that the magnetization of the IG should be still oriented in the sample plane, while $\mathbf{M}_2$ is oriented perpendicular to $\mathbf{M}_{IG}$. Therefore, the magnon propagation from the left part of the IG to the right part is prohibited in this initial state. In this geometry, the conductive F_2 layer can be connected to a current source. By taking advantage of e.g. the current-induced spin orbit torque effect [187], the magnetization of F_2 can be rotated electrically by a charge current. This allows for an all-electrical switching of the MCS in the second geometry. Of course, both geometries

will need a careful optimization of the material combination, growth, patterning and experimental investigation. Both approaches will provide further steps towards spintronic data processing.

However, not only the "classical", charge-driven spin caloritronics provide promising perspectives for future experiments. The observation of the spin Nernst effect (SNE) in platinum reported in Chapter 4 covered one of the last missing links in spin caloritronics. By now, the heat to spin current efficiency observed for platinum in this work is rather small ($\theta_{\mathrm{SN}} \approx -0.2$). However, as the spin Nernst angle θ_{SN} is related to the spin Hall angle θ_{SH}, one may think of θ_{SH} as an indicator for the conversion efficiency of the spin Nernst effect. Even though both quantities have been reported to differ in sign and magnitude (cf. Sec. 4.3.7), they are based on the same ground, the spin orbit interaction (SOI). One therefore can assume that materials with large SOI showing a large spin Hall angle, also exhibit a significantly large θ_{SN}. Identifying such materials will be the next step towards spin caloritronic applications of the SNE. Promising candidates are tantalum and tungsten, for which large spin Hall angles $\theta_{\mathrm{SH}}^{\mathrm{Ta}} \approx 0.15$ [188] and $\theta_{\mathrm{SH}}^{\mathrm{W}} \approx 0.4$ [189] have been reported. This represents an increase of about 50% (300%) with respect to Pt.

In Sec. 4.1.2 we already pointed out, that charge and spin current effects as well as electric and thermoelectric phenomena are linked closely. However, focusing on the combination of thermal gradients and spin currents, one can find additional connections in spin caloritronics itself. The first spin caloritronic effects reported in the literature focused on longitudinal effects, i.e. when the resulting effect is aligned parallel to the driving force. This contained for example the generation of a spin current along a heat current. Motivated by the Seebeck effect (cf. Sec. 4.1.1) as an electrical analog, this effect is referred to as the spin Seebeck effect (SSE) [31, 35–38]. While the original experiment in a transverse geometry [31, 35–37] was discussed controversially during the past years [43, 190, 191], Uchida *et al.* also suggested experiments in a longitudinal geometry [34] [depicted in Fig. 5.3 (a)]. These experiments, first reported in YIG/Pt bilayers, were repeated in various material combinations [33, 192–196] as well as in modified setups [41, 197]. However, the spin Nernst effect (SNE) reported in this work can be seen as a relative of the SSE. Here, the heat current evokes a spin current in perpendicular geometry [cf. Fig. 5.3(b)]. Even though an adjacent ferromagnetic insulator is not necessary for the generation of the SNE, the electrical read-out of $\mathbf{j}_{\mathrm{s}}$ is only possible in the presence of a FMI/N interface (spin Nernst magneto-thermopower, see Ch. 4).
Connected closely to the Seebeck effect, the Peltier effect describes the formation of a heat current from a charge current. A corresponding spin current effect, the spin Peltier effect (SPE)[cf. Fig. 5.3 (a)], was reported recently by Flipse *et al.* [159]. These authors
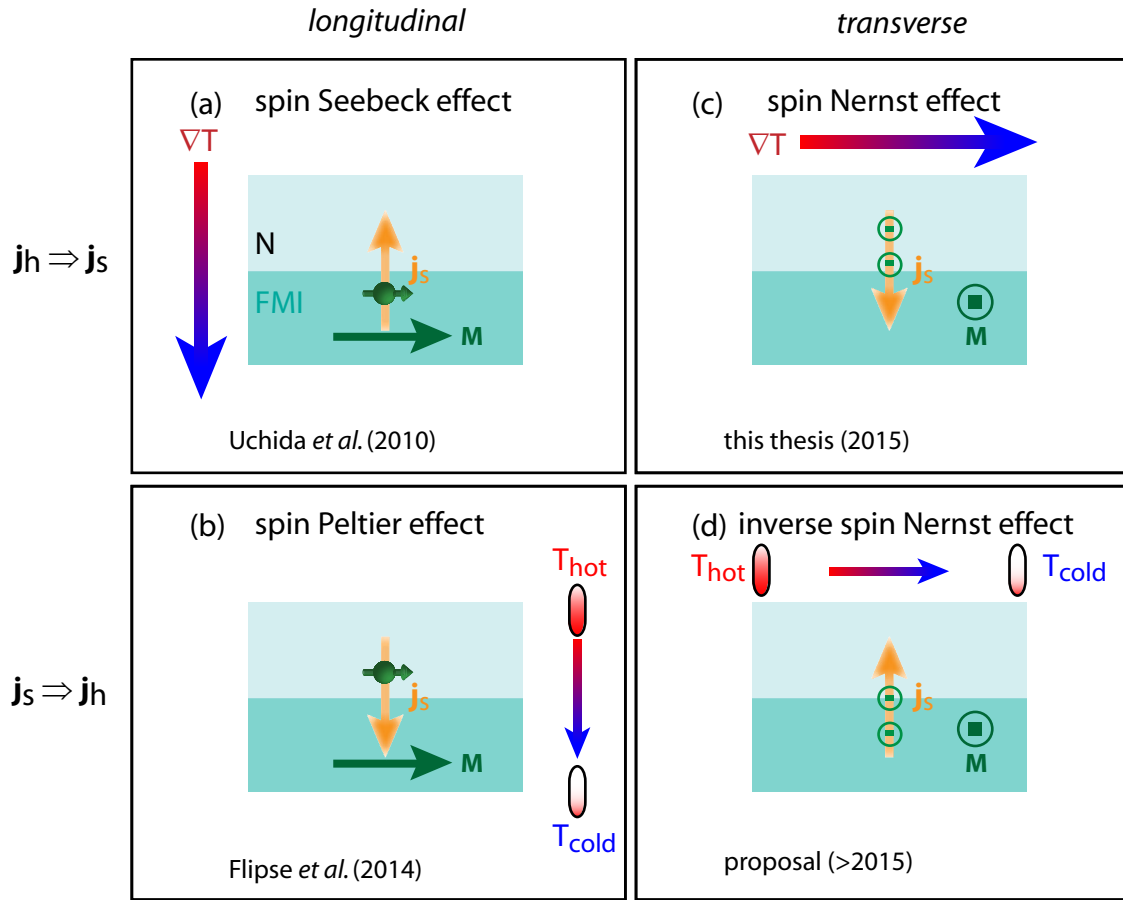
longitudinal   *transverse*

Figure 5.3: Longitudinal and transverse spincaloric effects: **(a)** the spin Seebeck effect (SSE) describes the conversion of a heat current to a spin current along ∇T. **(b)** Its inverse effect, the spin Peltier effect (SPE), is the generation of a heat current parallel to an initial spin current. **(c)** The spin Nernst effect reported in this work can be interpreted as a transverse relative of the SSE, i.e. the generation of a spin current perpendicular to ∇T. **(d)** In analogy to the SPE, we here propose the existence of an effect converting a spin current to a transverse heat current, i.e. the inverse spin Nernst effect.

also confirmed the connection between the SSE and the SPE via Onsager's reciprocal relations [170, 171].

Motivated by this connection, we here postulate the existence of an other spincaloric effect, the inverse spin Nernst effect (ISNE). As already stated by its name, the ISNE is the opposite effect of the SNE and describes the generation of a heat current transverse to a spin current $\mathbf{j}_{\mathrm{s}}$ with spin polarization $\mathbf{s}$. The mechanism behind the ISNE, like for the direct and inverse spin Hall effect (SHE and ISHE) discussed in Sec. 2.1.2, is the spin orbit interaction. We therefore propose that the heat current $\mathbf{j}_{\mathrm{h}}^{\mathrm{ISNE}} = -\kappa \nabla T$ is again proportional to the spin Nernst angle θ_{SN}, $\mathbf{j}_{\mathrm{h}}^{\mathrm{ISNE}} = \theta_{\mathrm{SN}} \left(\frac{2e}{\hbar} \right) \left(\frac{-\kappa \rho}{S} \right) (\mathbf{s} \times \mathbf{j}_{\mathrm{s}})$.

In experiments, we suggest to detect the ISNE in a SMR like geometry (cf. Fig. 5.4).

Considering a normal metal thin film like platinum, a spin current $\mathbf{j}_\mathrm{s}$ along $\mathbf{n}$ can be generated from the spin Hall effect by applying a charge current $\mathbf{j}_\mathrm{q}$ to N along $\mathbf{j}$. For the following discussion, we assume the spin polarization $\mathbf{s}$ of the resulting spin current to point along $\mathbf{t}$. By utilizing the spin transfer torque mechanism at a N/FMI interface, the spin current back flow in N can be modulated in a SMR like fashion (cf. Ch. 2). We here propose that both, $\mathbf{j}_\mathrm{s}$ and the back flow $\mathbf{j}_\mathrm{s}^\mathrm{back}$ are not only converted to charge currents via the ISHE, but also to a heat current along $\mathbf{j}$ via the ISNE. In the case of open spin current boundary conditions [cf. Fig. 5.4 (a)], one finds $\mathbf{j}_\mathrm{s}^\mathrm{back} = -\mathbf{j}_\mathrm{s}$, and thus no net spin current flows in N and one expects no contribution from the ISHE as well as from the ISNE. For closed spin current boundary conditions, however, the spin current back flow $\mathbf{j}_\mathrm{s}^\mathrm{back}$ is suppressed. In this case, both ISHE (not shown here) and ISNE act on $\mathbf{j}_\mathrm{s}$ [cf. Fig. 5.4 (b)]. The ISNE separates particles with higher entropy from particles with lower entropy. Both species, however, carry the same electric charge q and the same spin angular momentum $\mathbf{s}$. Thus, only a difference in entropy builds up along $\mathbf{j}$, while this contribution is not
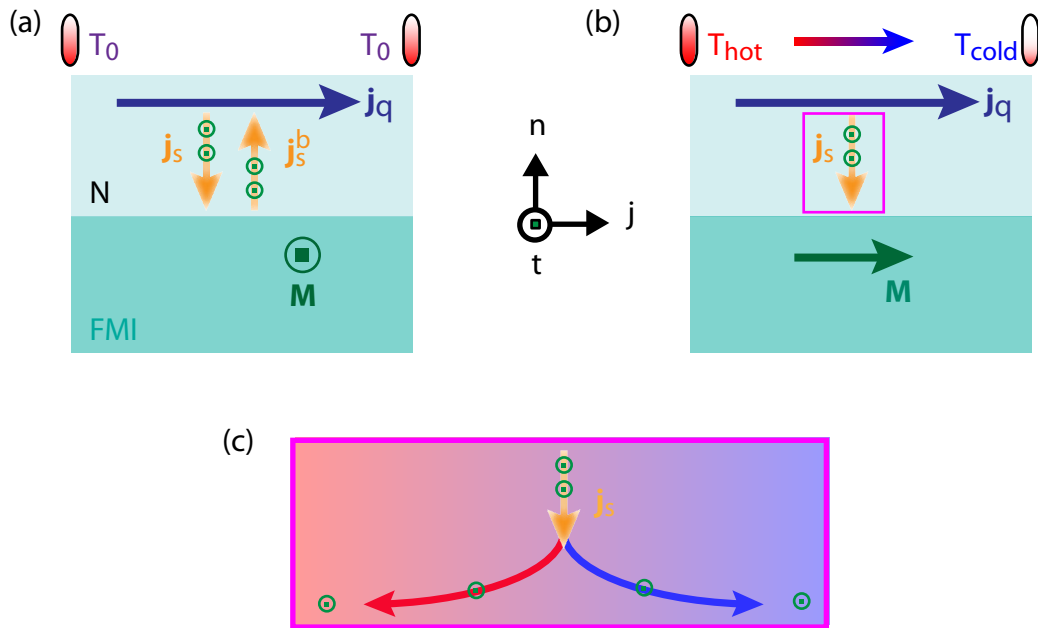
Figure 5.4: Experimental detection of the inverse spin Nernst effect: A charge current $\mathbf{j}_\mathrm{q} \parallel \mathbf{j}$ applied to a normal metal gives rise to a spin current $\mathbf{j}_\mathrm{s} \parallel -\mathbf{n}$ (green) with spin polarization $\mathbf{s} \parallel \mathbf{t}$ via the SHE. **(a)** For open spin current boundary conditions, the spin current back flow $\mathbf{j}_\mathrm{s}^\mathrm{back}$ compensates $\mathbf{j}_\mathrm{s}$. In this case, also the action of the ISNE on $\mathbf{j}_\mathrm{s}$ will be compensated by the ISNE acting on $\mathbf{j}_\mathrm{s}^\mathrm{back}$ and one finds a homogeneous temperature T_0 along $\mathbf{j}$. **(b)** For closed spin current boundary conditions, the spin current back flow $\mathbf{j}_\mathrm{s}^\mathrm{back}$ is suppressed and the ISNE merely acts on $\mathbf{j}_\mathrm{s}$. **(c)** The action of the ISNE leads to a separation of $\mathbf{j}_\mathrm{s}$ contributions with higher and lower entropy (indicated by the red and blue arrows), leading to an entropy accumulation at the interfaces of N along $\mathbf{j}$. This results in a heat current along $\mathbf{j}$.

accompanied by a charge or spin accumulation [see Fig. 5.4 (c)]. On the other hand, the action of the ISHE on the spin current leads to an electric field building up along $\mathbf{j}$, which is not accompanied by a net difference of entropy along $\mathbf{j}$. Thus, the observation of a temperature gradient along the initial charge current $\mathbf{j}_q$, i.e. in conventional SMR experiments as we reported them in Chapter 2, can be directly attributed to the inverse spin Nernst effect[2]. In particular, we suggest to detect the temperature profile of the Pt thin film along $\mathbf{j}$ as a function of the spin transfer torque modulated boundary conditions (i.e. via rotating the magnetization of the FMI in e.g. in-plane geometry), e.g. via infrared camera or thermocouples at both ends of a FMI/N Hall bar. One should find a $\cos^2(\alpha)$ shaped modulation of T as a function of the magnetization orientation. The modulation amplitude stemming from the interaction of the SHE and the ISNE will be proportional to $\theta_{SH}\theta_{SN}$. Thus, for experiments performed on YIG/Pt at room temperature, we expect $\Delta T/T$ to be of the order of 2×10^{-3}.

Taken together, we await a number of fascinating new experiments in the field of spin caloritronics. Therefor, only a slight modification of the current sample design and experimental setups is necessary. While all experiments proposed in this outlook can be performed on hybrid structures consisting of YIG and Pt, they are of course not restricted to this well-established material combination. The concepts developed in this thesis allow for both, the basic research on spin caloritronic effects and its search for most applicable material combinations as well as for a further development of spin current based data processing.

---

[2]We here assume the applied charge current $\mathbf{j}_q$ to be small enough to avoid heating effects.

6 Appendix

6.1 Samples

This section provides an overview of all samples investigated in this work.

6.1.1 YIG anisotropy

$T(\mathrm{K})$	$\rho_0(\mathrm{n\Omega m})$	oopj: $-\Delta\rho_1/\rho_0(\times 10^{-4})$	oopt: $\Delta\rho/\rho(\times 10^{-5})$	$B_\mathrm{u}(\mathrm{T})$
5	n.a.	n.a.	3.8	0.40
10	225	3.1	4.1	0.32
15	n.a.	n.a.	4.3	0.30
20	n.a.	n.a.	4.9	0.29
30	n.a.	n.a.	4.5	0.28
40	n.a.	n.a.	3.3	0.25
50	n.a.	n.a.	2.0	0.25
100	257	5.4	<1.0	0.25
300	335	6.4	n.a.	0.1

Table 6.1: Temperature dependent simulation parameters for the sample YIG61 (see Tab. 6.2). $-\Delta\rho_1/\rho_0$ extracted from oopj rotation simulations indicate the SMR ratio, while $\Delta\rho/\rho$ taken from oopt rotations at low temperatures represent the Pt-MR discussed in Sec. 2.4.3. All data including the shape anisotropy field B_u taken at $\mu_0 H = 1\,\mathrm{T}$.

6.1.2 YIG/Pt hybrids

sample ID	t_F(nm)	t_N(nm)	h(nm)	ρ_0(nΩm)	$-\Delta\rho_1/\rho_0(10^{-4})$	B_n(mT)	Figure
YY17	64.2	3.0	0.8	538	13.5	60	2.8, 2.16, 2.18, 2.19, 2.20
YY21	61.0	19.5	1.0	370	2.70	80	2.8, 2.16, 2.18, 2.19, 2.20, 3.4, 3.8
YY22	63.2	6.5	0.9	431	7.66	50	2.8, 2.10, 2.11, 2.16, 2.18, 2.19, 2.20, 3.4, 3.8
YY26	60.0	12.8	1.5	702	2.71	75	2.16
YY30	55.5	3.1	1.0	477	11.5	90	2.14, 2.21, 3.7, 3.8
YY32	53.6	2.5	1.1	358	10.6	80	2.16, 3.8
YY33	46.4	21.7	1.7	347	2.2	60	2.16
YY34	46.8	1.9	1.5	1331	6.76	n.a.	2.16
YY35	53.5	1.2	0.9	1462	6.0	70	3.8
YY42	48.7	2.0	0.6	648	9.5	70	2.16, 3.4, 3.6, 3.8
YY56	33.5	0.8	0.7	1166	6.0	n.a.	, 2.8, 2.18, 2.19, 2.16, 2.20, 3.8
YY58	57.0	2.0	0.8	368	10.5	60	, 2.8, 2.18, 2.19, 2.16, 2.20, 3.8
YIG20	53.7	6.1	0.7	356	5.6	n.a.	2.15
YIG53	53.4	2.5	0.5	833	10.8	120	2.8, 2.18, 2.19, 2.16, 2.20
YIG55	46.2	3.5	0.7	558	8.95	70	2.8, 2.18, 2.19, 2.16, 2.20
YIG56	68.7	2.7	0.3	454	10.54	150	2.16
YIG57	57.8	2.2	0.7	701	11.7	90	2.8, 2.10, 2.11, 2.12, 2.13, 2.18, 2.19, 2.16, 2.20
YIG59	60.7	11.1	0.6	284	4.58	n.a.	2.8, 2.18, 2.19, 2.16, 2.20, 3.8
YIG60	52.0	16.9	0.2	395	2.95	n.a.	2.10, 2.11, 2.16
YIG61	53.0	8.5	0.4	348	5.75	100	2.9 , 2.16, 2.17, 2.22, 2.23
YIG68	61.0	1.1	0.3	2330	3.64	n.a.	2.16
YIG69	54.0	1.2	0.4	2074	3.85	n.a.	2.16
YIG70	54.8	17.2	0.6	331	3.3	n.a.	2.8, 2.18, 2.19, 2.16, 2.20
YIG73	28.9	1.8	0.1	557	15.0	n.a.	2.16
YIG105	16.3	2.8	0.6	947	14.8	n.a.	2.28
YIG106	44.5	3.2	0.7	869	13.2	n.a.	2.28
YIG112	74.0	3.0	0.6	894	14.5	n.a.	2.28
YIG113	200^a	2.9	n.a.	883	13.6	n.a.	2.28
YIG145	3.9	3.2	0.5	920	4.1	n.a.	2.27, 2.28

Table 6.2: YIG thickness t_F, Pt thickness t_N, interface roughness h, sheet resistivity ρ_0, SMR amplitude $-\Delta\rho_1/\rho_0$ and ρ_2 for all samples investigated in this work. "YIG" indicates samples grown on (111)-oriented GGG substrates, while "YY" stands for samples grown on (111)-oriented YAG. While $-\Delta\rho_1/\rho_0$ is independent of the external magnetic field strength in good approximation, ρ_0 as well as ρ_2 represent the value taken at 1 T. All data taken at 300 K. The last column indicates the figures the respective sample was used for.

---

^{a}for $t \geq 100$ nm, the determination of the film thickness via X-ray reflectometry does not work properly.

6.1.3 SNMTP samples

name	sample ID	substrate	t_F(nm)	t_N(nm)	Figure
Ernst3	YIG101	GGG (111)	40	4.1	4.7 - 4.10, 4.12 - 4.14, 4.17, 4.18
Ernst4	YY79	YAG (111)	51	3.9	4.19

Table 6.3: Samples used for SNMTP measurements: Nonofficial and official sample ID, substrate material, YIG thickness t_F and Pt thickness t_N.

6.1.4 Thermal conductivity for GGG/YIG/Pt

Material	thermal conductivity [W/(Km)]	heat capacity [J/(kgK)]	density (kg/m^3)
Pt	72 (Ref. [198])	130 (Ref. [198])	21450 (Ref. [198])
YIG	6 (Ref. [199])	570 (Ref. [200])	5170 (Ref. [201])
GGG	8 (Ref. [180])	400 (Ref. [200])	7080 (Ref. [200])

Table 6.4: Material parameters used for the finite elements simulation of the temperature profile in our sample.

6.1.5 Pt on YAG substrate

Sample ID	t_N(nm)	ρ_0(nΩm)	Figure
PtY1	3.5	531	2.24, 2.25, 2.27, 2.28, 3.5, 3.8
PtY2	15.6	377	2.26, 3.5 , 3.8
PtY4	2.0	717	3.5, 3.8

Table 6.5: N layer thickness determined by HR-XRR and sheet resistivity ρ_0 taken at $300\,\text{K}$ for the Pt thin films deposited directly onto YAG substrates.

6.2 3D vector magnet cryostat "Chaos"

During the term course of this thesis, we set up a new measurement setup for magnetotransport experiments. An Oxford Instruments vector magnet cryostat was installed at the WMI in 2012. This system, called the "Chaos" cryostat[1] consists of a ^{4}He flow cryostat with a nitrogen (N_2) shield and includes a vertically oriented 6 T solenoid (z axis) combined with two horizontally oriented 2 T split coil pairs (x and y axis) (see Fig. 6.1). The magnet system can be operated in two ways:

- in a single axis mode, up to 6(2) T are provided in the vertical (horizontal) direction.

- in a combined operation, the flux density vector can be oriented in arbitrary orientations.

In the second case, the magnitude of the flux density vector is limited to that of the horizontal axis (2 T). The magnetic field is controlled by a Mercury IPS superconducting magnet power supply master/slave system. It provides output currents of up to 120 A in bipolar operation for each magnet axis. The control of the system is feasible either directly via touch-screen or remote using a LabView based software.

The Chaos cryostat has a IN100 variable temperature insert (VTI), enabling an operation for temperature setpoints between 1.5 K and 300 K. The temperature control of the sample space inside the VTI can be achieved via an auto needle valve drive for helium flow control and/or an auto heater system. The temperature of the VTI is read by a Cernox sensor fitted to the heat exchanger.

A remote control of the system is realized by a LabView based software. It provides control of the VTI (heater, needle valve, temperature setpoint) and the IPS (control of the magnetic field setpoints and energization rates for the x, y and z direction) as well as a display of the actual He and N_2 levels.

6.3 Design of a new dipstick for caloritronics

To optimize the control of the temperature gradient direction in spin caloritronic experiments, we performed our measurements in the absence of an exchange gas. Therefore, we developed a new dipstick design. We covered the whole sample space from the bottom of the VAC dipstick[2] up to the entrance of the VTI with a steel jacket. A T-shaped flange at the top provides the connection to a pumping station (Pfeiffer Hi cube 80 eco) to evacuate the jacket. The pressure inside the jacket is read by a combined pressure

---

[1]Chaos is an acronym for "Cold, Hot And Other Secret experiments", which is also the name of the new lab.
[2]VAC stands for Vacuum Assisted Caloritronics.
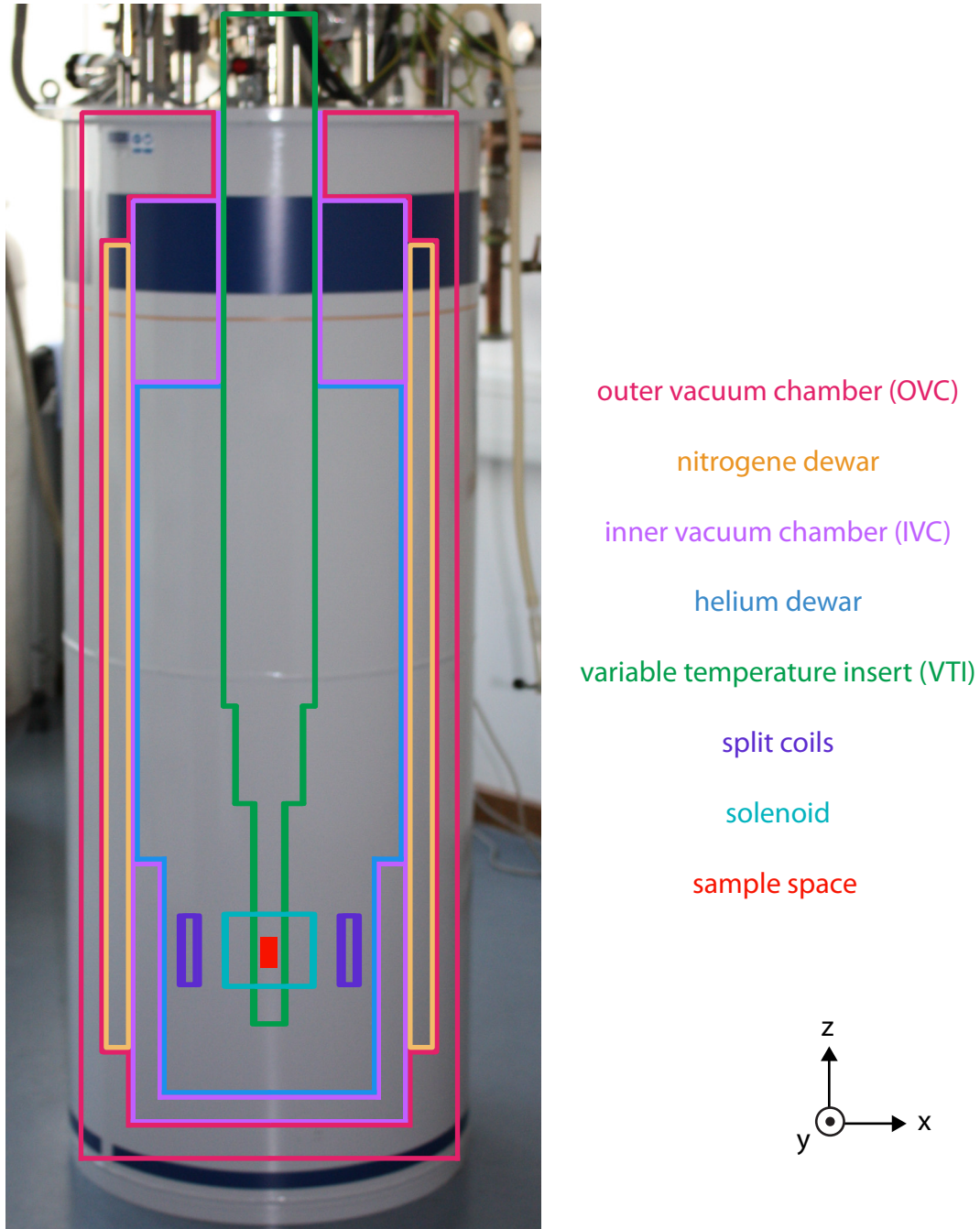
Figure 6.1: The "Chaos" cryostat (components see legend).

sensor (range from room pressure to 10^{-9} mbar) next to the connection to the pumping station (not shown here). Temperature dependent thermal extensions of the system are absorbed by a bellow (cf. Fig. 6.2) to guarantee a good thermal connection between the sample stage and the VTI (see below).

The temperature control of the sample space is provided by a $320\,\Omega$ resistive heater and a Cernox SD 1050 temperature sensor mounted to two cutouts at the dipstick's copper base. This base (labeled as "11" in Fig. 6.2) serves as a heat bath for the sample stage.
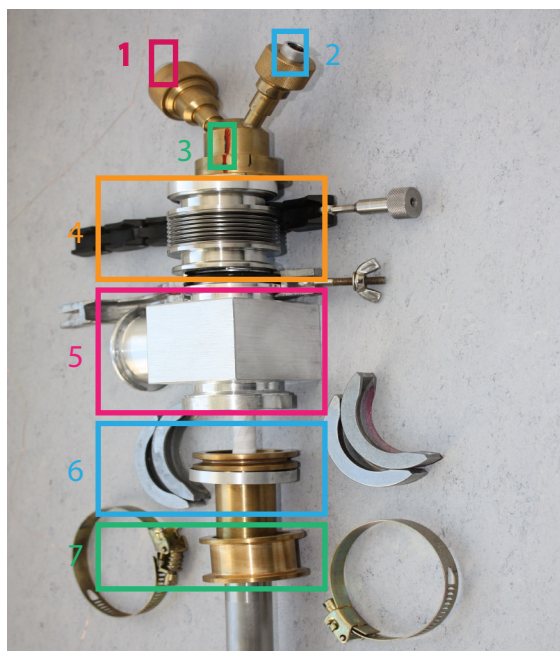
Upper part:

1   24 pin Fischer connector (sample wiring)
2   19 pin Fischer connector (temperature control)
3   alignment marker
4   20mm bellow
5   T flange
6   jacket top flange
7   adapter piece

Lower part:

8   dipstick
9   320 Ohm heater
10   Cernox sensor
11   copper base
12   wiring guides
13   cooling lines (silver)
14   sample stage
15   dipstick thermal contact plate (copper)
16   steel jacked
17   jacket thermal contact plate (copper)
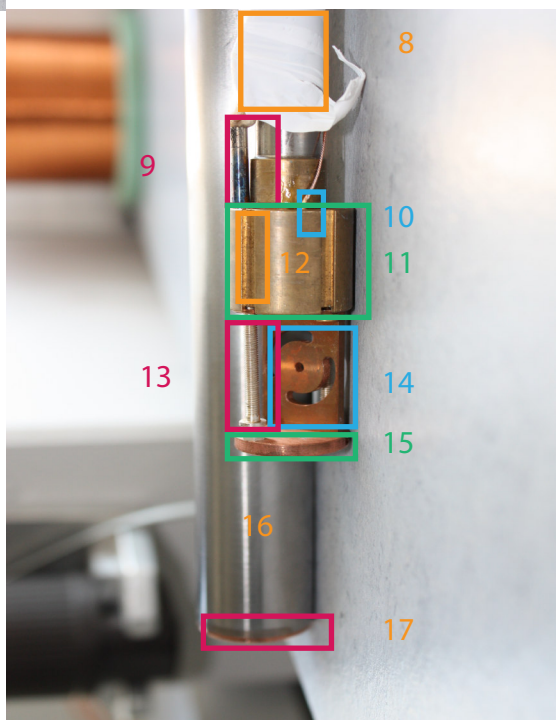
Figure 6.2: Dipstick components (see legend).

Cooling provided by the He gas inside the VTI is transferred to the inside of the jacket by a copper-made thermal contact plate at the lower end of the jacket. This plate ("17") is in direct thermal contact to a second copper plate ("15") on the top of the sample stage ("14"). To improve this thermal contact, we additionally added two silver-made cooling lines ("13") connecting the contact plate and the copper base.

The active temperature control of the sample holder mounted to the sample stage (see Fig. 6.3) is given by a Lakeshore LS340 temperature controller. Therefore, the wiring of
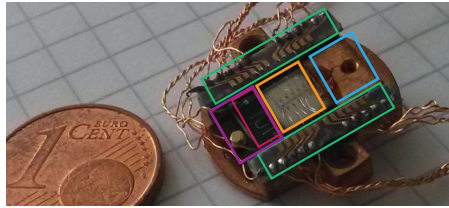
plastic block
bonding frame
100Ω resistive heater
sample
Copper block (heat sink)

Figure 6.3: Sample holder (components see legend). The one Euro cent coin serves for scaling.

the heater (two enameled copper wires) and the Cernox sensor (part of a 12×2 twisted pair manganin ribbon cable) is fed through the inside of the dipstick and leads to a 19 pin Fischer connector at the top of the dipstick ("2"). Eight wires leading to this Fischer connector end at two times four pins of female five-pin connectors at the middle part of the dipstick. The counter part of the first connector (labeled with "F") is linked to the wiring of the $100\,\Omega$ resistive heater and connectors for the on-chip heater, both placed on the sample holder. The counter part of the second connector (unlabeled) is linked with the wiring of the Cernox sensor. copper wires connecting the dipstick heater are directly fed into the Fischer connector.

The temperature control lines are separated from the sample holder wiring connected to the Hallbar. Four five-pin connectors (labeled with "A", "B", "C" , "D") are connected to 20 measurement wires attached to the bonding frame of the sample holder (see Fig. 6.3). The pin connectors can be plugged into four female five-pin connectors located around 15 cm above the sample space (again labeled with "A", "B", "C" , "D"). The latter are connected to a 24 pin Fischer connector at the top of the dipstick ("1") via a second 12×2 twisted pair manganin ribbon cable. The remaining contacts of the Fischer connector end at the lower part of the dipstick and are covered by Teflon band. They can be used e.g. for measurement lines at the sample stage in the future.

The Fischer connectors at the top of the dipstick can be linked to two separate measurement boxes. The electric signals from the bonding frame of the sample holder are guided to box 1 (see Fig. 6.4) via a female 24 pin Fischer connector soldered to one end of a 12×2 twisted pair Cu cable. On the other end, the shielded Cu wires of each line are capped by a gold plated crimp contact. Each crimp contact (see Tab. 6.6), is fed into a female banana plug in box 1, labeled with numbers 1 to 24. To avoid thermal voltages at the banana plugs, we only use gold plated banana pins and plugs and close box 1 during the measurements. To enable a wiring towards nanovoltmeters and current sources, the box has three Lemo four-pin connectors for nanovoltmeters and 3×4 banana contacts for source/measure units at its outer board (see legend of Fig. 6.4). Electric contacts to the 24 connectors are realized by gold plated banana pins connected flexible to each sourcemeter (nanovoltmeter) contact via shielded Cu wires (again with Au plated crimp
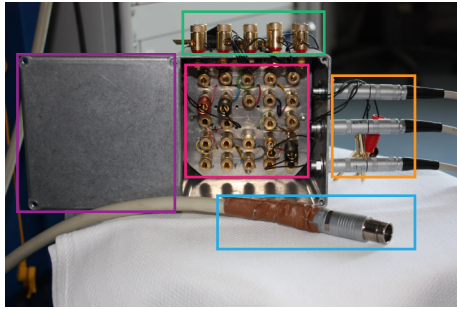
cover plate for box 1
banana to banana brigdes (to sourcemeters)
24 gold plated female banana contacts
4 pole Lemo connectors (to nanovoltmeters)
24 pin Fischer connector (to dipstick)

Figure 6.4: Measurement box 1 (components see legend).

contacts pressed into the Banana plug).

In a similar fashion, we designed a second contact box ("box 2") for the temperature control lines of the dipstick and the sample. The 19 pin Fischer connector at the top of the dipstick can be contacted via a 10×2 twisted pair shielded Cu cable soldered to a female 19 pin Fischer connector. On the other end of the cable, the Cu wires of each line are again capped by a gold plated crimp contact and each contact, labeled with numbers 1 to 19 (see Tab. 6.7), is fed into box 2. Box 2 (cf. Fig. 6.5) provides eight gold plated banana contacts at the front side. The respective lines from the data cable can be clamped into the side entrance of a banana contact. Source- and measurement devices can be directly connected to box 2 via banana to banana cables. At the moment, one of these contact pairs is used for the connection of the heater entrance of the LS340 to the contacts for the dipstick heater. A second and third pair of banana contacts provide connections between the OCH and the sample holder heater to current sources. Inside the box, the contacts for the Cernox sensor are soldered to the wires of a 2×2 twisted pair copper cable. The lose end of this cable is fed through the back side of the box and ends at a 6 pin DIN 45322 connector (two contacts are not used for LS340 operations) that can be directly connected to the sensor input of the LS340. Box 2 provides the option for a second Cernox sensor connection (not mounted). Four additional banana connectors at the back side of the box are not contacted at the moment. They may serve as connections e.g. for further temperature sensors or heaters.

6.4 Sample alignment

The sample holder (cf. Fig. 6.3) mounted to the sample stage of the dipstick (cf. Fig. 6.2) results in an orientation of the Hall bar in the previous sections) along the **z** axis of the Chaos cryostat. **z** thus corresponds to the **j** direction defined in Ch. 2. Using the alignment marker on top of the dipstick (representing the film normal), we define **x** corresponding to the **n** direction and **y** corresponding to the **t** direction in the coordinate system defined

box 2 (front view):
19 pol Fischer connector (to dipstick)
gold plated banana contacts
(OCH heater)
gold plated banana contacts
(sample holder heater)
gold plated banana contacts
(dipstick heater)

box 2 (back view):
19 pol Fischer connector (to dipstick)
6 pin connector for Cernox sensor
(to LS340)
gold plated banana contacts
(not used)
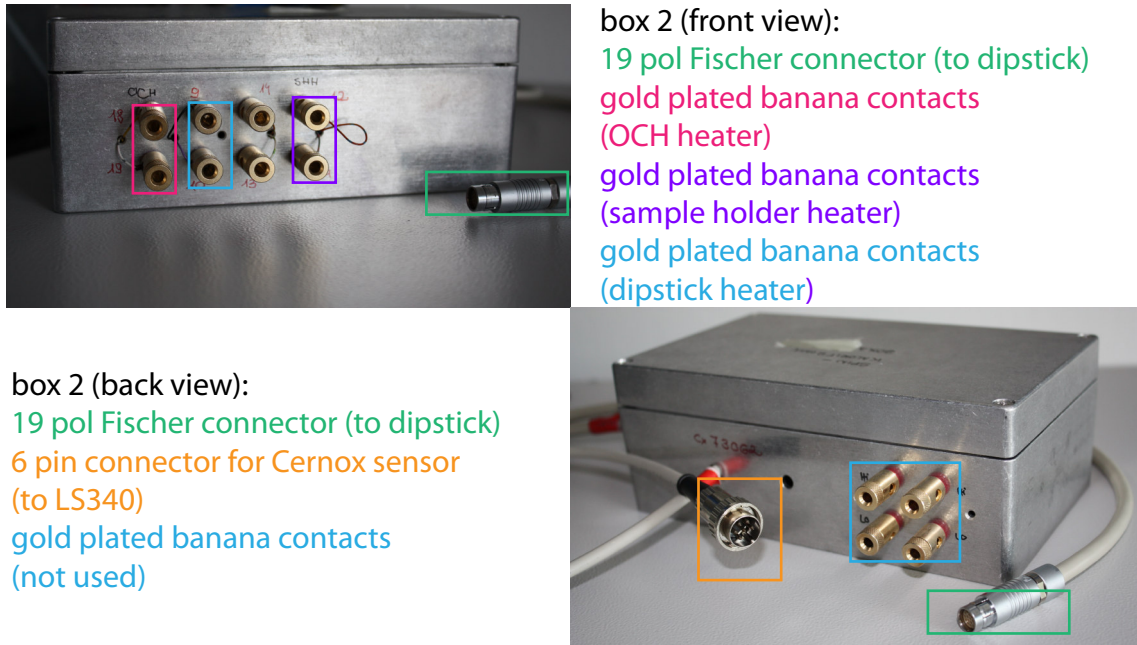
Figure 6.5: Measurement box 2 (components see legend).

contact number	shielding color	pin connector dipstick
1	white	A1
2	brown	A2
3	green	A3
4	yellow	A4
5	gray	A5
6	pink	B5
7	blue	B4
8	red	B3
9	black	B2
10	purple	B1
11	gray/pink	C1
12	red/blue	C2
13	white/green	C3
14	brown/green	C4
15	white/yellow	C5
16	brown/yellow	D5
17	white/gray	D4
18	brown/gray	D3
19	white/pink	D2
20	brown/pink	D1

Table 6.6: Contacts for measurement lines (24 pin connector, Box1).

in Ch. 2. To correct slight misalignments of **j**, **t** and **n**, we adjust the rotation planes used for magnetization orientation dependent experiments. Therefore, we utilize the Hall- and SMR effects in the YIG/Pt sample mounted and proceed as follows:

contact number	shielding color	contact name (dipstick)	function
1	white	E	Cernox 1
2	green	H	Cernox 1
3	yellow	G	Cernox 1
4	gray	F	Cernox 1
5	pink	C	Cernox 2 (not used)
6	blue	D	Cernox 2 (not used)
7	brown	B	Cernox 2 (not used)
8	red	A	Cernox 2 (not used)
9	black	P	OCH heater
10	purple	O	OCH heater
11	gray/pink	M	$100\,\Omega$ heater
12	red/blue	N	$100\,\Omega$ heater
13	white/green	L	-
14	brown/green	K	-
15	no contact	-	-
16	no contact	-	-
17	white/gray	-	-
18	brown/yellow	I	dipstick heater
19	white/yellow	J	dipstick heater

Table 6.7: Contacts for temperature control (19 pin connector, Box2).

1. First, we perform an oopj rotation (cf. Sec. 2.2.2) in e.g. two degree steps using an external field of $\mu_0 H = 1\,\mathrm{T}$ to determine the vector $\mathbf{n}'$ from the maximum Hall signal of the sample and $\mathbf{t}'$ from the vanishing Hall signal. We calculate $\mathbf{j}'$ from the cross product of $\mathbf{n}'$ and $\mathbf{t}'$.

2. We check the alignment of $\mathbf{n}'$ and $\mathbf{t}'$ using the Hall signal in an oopt rotation in two degree steps and adjust the vectors if necessary.

3. It is optional to repeat steps 1 and 2 to achieve appropriate results.

4. In the last step, we perform an in-plane rotation and check the position of the maximum and minimum longitudinal SMR signal (cf. Sec. 2.3.1).

Using this routine, an alignment error smaller than 1° can be achieved in the "Chaos'" cryostat.

Bibliography

[1] M. von Albrecht, *Publius Ovidius Naso: Metamorphosen (lateinisch und deutsch)* (Reclam, 1994).

[2] R. Franz and G. Wiedemann, Annalen der Physik **165**, 497 (1853).

[3] T. J. Seebeck, Annalen der Physik **6**, 253 (1826).

[4] J. Peltier, Physics 1–6 (1821).

[5] W. Thomson, Proceedings of the Royal Society of Edinburgh **3**, 91 (1857).

[6] G. E. Uhlenbeck and S. Goudsmit, Die Naturwissenschaften **13**, 953 (1925).

[7] F. Weinert, Studies in History and Philosophy of Science Part B: Studies in History and Philosophy of Modern Physics **26**, 75 (1995).

[8] M. Johnson and R. H. Silsbee, Physical Review B **35**, 4959 (1987).

[9] G. E. Bauer, A. H. MacDonald, and S. Maekawa, Solid State Communications **150**, 459 (2010).

[10] G. E. W. Bauer, E. Saitoh, and B. J. van Wees, Nature Materials **11**, 391 (2012).

[11] S. T. B. Goennenwein and G. E. W. Bauer, Nature Nanotechnology **7**, 145 (2012).

[12] G. E. Moore, Electronics **38**, 8 (1965).

[13] Intel, Intel homepage, http://www.intel.com/content/www/us/en/silicon-innovations/intel-tick-tock-model-general.html retrieved 01 October 2015 (2015).

[14] S. Murakami, N. Nagaosa, and S.-C. Zhang, Science **301**, 1348 (2003).

[15] Y.-T. Chen, S. Takahashi, H. Nakayama, M. Althammer, S. T. B. Goennenwein, E. Saitoh, and G. E. W. Bauer, Physical Review B **87**, 144411 (2013).

[16] Z. Qiu, Y. Kajiwara, K. Ando, Y. Fujikawa, K. Uchida, T. Tashiro, K. Harii, T. Yoshino, and E. Saitoh, Applied Physics Letters **100**, 022402 (2012).

[17] E. Saitoh, M. Ueda, H. Miyajima, and G. Tatara, Applied Physics Letters **88**, 182509 (2006).

[18] K. Ando, M. Morikawa, T. Trypiniotis, Y. Fujikawa, C. H. W. Barnes, and E. Saitoh, Journal of Applied Physics **107**, 113902 (2010).

[19] K. Ando, S. Takahashi, J. Ieda, H. Kurebayashi, T. Trypiniotis, C. H. W. Barnes, S. Maekawa, and E. Saitoh, Nature Materials **10**, 655 (2011).

[20] K. Ando, M. Morikawa, T. Trypiniotis, Y. Fujikawa, C. H. W. Barnes, and E. Saitoh, Applied Physics Letters **96**, 082502 (2010).

[21] K. Ando, S. Takahashi, J. Ieda, Y. Kajiwara, H. Nakayama, T. Yoshino, K. Harii, Y. Fujikawa, M. Matsuo, S. Maekawa, and E. Saitoh, Journal of Applied Physics **109**, 103913 (2011).

[22] A. Hoffmann, Physica Status Solidi (c) **4**, 4236 (2007).

[23] K. Ando and E. Saitoh, Nature Communications **3**, 629 (2012).

[24] F. D. Czeschka, L. Dreher, M. S. Brandt, M. Weiler, M. Althammer, I. Imort, G. Reiss, A. Thomas, W. Schoch, W. Limmer, H. Huebl, R. Gross, and S. T. B. Goennenwein, Physical Review Letters **107**, 046601 (2011).

[25] K. Uchida, T. An, Y. Kajiwara, M. Toda, and E. Saitoh, Applied Physics Letters **99**, 212501 (2011).

[26] M. Weiler, H. Huebl, F. S. Goerg, F. D. Czeschka, R. Gross, and S. T. B. Goennenwein, Physical Review Letters **108**, 176601 (2012).

[27] A. Brataas, Y. Tserkovnyak, G. E. W. Bauer, and B. I. Halperin, Physical Review B **66**, 060404 (2002).

[28] K. Uchida, T. Ota, Y. Kajiwara, H. Umezawa, H. Kawai, and E. Saitoh, Journal of Physics: Conference Series **303**, 012096 (2011).

[29] H. Adachi, J. Ohe, S. Takahashi, and S. Maekawa, Physical Review B **83**, 094410 (2011).

[30] H. Adachi, K. Uchida, E. Saitoh, J. Ohe, S. Takahashi, and S. Maekawa, Applied Physics Letters **97**, 252506 (2010).

[31] K. Uchida, S. Takahashi, J. Ieda, K. Harii, K. Ikeda, W. Koshibae, S. Maekawa, and E. Saitoh, Journal of Applied Physics **105**, 07C908 (2009).

[32] J. Xiao, G. E. W. Bauer, K. Uchida, E. Saitoh, and S. Maekawa, Physical Review B **81**, 214418 (2010).

[33] K. Uchida, T. Nonaka, T. Ota, and E. Saitoh, Applied Physics Letters **97**, 262504 (2010).

[34] K. Uchida, H. Adachi, T. Ota, H. Nakayama, S. Maekawa, and E. Saitoh, Applied Physics Letters **97**, 172505 (2010).

[35] K. Uchida, S. Takahashi, K. Harii, J. Ieda, W. Koshibae, K. Ando, S. Maekawa, and E. Saitoh, Nature **455**, 778 (2008).

[36] C. M. Jaworski, J. Yang, S. Mack, D. D. Awschalom, J. P. Heremans, and R. C. Myers, Nature Materials **9**, 898 (2010).

[37] K. Uchida, J. Xiao, H. Adachi, J. Ohe, S. Takahashi, J. Ieda, T. Ota, Y. Kajiwara, H. Umezawa, H. Kawai, G. E. W. Bauer, S. Maekawa, and E. Saitoh, Nature Materials **9**, 894 (2010).

[38] C. M. Jaworski, J. Yang, S. Mack, D. D. Awschalom, R. C. Myers, and J. P. Heremans, Physical Review Letters **106**, 186601 (2011).

[39] J. Le Breton, S. Sharma, H. Saito, S. Yuasa, and R. Jansen, Nature **475**, 82 (2011).

[40] A. Slachter, F. L. Bakker, J. Adam, and B. J. van Wees, Nature Physics **6**, 879 (2010).

[41] M. Weiler, M. Althammer, F. D. Czeschka, H. Huebl, M. S. Wagner, M. Opel, I. Imort, G. Reiss, A. Thomas, R. Gross, and S. T. B. Goennenwein, Physical Review Letters **108**, 106602 (2012).

[42] V. Cherepanov, I. Kolokolov, and V. L'vov, Physics Reports **229**, 81 (1993).

[43] S. Y. Huang, X. Fan, D. Qu, Y. P. Chen, W. G. Wang, J. Wu, T. Y. Chen, J. Q. Xiao, and C. L. Chien, Physical Review Letters **109**, 107204 (2012).

[44] H. Nakayama, M. Althammer, Y.-T. Chen, K. Uchida, Y. Kajiwara, D. Kikuchi, T. Ohtani, S. Geprägs, M. Opel, S. Takahashi, R. Gross, G. E. W. Bauer, S. T. B. Goennenwein, and E. Saitoh, Physical Review Letters **110**, 206601 (2013).

[45] N. Vlietstra, J. Shan, V. Castel, B. J. van Wees, and J. Ben Youssef, Physical Review B **87**, 184421 (2013).

[46] M. Althammer, S. Meyer, H. Nakayama, M. Schreier, S. Altmannshofer, M. Weiler, H. Huebl, S. Geprägs, M. Opel, R. Gross, D. Meier, C. Klewe, T. Kuschel, J.-M. Schmalhorst, G. Reiss, L. Shen, A. Gupta, Y.-T. Chen, G. E. W. Bauer, E. Saitoh, and S. T. B. Goennenwein, Physical Review B **87**, 224401 (2013).

[47] Y. M. Lu, J. W. Cai, S. Y. Huang, D. Qu, B. F. Miao, and C. L. Chien, Physical Review B **87**, 220409 (2013).

[48] M. Isasa, A. Bedoya-Pinto, S. Velez, F. Golmar, F. Sanchez, L. Hueso, J. Fontcuberta, and F. Casanova, Applied Physics Letters **105**, 142402 (2014).

[49] Y. M. Lu, Y. Choi, C. M. Ortega, M. X. Cheng, J. W. Cai, S. Y. Huang, L. Sun, and C. L. Chien, Physical Review Letters **110**, 147207 (2013).

[50] S. Meyer, M. Althammer, S. Geprägs, M. Opel, R. Gross, and S. T. B. Goennenwein, Applied Physics Letters **104**, 242411 (2014).

[51] O. Stern, Zeitschrift für Physik **7**, 249 (1921).

[52] W. Gerlach and O. Stern, Zeitschrift für Physik **9**, 353 (1922).

[53] J. J. Sakurai, *Modern Quantum Mechanics (Revised Edition)* (Addison Wesley, 1993), 1st ed.

[54] F. D. Czeschka, *Spin Currents in Metallic Nanostructures*, Ph.D. thesis, Technische Universität München (2011).

[55] M. Dyakonov and V. Perel, Physics Letters A **35**, 459 (1971).

[56] J. E. Hirsch, Physical Review Letters **83**, 1834 (1999).

[57] R. Karplus and J. M. Luttinger, Physical Review **95**, 1154 (1954).

[58] L. Berger, Physical Review B **2**, 4559 (1970).

[59] M. V. Berry, Proceedings of the Royal Society of London A: Mathematical, Physical and Engineering Sciences **392**, 45 (1984).

[60] N. Nagaosa, S. Onoda, A. H. MacDonald, and N. P. Ong, Review of Modern Physics **82**, 1539 (2010).

[61] S. Onoda, N. Sugimoto, and N. Nagaosa, Physical Review Letters **97**, 126602 (2006).

[62] S. Onoda, N. Sugimoto, and N. Nagaosa, Physical Review B **77**, 165103 (2007).

[63] M. Reinwald, *Herstellung und Charakterisierung von ferromagnetischem (Ga,Mn)As auf der GaAs (001)- und (311)A-Oberfläche*, Ph.D. thesis, Universität Regensburg (2005).

[64] S. Lowitzer, M. Gradhand, D. Ködderitzsch, D. V. Fedorov, I. Mertig, and H. Ebert, Physical Review Letters **106**, 056601 (2011).

[65] C. M. Hurd, *The Hall effect in metals and alloys* (Plenum Press, 1972).

[66] E. H. Hall, American Journal of Mathematics **2**, 287 (1879).

[67] Y. K. Kato, R. C. Myers, A. C. Gossard, and D. D. Awschalom, Science **306**, 1910 (2004).

[68] D. Qu, S. Y. Huang, B. F. Miao, S. X. Huang, and C. L. Chien, Physical Review B **89**, 140407 (2014).

[69] C.-F. Pai, L. Liu, Y. Li, H. W. Tseng, D. C. Ralph, and R. A. Buhrman, Applied Physics Letters **101**, 122404 (2012).

[70] R. Gross and A. Marx, *Festkörperphysik* (Oldenbourg Verlag München, 2012).

[71] S. Datta, *Electronic transport in mesoscopic systems* (Cambridge University Press, 2007).

[72] N. H. Long, P. Mavropoulos, B. Zimmermann, D. S. G. Bauer, S. Blügel, and Y. Mokrousov, Physical Review B **90**, 064406 (2014).

[73] M. Isasa, E. Villamor, L. E. Hueso, M. Gradhand, and F. Casanova, Physical Review B **91**, 024402 (2015).

[74] M. Obstbaum, M. Härtinger, H. G. Bauer, T. Meier, F. Swientek, C. H. Back, and G. Woltersdorf, Physical Review B **89**, 060407 (2014).

[75] V. Vlaminck, J. E. Pearson, S. D. Bader, and A. Hoffmann, Physical Review B **88**, 064414 (2013).

[76] W. Zhang, V. Vlaminck, J. E. Pearson, R. Divan, S. D. Bader, and A. Hoffmann, Applied Physics Letters **103**, 242414 (2013).

[77] A. Azevedo, L. H. Vilela-Leão, R. L. Rodríguez-Suárez, A. F. Lacerda Santos, and S. M. Rezende, Physical Review B **83**, 144402 (2011).

[78] S. Maekawa, *Concepts in Spin Electronics* (Oxford University Press, 2008).

[79] J. Slonczewski, Journal of Magnetism and Magnetic Materials **159**, 1 (1996).

[80] L. Berger, Physical Review B **54**, 9353 (1996).

[81] E. B. Myers, D. C. Ralph, J. A. Katine, R. N. Louie, and R. A. Buhrman, Science **285**, 867 (1999).

[82] J. Xiao, Introduction to spin transfer torque., Webpage Fudan University, http://homepage.fudan.edu.cn/jxiao/research/spin-transfer-torque retrieved 22 April 2015.

[83] M. D. Stiles and A. Zangwill, Physical Review B **66**, 014407 (2002).

[84] A. Brataas, G. E. Bauer, and P. J. Kelly, Physics Reports **427**, 157 (2006).

[85] Y. Tserkovnyak, A. Brataas, and G. E. W. Bauer, Physical Review B **66**, 10 (2002).

[86] K. Xia, P. Kelly, G. E. W. Bauer, A. Brataas, and I. Turek, Physical Review B **65**, 220401 (2002).

[87] D. Huertas Hernando, Y. Nazarov, A. Brataas, and G. E. W. Bauer, Physical Review B **62**, 5700 (2000).

[88] A. Brataas, Y. V. Nazarov, and G. E. W. Bauer, Physical Review Letters **84**, 2481 (2000).

[89] M. D. Stiles and A. Zangwill, Physical Review B **66**, 014407 (2002).

[90] Z. Wang, Y. Sun, M. Wu, V. Tiberkevich, and A. Slavin, Physical Review Letters **107**, 146602 (2011).

[91] E. Padron-Hernandez, A. Azevedo, and S. M. Rezende, Applied Physics Letters **99**, 192511 (2011).

[92] D. C. Ralph and M. D. Stiles, Journal of Magnetism and Magnetic Materials **320**, 1190 (2008).

[93] Z. Wang, Y. Sun, Y.-Y. Song, M. Wu, H. Schultheiß, J. E. Pearson, and A. Hoffmann, Applied Physics Letters **99**, 162511 (2011).

[94] Y. Kajiwara, K. Harii, S. Takahashi, J. Ohe, K. Uchida, M. Mizuguchi, H. Umezawa, H. Kawai, K. Ando, K. Takanashi, S. Maekawa, and E. Saitoh, Nature **464**, 262 (2010).

[95] N. Vlietstra, J. Shan, V. Castel, J. Ben Youssef, G. E. W. Bauer, and B. J. v. Wees, Applied Physics Letters **103**, 032401 (2013).

[96] C. Hahn, G. de Loubens, O. Klein, M. Viret, V. V. Naletov, and J. Ben Youssef, Physical Review B **87**, 174417 (2013).

[97] S. Cho, S.-H. C. Baek, K.-D. Lee, Y. Jo, and B.-G. Park, Scientific Reports **5**, 14668 (2015).

[98] J. Kim, P. Sheng, S. Takahashi, S. Mitani, and M. Hayashi, ArXiv e-prints 1503.08903 (2015).

[99] R. Gross, Spintronics. lecture notes, TU München (2004).

[100] I. A. Campbell, Proceedings of the Physical Society **89**, 71 (1966).

[101] G. Bergmann, Physical Review Letters **41**, 264 (1978).

[102] W. Thomson, Proceedings of the Royal Society of London **8**, 546 (1856).

[103] T. McGuire and R. Potter, IEEE Transactions on Magnetics **11**, 1018 (1975).

[104] A. Hoffmann, J. W. Seo, M. R. Fitzsimmons, H. Siegwart, J. Fompeyrine, J.-P. Locquet, J. A. Dura, and C. F. Majkrzak, Physical Review B **66**, 220406 (2002).

[105] F. Wilhelm, P. Poulopoulos, G. Ceballos, H. Wende, K. Baberschke, P. Srivastava, D. Benea, H. Ebert, M. Angelakeris, N. K. Flevaris, D. Niarchos, A. Rogalev, and N. B. Brookes, Physical Review Letters **85**, 413 (2000).

[106] S. Geprägs, S. Meyer, S. Altmannshofer, M. Opel, F. Wilhelm, A. Rogalev, R. Gross, and S. T. B. Goennenwein, Applied Physics Letters **101**, 262407 (2012).

[107] T. Kuschel, C. Klewe, J.-M. Schmalhorst, F. Bertram, O. Schuckmann, T. Schemme, J. Wollschläger, S. Francoual, J. Strempfer, A. Gupta, M. Meinert, G. Götz, D. Meier, and G. Reiss, Physical Review Letters **115**, 097401 (2015).

[108] W. J. Antel, M. M. Schwickert, T. Lin, W. L. O'Brien, and G. R. Harp, Phys. Rev. B **60**, 12933 (1999).

[109] S. Geprägs, S. T. B. Goennenwein, M. Schneider, F. Wilhelm, K. Ollefs, A. Rogalev, M. Opel, and R. Gross, submitted (2013).

[110] M. Althammer, *Spin-transport-penomena in metals, semiconductors, and insulators*, Ph.D. thesis, Technische Universität München (2012).

[111] D. Irber, Spin hall magnetoresistance in FMI/N/FMI trilayers, Bachelor's thesis, TU München (2013).

[112] W. Limmer, M. Glunk, J. Daeubler, T. Hummel, W. Schoch, R. Sauer, C. Bihler, H. Huebl, M. S. Brandt, and S. T. B. Goennenwein, Physical Review B **74**, 205205 (2006).

[113] W. Limmer, J. Daeubler, L. Dreher, M. Glunk, W. Schoch, S. Schwaiger, and R. Sauer, Physical Review B **77**, 205210 (2008).

[114] O. Panchenko, P. Lutsishin, and Y. G. Ptushinskii, Journal of Experimental and Theoretical Physics **29**, 134 (1969).

[115] R. Schlitz, Hall effect measurements in YIG/Pt hybrids, Bachelor's thesis, TU München (2013).

[116] D. B. Poker and C. E. Klabunde, Physical Review B **26**, 7012 (1982).

[117] G. Fischer, H. Hoffmann, and J. Vancea, Physical Review B **22**, 6065 (1980).

[118] J. Zhang, Y. Nagao, S. Kuwano, and Y. Ito, Japanese Journal of Applied Physics **36**, 834 (1997).

[119] T. Meier, High resolution resistance measurements, Bachelor's thesis, TU München (2014).

[120] S. Meyer, *Magneto-themogalvanische Experimente an (Ga,Mn)As Dünnfilmen*, Diploma thesis, LMU München (2012).

[121] C. Bihler, M. Althammer, A. Brandlmaier, S. Geprägs, M. Weiler, M. Opel, W. Schoch, W. Limmer, R. Gross, M. S. Brandt, and S. T. B. Goennenwein, Physical Review B **78**, 045203 (2008).

[122] P. Muduli, K. Friedland, J. Herfort, H. Schönherr, and K. Ploog, Physical Review B **72**, 104430 (2005).

[123] S. A. Manuilov, R. Fors, S. I. Khartsev, and A. M. Grishin, Journal of Applied Physics **105**, 033917 (2009).

[124] K. Ganzhorn and M. Althammer, private communication.

[125] S. Altmannshofer, *Epitaxie und Characterisierung von dünnen Schichten des ferromagnetischen Isolators* $Y_3Fe_5O_{12}$, Master's thesis, TU München (2012).

[126] X. Jia, K. Liu, K. Xia, and G. E. W. Bauer, Europhysics Letters **96**, 17005 (2011).

[127] Lotze, *Spin pumping in ferrimagnet/normal metal bilayers*, Ph.D. thesis, Technische Universität München (2015).

[128] S. R. Marmion, M. Ali, M. McLaren, D. A. Williams, and B. J. Hickey, Physical Review B **89**, 220404 (2014).

[129] K. Uchida, Z. Qiu, T. Kikkawa, R. Iguchi, and E. Saitoh, Applied Physics Letters **106**, 052405 (2015).

[130] H. Ulrichs, V. E. Demidov, S. O. Demokritov, W. L. Lim, J. Melander, N. Ebrahim-Zadeh, and S. Urazhdin, Applied Physics Letters **102**, 132402 (2013).

[131] L. Vila, T. Kimura, and Y. Otani, Physical Review Letters **99**, 226604 (2007).

[132] H. Kurt, R. Loloee, K. Eid, W. P. Pratt, and J. Bass, Applied Physics Letters **81**, 4787 (2002).

[133] T. Kimura, Y. Otani, T. Sato, S. Takahashi, and S. Maekawa, Physical Review Letters **98**, 156601 (2007).

[134] K. Ando, S. Takahashi, K. Harii, K. Sasage, J. Ieda, S. Maekawa, and E. Saitoh, Physical Review Letters **101**, 036601 (2008).

[135] T. Seki, Y. Hasegawa, S. Mitani, S. Takahashi, H. Imamura, S. Maekawa, J. Nitta, and K. Takanashi, Nature Materials **7**, 125 (2008).

[136] M. Gradhand, D. V. Fedorov, P. Zahn, and I. Mertig, Physical Review B **81**, 245109 (2010).

[137] R. Rösselhuber, *Photoconductivity Measurements in Yttrium Iron Garnet Thin Films*, Master's thesis, TU München (2014).

[138] G. Winkler, *Magnetic garnets*, Vieweg tracts in pure and applied physics (Vieweg, 1981).

[139] H. Hoffmann, F. Hofmann, and W. Schoepe, Physical Review B **25**, 5563 (1982).

[140] E. Abrahams, P. W. Anderson, D. C. Licciardello, and T. V. Ramakrishnan, Physical Review Letters **42**, 673 (1979).

[141] B. L. Altshuler, D. Khmel'nitzkii, A. I. Larkin, and P. A. Lee, Physical Review B **22**, 5142 (1980).

[142] F. Schade, Fabrication and characterization of $Y_3Fe_5O_{12}/Pt/Y_3Fe_5O_{12}$ trilayers for spin current based experiments, Bachelor's thesis, TU München (2013).

[143] O. d'Allivy Kelly, A. Anane, R. Bernard, J. Ben Youssef, C. Hahn, A.-H. Molpeceres, C. Carrétéro, E. Jacquet, C. Deranlot, P. Bortolotti, R. Lebourgeois, J.-C. Mage, de, O. Klein, V. Cros, and A. Fert, Applied Physics Letters **103**, 082408 (2013).

[144] S. Klingler, private communication.

[145] T. Aderneuer, Dependence of the spin hall magnetoresistance on the interface magnetic moment density in $Pt/Y_3Fe_5O_{12}$ bilayers, Bachelor's thesis, TU München (2014).

[146] H. Maier-Flaig, private communication.

[147] T. Lin, C. Tang, and J. Shi, Applied Physics Letters **103**, 132407 (2013).

[148] S. Meyer, R. Schlitz, S. Geprägs, M. Opel, H. Huebl, R. Gross, and S. T. B. Goennenwein, Applied Physics Letters **106**, 132402 (2015).

[149] E. H. Hall, Philosopical Magazine **12** (1881).

[150] P. Gehlhoff, E. Justi, and M. Kohler, Zeitschrift für Naturforschung **5a**, 16 (1950).

[151] S. Shimizu, K. S. Takahashi, T. Hatano, M. Kawasaki, Y. Tokura, and Y. Iwasa, Physical Review Letters **111**, 216803 (2013).

[152] B. F. Miao, S. Y. Huang, D. Qu, and C. L. Chien, Physical Review Letters **112**, 236601 (2014).

[153] Y. Shiomi, T. Ohtani, S. Iguchi, T. Sasaki, Z. Qiu, H. Nakayama, K. Uchida, and E. Saitoh, Applied Physics Letters **104**, 242406 (2014).

[154] S.-C. Shin, G. Srinivas, Y.-S. Kim, and M.-G. Kim, Applied Physics Letters **73**, 393 (1998).

[155] D. K. Satapathy, M. A. Uribe-Laverde, I. Marozau, V. K. Malik, S. Das, T. Wagner, C. Marcelot, J. Stahn, S. Brück, A. Rühm, S. Macke, T. Tietze, E. Goering, A. Frañó, J. H. Kim, M. Wu, E. Benckiser, B. Keimer, A. Devishvili, B. P. Toperverg, M. Merz, P. Nagel, S. Schuppler, and C. Bernhard, Physical Review Letters **108**, 197201 (2012).

[156] S. Datta and B. Das, Applied Physics Letters **56**, 665 (1990).

[157] J. Wunderlich, B.-G. Park, A. C. Irvine, L. P. Zarbo, E. Rozkotova, P. Nemec, V. Novak, J. Sinova, and T. Jungwirth, Science **330**, 1801 (2010).

[158] C. Betthausen, T. Dollinger, H. Saarikoski, V. Kolkovsky, G. Karczewski, T. Wojtowicz, K. Richter, and D. Weiss, Science **337**, 324 (2012).

[159] J. Flipse, F. K. Dejene, D. Wagenaar, G. E. W. Bauer, J. B. Youssef, and B. J. van Wees, Physical Review Letters **113**, 027601 (2014).

[160] J. Flipse, F. L. Bakker, A. Slachter, F. K. Dejene, and B. J. van Wees, Nature Nanotechnology **7**, 166 (2012).

[161] S.-G. Cheng, Y. Xing, Q.-F. Sun, and X. C. Xie, Physical Review B **78**, 045302 (2008).

[162] X. Liu and X. Xie, Solid State Communications **150**, 471 (2010).

[163] K. Tauber, D. V. Fedorov, M. Gradhand, and I. Mertig, Physical Review B **87**, 161114 (2013).

[164] S. Wimmer, D. Ködderitzsch, K. Chadova, and H. Ebert, Physical Review B **88**, 201108 (2013).

[165] S. Wimmer, D. Koedderitsch, and H. Ebert, Spin nernst angle of platinum from first principles, unpublished.

[166] S. Meyer, Y.-T. Chen, S. Wimmer, M. Althammer, M. Frank, M. Schreier, J. Lotze, S. Geprägs, H. Huebl, D. Koedderitsch, H. Ebert, G. E. W. Bauer, R. Gross, and S. T. B. Goennenwein, Experimental observation of the spin nernst effect, unpublished.

[167] A. von Ettingshausen and W. Nernst, Annalen der Physik **265**, 343 (1886).

[168] R. Lück and T. Ricker, Physica Status Solidi **7**, 817 (1964).

[169] S. Takahashi and S. Maekawa, Science and Technology of Advanced Materials **9**, 014105 (2008).

[170] L. Onsager, Physical Review **37**, 405 (1931).

[171] L. Onsager, Physical Review **38**, 2265 (1931).

[172] P. C. van Son, H. van Kempen, and P. Wyder, Physical Review Letters **58**, 2271 (1987).

[173] W.-L. Lee, S. Watauchi, V. L. Miller, R. J. Cava, and N. P. Ong, Physical Review Letters **93**, 4 (2004).

[174] Y. Pu, E. Johnston-Halperin, D. D. Awschalom, and J. Shi, Physical Review Letters **97**, 036601 (2006).

[175] Y. Pu, D. Chiba, F. Matsukura, H. Ohno, and J. Shi, Physical Review Letters **101**, 117208 (2008).

[176] J. P. Moore and R. S. Graves, Journal of Applied Physics **44**, 1174 (1973).

[177] L. Aksyutov, Journal of engineering physics **27**, 913 (1974).

[178] A. W. Smith, Physical Review Series I **33**, 295 (1911).

[179] Crystran, Yttrium aluminium garnet data stheet, Tech. rep., Crystran Ltd. (2012).

[180] N. N. Sirota, P. A. Popv, and I. A. Ivanov, Crystal Research and Technology **27**, 535 (1992).

[181] L. J. Cornelissen, J. Liu, R. A. Duine, J. B. Youssef, and B. J. van Wees, Nature Physics **advance online publication**, (2015).

[182] S. T. B. Goennenwein, R. Schlitz, M. Pernpeintner, M. Althammer, R. Gross, and H. Huebl, Applied Physics Letters **107**, 172405 (2015).

[183] Z. Qiu, D. Hou, T. Kikkawa, K. Uchida, and E. Saitoh, Applied Physics Express **8**, 083001 (2015).

[184] M. A. El Khakani, M. Chaker, and E. Gat, Applied Physics Letters **69**, 2027 (1996).

[185] K. Ganzhorn, *Experimental Study of Spin Currents in Compensated Rare Earth Garnets*, Master's thesis, TU München (2014).

[186] F. Della Coletta, *Spin Seebeck Effect in Rare Earth Iron Garnets*, Master's thesis, TU München (2015).

[187] M. Akyol, G. Yu, J. G. Alzate, P. Upadhyaya, X. Li, K. L. Wong, A. Ekicibil, P. Khalili Amiri, and K. L. Wang, Applied Physics Letters **106**, 162409 (2015).

[188] L. Liu, C.-F. Pai, Y. Li, H. W. Tseng, D. C. Ralph, and R. A. Buhrman, Science **336**, 555 (2012).

[189] Q. Hao and G. Xiao, Physical Review Applied **3**, 034009 (2015).

[190] T. Kuschel, C. Klewe, J.-M. Schmalhorst, F. Bertram, O. Kuschel, T. Schemme, J. Wollschläger, S. Francoual, J. Strempfer, A. Gupta, M. Meinert, G. Götz, D. Meier, and G. Reiss, Physical Review Letters **115**, 097401 (2015).

[191] D. Meier, D. Reinhardt, M. Schmid, C. H. Back, J.-M. Schmalhorst, T. Kuschel, and G. Reiss, Phys. Rev. B **88**, 184425 (2013).

[192] D. Qu, S. Y. Huang, J. Hu, R. Wu, and C. L. Chien, Physical Review Letters **110**, 067206 (2013).

[193] K. Uchida, T. Nonaka, T. Kikkawa, Y. Kajiwara, and E. Saitoh, Physical Review B **87**, 104412 (2013).

[194] T. Kikkawa, K. Uchida, S. Daimon, Y. Shiomi, H. Adachi, Z. Qiu, D. Hou, X.-F. Jin, S. Maekawa, and E. Saitoh, Physical Review B **88**, 214403 (2013).

[195] K. Uchida, M. Ishida, T. Kikkawa, A. Kirihara, T. Murakami, and E. Saitoh, Journal of Physics: Condensed Matter **26**, 343202 (2014).

[196] G. Siegel, M. C. Prestgard, S. Teng, and A. Tiwari, Scientific Reports **4**, 4429 (2014).

[197] M. Schreier, N. Roschewsky, E. Dobler, S. Meyer, H. Huebl, R. Gross, and S. T. B. Goennenwein, Applied Physics Letters **103**, 242404 (2013).

[198] D. Lide, *CRC Handbook of Chemistry and Physics, 89th Edition* (Taylor & Francis, 2008).

[199] N. P. Padture and P. G. Klemens, Journal of the American Ceramic Society **80**, 1018 (1997).

[200] A. Hofmeister, Physics and Chemistry of Minerals **33**, 45 (2006).

[201] A. E. Clark and R. E. Strakna, Journal of Applied Physics **32**, 1172 (1961).

List of publications

1. S. Geprägs, S. Meyer, S. Altmannshofer, M. Opel, F. Wilhelm, A. Rogalev, R. Gross, and S. T. B. Goennenwein, *Investigation of induced Pt magnetic polarization in Pt/Y₃Fe₅O₁₂ bilayers*, Applied Physics Letters **101**, 262407 (2012).

2. M. Althammer, S. Meyer, H. Nakayama, M. Schreier, S. Altmannshofer, M. Weiler, H. Huebl, S. Geprägs, M. Opel, R. Gross, D. Meier, C. Klewe, T. Kuschel, J.-M. Schmalhorst, G. Reiss, L. Shen, A. Gupta, Y.-T. Chen, G. E. W. Bauer, E. Saitoh and S. T. B. Goennenwein, *Quantitative study of the spin Hall magnetoresistance in ferromagnetic insulator/normal metal hybrids*, Physical Review B **87**, 224401 (2013).

3. M. Weiler, M. Althammer, M. Schreier, J. Lotze, M. Pernpeintner, S. Meyer, H. Huebl, R. Gross, A. Kamra, J. Xiao, Y.-T. Chen, H. Jiao, G. E. W. Bauer, and S. T. B. Goennenwein, *Experimental test of the spin mixing interface conductivity concept*, Physical Review Letters **111**, 176601 (2013).

4. M. Schreier, N. Roschewsky, E. Dobler, S. Meyer, H. Huebl, R. Gross and S. T. B. Goennenwein, *Current heating induced spin Seebeck effect*, Applied Physics Letters **103**, 242404 (2013).

5. S. Meyer, M. Althammer, S. Geprägs, M. Opel, R. Gross and S. T. B. Goennenwein, *Temperature dependent spin transport properties of platinum inferred from spin Hall magnetoresistance measurements* , Applied Physics Letters **104**, 242411 (2014).

6. N. Roschewsky, M. Schreier, A. Kamra, F. Schade, K. Ganzhorn, S. Meyer, H. Huebl, S. Geprägs, R. Gross, and S. T. B. Goennenwein, *Time resolved spin Seebeck effect experiments*, Applied Physics Letters **104**, 202410 (2014).

7. A. Kamra, F. Witek, S. Meyer, H. Huebl, S. Geprägs, R. Gross, G. E. W. Bauer and S. T. B. Goennenwein, *Spin Hall noise*, Physical Review B **90**, 214419 (2014).

8. S. Meyer, R. Schlitz, S. Geprägs, M. Opel, H. Huebl, R. Gross, and S. T. B. Goennenwein, *Anomalous Hall effect in YIG/Pt bilayers*, Applied Physics Letters **106**, 132402 (2015).

9. S. Geprägs, A. Kehlberger, T. Schulz, C. Mix, F. Della Coletta, S. Meyer, A. Kamra, M. Althammer, G. Jakob, H. Huebl, R. Gross, S. T. B. Goennenwein and M. Kläui *Origin of the spin Seebeck effect probed by temperature dependent measurements in* $Gd_3Fe_5O_{12}$, submitted (2015).

10. S. Meyer, Y.-T. Chen, S. Wimmer M. Frank, M. Althammer, M. Schreier, J. Lotze, H. Huebl, R. Gross, D. Koedderitzsch, H. Ebert, G. E. W. Bauer, and S. T. B. Goennenwein, *Experimental observation of the spin Nernst effect*, in preparation (2015).

11. S. Meyer, M. Althammer, H. Huebl, R. Gross, and S. T. B. Goennenwein, *Absence of Onsager reciprocal relations in magnetothermopower experiments on (Ga,Mn)As*, in preparation (2015).

Acknowledgment

This thesis would have never been created without the support and the contribution of several people. Therefore, I address my sincere thanks to my supervisors, collaborators, colleagues and friends, in particular to

- *Prof. Dr. Rudolf Gross,* for giving me the opportunity to become a member of the Walther Meißner Institut. Professor Gross always supported my work with fruitful discussions and ideas for improvement. I appreciate that he shared his broad knowledge with me and gave me the freedom of choice to develop new ideas.

- *Dr. Sebastian T. B. Goennenwein,* for supervising this thesis and inspiring me with his enthusiasm for physics. Sebastian always encouraged me to find new ways for solving issues and to follow new ideas. His valuable comments improved the interpretation of my obtained results and the quality of my manuscripts.

- *Dr. Stephan Geprägs,* for introducing me to the growth of yttrium iron garnets via PLD, and for keeping the sample growth alive whatever happened. Numerous fruitful discussions and lots of tips from Steve not only improved the quality of my samples, but also my understanding of physics.

- *Dr. Matthias Opel,* for his guidance during various VTI-"surgeries" and for keeping up a good atmosphere even when everything seemed to crash down. I furthermore acknowledge Matthias for contributing SQUID measurements, and for valuable discussions and comments on my experiments and manuscripts.

- *Dr. Matthias Althammer,* for sharing his profound knowledge on both spin currents and measurement equipment and always having an open ear to my questions. Additionally, I want to thank Matthias for proofreading this thesis and his suggestions for improvement.

- *Dr. Hans Hübl,* for taking his time to discuss my data, and finding both hidden links and issues by asking the right questions. Even though this sometimes taught me to go back to the drawing-board again, I learned to try to get to the bottom of everything.